



**HAL**  
open science

## Oxidation stability of fuels in liquid phase

Karl Chatelain

► **To cite this version:**

Karl Chatelain. Oxidation stability of fuels in liquid phase. Chemical engineering. Université Paris Saclay (COmUE), 2016. English. NNT : 2016SACL020 . tel-01958391

**HAL Id: tel-01958391**

**<https://pastel.hal.science/tel-01958391>**

Submitted on 18 Dec 2018

**HAL** is a multi-disciplinary open access archive for the deposit and dissemination of scientific research documents, whether they are published or not. The documents may come from teaching and research institutions in France or abroad, or from public or private research centers.

L'archive ouverte pluridisciplinaire **HAL**, est destinée au dépôt et à la diffusion de documents scientifiques de niveau recherche, publiés ou non, émanant des établissements d'enseignement et de recherche français ou étrangers, des laboratoires publics ou privés.

NNT : 2016SACLAY020

**THÈSE DE DOCTORAT  
DE L'UNIVERSITE PARIS-SACLAY**

préparée à

**L'ENSTA ParisTech**

ÉCOLE DOCTORALE N°579

Sciences Mécaniques et Énergétiques, Matériaux et Géosciences (SMEMAG)

Spécialité de doctorat : Génie des procédés

par

**Karl CHATELAIN**

Etude de la stabilité à l'oxydation des carburants  
en phase liquide

**Thèse présentée et soutenue à Rueil-Malmaison, le 15 décembre 2016**

**Composition du jury :**

Dr. André NICOLLE	Président	IFP Energies nouvelles, R102
Pr. Richard WEST	Rapporteur	Northeastern University, Boston, CoMoChEng
Pr. Pierre-Alexandre GLAUDE	Rapporteur	CNRS Nancy, LRGF
Dr. Mickael SICARD	Examineur	ONERA, DEFA
Dr. Thomas DUBOIS	Examineur	TOTAL ACS
Dr. Laurie STARCK	Examineur	IFP Energies nouvelles, R104
Mme. Arij BEN AMARA	Examineur	IFP Energies nouvelles, R104
Pr. Laurent CATOIRE	Directeur de Thèse	ENSTA ParisTech, Université Paris-Saclay, UCP



# Acknowledgements

This work was made possible thanks to the support of the *IFP Energies nouvelles (IFPEN)* and the chemical engineering laboratory (UCP) of the *ENSTA ParisTech, Université Paris-Saclay*. It was mainly performed at IFPEN in partnership with several divisions: *powertrain and vehicule (R10) mostly, physics and analysis (R05) and process experiments (R15)*. It also includes several months spent in the *Massachusetts Institute of Technology (MIT)* in Cambridge (MA,USA) as a visiting researcher.

First, I would like to thank the committee for accepting to evaluate this work. In particular, Professor Richard West from *Northeastern University* in Boston and Professor Pierre-Alexandre Glaude from the *CNRS Nancy* for accepting to review my thesis.

I also thank all others committee members, notably Doctor Mickael Sicard from *ONERA* and Doctor Thomas Dubois from *Total ACS*, for their interest in this topic and our fruitful discussions during and after the defence.

I would like to thank Profesor Laurent Catoire, as the laboratory head of *UCP* and my PhD advisor, for his scientific contribution, his time and the trust he placed in me to accomplish this research. In addition, I thank Doctor Laurie Starck for promoting this stimulating research topic at *IFPEN* involving both experimental and modeling work on fuel autoxidation. In addition, I am grateful for the opportunity she gave me to accomplish part of this work in *MIT*. Thus, I am also thankful to Professor William Green and his group for welcoming me as a visiting researcher.

I appreciated the regular discussions and meetings on this research topic with Doctor André Nicolle and Arij Ben Amara, thank you very much for your investment.

I would like to thank all people who contributed to the success of this experimental work, Doctor Maira Alves-Fortunato, Pascal Hayrault, Michel Chardin, Benjamin Veyrat and also the students who contributed to part of the data acquisition Skander and Clara.

Now I would like to thank all colleagues and friends who contributed indirectly to the success of this work with our discussions or just by sharing common hobbies. The IFPEN runners: Mickael, Lama, Jan, Guillaume, Pascal and Patricia. My office mates: Betty, Elias, Benjamin, Edouard and Eleftherios. All others IFPEN colleagues: Sophie, Federico, Valerio, Gorka, Antoine and Detlev. My ENSTA colleagues: Aurélien, Julien, Amir, Zhewei and Johnny. And the others friends not mentioned earlier: Olivier, Larysa, Audrey, Sébastien, Amélie and Romain.

Before to conclude, I especially thank my previous advisors, Pr. Rémy Mével and Pr. Joseph Shepherd with whom my interest in Research started, thanks to their stimulating research topics in the *Explosion Dynamics Laboratory (EDL)* in the *California Institute of Technology (Caltech)*.

Finally, and most importantly, I would like to thank my parents, my family and especially my wife Tiphaine for their understanding, their care and patience during the last three years.



# List of Figures

1.1	CO <sub>2</sub> concentration evolution in the atmosphere over the last ten thousand years [1] . . . . .	2
1.2	Illustration of a local pollution episode which occurred during Spring 2014 in Paris [2] . . . . .	2
1.3	Simplified representation of a common rail injection system in a 4-cylinder engine from [3]. Text in purple represents issues caused by fuel autoxidation. Red dashed blocks represent areas with fuel stresses. Black and grey arrows stand for the fuel flow. Fouling induced by heterogeneous catalysis are not represented but should be considered in every lines. . . . .	2
1.4	Injector deposit formation after 1016 hours of operation with Rapeseed Biodiesel observed by Sem [4] . . . . .	3
1.5	Effect of water on the decomposition of urea [5] . . . . .	3
2.1	Examples of experimental apparatus used in liquid phase autoxidation studies . . . . .	6
2.2	Fuel composition impact on autoxidation rate . . . . .	7
2.3	Impact of oxygen on autoxidation . . . . .	7
2.4	Typical molecule from each antioxidant family. a), b) and c) are respectively H donor, peroxy inhibitor and complexing agent . . . . .	8
2.5	Antioxidant types and concentration effects on autoxidation kinetics. . . . .	8
2.6	Chain length impact on the autoxidation kinetics . . . . .	9
2.7	Uncertainties on the branching impact on autoxidation kinetics . . . . .	9
2.8	Insaturation impact on autoxidation kinetics . . . . .	10
2.9	Specific effect of blending on autoxidation kinetics. . . . .	10
2.10	General presentation of a chain mechanism . . . . .	11
2.11	Global mechanism for liquid phase autoxidation proposed by Zongo [6] . . . . .	11
2.12	Potential initiation steps of liquid phase autoxidation . . . . .	12
2.13	Major pathways leading to oxygenated species formations . . . . .	13
2.14	Major pathways leading to lighter oxidation products formation . . . . .	14
2.15	Major reaction steps from the Bayer-Villiger reaction [7, 8, 9] . . . . .	15
2.16	Illustration of the close relation between chemical and physical processes on deposition mechanism. Modified scheme from Beaver et al. [10] . . . . .	15
2.17	Global process for the deposit formation. The bulk reactivity path (i) is represented with black arrows. The catalytic oxidation path (ii) is represented with purple arrows. The solubility of deposit into fresh solvent (iii) is represented with grey arrows. . . . .	16
2.18	Temperature profile during the autoxidation of several compounds [11] . . . . .	16
2.19	Illustration of Reverse Micelle formation and its implication in the chain mechanism of autoxidation . . . . .	17
2.20	Whitman model presentation for a reacting system consuming A in the liquid phase. $P_A$ is the partial pressure and $C_{A,g}$ the concentration of species A in the gas phase. Indices $g$ , $l$ and $i$ respectively stand for gas liquid, and interface. . . . .	18

2.21	Thermodynamic cycle presenting solvation process. Grey arrow represents the Free energy change between ideal gas to diluted solute in solvent. Diagram is from Jalan et al. [12]	19
2.22	Solvent model illustration from discrete (a) to continuum model (f). Illustration is from Jalan et al. [12]	19
2.23	Solvation effects on activation energies	21
2.24	Typical size of detailed and skeletal mechanisms for hydrocarbon fuels. The figure is from Lu and Law [13]. As presented with the mechanism selected, mechanism size is linearly correlated with the number of species, $Number_{Rxn} = 5 \times Number_{SpC}$	23
3.1	PetroOxy device representation and its typical experimental result	26
3.2	Autoclave scheme and typical experimental signal	27
3.3	Gas chromatograph presentation and a scheme presenting Mass Spectrometer (MS) working principle.	29
3.4	Fourier Transform InfraRed (FTIR)-Attenuated Total Reflectance (ATR) working principle and typical signal presentation	30
3.5	Comparison of HP-5 and DB-FFAP separation capability on an oxidation residual sample.	31
3.6	Illustration of valve timing with the Gas Chromatograph (GC)-Thermal Conductivity Detector (TCD). Area (a) represents the injection loop loading. Area (b) stands for all products elution. At the beginning of the (c) area, the valve V2 switches and traps all light products, and during this period, heavier ones are eluted. In (d), the valve V2 switches back and releases light products trapped in step (b).	33
3.7	Example of Detector Response calculation using the Equivalent Carbon Number (ECN) model. a.u stands for area units. HMF stands for 5-Hydroxymethyl-2-furaldehyde.	34
3.8	Relative Errors ( $RelativeError(RE) = \Delta(D.R.ECN,i - D.R.Exp,i)/D.R.Exp,i$ ) on Detector Response (DR) prediction over the 6 molecules tested for a given ECN reference compound. "Ref. C8" means octane is selected as a reference compound ( $DR_{ref}$ ) in the ECN model	35
3.9	Final predictions on the detector response according to typical chemical families of oxidation products. C <sub>8</sub> and C <sub>12</sub> predictions are obtained according to FID linearity rule and oxygenated molecules predictions are obtained according to the ECN models.	36
3.10	Techniques used to extract Induction Period (IP) from experimental data containing different type of data: Species profiles, macroscopic measurements.	37
3.11	General modeling chain from fuel to reactor	38
3.12	Multi-Scale Approach (MSA) presentation.	38
3.13	Decision diagram presentation	39
3.14	RMG generation process illustration. Species A, B, C and D are reactants. During the initialization step, the algorithm is finding reactions matching those species. After a given reaction time, Species E is passing the tolerance threshold and is added to the core mechanisms. Then new paths are investigated with species E in the core mechanism. Illustration was extracted from a RMG study group presentation [14].	40
3.15	Geometry optimisation process	42
3.16	Potential Energy Surface (PES) with low energy barrier (D step) obtained by Jalan et al. [15] for the Korcek's reaction	42
3.17	Impact of the Absolute TOLerance (ATOL) and Relative TOLerance (RTOL) parameters on the mechanism size.	44
3.18	Adjacency lists illustration. * means this adjacency list contains explanatory H atoms, whereas they are not mandatory. The very first number represents the position of atoms. Then, C and O represent the atoms, then the number stand for the number of radical on the atom, then the list of connection of this atoms are presented between brackets: first number is referring to the atom number and then the letter to the bound type (S: single, D:double)	45

4.1	Typical experimental results and initial oxygen pressure effect on IP measurements . . . . .	48
4.2	Measurements uncertainties induced by purity levels . . . . .	49
4.3	Impact of the chain length on n-alkanes autoxidation within the 393-433 K temperature range.	50
4.4	Impact of the blending on n-paraffins autoxidation using two blends . . . . .	50
4.5	Model validation with current and literature data. Blue and black symbols respectively stand for present study and literature data results. Red dashed and black solid lines respectively stand for fit of experimental data and model predictions. Data are available as a supplementary material. . . . .	53
4.6	Species profile validation of n-decane and n-dodecane mechanisms with literature data. . . . .	54
4.7	Comparison of predicted and experimental IPs for the n-alkanes range. Symbols represent values from the above-mentioned fit of our experimental data. Solid lines correspond to model predictions. . . . .	55
4.8	Fuel RoC analysis performed on $C_8$ and $C_{12}$ mechanisms. IPs are respectively reached at $t = 6890$ s and $t = 4460$ s for $C_8$ and $C_{12}$ models. . . . .	55
4.9	RoC analysis of both HO and HO <sub>2</sub> radicals between $C_8$ and $C_{12}$ mechanisms . . . . .	55
4.10	Reaction families involved in the fuel rate of consumption between $C_8$ and $C_{12}$ mechanisms. Solid and dashed lines, respectively, represent $C_8$ and $C_{12}$ models. . . . .	56
4.11	Macroscopic results for n-octane (n-C8) oxidation at 383 K and 1000 kPa in autoclave . . . . .	58
4.12	Total Ions Current (TIC) MS spectrum for oxidized n-C8 sample filtered with specific m/z ions.	59
4.13	FTIR-ATR analysis of n-C8 sample after 94 h oxidation. Absorption bands 1 and 3 are relevant to C-H bond stretch respectively from CH <sub>3</sub> and CH <sub>2</sub> groups. The absorption band 2 is relevant to C=O bond stretch from n-C8 ketones isomers formed during autoxidation . . . . .	59
4.14	Species profiles of major species identified during n-C8 oxidation at 383 K. . . . .	60
4.15	Species profiles of minor species identified during n-C8 oxidation at 383 K. . . . .	60
4.16	Example of an esterification reaction [16] . . . . .	61
4.17	IP=f(1/T) for the four molecules investigated. . . . .	63
4.18	IP evolution with the number of ramification on $C_8$ alkanes at several temperature . . . . .	64
4.19	Assessment of regressions performance with the ratio of the regression error ( $\Delta(IP_{Reg.} - IP_{Exp.})$ ) over experimental errors ( $\Delta(IP_{Exp.})$ ). When $ Ratio  < 1$ , the error from the regression ( $\Delta(IP_{Reg.} - IP_{Exp.})$ ) is lower than experimental uncertainties. . . . .	65
4.20	Models prediction on IP against present study (blue symbols) and literature data (black symbols). For clarity sake, a regression on present study data (dashed blue line) is performed to assess models (solid black lines) performance. Uncertainties on models prediction correspond to IPs variations between 50-20000 ppm initial Oxygen concentration. . . . .	67
4.21	Model prediction of the branching impact on paraffins oxidation kinetics . . . . .	68
4.22	RE calculations on both present and literature data models to predict IP at several temperatures. . . . .	68
4.23	Effect of both oxygen concentration and temperature on the sum of fuel Rate of Production (RoP) and Rate of Consumption (RoC) respectively presented on the upper and lower parts of each chart. Analysis was conducted at 423 K with 20000 ppm and 1000 ppm of oxygen respectively in solid and dashed lines. . . . .	70
4.24	Effect of oxygen concentration on fuel RoC distribution. Analysis was conducted at 423 K with 20000 ppm and 1000 ppm of oxygen respectively in solid and dashed lines. rOO° stands for the sum of light hydroperoxides from $C_1$ to $C_7$ . . . . .	71
4.25	Effect of oxygen concentration on major species formation. Analysis was conducted at 423 K with 20000 ppm and 1000 ppm of oxygen respectively in solid and dashed lines. . . . .	72
4.26	Temporal evolution of the sum of RoC and RoP with two different pairs of mechanisms. . . . .	74
4.27	Temporal evolution of the RoC distribution with different pairs of mechanisms. . . . .	75



4.28	Macroscopic results for 2-methylheptane (MH) oxidation at 383 K and 1000 kPa in autoclave .	77
4.29	TIC MH spectrum for oxidized octane sample filtered with specific m/z ions. . . . .	78
4.30	FTIR-ATR analysis of MH sample after 24 h oxidation. Absorption bands 1 and 3 are relevant to C-H bond stretch respectively from CH <sub>3</sub> and CH <sub>2</sub> groups. The absorption band 2 is relevant to C=O bond stretch from MH ketones isomers formed during autoxidation. . . . .	78
4.31	Species profiles of major species identified during MH oxidation at 383 K. . . . .	79
4.32	Species profiles of minors species identified during MH oxidation at 383 K. . . . .	80
4.33	Evolution of both IPs and regression parameters as function of the number of carbons of all n-paraffins studied. . . . .	81
4.34	Evolution of both IPs and regression parameters as function of the number of carbons of all iso-paraffins studied. . . . .	81
4.35	Validation of the extended model for n-paraffins chemical families . . . . .	82
4.36	Validation of the extended model for iso-paraffins chemical families . . . . .	82
4.37	Measured IPs for MH according to both experiments . . . . .	83
4.38	Pictures of samples and autoclave content for both n-C8 and MH . . . . .	85
4.39	Two phases analysis on the most oxidized sample of n-C8 experiment . . . . .	86
4.40	Two phases analysis on the most oxidized sample of MH experiment . . . . .	86
4.41	Two phases analysis on the most oxidized sample of n-C8 experiment and theoretical IR spectrum of water from NIST. The area 1 represents the water signal contribution. The area 2 represents the C-H bonds vibrations. The area 3 represents contribution of the C=O bands. . . . .	87
4.42	Example of an esterification reaction [16] . . . . .	87
4.43	Species profiles agreement between experimental results and model predictions on n-C8 at 383K and 10 bars. . . . .	88
4.44	Species profiles agreement between experimental results and model predictions on MH at 383K and 10 bars. . . . .	88
4.45	Species profiles agreement between experimental results and model predictions on n-C8 at 383K and 10 bars with an hypothetical new reactor model. . . . .	90
4.46	Species profiles agreement between experimental results and model predictions on MH at 383K and 10 bars with an hypothetical new reactor model. . . . .	90
4.47	Representation of the sum of products remained in the liquid phase from both n-C8 and MH models predictions at 383 K. . . . .	91
5.1	Schematic presenting the overall methodology used here. The framed block and arrow in green aim to emphasize the current modeling limitation pointed during this work. . . . .	94
6.1	Current liquid phase reactor model representing an homogeneous liquid phase with a set of species (SPC) and its associated mechanism. . . . .	96
6.2	Hypothetical new reactor model with four distinct phases: <i>gas</i> , <i>liquid1</i> , <i>liquid2</i> and <i>solid</i> . Every phase has its own set of species with its own mechanism. Three distincts interfaces are represented in purple to represent the species transport from one phase to another. . . . .	96
6.3	Global process for the deposit formation. The bulk reactivity path (i) is represented with black arrows. The catalytic oxidation path (ii) is represented with purple arrows. The solubility of deposit into fresh solvent (iii) is represented with grey arrows. . . . .	96
4	Thermodynamic cycle to determine formation enthalpy at 298 K for a given hydrocarbon C <sub>x</sub> H <sub>y</sub> . <i>Atom.Energ.</i> correspond to atomization energy. . . . .	107
5	General presentation of each hierarchy defined by Wheeler et al [17]. . . . .	107

6	Comparison of average errors using atomization energies and the new homodesmotic hierarchy presented by Wheeler et al. [17] obtained for conjugated hydrocarbons or not against common theory levels. The two cut off values are respectively from left to right 342 and 36 kcal/mol. . . . .	108
7	Free rotors examples . . . . .	110
8	IP validation with both RMG Java version: 3.2.1 and 4.0.1 . . . . .	112
9	Accuracy of thermochemistry calculations of RMG 3.2.1 and RMG 4.0.1. . . . .	113
10	Illustration of the group representation used in RMG . . . . .	113
11	Presentation of the Evans-Polanyi expression to obtain $E_a$ from the empirical law (4). . . . .	114
12	Impact of both temperature and oxygen concentration on the sum of $\text{HO}_2^\circ$ radical RoP and RoC respectively presented on upper and lower part of each chart. . . . .	115
13	Impact of both temperature and oxygen concentration on the sum of $\text{OH}^\circ$ radical RoP and RoC respectively presented on upper and lower part of each chart. . . . .	116
14	Species profiles agreement between experimental results and model predictions on n-C8 at 383K and 10 bars. . . . .	117
15	Species profiles agreement between experimental results and model predictions on MH at 383K and 10 bars. . . . .	117



# List of Tables

3.1	Typical InfraRed (IR) absorption bands for oxidized paraffins with vibrational mode informations in bracket. . . . .	30
3.2	List of all analytical devices. * sign means those analyses were set for autoclave study and was not available for previous studies. If no holding time are provided in oven programs it means this value equals 0. . . . .	32
3.3	The value of carbons and chemical functions penalties used in the ECN model. . . . .	34
3.4	Summary of ECN model deviation on predicting $D.R._{comp}$ from a given reference compound. S1 corresponds to the sum of the absolute relative errors obtained over the 6 molecules tested for a given reference compound, with $RE = \Delta(D.R._{ECN,i} - D.R._{Exp,i})/D.R._{Exp,i}$ . S2 represents the sum of the absolute relative errors for oxygenated molecules only. . . . .	35
4.1	Identified products in n-alkanes autoxidation in the present study and literature. Lines starting with asterisks correspond to chemical families for which previous studies may not present the full isomer distinction. . . . .	51
4.2	Mechanisms obtained with four n-alkanes . . . . .	52
4.3	Summary of Literature Data Used for Validation. Operating conditions and reconstruction techniques are given to make comparison easier between experimental data. "5% sum of products" means that IP is obtained when the products concentrations sum reaches 5% of initial fuel concentration. PMC stands for Partially Mixed and Closed. "*" means the experimental device has a bubbling system. . . . .	52
4.4	Summary of reactions involved in the RoC analysis of fuel with reaction examples for the octane model with typical kinetic parameters . . . . .	56
4.5	Summary of experimental conditions tested in the present work. . . . .	61
4.6	Mechanisms obtained with the four C <sub>8</sub> -alkanes. . . . .	62
4.7	Coefficients of both linear and exponential regressions . . . . .	64
4.8	Similarities and differences of oxidation products formed between the tested isomers of C <sub>8</sub> . ✓, - and ~ signs respectively mean compounds identified, not identified and traces suspected. . . . .	65
4.9	Literature data used for validation with their associated detection technique.* Due to the possible existence of two oxidation regimes, data below 393 K are not conserved for the validation of 2,2,4-trimethylpentane (TMP) . . . . .	66
4.10	Summary of reactions involved in the RoC analysis of fuel with corresponding kinetic parameters within each label. * Means parameters are identical on each mechanisms. I, II and III mean there is no rate constant distinction if the radical is respectively on a primary, secondary and tertiary carbon. . . . .	69
4.11	Performance of the extended empirical model according to both chemical families and IPs values . . . . .	83
1	Gaussian input file example. The effective input file is within the section filled in grey and comments on each line are in parenthesis. . . . .	109

2	Number of conformers obtained for C <sub>2</sub> -C <sub>16</sub> paraffins with 2 and 3 rotations per rotor following the expression: $Rot^{Number_{dihedrals}}$ . With $Rot$ corresponding to the number of twist per rotors and $Number_{dihedrals} = N_{carbons-1}$ for n-paraffins . . . . .	109
3	RMG input file example. The effective input file is within the section filled in grey and comments on each line are in parenthesis. . . . .	110
4	Elements used in the group definition . . . . .	114

# Abbreviations

<b>A</b> Preexponential factor.	<b>LPA</b> Liquid Phase Autoxidation.
<b>AE</b> Absolute Error.	<b>LSER</b> Linear Solvation Energy Relation.
<b>AH</b> Antioxidant.	<b>MH</b> 2-methylheptane.
<b>ASTM</b> American Society for Testing and Materials.	<b>MS</b> Mass Spectrometer.
<b>ATOL</b> Absolute TOLerance.	<b>MSA</b> Multi-Scale Approach.
<b>ATR</b> Attenuated Total Reflectance.	
<b>BDE</b> Bond Energy Dissociation.	<b>n-C8</b> n-octane.
<b>BtL</b> Biomass to Liquid.	<b>NPD</b> Nitrogen-Phosphorus Detector.
<b>CtL</b> Coal to Liquid.	<b>PES</b> Potential Energy Surface.
<b>DMH</b> 2,5-dimethylheptane.	<b>RE</b> Relative Error.
<b>DR</b> Detector Response.	<b>RF</b> Response Factor.
<b>Ea</b> Activation Energy.	<b>RM</b> Reversed Micelles.
<b>ECN</b> Equivalent Carbon Number.	<b>RMG</b> Reaction Mechanism Generator.
<b>ESC</b> Electronic Structure Calculation.	<b>RoC</b> Rate of Consumption.
<b>FID</b> Flame Ionization Detector.	<b>ROO°</b> alkyl-peroxy radical.
<b>FTIR</b> Fourier Transform InfraRed.	<b>ROOH</b> alkyl-mono-hydroperoxide.
<b>GC</b> Gas Chromatograph.	<b>RoP</b> Rate of Production.
<b>GtL</b> Gas to Liquid.	<b>RSSOT</b> Rapid Small Scale Oxidation Test.
<b>HC</b> Hydrocarbon.	<b>RTOL</b> Relative TOLerance.
<b>HL</b> Henry's Law.	<b>SATP</b> Standard Ambient Temperature and Pressure.
<b>HOOQOO°</b> $\gamma$ -peroxy-alkylhydroperoxy radical.	<b>SCRf</b> Henry's Law.
<b>HOOQOOH</b> alkyl-di-hydroperoxide.	<b>TCD</b> Thermal Conductivity Detector.
<b>IP</b> Induction Period.	<b>THF</b> TetraHydroFuran.
<b>IR</b> InfraRed.	<b>TIC</b> Total Ions Current.
<b>KHP</b> Keto-Hydro-Peroxide.	<b>TMP</b> 2,2,4-trimethylpentane.
<b>KSE</b> Kinetic Solvent Effect.	<b>TST</b> Transition State Theory.
	<b>UV</b> Ultra-Violet.



# Contents

<b>1</b>	<b>Context of the study</b>	<b>1</b>
<b>2</b>	<b>Literature review</b>	<b>5</b>
2.1	Liquid phase autoxidation . . . . .	5
2.1.1	Experimental results of autoxidation studies . . . . .	5
2.1.2	Chemical kinetics of autoxidation . . . . .	9
2.1.3	Oxidation products and deposition processes . . . . .	12
2.2	Solvent modeling . . . . .	15
2.2.1	Heterogeneity inside the liquid bulk . . . . .	15
2.2.2	Phase equilibrium in liquid phase autoxidation . . . . .	17
2.2.3	Solvent effects in liquid phase autoxidation . . . . .	18
2.3	Modeling tools . . . . .	22
2.3.1	Mechanism generators . . . . .	22
2.3.2	Electronic structure calculations . . . . .	23
2.4	Conclusions . . . . .	24
<b>3</b>	<b>Material and Methods</b>	<b>25</b>
3.1	Experimental devices . . . . .	25
3.1.1	PetroOxy experiment . . . . .	25
3.1.2	Autoclave experiment . . . . .	26
3.1.3	Analytical devices . . . . .	28
3.1.4	Calibration coefficient estimation . . . . .	32
3.1.5	Induction Period definitions . . . . .	36
3.2	Molecular modeling approach . . . . .	37
3.2.1	Description of the methodology . . . . .	38
3.2.2	Models coupling . . . . .	39
3.2.3	Key steps of the multi-scale approach . . . . .	43
3.3	Conclusion . . . . .	44
<b>4</b>	<b>Results and Discussions</b>	<b>47</b>
4.1	N-paraffins studies . . . . .	47
4.1.1	Preliminary study with PetroOxy . . . . .	47
4.1.2	Detailed results with autoclave . . . . .	57
4.2	Iso-paraffins studies . . . . .	61
4.2.1	Preliminary study with PetroOxy . . . . .	61
4.2.2	Detailed results with autoclave . . . . .	76



4.3	Discussions . . . . .	79
4.3.1	Structure reactivity impact on paraffins autoxidation . . . . .	79
4.3.2	Experimental results discussions . . . . .	83
4.3.3	Modeling results discussions . . . . .	85
4.4	Conclusion . . . . .	91
<b>5</b>	<b>General conclusions</b>	<b>93</b>
<b>6</b>	<b>Perspectives</b>	<b>95</b>
6.1	New chemical systems . . . . .	95
6.2	New reactor model . . . . .	95
6.3	Reaction Mechanism Generator (RMG) upgrades . . . . .	97
6.3.1	Solvent database upgrade . . . . .	97
6.3.2	Solvent effects on the thermokinetics . . . . .	97
	<b>Bibliography</b>	<b>99</b>
	<b>Appendices</b>	<b>107</b>
.1	Electronic Structure Calculation (ESC) supplementaries . . . . .	107
.2	RMG supplementaries . . . . .	110
.2.1	Reactivity difference between RMG3 and RMG4 mechanisms . . . . .	110
.2.2	Correction on the Free energy of solvation calculation implemented since RMG4 . . . . .	110
.2.3	RMG input file . . . . .	110
.2.4	Molecule identification and thermo-kinetic calculations . . . . .	111
.2.5	RMG thermochemistry calculation . . . . .	112
.2.6	RMG kinetic rate estimation . . . . .	113
.3	Complementary iso-paraffins mechanisms analyses . . . . .	115
.4	Additional figures for species profiles agreements . . . . .	117

# Chapter 1

## Context of the study

Liquid phase stability is a major concern in the transportation and the energy field. Relevant examples are fuels, lubricants and additives which have to be stable from the refinery to their application (engine, combustors). However, liquid phase reactivity can occur even at low or high temperature under many different conditions such as pyrolytic/oxidative, photo-chemically activated, microbiological (aerobic or anaerobic conditions), under atmospheric or pressurized conditions. Different applications can be cited from fuel stability under storage [18] or operating conditions [4] to production industries or health sector such as food, cosmetics and fragrances. In this thesis, fuel stability under both storage and operating conditions are considered where degradations are more likely occurring under the low temperature regime also defined as autoxidation [19].

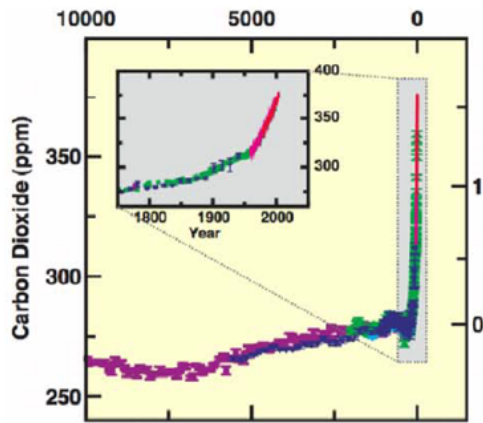
The fuel and transport field is constantly changing due to recent environmental considerations with the reduction of greenhouse gas emissions and the improvement of local air purity respectively presented in [Figure 1.1](#) and [Figure 1.2](#). On one hand, those considerations impact fuel compositions with the increasing use of biofuels (E10, B7) and the diversification of additive packages whose chemistry and interaction with conventional fuel fractions is poorly assessed. On the other hand, they are also the source of many technology improvements (engine downsizing, flex fuels and engine hybridation) or the development of breakthrough technologies and concepts (E100<sup>1</sup>, HCCI<sup>2</sup> engine, RCCI<sup>3</sup> engines, fuel cells). However, technologies using conventional liquid fuels have to be compatible with our current fuel design and engine technologies, particularly in aeronautics where an aircraft lifetime is close to 40 years.

---

<sup>1</sup>E100 stands for pure Ethanol fuel

<sup>2</sup>Homogenous Charge Compression Ignition

<sup>3</sup>Reactivity Controlled Compression Ignition



**Figure 1.1:** CO<sub>2</sub> concentration evolution in the atmosphere over the last ten thousand years [1]

Good air quality

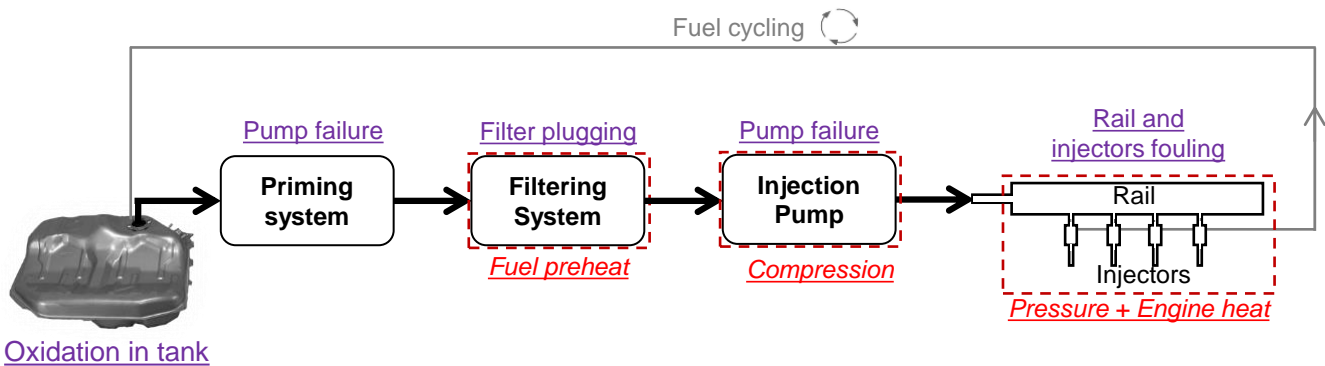


Poor air quality



**Figure 1.2:** Illustration of a local pollution episode which occurred during Spring 2014 in Paris [2]

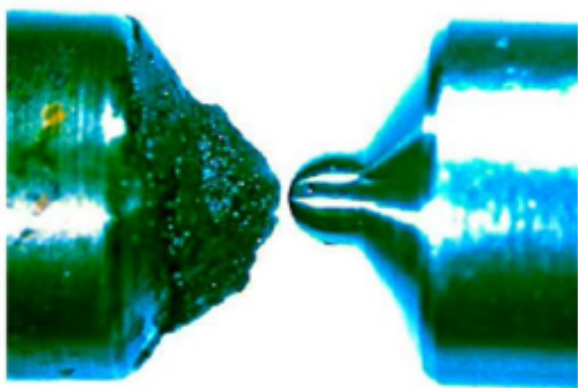
As an example, before the 2000's and the arrival of the direct injection engines in automotive, injection pressures were about 200 bar. Now, with the 4<sup>th</sup> generation of diesel piezo injector, new studies investigate injection pressures above 2500 bar [20, 21]. This drastic pressure increase combined to both engine heat release and fuel cycling increase fuel stresses. In aeronautic field, fuel stress is also occurring where fuel is used as an engine coolant [22, 23, 24], hydraulic fluid and consequently stressed by the variations of temperature and pressure during flight conditions. Those stresses can degrade both jet fuels [25, 26] and diesel fuels [4, 27, 28] to form gums or deposits. Deposits affect the whole engine efficiency, thereby degrading operation of injection units, pumps or filtering system as summarized in Figure 1.3.



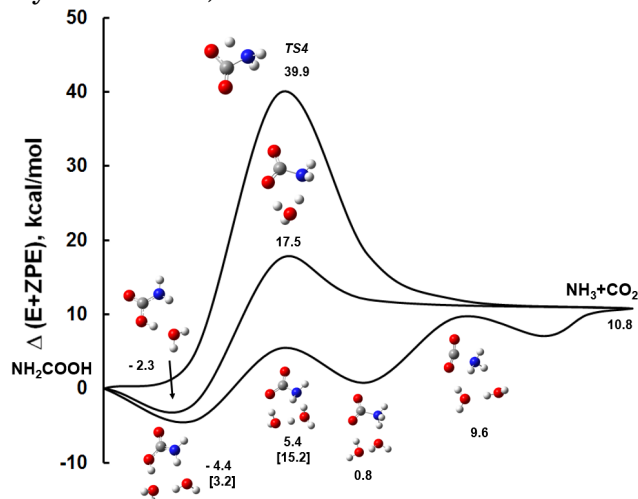
**Figure 1.3:** Simplified representation of a common rail injection system in a 4-cylinder engine from [3]. Text in purple represents issues caused by fuel autoxidation. Red dashed blocks represent areas with fuel stresses. Black and grey arrows stand for the fuel flow. Fouling induced by heterogeneous catalysis are not represented but should be considered in every lines.

Another consequence is the fuel composition change, which may significantly modify fuel properties. For example, hydroperoxides, a known oxidation product in Liquid Phase Autoxidation (LPA) [29, 30, 31, 32, 33], was shown to impact fuel ignition delays [34]. Viscosity may also be impacted by autoxidation process and may increase up to 60-fold in n-alkane autoxidation [35]. To solve these old and well known degradation issues [36, 37], antioxidants are added to the fuel. Antioxidants have a bivalent behaviour according to their concentration or the temperature and can respectively inhibit or promote autoxidation processes as presented by Zabarnick et al. [38]. This bivalent behaviour emphasizes the requirement of an in-depth

knowledge of the autoxidation chemistry. In addition, it had been demonstrated that autoxidation processes cannot be modeled as gas-phase processes [19, 39]. Figure 1.5 presents an example on how solvent can impact both thermochemistry and kinetics. Thus, the modeling of liquid phase autoxidation processes has to integrate solvent effects (on both thermochemistry and kinetics).



**Figure 1.4:** Injector deposit formation after 1016 hours of operation with Rapeseed Biodiesel observed by Sem [4]



**Figure 1.5:** Effect of water on the decomposition of urea [5]

This thesis aims to develop and validate a complete methodology combining both experimental data acquisition and the development of kinetic models for LPA of fuels. However, due to both the variability<sup>4</sup> and the complexity<sup>5</sup> of real fuels composition, the direct kinetic study of fuel autoxidation is not realistic. In agreement with the majors constituents of real fuels [40], and due to their increasing interest as a drop-in fuel, normal and iso-paraffins were subsequently investigated as a fuel surrogate to validate the developed methodology.

The first part of this manuscript will present the state of the art of LPA. From literature review, it highlights the key parameters of autoxidation, well known oxidation pathways and both common experimental and modeling tools used in LPA.

Then, material and methodologies selected and developed within the framework of this thesis are presented. Experimentally, it combines both industrial and research oriented apparatus with several analytical devices. Numerically, a multi-scale methodology developed to generate detailed kinetic models for liquid phase is presented. It is based on an open source code called RMG which generate kinetic models with some solvent effects in the kinetic models. This methodology is then validated with the two experimental devices on both normal and iso paraffins systems. The combination of both results gives access to macroscopic reactivity descriptor IP and detailed species profiles over reaction time. Then, agreements between experimental data and model are discussed quantitatively and qualitatively. In addition to species identification similarities, the mechanisms analyse pointed common oxidation pathways between normal and iso-paraffins compounds.

<sup>4</sup>Variability between seasons for automotive fuels and the Jet A and Jet A-1 differences

<sup>5</sup>Number of species or additives



# Chapter 2

## Literature review

To study liquid phase fuel stability, aspects covering this topic are presented according to three axes. The first is based on experimental literature review to present systems already studied, identify relevant kinetic paths and suspected deposition processes. The second part is focused on presenting chemical engineering aspects involving liquid phase heterogeneity, multi phases interactions, solvent effects occurring in LPA. The last part is devoted to a general presentation of the modeling tools available in literature to perform autoxidation kinetics.

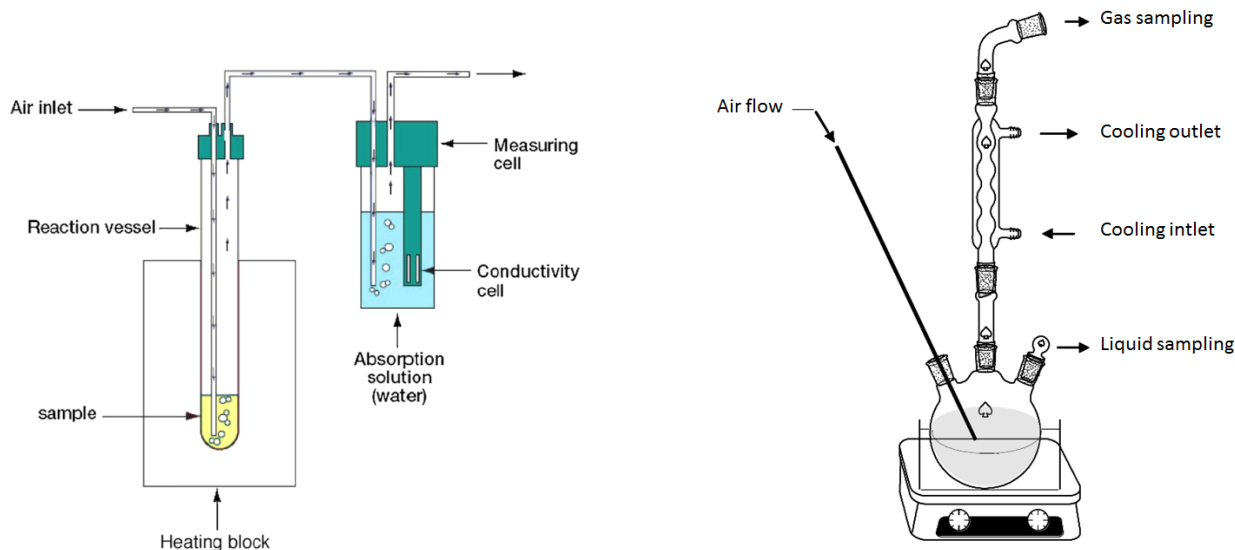
### 2.1 Liquid phase autoxidation

As presented earlier, fuel autoxidation was studied in several industrial contexts starting from crude oil and refinery fouling [41] to fuel aging [4] within fuel injection systems. Due to the complex fuel composition [42, 25, 43], one can distinguish two kinds of literature data. The first one is dedicated to real fuel autoxidation investigating reactivity promoters and inhibitors. The second is more specific to fuel surrogates with studies on specific chemical family (paraffins or aromatics) to reproduce either the reactivity or the deposits formation. Based on this distinction, a first part of the literature review is dedicated to experimental observations to identify relevant parameters and species to consider in LPA. Then, kinetic processes are discussed as well as the chain reactivity of LPA. Finally, a bibliographic review of deposition processes and their relationship with autoxidation phenomena is presented.

#### 2.1.1 Experimental results of autoxidation studies

Autoxidation studies were performed using a variety of experimental apparatus from Rapid Small Scale Oxidation Test (RSSOT) to more research-oriented apparatus (reflux reactor, closed reactors coupled to analytical devices). Due to their specificity, reactor configurations, the mixing system, reactor materials or operating conditions, the results obtained in all these studies may differ from one author to another. In addition, the parameters followed to measure the overall reactivity bring an additional variability of the results. As an example, some authors focused on macroscopic observables such as pressure [9, 44], acidity [45] or conductivity [46] and proposed correlations to obtain the equivalent extent of the fuel consumption. As most of these macroscopic descriptors are presented in section 3, their description is not performed in this review. Other authors performed on-line or off-lines analyses to evaluate oxidation products profiles. In this case, the sampling system and/or the detection technique chosen can induce uncertainties on the quantification that are higher for off-line analysis. These two types of results can be obtained with the

apparatuses presented in [Figure 2.1](#). In order to compare one experiment to another, a set of key parameters is presented to understand promoting or inhibiting effects between each experiment. For the sake of simplicity, those parameters are classified according to their importance.



(a) Example of open-reactor with the monitoring of a macroscopic parameter, the conductivity using the Rancimat experiment [46]

(b) Example of open-reactor with species profile measurements: a reflux reactor with sampling systems [33]

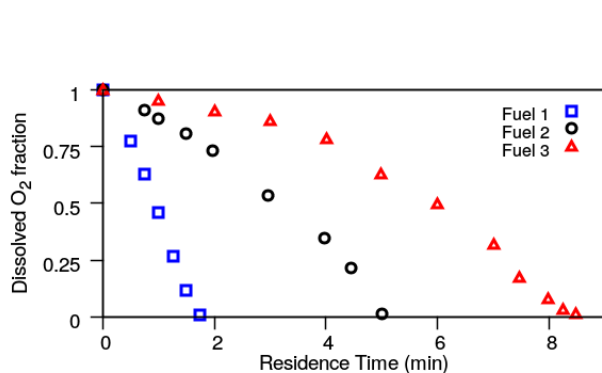
**Figure 2.1:** Examples of experimental apparatus used in liquid phase autoxidation studies

### Key parameters in liquid phase autoxidation

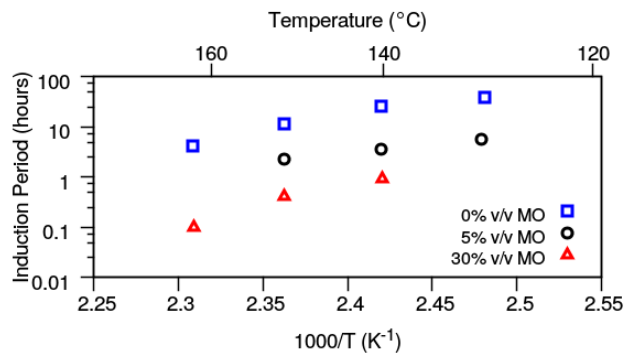
Due to Arrhenius expression, the first key parameter in LPA is the temperature. Thus, as presented in many studies, the reactivity increases exponentially with the temperature. In second, it is the reactant itself (or fuel composition) for which reactivity is highly correlated with the chemical structure. Its impact on the reactivity is well illustrated by C-H Bond Energy Dissociation (BDE) which differs from one chemical species to another [8]. This behaviour is also illustrated by the comparison of different JET A-1 autoxidation tendencies at 185°C [Figure 2.2a](#). This composition effect is also presented in [Figure 2.2b](#) illustrating that methylolate addition into dodecane contributes to increase reactivity. This demonstrates the requirement of multi-component fuel surrogate to model real fuel autoxidation and capture all interactions between each chemical families.

The third major parameter is the oxygen availability in the liquid phase. From the deposition rate presented in [Figure 2.3a](#), two reaction regimes can be identified: (i) a pyrolytic regime common to oxygenated and de-oxygenated fuels and (ii) an autoxidation regime driven by the oxygen concentration in the system. This oxygen requirement is also illustrated in the literature [30, 33], where autoxidation can be accelerated by increasing the oxygen flow ([Figure 2.3b](#)). This illustrates (1) the existence of two chain mechanisms leading to deposits (one oxidative and one pyrolytic) and (2) the diffusion limitation that may be encountered under these operating conditions. As the temperature range considered in our study lies below 750 K, the oxygen concentration in the system is an important parameter to consider in experimental data collection.

Heteroatomic species (as nitrogen, sulfur or oxygen containing molecules) present in the fuel promote deposits formation [37, 26, 25]. Without any distinction of chemical groups in the fuel, polar species have been shown to promote deposit formation [25]. One of the most impacting heteroatomic species are the

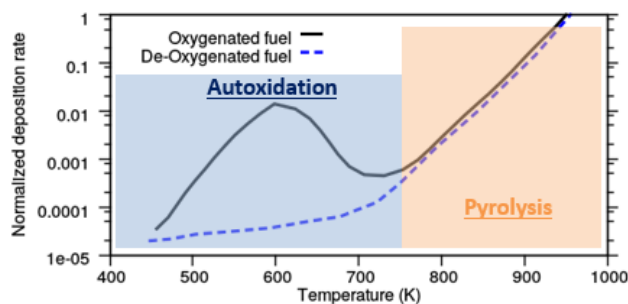


(a) Oxygen consumption as function of time for 3 different fuels. Data were obtained in Near Isothermal Flowing Test Rig (NIFTR) at 185°C from Jones et al. [47]

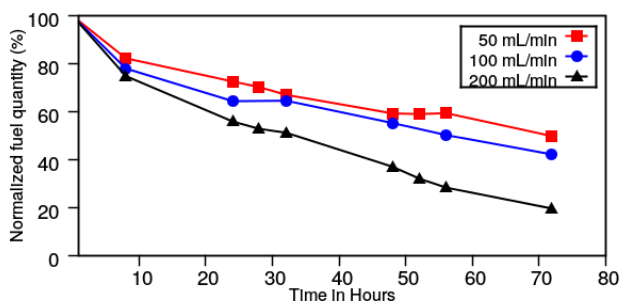


(b) IP measurements from Ben Amara et al. [46] for different n-dodecane/Methyl-Oleate mixtures as function of temperature

**Figure 2.2:** Fuel composition impact on autoxidation rate



(a) Deposition rate as function of temperature for oxygenated and de-oxygenated fuel from Spadaccini et al. [48]



(b) Fuel consumption over time with several oxygen flows. Results were obtained with a reflux reactor [33]

**Figure 2.3:** Impact of oxygen on autoxidation

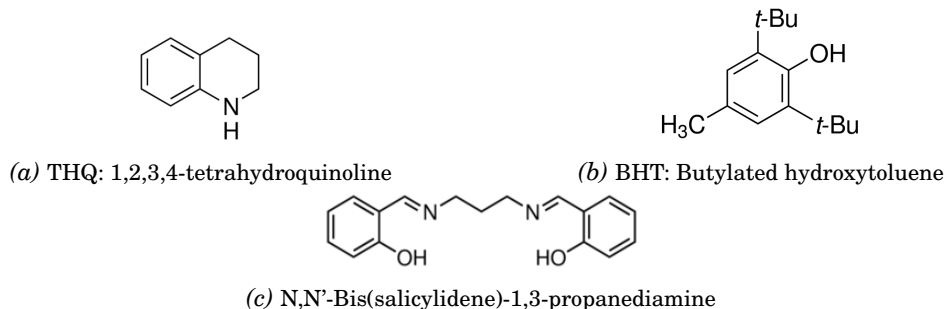
hydroperoxides which were found to be key species in LPA [8] and strong reactivity promoters [49, 50].

The last promoting effect underlined in literature are the homogeneous catalytic effect of dissolved metals and the heterogeneous catalytic effects of walls. To reduce heterogeneous catalytic effects, passivation processes have been investigated in literature and demonstrated a reactivity decrease [51]. As dissolved metals are present in fuels [47, 26], initiation steps involving dissolved metals should be considered when studying real fuels autoxidation. As can be concluded, reactivity can be highly enhanced by trace level species.

To reduce all those impacts, stabilizing species, called Antioxidants (AHs), are usually added into the fuels to limit their low temperature reactivity [52, 53] and their deposits formation tendencies. Several families of antioxidants are commonly added to the fuels such as peroxy inhibitors, hydrogen donors and complexing agents. A typical antioxidant from each family is presented in Figure 2.4.

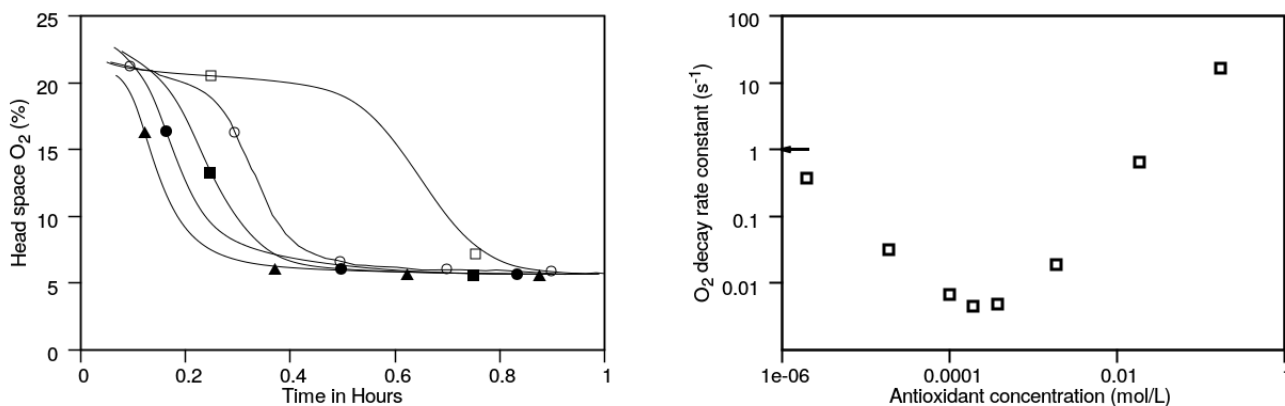
In addition, Zabarnick [38] pointed out a somewhat ambivalent behavior of antioxidants in oxidative fuel stability. In his study, the introduction of AH at low concentrations (< 6000 ppm) resulted in the increase of fuel stability and a maximum stability was reached at 60 ppm. However, at higher concentrations (> 6000 ppm) the introduction of antioxidant contributes to accelerate the oxidation process as shown in Figure 2.5b. As can be expected, this critical concentration depends on each fuel [54]. In addition to the concentration effect, antioxidant efficiency has to be considered as presented in Figure 2.5a where Para-PhenyleneDiamine (PPD) increases by a factor of two the delay to consume similar O<sub>2</sub> amounts compared to BHT. This stabilizing effect resulting from the addition of trace species makes the study of real fuels





**Figure 2.4:** Typical molecule from each antioxidant family. a), b) and c) are respectively H donor, peroxy inhibitor and complexing agent

even more complex. Before attempting to work with all those interactions, detailed mechanisms will have to be validated on the oxidation of individual chemical families without additives.



(a) Antioxidant effect on head space oxygen consumption on JP-5 at 180°C [55]. Results with no additives are represented with ▲, results with addition of 25 mg/L and 100 mg/L of BHT are respectively with ● and ■ symbols, results with addition of 25 mg/L and 100 mg/L of PPD are presented with ○ and □.

(b) Antioxidant effect on O<sub>2</sub> decay rate. Data were obtained with n-dodecane at 200°C from Zabarnick [38]. The arrow illustrates the O<sub>2</sub> decay without antioxidant. In this case, the AH effect is maximized for an AH concentration of  $2 \times 10^{-4}$  mol/l ( $\approx 60$  ppm)

**Figure 2.5:** Antioxidant types and concentration effects on autoxidation kinetics.

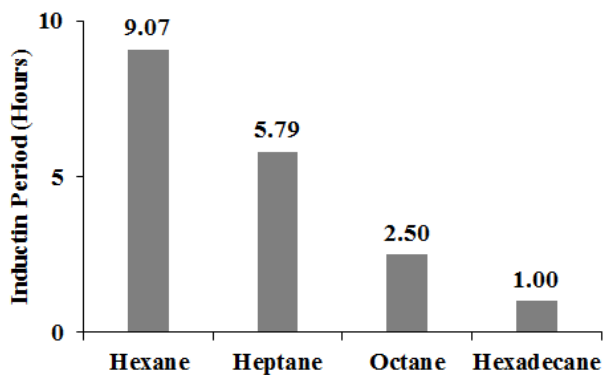
## Structure-reactivity relations in autoxidation

As presented earlier, real fuels are a complex blend of hundreds of species involving several chemical families. To understand the stability of such media, we already highlighted the influence of the chemical composition on the oxidation stability. Yet, more precise chemical informations are still required to better describe the autoxidation stability of the different chemical families.

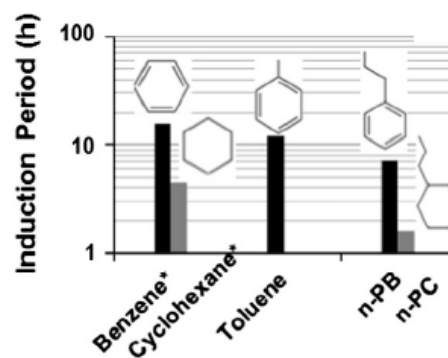
As an example, an overall reactivity increase with the paraffinic chain length has been reported in literature over several chemical families [56, 40, 57]. This is illustrated in Figure 2.6a and Figure 2.6b where the increase of the paraffinic chain length leads to a decrease of the oxidation stability on both n-paraffins and cyclic molecules.

In addition, an unclear impact of molecules branching is also observed depending on the chemical family investigated [57, 40]. As presented in Figure 2.7a, the stability tends to increase with branching level for paraffins whereas this impact is not observed for aromatics in Figure 2.7b.

From Figure 2.6b and Figure 2.8, previous works present different impacts of the insaturations

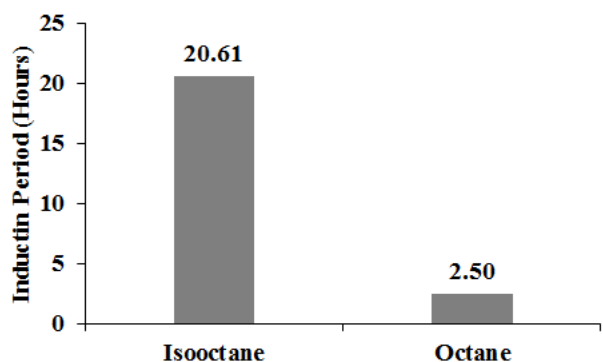


(a) IP measurements for several n-alkanes obtained at 140°C and 500 kPa of pure O<sub>2</sub> [57].

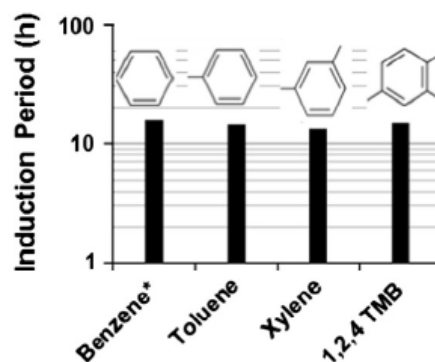


(b) IP measurements for several cyclic molecules obtained at 140°C and 700 kPa of pure O<sub>2</sub> [40]

**Figure 2.6:** Chain length impact on the autoxidation kinetics



(a) IP measurements for a normal and iso paraffin obtained at 140°C and 500 kPa of pure O<sub>2</sub> [57]. Isooctane stands for 2,2,4-trimethylpentane



(b) IP measurements for several aromatic molecules with several branching levels obtained at 140°C and 700 kPa of pure O<sub>2</sub> [40]

**Figure 2.7:** Uncertainties on the branching impact on autoxidation kinetics

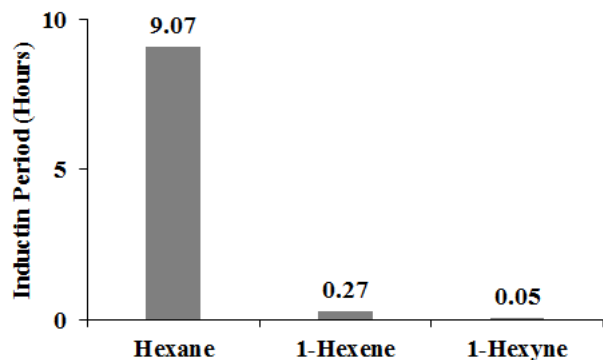
number for a given number of carbons, an increase of insaturation degree stabilises cyclic and aromatic molecules. On the contrary, an increase of the insaturations number on alkanes decreases the stability as presented in Figure 2.2a.

Other results present a specific blending behaviour according to each component chemistry. As illustrated in Figure 2.9a, autoxidation of blends may evolve linearly according to the proportion of individual components. While, in other conditions, the reactivity of blends may be very specific to the molecules selected. As presented in Figure 2.9b, the stability of decane blends may be either strongly or poorly impacted by a 10% addition of cyclic component. Surprisingly, a strong stabilizing effect is observed with the tetralin where the 10% blend of tetralin in decane is much stable than individual constituents.

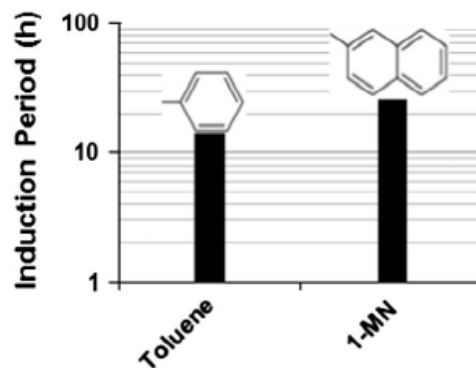
This section illustrates the importance of understanding the oxidation kinetics of individual components. Yet, the study of the interaction of different components is also important to assess the complex phenomena occurring in real fuels LPA.

### 2.1.2 Chemical kinetics of autoxidation

As presented in the previous section, oxygen presence is a prerequisite for low temperature deposit formation in the liquid phase. From the Semenov's theory, autoxidation process are assumed to proceed through

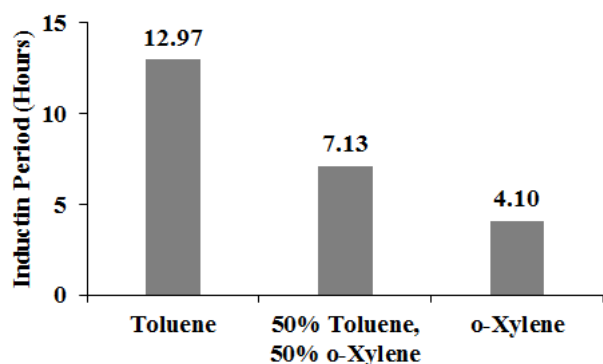


(a) IP measurements for a normal and unsaturated alkanes obtained at 140°C and 500 kPa of pure O<sub>2</sub> [57].

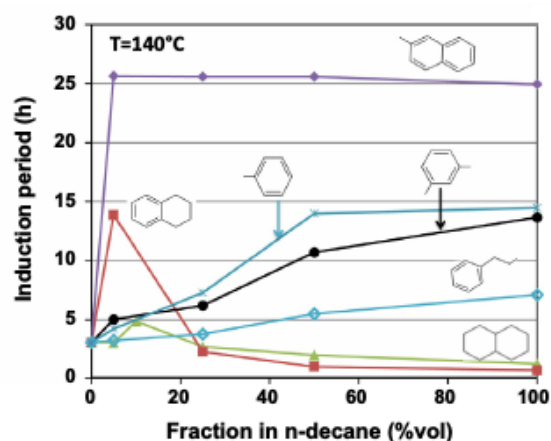


(b) IP measurements for several mono and poly aromatic molecules obtained at 140°C and 700 kPa of pure O<sub>2</sub> [40].

**Figure 2.8:** Insaturation impact on autoxidation kinetics



(a) IP measurements for an aromatic blend obtained at 140°C and 500 kPa of pure O<sub>2</sub> [57]. Percentages are given by volume.



(b) IP measurements for blends cyclic compound in decane obtained at 140°C and 700 kPa of pure O<sub>2</sub> [40].

**Figure 2.9:** Specific effect of blending on autoxidation kinetics.

a chain mechanism. As presented in Figure 2.10, the chain reaction is composed of three distinct steps: Initiation, Propagation and Termination. In literature, global chemical mechanisms [26, 38, 58] for fuel autoxidation were proposed with similar chain mechanisms (C.f Figure 2.11) involving lumped species<sup>1</sup>. However, as commercial fuels are complex blends of compounds from several chemical families, appropriate thermochemical and kinetic data are required to get a meaningful mechanism. While, lumped species are used to describe oxidation pathways, structural isomers must be considered in each of them.

### The initiation step

In low temperature regime, the thermal energy in liquid phase system is modest and the initiation step is still not fully elucidated. For this reason, the initiation step may be presented in several ways (Figure 2.12). Some authors consider the initiation step as resulting from trace level species (hydroperoxides decomposition, azo-compounds decomposition), concerted H abstraction with O<sub>2</sub> [38, 8] or photochemical reactions<sup>2</sup>.

<sup>1</sup>Lumped species correspond to a mixture of several distinct molecules showing similar properties

<sup>2</sup>This initiation is not considered in all systems, such as tanks which are opaque to UV-visible light.

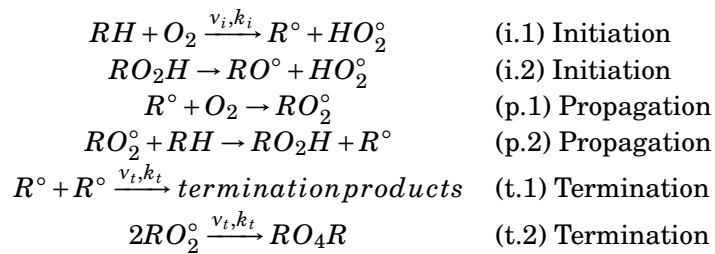


Figure 2.10: General presentation of a chain mechanism

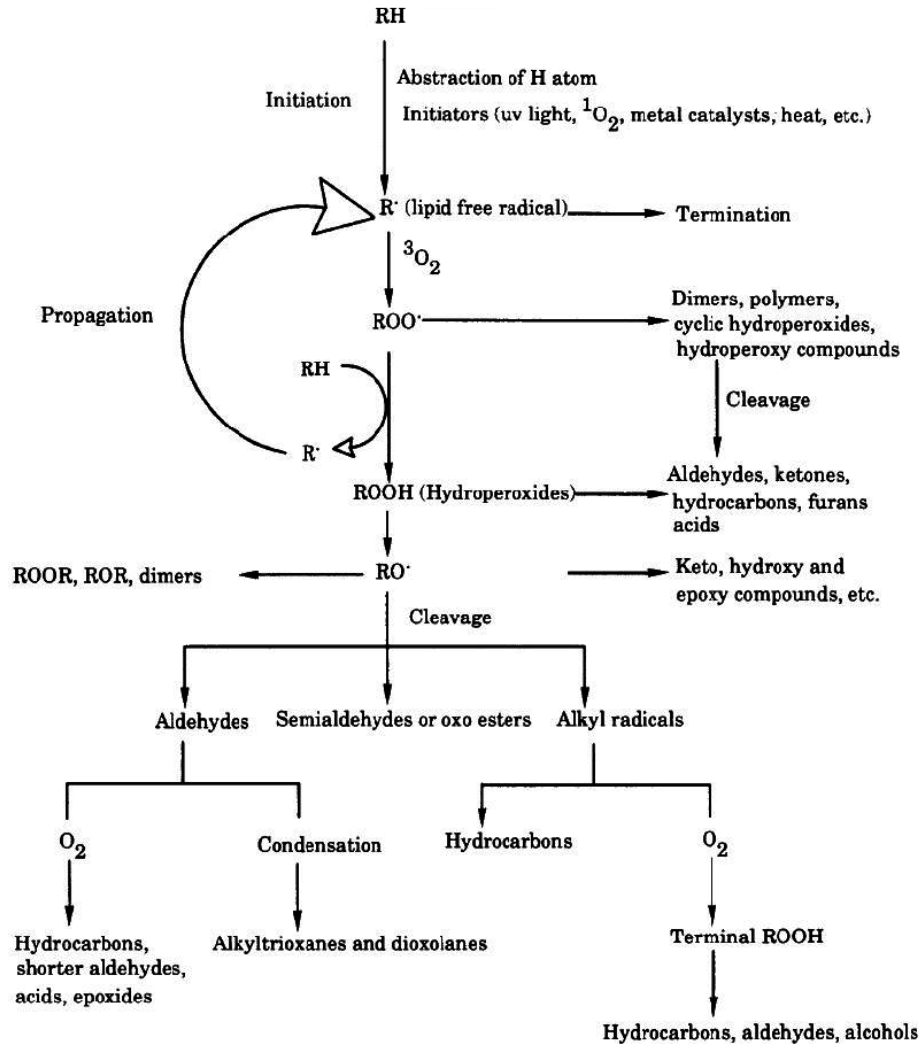
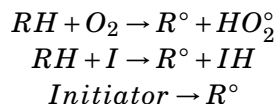


Figure 2.11: Global mechanism for liquid phase autoxidation proposed by Zongo [6]

Others, consider the first step as unknown and introduce a lumped species (Initiator) to obtain the first alkyl radical. In addition, the initiation step may be catalytically enhanced by dissolved metals, surface effects, acid catalyzed and ionic reactions.

### Propagation step

The reaction (p.1) between alkyl radicals and molecular oxygen is the main propagation path due to its low energy barrier (close to 0 kcal/mol) [26, 59]. Chain mechanism proceeds then through reaction (p.2) according to which the peroxy radical reacts with the initial hydrocarbon to form hydroperoxides and a new alkyl radicals. Then  $RO_2H$  decomposes (i.2) and forms new radicals which can also react with RH



**Figure 2.12:** Potential initiation steps of liquid phase autoxidation

to produce more alkyl radicals. Those, in turn contribute to increase the chain reactivity. This chain mechanism is now well established in literature [31, 60, 6, 46] from the 1930's with Semenov theory [61]. Recent experimental observations [62] of the QOOH radicals corroborate the consistency of such chain mechanism.

### Termination step

The termination can be simplified as a sum of all intermediates reaction paths through dimerization [63], tetroxide formation [64], peracid formation, decarboxylation process, intra-molecular reactions, concerted acid and ketone formations, disproportionation reactions. As presented here, LPA is governed by a radical chain mechanism where overall reactivity is induced by branching steps (producing more radicals in the system). For short conversion system, the overall reaction can be expressed following few parameters [65] ( $k_p, k_i$  and  $k_t$  and fuel concentration) as presented on equation 2.1. Based on same principle, Bolland [66] proposed an oxidability criteria based on the ratio of propagation rates and termination rates as presented in equation 2.2.

$$V = \sqrt{\frac{k_i}{2k_t}} \cdot k_p \times [RH] \quad (2.1)$$

$$K = \frac{k_p}{\sqrt{2k_t}} = \frac{V}{[RH] \cdot \sqrt{V_i}} \quad (2.2)$$

As presented here, chemical kinetics involved in autoxidation is relatively well known for major product formation. However, the addition of isomers in all those steps cannot be performed manually. That is why the approach proposed in this manuscript relies on an automated mechanism generation in order to integrate all reactions - as comprehensively as possible - in oxidation mechanisms.

### 2.1.3 Oxidation products and deposition processes

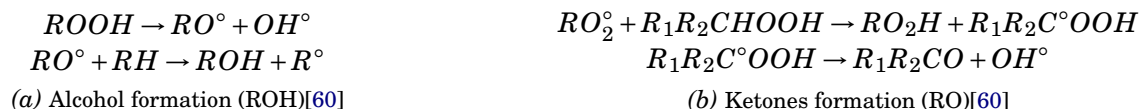
In order to study the deposition process involved in LPA, it is a major concern to identify the deposit precursors and the pathways involved in their formation. Those need to be integrated into kinetic mechanisms. As paraffins are usually the main fuel constituents and the resulting products from all drop-in fuels like Biomass to Liquid (BtL), Coal to Liquid (CtL) and Gas to Liquid (GtL), they were selected during this thesis to evaluate the robustness of liquid phase mechanism generation methodology. For this reason, the present literature review of oxidation products formation focuses mainly on this chemical family as presented in this section. Studies investigating other fuel constituents like naphthenes, cycloalkanes or oxygenated compounds are available <sup>3</sup> but are out of the scope of the present work. For the sake of clarity, the oxidation pathways are presented with lumped species, structural isomers should be considered for these species when it applies.

---

<sup>3</sup>Complementary informations on appendices

## Oxidation products formation

Hydroperoxides have been widely described in literature [8, 31, 67, 44] as the first oxidation product. These highly reactive species, even at very low concentration, are formed mainly by oxygen addition on alkyl radicals and a subsequent H-abstraction as presented in Figure 2.10. They thermally decompose to produce two radicals which subsequently produce first stage oxidation products, alcohols and ketones, as shown in Figure 2.13.



**Figure 2.13:** Major pathways leading to oxygenated species formations

Second stage oxidation products include to several oxidized products including most likely lower molecular weight products compare to fuel like ketones, acids and aldehydes. Many pathways were proposed in the literature for the formation of those species. Due to the mechanism generator requirements, our interest was focused on reactions describing elementary steps only.

As observed in the gas phase [68], an isomerization step of alkyl-peroxy radical ( $ROO^\circ$ ) radicals is competing with  $ROOH$  formation as proposed by Korcek et al [31] and presented in Figure 2.14a. This competition leads to the formation of Keto-Hydro-Peroxide (KHP) and initiates the "so-called" Korcek's reaction (Figure 2.14b). Thanks to a recent work from Jalan et al. [69], Electronic Structure Calculations (ESC) validated this two-step reaction formulated by Korcek in the 70's. This reaction starts with a concerted keto-hydroperoxide cyclisation, then the cycle breaks following two pathways: to form either acids and ketones or acids and aldehydes depending on the  $R_1$  and  $R_2$  groups on the molecule. Another pathway leading to the lighter oxidation products formation is the direct homolytic C-C bond breaking. These reactions may occur through either  $\alpha/\beta$  decarbonylation or cracking reactions (Figure 2.14c). This leads to the formation of lower n-alkanes, alkenes, carbonyles and light gases like CO,  $CO_2$ , water [29, 70, 44, 71, 72].

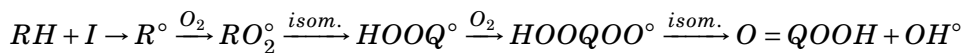
Finally, a group of reactions, involving late oxidation reactions with a maintain or a growth of oxidation products size may be presented. One of them is the Baeyer-Villiger rearrangement which conserves reactant size. This reaction starts from peracids [8, 9] and leads to acids and esters formation through several intramolecular and concerted steps Figure 2.15. Still maintaining reactants size, oxygenated cycle like lactones, furanones or epoxides [73, 67, 8, 63] may be formed with not well known chemical pathways<sup>4</sup>. Further investigations are still required to get relevant pathways for these products. Finally, all the reticulation/termination steps that form heavier oxidation products like Tetroxides ( $RO_4R'$ )[64] or alkanes ( $R'R$ )[63] are well defined in literature.

Despite the apparent simplicity of the above-mentioned autoxidation paths, co-oxidation or poly-substituted products formation (poly-substituted hydroperoxides [31, 8]) must be considered.

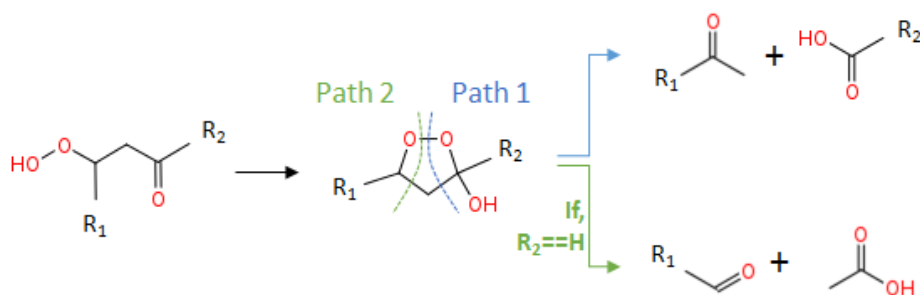
## Deposition process

Deposition issues, involved in refinery and fuel injection systems, have been already studied for several decades [22, 74, 41]. Due to the complexity of the deposition processes, this section aims to briefly introduce the overall phenomenology of deposit formation with its key parameters. As mentioned in Figure 2.3a, autoxidation regimes influences the kind of deposits formed. Two types of deposits can be distinguished. A

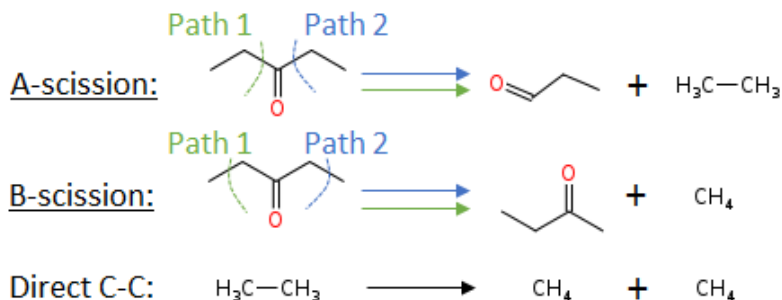
<sup>4</sup>Except for the epoxides formation



(a) Korcek's initiation: KHP formation



(b) Major steps presenting Korcek's reaction. As presented, the second path requires  $R_2$  as an H to be possible. Further information with the detailed PES are available in literature [69].



(c) Major intermediates in the CC bond breaking reactions. All alkyl radicals intermediates can lead to alkenes as presented in Zador et al. [68]

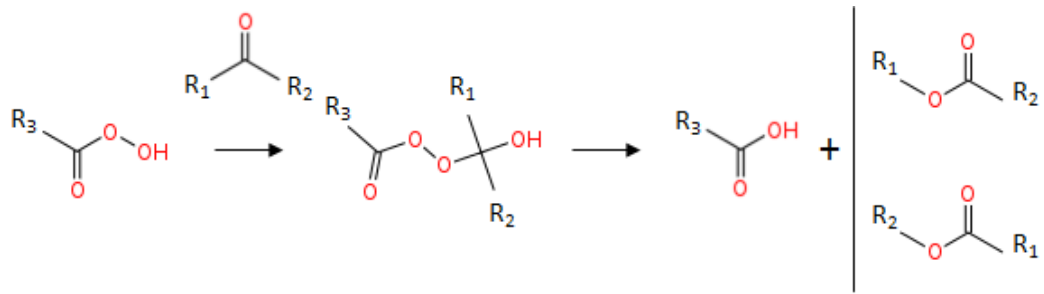
**Figure 2.14:** Major pathways leading to lighter oxidation products formation

first one which is pyrolytic (coke composed mostly of C and H atoms) and a second with oxygenated deposits. Other types of deposits have been evidenced in literature, like the soap deposits, but they are not presented in this work [75, 3].

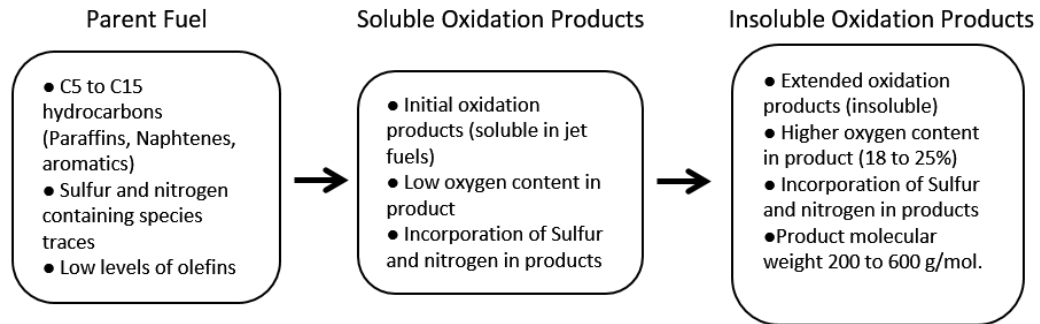
A first approach, is to consider only the reactivity inside liquid bulk to form deposits as presented in Figure 2.16 [76, 10]. This process is a sum of a chemical process corresponding to the autoxidation inside the liquid bulk then a physical process with the deposit formation on wall-surfaces. First, fuel autoxidation leads to the formation of deposit precursors in the liquid phase. These precursors agglomerate into bigger molecular weight products. Those may interact finally with the surface, or they continue growing until reaching their solubility limit and accumulate on side-walls. The sediments then react by thermal degradation or surface reaction to form varnish which in turn capture deposits precursor and increase the overall deposit size.

Another approach is to consider catalytic interactions between fuel and surfaces with heated plate experiments. Recent work presented specific fuel-surface interactions for several biodiesel blends [3] and identified specific surfaces that increased the deposition rates and influence deposit morphology. A reduction of deposits amount is also observed in literature when fresh fuel is solubilizing a fraction of the deposit [77]. This deposition reduction process is called the "washing" and illustrates a possible equilibrium between deposits and the liquid bulk.

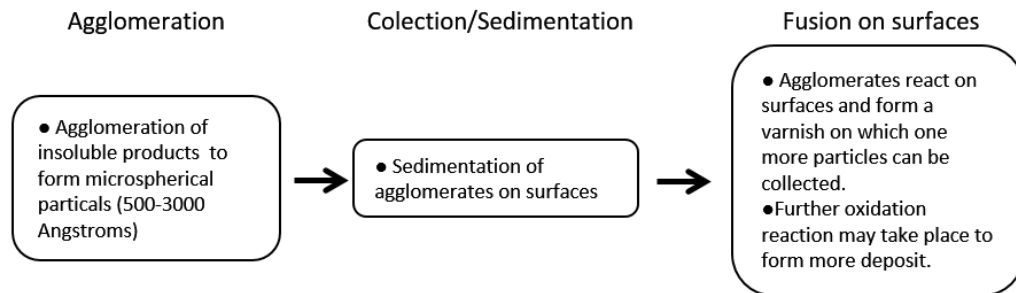
To conclude, the overall process of deposit formation from fuel autoxidation may be represented as shown in Figure 2.17 with all the interactions previously presented: (i) bulk reactivity, (ii) catalytic reactions with the surfaces and (iii) the deposit-bulk equilibrium caused with washing phenomenon.



**Figure 2.15:** Major reaction steps from the Bayer-Villiger reaction [7, 8, 9]



(a) Chemical processes involved in deposit formation



(b) Physical processes involved in deposit formation

**Figure 2.16:** Illustration of the close relation between chemical and physical processes on deposition mechanism. Modified scheme from Beaver et al. [10]

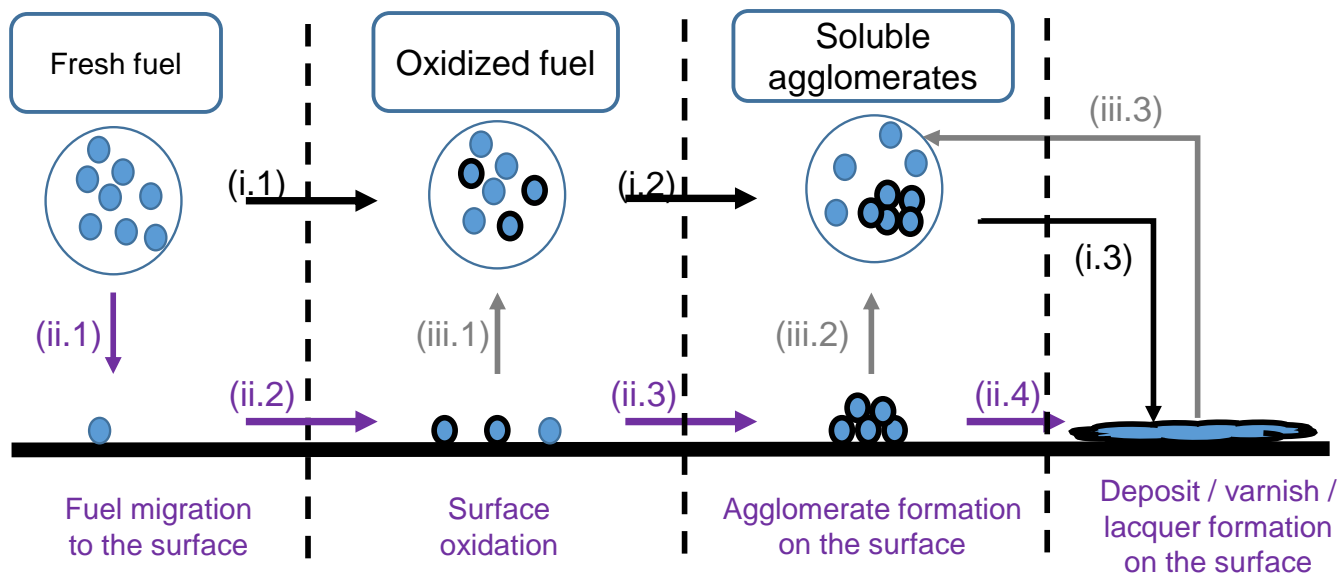
## 2.2 Solvent modeling

The previous section presented key steps of fuel autoxidation in liquid phase. This section aims to present chemical engineering aspects governing LPA. The presentation of the multiphase competition in LPA is presented, then the solvent effects on both thermochemistry and kinetic are discussed. First, a brief presentation of the heterogeneity of LPA is introduced and illustrated with experimental observations.

### 2.2.1 Heterogeneity inside the liquid bulk

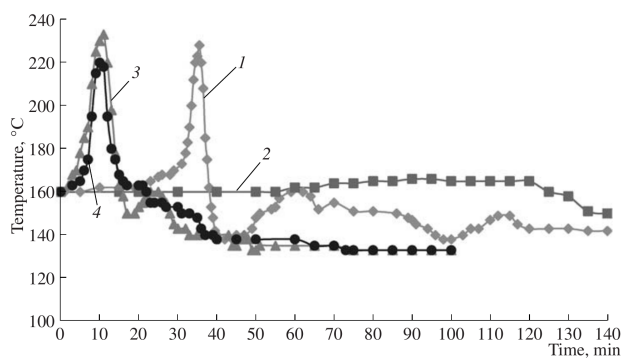
In most autoxidation studies, the liquid phase is considered as an homogeneous media often isothermal. However, the oxidation media is not always homogeneous, for example, multiphases temperature spikes may be observed during autoxidation of fatty-compounds and heavy hydrocarbons [78, 11]. This high energy release is not systematic as observed for iso-hexadecane in Figure 2.18a and is linked to the hydroperoxides decomposition rate which is a very exothermic step. Similarly to gas phase with ignition delay, in one condition the system generates high amounts of hydroperoxides before they decompose. The accumulation step induces a high energy release when the hydroperoxides decompose, assimilable to a thermal runaway



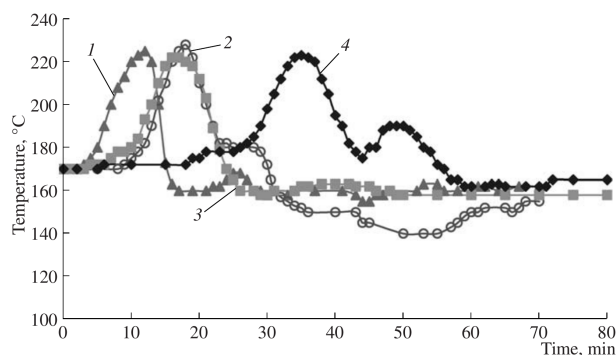


**Figure 2.17:** Global process for the deposit formation. The bulk reactivity path (i) is represented with black arrows. The catalytic oxidation path (ii) is represented with purple arrows. The solubility of deposit into fresh solvent (iii) is represented with grey arrows.

in the gas phase. While in other conditions, the smaller hydroperoxide accumulation induces a smaller and slower energy release which is progressively absorbed and diffused inside the whole liquid.



(a) Autoxidation of paraffins at 160°C [11]: (1) hexadecane, (2) isohexadecane (heptamethylnonane), (3) squalane (hexamethyltetracosane), and (4) pristine (tetramethylpentadecane)

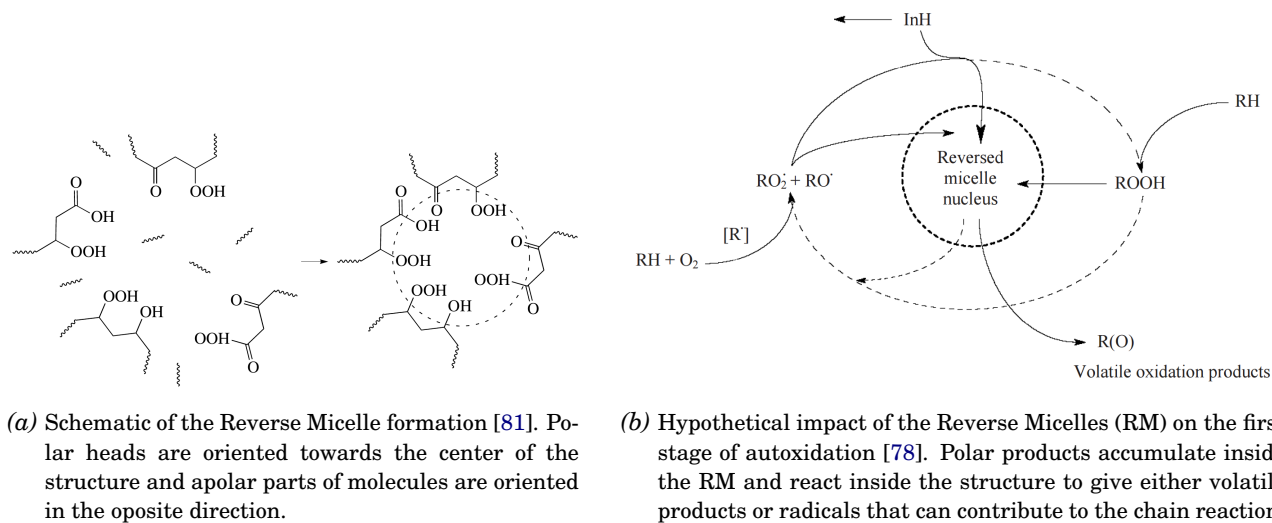


(b) Autoxidation of esters at 170°C [11]: (1) dimethyl sebacate, (2) dibutyl sebacate, (3) dioctyl sebacate, and (4) pentaerythritol ester

**Figure 2.18:** Temperature profile during the autoxidation of several compounds [11]

In addition, as presented in [Figure 2.19a](#), polar molecules like hydroperoxides and oxygenated products self-assemble into Reversed Micelles (RM) during the autoxidation processes [79, 80, 11, 78]. The formation of such structure reveals the existence of a network of RMs inside the liquid bulk during autoxidation process and indeed a high concentration gradient of hydroperoxides between RM and the liquid bulk. As considered with the chain mechanism presented in [Figure 2.19b](#), these RMs may interact with the formation of first oxidation products.

This section introduced the liquid phase heterogeneity that may occur during the autoxidation according to two aspects: the possible non isothermal conditions and the nanoreactor structures (RM) that may play a role in the chain reaction process.



**Figure 2.19:** Illustration of Reverse Micelle formation and its implication in the chain mechanism of autoxidation

## 2.2.2 Phase equilibrium in liquid phase autoxidation

### Gas diffusion towards liquid phase

As presented in the previous section,  $O_2$  is a key species to consider in liquid phase autoxidation. Contrary to gas phase, liquid phase concentration of oxygen (or any other gases) is limited by its solubility in the solvent of interest. Henry's Law (HL) Equation (2.3) gives oxygen concentration calculation into the liquid at the limit of diluted solutions. The relation links partial pressure,  $p_i$ , of a species  $i$  to its liquid phase concentration,  $c_i$  with Henry's coefficient,  $k_h$ .

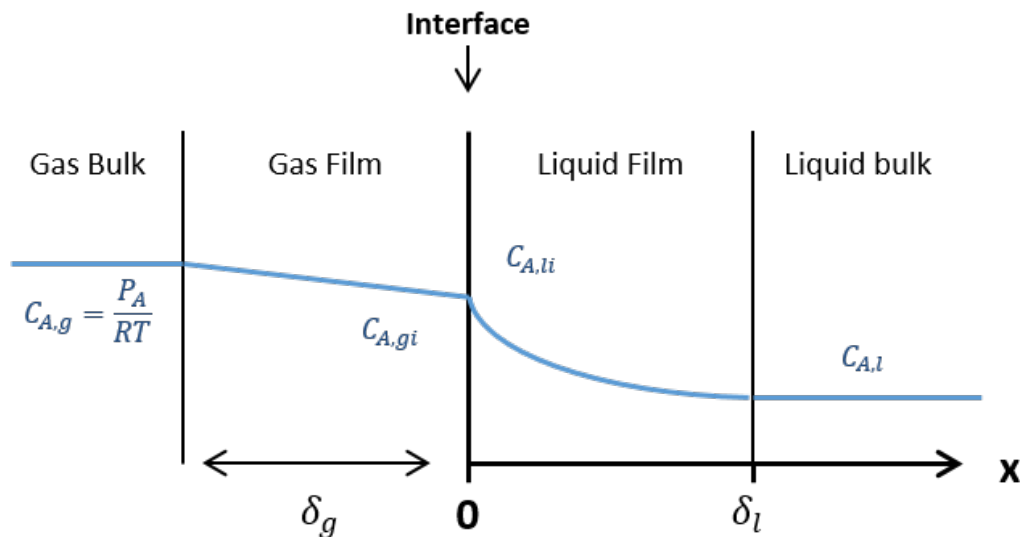
$$p_i = k_h \times c_i \quad (2.3)$$

HL coefficients are available for many gases ( $H_2$ , He, Ne,  $O_2$ ,  $N_2$ ,  $CO_2$ , ...) in several solvents (alkanes, alcohols, esters, cycloalkanes, aromatics). However, only few experimental data for hydrocarbons/molecular oxygen mixtures are available. Pure solvent estimation of HL are available in DETHERM database [82] using empirical relations. In addition, some chemical structure-property relationships have been presented in literature [83, 84, 85]. HL data are limited to steady states conditions but for real reacting system,  $O_2$  may not reach the steady state due to diffusional limitations. The diffusion inside the bulk is linked to the interfacial areas which can be either natural (free interface between gas and liquid) or forced (bubbling system with multiple spherical interfaces). In both cases, the diffusion process can be expressed using a film model such as the Whitman model presented in Figure 2.20 for a reacting system. When the system is perfectly mixed (no diffusion limit) or at the equilibrium, film sections (gas and liquid) does not exist ( $\delta_g = 0$  and  $\delta_l = 0$ ) and concentration gradients inside each phase become negligible.

As the molecular oxygen concentration in the liquid phase is very low (typically 1000 ppm for n-paraffins at 298 K), a competition between oxygen diffusion into the solvent bulk and its consumption may occur easily in highly reactive conditions.

### Gas desorption from liquid

Due species volatility, some lighter compounds may diffuse from the liquid phase to the gas phase (such as  $H_2$ , CO,  $CO_2$  or light oxygenated products). Vapor pressure can be calculated using the empirical Antoine



**Figure 2.20:** Whitman model presentation for a reacting system consuming A in the liquid phase.  $P_A$  is the partial pressure and  $C_{A,g}$  the concentration of species A in the gas phase. Indices  $g$ ,  $l$  and  $i$  respectively stand for gas liquid, and interface.

equation (2.4). This equation allows to quantify evaporation rate of liquid products in the gas phase (A and B being two parameters relevant to the molecule volatility). Multiphase mass transfer issues presented in this part underlines the need of a specific multiphase reactor for the modeling of these phenomena. Thus, the multiphase reactor will have to consider both HL coefficient of gas phase species and product partial pressure of liquid phase species to model those equilibrium states.

$$\log_{10}(P) = A - \frac{B}{(T + C)} \quad (2.4)$$

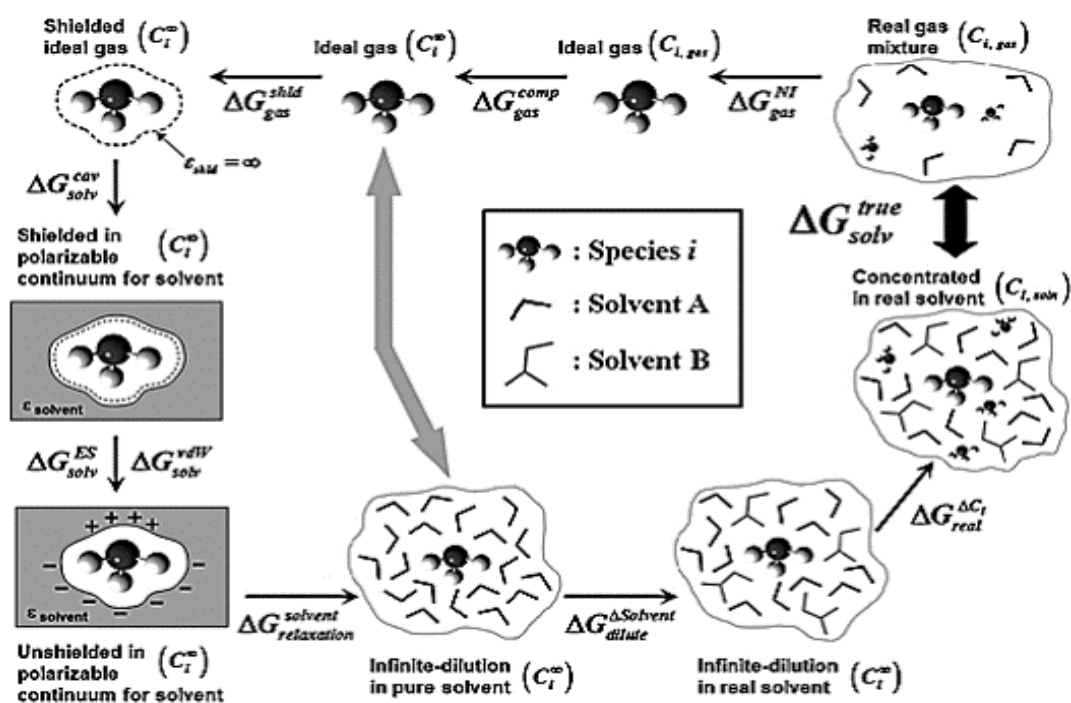
### 2.2.3 Solvent effects in liquid phase autoxidation

As presented in Figure 2.23, the solvent impacts both thermochemistry and apparent kinetic rates. This statement has been discussed by various authors [8, 86, 12]. Although thermochemical and the kinetic data in liquid phase can be measured directly from experimental data, defining both parameters in all solvent of interest is not realistic. On the other hand, there is a growing interest in correcting the gas phase data from literature by applying corrections corresponding to the solvent effect. This section aims to presents how those data can be obtained. Each section is divided into two parts, the first one presents the tools available in literature to calculate solvent corrections. The second one is devoted to the method used in the present work.

#### Impact on the thermochemistry

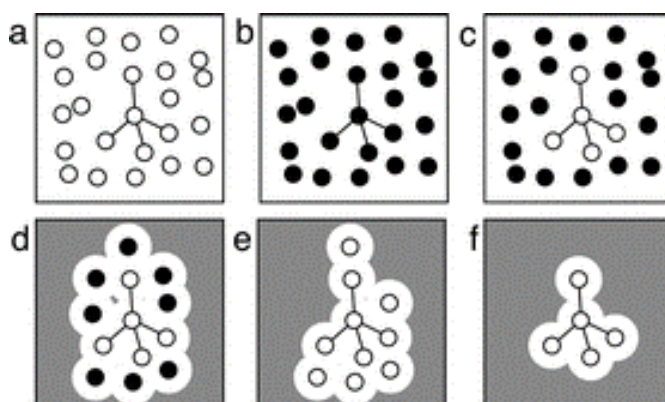
To present the liquid phase correction,  $\Delta G_{solv}$ , a thermodynamic cycle is given in Figure 2.21. It includes all individual corrections to consider from real gas mixture to concentrated solute in solvent. Corrections can be divided into four main steps [86]: (1) ideal states corrections (where gases and liquids are moved from concentrated to diluted conditions), (2) cavity formations correction, (3) Van der Waals corrections (also called dispersion-repulsion forces) and (4) electrostatic contributions referring to the charge distribution in the solvent.

The accuracy of the results is indeed a function of each correction which can be evaluated separately (by molecular modeling) or corrected collectively (using semi-empirical methods). The accuracy of the methods relies on the description of solute-solvent interactions on both semi-empirical methods (with solute-solvent descriptors) and computational modeling methods (using different solvent description theories). The level of description of solvation in molecular modeling is presented in Figure 2.22. Solvation models can be divided into two approaches. In the first one, solvent molecules surrounding the solute are represented explicitly (in a, b and c). In the second one, a continuum model is used to model all (in f) or part of the solvent (d and e). In both approaches, molecules can be either described using Quantum Mechanics (QM) or Molecular Mechanics (MM). Assessment of these methods and their accuracies have been performed in literature [86].



**Figure 2.21:** Thermodynamic cycle presenting solvation process. Grey arrow represents the Free energy change between ideal gas to diluted solute in solvent. Diagram is from Jalan et al. [12]

To overcome these limitations, semi-empirical methods, like the Linear Solvation Energy Relation (LSER) method described are still widely explored. These methods require parameters, mainly based on physical properties of both solute and solvent to obtain solvation corrections. Many species/solvent pairs can



**Figure 2.22:** Solvent model illustration from discrete (a) to continuum model (f). Illustration is from Jalan et al. [12]

be investigated and the solvation correction is obtained using a small set of equations (Cf. Equations (2.5) to (2.9)). However, only stable products parameters can be obtained experimentally and calculations are still required for radicals or short life-time species. This is the main reason why this method was retained in RMG to obtain high-throughput solvation estimation for all species involved in the mechanism[69].

In RMG, the liquid phase thermochemistry is calculated according to two steps, both using LSER methods. The first one, expressed in (2.5), consists in calculating the liquid phase Free Energy of the species,  $G_{liq}$ , using the Free Energy of solvation,  $\Delta G_{solv}$ , on its gas phase Free Energy,  $G_{gas}$ .  $\Delta G_{solv}$  is obtained with (2.6) and the partition function,  $k_{vapor-solvent}$  of a given solute-solvent pair given by (2.7). LSER method based on Abraham's models (presented in (2.7)) [87] provides an estimation of this partition coefficient at 298 K. In these coefficients, a first set is referring to solute descriptors (E,S,A,B,L) and a second to solvent descriptors (c,e,s,a,b,I). The second step of the calculation is to calculate the enthalpy of solvation ( $\Delta H_{solvation}$ ) at 298 K using Mintz's model, also based on Abraham's model. With Mintz's model, solute descriptors remain the same and solvent descriptors (c',e',s',a',b',I') are obtained through a new empirical correlation [88] and give  $\Delta H_{solvation}$  at 298 K is obtained using (2.8). Decomposing  $\Delta G_{solv}(298K)$  in  $H-TS$ , gives  $\Delta S_{solv}(298K)$ . As  $\Delta H_{solv}$  and  $\Delta S_{solv}$  are assumed to be temperature independent,  $\Delta G_{solv}$  can be expressed as a function of temperature following (2.9). Those assumptions give reasonable agreements (0.5 kcal/mol RMSE<sup>5</sup>) in many systems as presented by Jalan et al. [15] over 900 data points. Further work is required to better predict the thermochemistry of oxygenated solvents.

$$G_{liq} = G_{gas} + \Delta G_{solv} \quad (2.5)$$

$$\Delta G_{solv} = -RT \ln(K_{vapor-solvent}) \quad (2.6)$$

$$\log K_{vapor-solvent} = c + eE + sS + aA + bB + lL \quad (2.7)$$

$$\Delta H_{solv}(298K) = c' + a'A + b'B + e'E + s'S + l'L \quad (2.8)$$

$$\Delta G_{solv}(T) = \Delta H_{solv}(298K) - T\Delta S_{solv}(298K) \quad (2.9)$$

In equations (2.7) and (2.8), sS term corresponds to the electrostatic interactions, eE accounts for residual contributions from dipolarity/polarizability, lL term is attributed to the cavity formation and dispersion interactions, aA and bB terms respectively stand for the ability to donate hydrogen (acidity) and accept hydrogen (basicity).

## Impact on the kinetics

**Transition State Theory** Solvents effects impacts rates according to three different effects: (1) by increasing or decreasing the activation energy (Ea) (as presented in Figure 2.23), (2) barrier recrossing and (3) by local diffusion-reaction competition(cage scale). Many observations of solvent effects on kinetic are presented in literature. They indicate a modification of the liquid phase kinetics compare to gas phase values [8, 89]. Kinetic Solvent Effect (KSE) on energy barrier may be explained by the Menschutkin effect (Cf. Figure 2.23b). When a Transition State (TS) is more polar than the Reactant (RCT), the use of polar solvent stabilizes TS and decreases Ea value.

Then, as presented by Hynes [90], the solvent may induce barrier recrossing and reaction coordinate due to solvent friction( $\zeta$ ). In chemical system with competing reactions, a reaction coordinate less impacted by solvent friction may become predominant beside (origin) major one highly impacted by solvent effects. The relation derived from Kramers's theory (2.10) demonstrates that for low friction ( $\frac{\zeta}{2 \cdot \omega_b} \ll 1$ ),  $k \approx k^{TST}$

<sup>5</sup>Root Mean Square Error

and indeed for system with higher frictions,  $k$  value decreases compared to its Transition State Theory (TST) value.

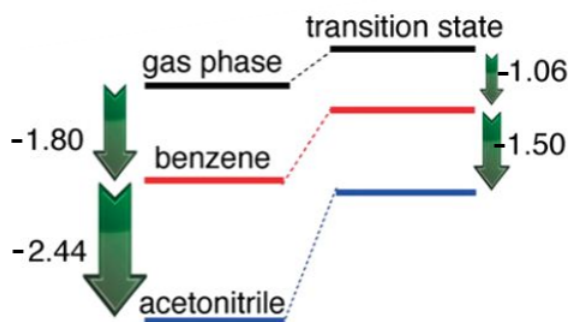
$$\frac{k}{k^{TST}} = \left[ 1 + \left( \frac{\zeta}{2\omega_b} \right)^2 \right]^{\frac{1}{2}} - \frac{\zeta}{2\omega_b} \quad (2.10)$$

Although (1) and (2) might be calculated with ESC, experimental measurements [8] comparison may help to estimate the KSE through the equations (2.11) and (2.13). Activation Energy ( $E_a$ ) corrections are proposed (2.11) in literature [15] to obtain Arrhenius expression (Cf. (2.12)) as a function of gas phase Arrhenius parameters ( $A, n$  and  $E_a$ ) and the liquid phase corrections ( $\alpha_{KSE}$ ). This correction lumps together both KSE ( $E_a$  value change and solvent friction). As  $\Delta\Delta G_{solv}^{TS-Rct}$  is known from thermochemical corrections, this technique may be implemented to transpose gas phase kinetics to liquid phase.

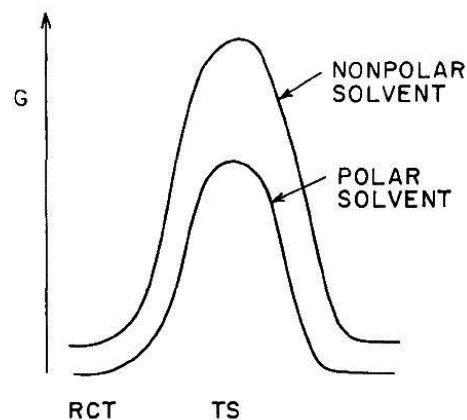
$$\frac{k_{liq}}{k_{gas}} = \alpha_{KSE} \exp\left(\frac{-\Delta\Delta G_{solv}^{TS-Rct}}{RT}\right) \quad (2.11)$$

$$k_{liq} = A \left(\frac{T}{1K}\right)^n \exp\left(\frac{-E_a}{RT}\right) \alpha_{KSE} = A \left(\frac{T}{1K}\right)^n \exp\left(\frac{-(E_a + \Delta\Delta G_{solv}^{TS-Rct})}{RT}\right) \quad (2.12)$$

$$\Delta\Delta G_{solv}^{TS-Rct} = \Delta G_{solv}^{TS} - \sum_i^{reactants} \Delta G_{solv}^i \quad (2.13)$$



(a) Impact of solvation on molecule Gibbs energy for an H-abstraction reaction. In this case,  $\Delta\Delta G_{Acetonitrile}^{TS-Rct} = -1.68$  kcal/mol,  $\Delta\Delta G_{Benzene}^{TS-Rct} = -0.74$  kcal/mol. [91]



(b) Menshutkin effect illustration. Transition State is more polar than reactant and the use of polar solvent stabilizes the TS.

**Figure 2.23:** Solvation effects on activation energies according to solute-solvent affinities

**Cage effect** Once the kinetic rate has been corrected for solvent effects, the diffusional limitations have to be considered at the cage scale. This cage-level diffusion should not be confused with the macroscopic gas diffusion presented in Figure 2.20. For bimolecular reactions, reactants have to diffuse inside a solvent cage before reacting. The theory, was presented by Rice [92], (2.14) can be used to estimate those limitations. Where an effective rate constant ( $k_{eff}$ ) is calculated using an intrinsic reaction rate ( $k_{int}$ ), sum of reactants radii ( $R$ ), sum of diffusivities of reactants ( $D$ ). From this equation, when  $\frac{k_{int}}{4\pi RD} \ll 1$ , this effect may be neglected  $k_{eff} \approx k_{int}$ . This can be reached when either a very low rate ( $k_{int}$ ) or a very high diffusivity ( $D$ ).

$$k_{eff} = \frac{4\pi RD k_{int}}{4\pi RD + k_{int}} \quad (2.14)$$

$$D = \frac{k_b T}{6\pi\eta r} \quad (2.15)$$

In RMG, the cage-scale diffusional limitation is the only solvent effect implemented on the kinetics. Jalan et al. [15] presented the consistency of the correction using (2.12) and (2.13) on a specific reaction. As it is not possible to estimate the transition state for thousands of reactions investigated during the mechanism generation, the methodology was not implemented into the code. In contrary, diffusion limits are calculated using (2.14) and (2.15). Where  $D$  and  $R$  are respectively calculated using Stokes-Einstein (using "user specified" viscosity,  $\eta$ , equation (2.15) and the McGowan method implemented into the code (as presented on [15]). While it is calculated and its effect on the kinetic displayed on the output file, gas phase Arrhenius parameters are not modified. Thus, specific post processing are required to consider it in the modeling.

## 2.3 Modeling tools

The chemical kinetic work presented in this thesis is based on (i) the development of detailed kinetic mechanisms, (ii) their usage in a kinetic solver for predicting application and (iii) the mechanisms improvement through ESC. The selected software are presented within the overall methodology in the next section. In this section, only the overall philosophy of automated mechanism generator and Electronic Structure Calculations is introduced.

### 2.3.1 Mechanism generators

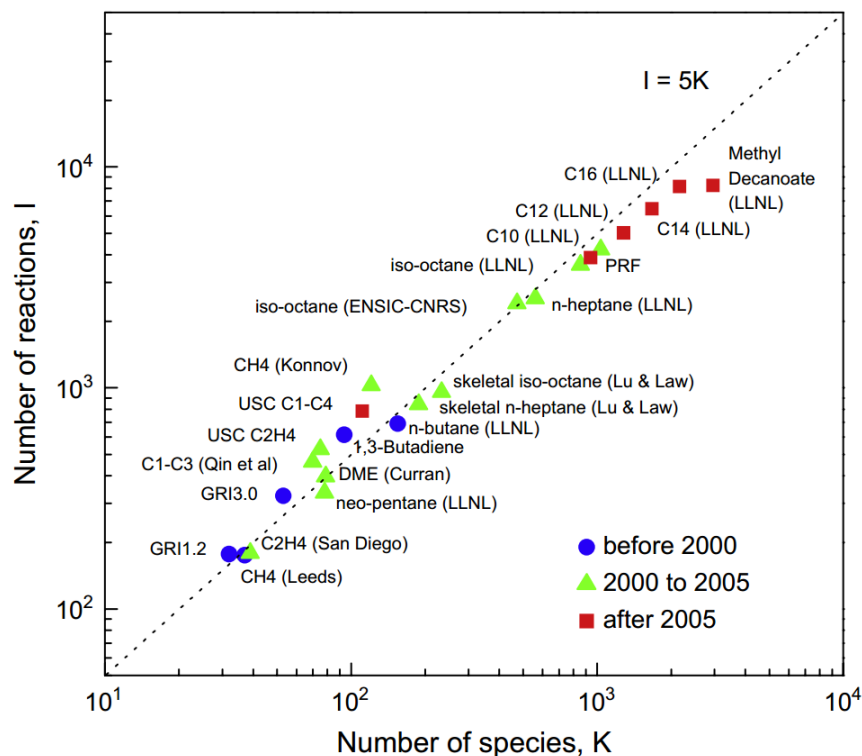
As recently presented by Lu and Law [13], detailed mechanism size for oxidation increases linearly with the number of species per individual fuel. Thus, mechanisms for real-fuels blends, centered around C<sub>10</sub>-C<sub>12</sub> and containing up thousands individual constituents, may quickly cross the million of reactions. Building such complex system cannot be considered by hand and the use of mechanism generator becomes critical for kinetic modeling. Several tools, like ExGAS, RMG, MAMOX, REACTION or Genesis, are available in literature and give applied answer to very complex system like the JP-10 combustion [93]. Only the general philosophy of an automated mechanism generator is introduced in this section. Further informations on each software specificity are available in literature [94, 95] or in their documentations.

As presented in [94], all generators have a set of common modules that can be classified as *generator engines*, *the species pools*, *the molecule database* and *the reaction database*.

The *generator engines* can be assimilated as the main algorithm which handle all major steps like the *Initialization*, the *Addition of new reactions*, the *Addition of new species*, *termination criteria*.

The *species pool* corresponds to all species involved during each iteration of the generator and is updated along the generation.

The *Molecule* and the *Reaction class database* is where all the chemo-informatic work is performed including "molecule identification", "checks on possible reactions" according to the *species pool*, determination of thermochemical and kinetic parameters from the implemented database. The mechanism generation process covers all those steps for a given list of initial molecules and gives as an output a reaction mechanism with all initial species, all new species, and reactions matching *the species pool*. To contain mechanism size, some generators provide a reduction step presented as a lumping step or a reduction step based on flux analysis.



**Figure 2.24:** Typical size of detailed and skeletal mechanisms for hydrocarbon fuels. The figure is from Lu and Law [13]. As presented with the mechanism selected, mechanism size is linearly correlated with the number of species,  $Number_{Rxn} = 5 \times Number_{Sp}$ .

Finally once the generation is completed, the mechanism can be coupled to a kinetic solver like Cantera or Chemkin suite softwares to model specific conditions. In the case of a rate based generator, like RMG, the reactor model already influence the generation process. Thus, the implementation of new reactor model may become critical to increase mechanism generator capability.

### 2.3.2 Electronic structure calculations

ESC They are all based on the laws of Quantum Mechanics (QM) and predict molecules structures, energies, vibrational frequencies and reactions pathways of a variety of chemical compounds (stable or transition structures).

To perform these calculations, the algorithm is solving the Schrödinger equation (Cf. (2.16)) to find the different stationary states of the species considered. In equation (2.16),  $\psi$  is the wave function (whose squared norm represents the probability of presence),  $H$  is the Hamiltonian operator and  $E$  the energy of the particle. However, this equation is analytically not solvable for polyelectronic systems.

$$H\psi = E\psi \quad (2.16)$$

According to the electronic structure method selected, modeling approaches are required to solve (2.16). There are two main classes of methods. Semi-empirical methods such as AM1, PM3, PM6 that use parameters extracted from experimental data to simplify the equations. There are many different semi-empirical methods available and their accuracy depends on each system. Ab initio methods rely on a small number of physical constants for the basis of their computations. In Hartree-Fock (HF) approach,



the solution of Schrödinger equation assumes the wave function to be an antisymmetrized product of one-electron spin-orbitals. Hence, each electron is treated separately and the effect of all the other electrons is globalized through an effective potential (central-field approximation) determined in a self-consistent way. The difference between the exact nonrelativistic energy and the HF energy is the correlation energy of the molecule. Electron correlation is not accounted in HF approach, it is addressed by post-HF methods, such as coupled cluster theory. However, post-HF methods can become computationally prohibitive for geometry searches if more than 10 heavy atoms are involved, DFT becoming then the method of choice. DFT methods are based on the Hohenberg-Kohn theorems which state that the ground state properties of a many-electron system are uniquely determined by an electron density that depends on only 3 spatial coordinates (instead of  $3N$  dimensions) and that minimizes an energy functional. The accuracy of DFT depends on the quality of the exchange-correlation functional.

As presented earlier ([subsection 2.2.3](#)), calculations can be performed with the solvent to calculate liquid phase interactions. To model those interactions, calculations are performed placing a solute in a solvent cavity. Those methods are called Henry's Law (SCRF). Several levels of solvent description can be selected from the simplest one (Dipole & Sphere model, also called Onsager's model) to the most realistic one (Self Consistent Isodensity Polarized Continuum Model) (C.f [Figure 2.22](#) for solvent model presentation). Due to computational limitations, the SCRF model selection depends on each system (number of atoms and electrons of the molecules).

## 2.4 Conclusions

In this part, the state of the art of liquid phase autoxidation has been presented. First, a review of autoxidation literature study was performed highlighting the key parameters of oxidation kinetics and introduced the principle of structure-reactivity relations. Then, the theory behind the chain reaction in liquid phase have been presented with most relevant oxidation pathways and the expected products in the conditions investigated in this manuscript.

Second, chemical engineering aspects identified in LPA were presented including the liquid bulk heterogeneity, phase equilibrium phenomena and solvent effects on both thermochemistry and kinetics. Finally, a review of the main modeling tools employed in this work are presented.

In the next chapter, the experimental and modeling methodologies are presented in details. A presentation of both experimental apparatus with analytical devices is performed. Then the proposed MultiScale Approach used to build relevant liquid phase kinetic models for fuel surrogate autoxidation is presented.

# Chapter 3

## Material and Methods

The study of liquid phase oxidation of fuels involves long time scales phenomena. To reduce experimental cost and operating time, a set of experimental apparatuses. The RSSOTs, aims to reproduce real oxidative conditions in shorter amount of time. Coupled to liquid residual analysis, they give interesting results for models validation. A complementary approach is to use more research oriented devices with complex sampling systems to analyse in-line or off-line the reacting mixture at several time steps. These two approaches are conducted within this work with a PetroOxy and an autoclave associated to qualitative and quantitative analyses.

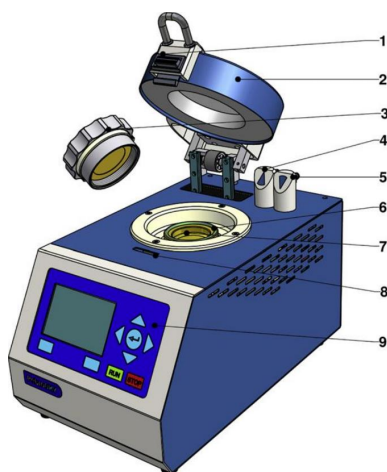
To model such long time scales phenomena, it is a major concern to develop associated detailed kinetic models for the liquid phase. This chapter introduces both the experimental and modeling methodology employed in this work to study the liquid phase oxidation kinetics.

### 3.1 Experimental devices

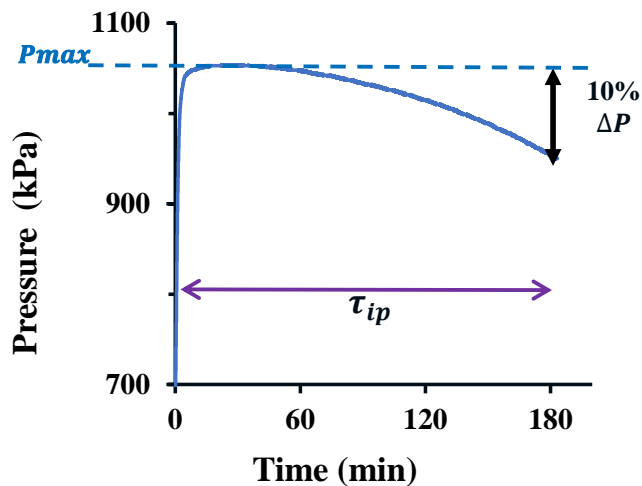
In this section, the PetroOxy and autoclave experiments with their analytical devices are presented in details with their operating methods. For a sake of clarity, the macroscopic parameter, IP, widely used in models validation is defined with its majors experimental observations.

#### 3.1.1 PetroOxy experiment

Experiments were performed with a PetroOxy apparatus from Petrotest Instruments GmbH & Co. KG. It is one of the existing reference instruments to perform RSSOT of fuels and fuel surrogates as described in American Society for Testing and Materials (ASTM) 7545 methods [96]. This equipment, presented in [Figure 3.1a](#), offers convenient features such as a small volume of samples, gold plated test cell (7) and a high pressure cell with typical operating ranges up to 700 kPa of initial oxygen and 160° C. Previous works [44, 97] have successfully employed this device to study liquid phase autoxidation kinetics. In addition, PetroOxy measurements obtained over a large data set present a high reproducibility, the absolute average deviation of results may be expressed as function of the measured IP according to  $\Delta_{IP(hours)} = 0.018 \times IP(hours)$ . A higher deviation (around 6 % in average) was previously obtained [98] with a smaller data set of bio-diesel experimental results only with very low IP measurements.



(a) PetroOxy device presentation



(b) Typical IP measurements with the 10% total pressure decrease. Results correspond to n-decane at 413 K and 700 kPa of cold molecular oxygen

**Figure 3.1:** PetroOxy device representation and its typical experimental result

## Operation

The PetroOxy cell is filled with 5mL of the test sample at room temperature and atmospheric pressure. Experimental conditions are set with the built-in control panel (9) and results are stored either with device internal memory or by connecting a computer. Then, the apparatus is closed subsequently with the tapped cover (3) and the protective cap (2) electronically locked with (1) and (8). The cell is automatically flushed once with pure O<sub>2</sub> to remove air using inlet and vent respectively in (5) and (4). Then, oxygen is added up to the requested pressure. The heating system and the data recorder start simultaneously after pressure stabilization. From this experiment, we can extract the IP which corresponds to the time required to reach a typical 10% pressure decrease ( $P_{IP}/P_{max} = 0.9$ )<sup>1</sup> [99, 96] as presented in Figure 3.1a. This criterion is assumed to correspond to 5% of fuel consumption [46] and is physically correlated with the hydroperoxide build up and first deposit precursors formation.

A typical experimental result is presented in Figure 3.1b which shows that the time to reach the requested temperature is included in the IP. This delay is below four minutes in all experiments and is therefore negligible regarding to IP in the conditions tested previously. Thus, IP measurements below 30 minutes should not be considered as an acceptable value due to a high uncertainty in IP measurements.

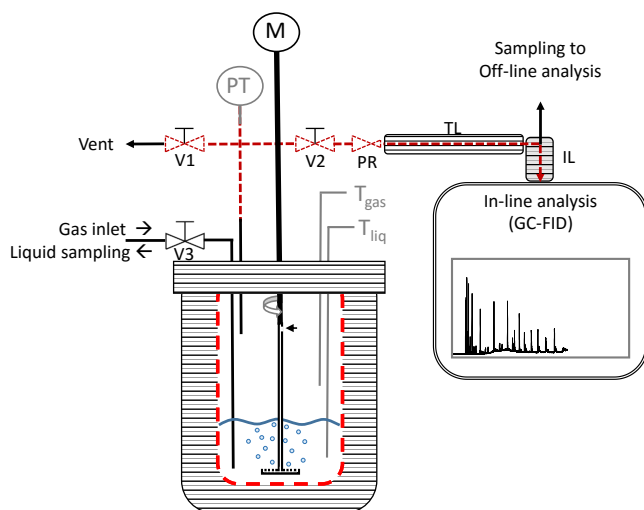
### 3.1.2 Autoclave experiment

Autoclave experiment is based on a 250mL Anton Parr reactor 4570 series, made in Hasteloy to limit catalytic effects from the side walls. As presented in Figure 3.2a, this device is a closed reactor equipped with a mixing system (M) applying both agitation and bubbling into the liquid, a Pressure Transducer (PT), 2 thermocouples ( $T_{gas}$  and  $T_{liq}$ ) and a heating system. In Figure 3.2a scheme, all heated sections are represented with red dashed lines, insulated part with shaded blocks, monitoring instruments (PT,  $T_{gas}$  and  $T_{liq}$ ) in grey and fluid flows (inlet/outlet) with arrows. While this device is build to cover temperature and pressure ranges respectively up to 623 K and 40 MPa, typical operating conditions are 383-403 K and 1 MPa.

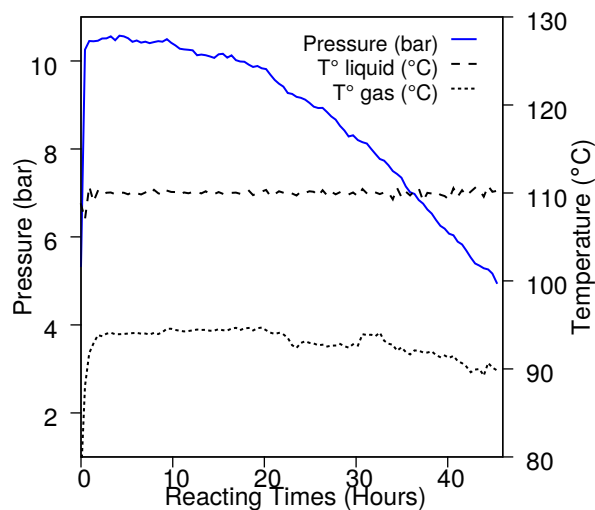
Real time sampling is performed as samples are collected using valves V3 and V2 in the liquid and gas

<sup>1</sup>This parameter may be adjusted on the control panel

phase. As presented on the scheme, the same line is used to perform both gas loading and liquid sampling. In addition, a heated transfer line (*TL*) establishes the connection between the autoclave and the GC-Flame Ionization Detector (FID) injection loop (*IL*). To avoid pressure surges between the reactor and the sampling part, a Pressure Reducer (*PR*) is set after the sampling valve (*V2*). As observed in the scheme, a last sample is performed from the GC injection loop with Tedlar Bags to perform off-line analysis by the GC-TCD.



(a) Scheme representing the autoclave experiment with the GC coupling. Measurements monitoring are presented in grey: the Pressure Transducer (PT) and the thermocouples ( $T_{gas}$  and  $T_{liq}$ ). Heated and insulated sections are respectively dashed red lines and shaded blocks. M, PR, IL respectively stands for the Mixing system, Pressure Reducer and Injection loops.



(b) Typical experimental signals obtained with the autoclave. The presented experiment is Aut07, n-octane at 110 °C with 8-9 bars of Oxygen pressure.

**Figure 3.2:** Autoclave scheme and typical experimental signal

## Operation

Typical experiments are proceed in four steps: device loading, initialization, starting time and sampling.

First, the autoclave is filled with 50mL of liquid reactant. Once the top cover of the autoclave is closed with all bolts tighten at the appropriate torque, the autoclave is flushed with He to remove air from the cell<sup>2</sup>.

Still under inert conditions, the device is heated up to the requested temperature until liquid temperature stabilization.

At this time, typical pressure is below 5 bars before O<sub>2</sub> addition. Then, a subsequent oxygen addition up to 15 bars and vessel venting up to 5 bars is performed. This first oxygen pressure onset represents the starting time of the experiment. This addition-venting cycle is reproduced 3 times before adding oxygen to the requested pressure, typically 10 bars. As demonstrated in the set of equations (3.1), this dilution process permits to reduce Helium gas fraction below 1.5% with conservative numerical values<sup>3</sup>. In addition, as helium diffusivity is greater than oxygen, this value is overestimated compared to the effective helium

<sup>2</sup>He was selected rather than N<sub>2</sub> due to N<sub>2</sub> co-elution with oxygen on the GC-TCD. In addition, helium diffusivity facilitates air removal from the liquid.

<sup>3</sup>The numerical application assumes a fuel evaporation contribution of 1 bar on initial pressure of 5 bars.

fraction.

$$\begin{aligned}
\text{Using Dalton' Law,} \quad x_i &= \frac{P_i}{P_{Total}} \\
x_{He,Final} &= \frac{x_{He,cycle_n}}{P_{Final}} \\
\text{Defining,} \quad x_{He,cycle_n} &= \frac{x_{He,cycle_{n-1}} \times P_{Low}}{P_{High}} \\
x_{He,cycle_{n-1}} &= \frac{x_{He,cycle_{n-2}} \times P_{Low}}{P_{High}} \\
x_{He,cycle_1} &= \frac{P_{He,ini}}{P_{High}} \\
\text{The generalized form is,} \quad x_{He,Final} &= \frac{P_{He,ini}}{P_{Final}} \times \left( \frac{P_{Low}}{P_{Final}} \right)^{n_{cycles}} \\
\text{Using, } P_{He,ini} = 4 \text{ bars, } P_{Final} = 10 \text{ bars, } \frac{P_{Low}}{P_{High}} = \frac{5}{15}, n_{cycles} = 3 \\
x_{He,final} &\approx 0.015
\end{aligned} \tag{3.1}$$

During the experiments, samples are prepared by pumping the section after V2 to remove trace level species. Then, they are performed by actioning V2 to simultaneously load the GC-FID injection loop and perform the sampling for the GC-TCD analysis. To minimize equilibrium changes due to the sampling, oxygen is added to compensate for the pressure loss which is typically close to 1 bar. Preliminary tests have demonstrated a negligible impact of this oxygen addition on the overall kinetics considering the measurement uncertainties. Finally, liquid sampling is performed with a vial under vacuum and a needle mounted on V3.

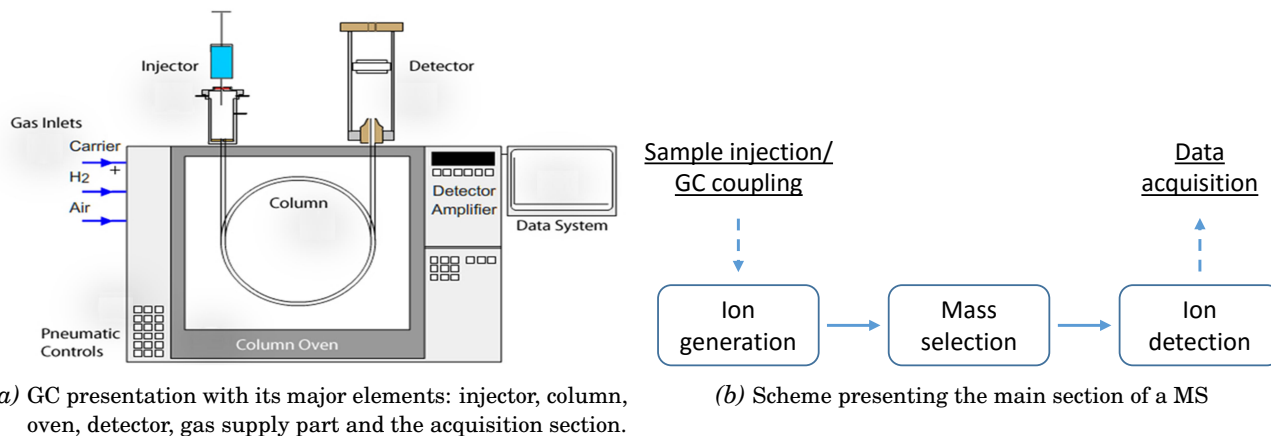
### 3.1.3 Analytical devices

In the experimental results presented in the next chapter, analyses were performed with several devices to characterize oxidation products formation. All analytical techniques used within this work are presented with a brief working principle description.

#### Gas Chromatograph principle

As illustrated in [Figure 3.3a](#), individual constituents of the sample injected inside a GC may be separated thanks to their respective affinities with the column and monitored at the end with a detector. This affinity is specific to either GC parameters (initial oven temperature, oven temperature program, injection temperature, carrier gas selection and velocity) or by the column specifications (length, film thickness, internal diameters, active surfaces/polarity). After separation, products can be detected according to different techniques like the FID, TCD, MS, Nitrogen-Phosphorus Detector (NPD), Ultra-Violet (UV) for the most famous. A working principle of each detector used in the present study is introduced.

While the FID is a destructive detection technique, it is also the most widely used detector for hydrocarbons analysis. This is due to its high and linear response evolution with respect to the carbon weight inside most conditions. The working principle of this detector is simple, an hydrogen-oxygen flame is operated at the exhaust of the column. All the products are burnt into that flames and generate ions which are collected with an electrode and then converted into a voltage signal directly linked to products quantity. The TCD detectors is commonly used for light gases analysis, with commonly with up to 5 carbons. The detection principle is based on a conductivity difference between the column exit, composed of the carrier



**Figure 3.3:** Gas chromatograph presentation and a scheme presenting MS working principle.

gas and eluted products, and the carrier gas used as a reference. Thus, due to similar thermal conductivity, H<sub>2</sub> detection sensibility is not satisfactory when Helium is selected as carrier gas.

The MS is an analytical technique by itself and can be used without a GC. When it is used as a detector, it simplifies mass spectrum analysis thanks to the GC separation. As illustrated in Figure 3.3b, the MS is composed of three parts: Ion generation, Mass selection and Ions detection. For each part of the MS several techniques exist, our interest is focused on the one in use with our MS. In the conditions of the present study, ions fragments are generated by electron impact generated itself with a high temperature filament. Then, mass are sorted specifically according to their mass over a charge ratio ( $m/z$ ) with a quadrupole generating an oscillating magnetic field. Finally, ions are monitored with an ion multiplier detector.

### FTIR-ATR principle

Although this technique is less accurate and selective than GCs, the FTIR analysis is a non destructive technique allowing structural information without applying any thermal stress on the samples. For this reason, it is used to complete and confirm specific GC conclusions but not as a standard procedure.

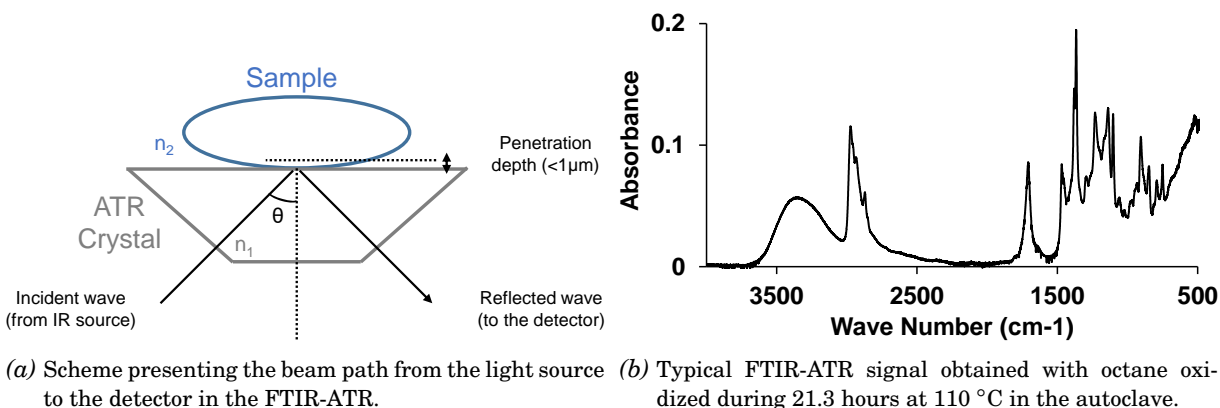
Signal acquisition from FTIR-ATR is similar to transmission FTIR and based on the Beer-Lambert's law (3.2). With, the Absorbance ( $A$ ) defined as the logarithm of incoming over outgoing lights ratio ( $\frac{I_0}{I}$ ). The IR light is absorbed and excites the molecules according to vibrational, rotational and translational modes as presented in Table 3.1. Thus, absorption signal of a given molecule is function of its extinction coefficient ( $\epsilon$  in  $cm^3 \cdot mol^{-1} \cdot cm^{-1}$ ), the optical path ( $l$  in  $cm$ ) and its concentration ( $c$  in  $mol \cdot cm^{-3}$ ) and is expressed as a sum of individual absorption in case of blends (3.2).

In the case of the FTIR-ATR, the incident beam crosses an ATR crystal, then totally reflects on the sample-crystal interface and finally crosses out the crystal to the detector. This *Total Reflection* is obtained when a IR beam, with a high incident angle ( $\theta$ ), crosses an optically thinner material ( $n_2 < n_1$ ). In such configuration, only sample-crystal interface (few  $\mu m$ ) contributes to the IR signal attenuation as presented Figure 3.4a. Further informations on this specific techniques are available in literature [100].

$$\begin{aligned} \text{From Beer's Law} \quad A &= -\log \frac{I_0}{I} = \epsilon \times l \times c \\ \text{With a blend of } n \text{ compounds,} \quad A &= \sum_{i=1}^n \epsilon_i \times l \times c_i \end{aligned} \quad (3.2)$$

The FTIR-ATR (*Vertex 70* from *Bruker*) is operated placing few drops of the sample on the mono reflection horizontal diamond. The final spectrum is obtained averaging 8 scans over wave number range

from 500 to 4000  $\text{cm}^{-1}$  with a resolution of 0.2  $\text{cm}^{-1}$ .



**Figure 3.4:** FTIR-ATR working principle and typical signal presentation

**Table 3.1:** Typical IR absorption bands for oxidized paraffins with vibrational mode informations in bracket.

Chemical family	Wave number ( $\text{cm}^{-1}$ )	Bonds involved
<u>Alkanes</u>	3000-2850	C-H (stretching)
	1470-1450	C-H (bending)
	1380-1370	C-H (bending)
<u>Carbonyles</u>		
ketones/aldehydes	1740-1650	C=O (stretching)
<u>Acids</u>		
	3400-2500	O-H (stretching)
	1740-1660	C=O (stretching)
	1320-1210	C-O (stretching)
<u>Esters</u>		
	1750-1730	C=O (stretching)
	1300-1000	C-O (stretching)
<u>Alcohols</u>		
	3600-3200	O-H (stretching)
Primary	1080-1000	C-O (stretching)
Secondary	1160-1050	C-O (stretching)

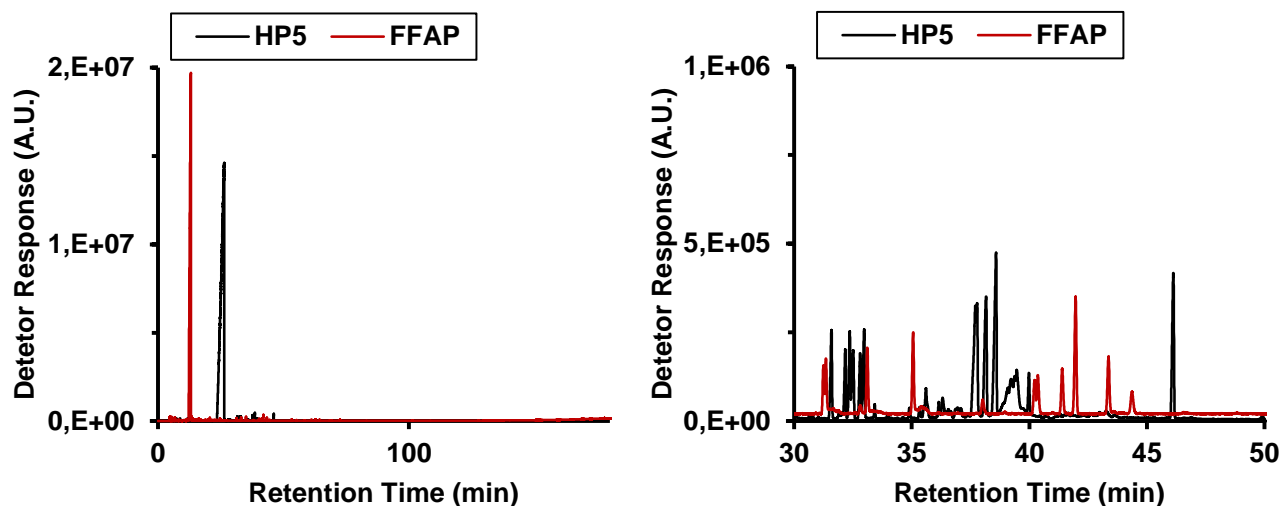
### GC preliminary study

Due to the large amounts of potential oxidation products. A preliminary study was performed in order to identify appropriate GC settings and more specifically the column itself. In this preliminary study three columns were tested: a DB-1, a HP-5 and DB-FFAP, with several GC settings to identify which one allows high peaks resolution for most of the oxidation products. An oxidized residual of decane obtained at 160 °C from PetroOxy experiment was selected to assess columns capability.

As observed in literature [56], peak resolution with the DB-1 column is not satisfactory, with many co-elution phenomena behind the solvent peak. As all those co-eluted peaks contain most of the first oxidation products like ketones, alcohols, acids, the separation capability of the DB-1 is not satisfactory for semi-quantitative applications.

As observed in Figure 3.5, typical elution from DB-1 and DB-FFAP columns is presented with which com-

pounds are respectively sorted according to compound molecular weights and polarity. While HP-5 separation is greater than the DB-1, DB-FFAP results offer greater separation between major products as presented in [Figure 3.5b](#). As most of products of interest are oxygenated molecules like ketones and alcohols with identical chain length as the initial fuel, many co-elution phenomena may occur behind the fuel peak using HP-5 or DB-1 column. Thus, the DB-FFAP was selected as a standard column for oxidation product analyses in the present work ([Table 3.2](#)).



(a) Full scale chromatogram of oxidized decane at 160 °C using both HP-5 and DB-FFAP columns. A.U. stands for Arbitrary Units

(b) Zoomed chromatogram of oxidized decane at 160 °C using both HP-5 and DB-FFAP columns. A.U. stands for Arbitrary Units.

**Figure 3.5:** Comparison of HP-5 and DB-FFAP separation capability on an oxidation residual sample.

### List of all devices

As presented through this section, several analytical devices are used within this work. [Table 3.2](#) summarises all previously presented techniques with their final operating conditions. From this table, it can be noticed that the GC-FID and the GC-MS are equipped with a similar column in order to get comparable chromatograms. Indeed, liquid and gas phase samples are operated differently into the GC. Indeed, liquid samples are injected from a vial with autosamplers, whereas external injections loops are filled for gas phase analyses and then injected inside the GC with pneumatic valve switch. Finally, this tabular also classifies techniques according to their qualitative or quantitative capability.

As observed in [Table 3.2](#), TCD analyses are carried out with several columns and specific valve timing. The separation capability of this devices is assured with a molecular sieve coupled to appropriate valve switching delays. The specific working principle of this device is presented in [Figure 3.6](#). The first step is the loading position (a) where products are collected in the injection loop. Then the first Valve (V1) rotates and products separation starts with the retainment of heavier product on the first column. Then, the valve (V2) permits to trap light products like oxygen, nitrogen and methane within the molecular sieve and, during this period (c), heavier products like CO<sub>2</sub>, ethane and propane are eluted. At the end of the method (d), the valve (V2) switch back to its original position and release the light compounds. Finally the first valve V1 switch back to its original position to prepare next injection.



**Table 3.2:** List of all analytical devices. \* sign means those analyses were set for autoclave study and was not available for previous studies. If no holding time are provided in oven programs it means this value equals 0.

## Techniques Phase analysed In experiments

### Qualitative Analyses

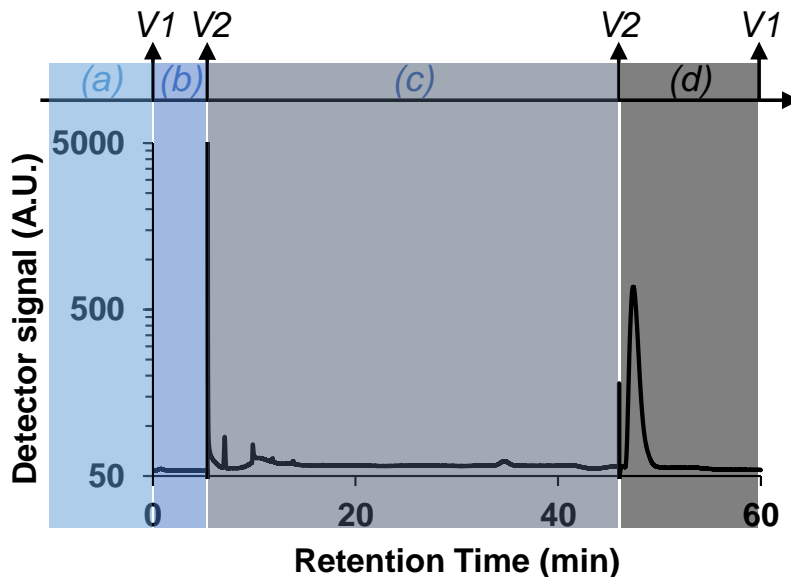
GC-MS	Liquid and Gas	Petroxy and Autoclave
<p><u>Specifications:</u> GC 6890N coupled to a MS 5973 both from <i>Agilent</i>. The GC is equipped with an autosampler G4513A and a DB-FFAP column (30 m × 0.25 mm × 0.25 μm); GC settings are: carrier gas: He with constant flow 0.5 mL/min; Split/splitless injector 275°C, 1 μL sample with a 150:1 split ratio; Oven program: <math>T_{init}=40^{\circ}\text{C}</math> for 10min, then 5°C/min up to 100°C, 1°C/min up to 150°C and 20°C/min up to 250°C held 13 min. MS settings (electron impact (70 eV); quadrupole detector in full scan mod, m/z range from 10 to 600)</p>		
FTIR-ATR	Liquid	Petroxy and Autoclave
<p><u>Specifications:</u> The FTIR-ATR involve a mono-reflexion ATR cell equipped with an horizontal crystal in diamond. Spectra are obtained in atmospheric conditions averaging 8 scans over the wave numbers range 500-4000 <math>\text{cm}^{-1}</math> with a resolution of 0.2 <math>\text{cm}^{-1}</math>.</p>		

### Semi-quantative Analyses

GC-FID	Liquid	Autoclave*
<p><u>Specifications:</u> GC 6890N from <i>Agilent</i> with an auto-sampler 7683 series and a DB-FFAP (60 m×0.25 mm× 0.25 μm). GC settings are: carrier gas: He with constant flow: 0.7mL/min; Split/splitless injector 200°C, 1 μL sample with a 500:1 split ratio; Oven program: <math>T_{init}=40^{\circ}\text{C}</math> for 10min, then 5°C/min up to 100°C, then 1°C/min up to 150°C and 20°C/min up to 250°C held 13 minutes. Detector settings: 200 °C, flows: H<sub>2</sub> 30 mL/min, air 350 mL/min, makeup 25 mL/min.</p>		
GC-TCD	Gas	Autoclave*
<p><u>Specifications:</u> GC 6890N from <i>Agilent</i> equipped with a 250 μL heated injection loop (150°C), a Porapak Q (packed column: OD=1/8", ID=2.5 mm and l=4.5m) and 5 Å molecular sieve (packed column: OD=1/8", ID=2.5 mm and l=7.6m). GC settings are: Carrier gas: He, constant flow 30mL/min; injection loop is the injector; Valve timing: 0.00 min V1 et V2 OFF, 0.10 min V1 ON, 5.40 min V2 ON, 46.0 min V2 OFF, 60.0 V1 OFF; Oven program: <math>T_{init}=50^{\circ}\text{C}</math> during 5 min, then 5°C/min up to 55°C and 55°C/min up to 245°C) held 32 min, cooling up to 70°C at 40°C/min held 14 min; Detector settings: Temperature:250 ° C, reference flow: 40 mL/min.</p>		
GC-FID	Gas	Autoclave*
<p><u>Specifications:</u> <i>Varian GC/450</i> equipped with a 20 mL heated injection loop (180°C) and DB-FFAP column (30 m × 0.25 mm × 0.25 μm). GC settings are: Carrier gas: He, constant flow 1mL/min; Split/splitless injector (1177): 275°C, split ratio: 250:1; Oven program: <math>T_{init}=30^{\circ}\text{C}</math> during 5 min, then 5°C/min up to 150°C and 15°C/min up to 245°C) held 10 min; Detector settings: 275 °C, flows: H<sub>2</sub> 30 mL/min, air 300 mL/min, makeup 20 mL/min.</p>		

### 3.1.4 Calibration coefficient estimation

As introduced in the section 2 and presented in the preliminary study, numerous oxidation products are formed during autoxidation. For kinetic modeling validation, most of them have to be quantified or semi-quantified. Due to the size of the experimental matrix (Cf. chapter 4), the establishment of an external calibration for individual constituents is not realistic. This section introduces the methodology used to estimate FIDs DRs for liquid and gas phase species quantified with the GC-FID. In contrary, due to the limited number of species of interest in the GC-TCD analyses, their quantification is performed with an external calibration using a single gas calibration standard.



**Figure 3.6:** Illustration of valve timing with the GC-TCD. Area (a) represents the injection loop loading. Area (b) stands for all products elution. At the beginning of the (c) area, the valve V2 switches and traps all light products, and during this period, heavier ones are eluted. In (d), the valve V2 switches back and releases light products trapped in step (b).

### ECN method presentation

This method calculates a set of relative Response Factor (RF), using the ratio of ECN coefficients between a given compound and a reference as described in (3.3). As presented in Table 3.3, these coefficients are obtained by summing and subtracting respectively each carbons types and penalties according to the chemical functions present in the molecule. As FID detectors get a linear response over carbon weight, RF expression is chosen by weight. Then, using RF definition from (3.4), we can express compound mass fraction  $w_{comp}$  according to the weighted RF ( $RF(wt)$ ), areas ( $Area_{ref}$  and  $Area_{comp}$ ) and the reference mass fraction ( $w_{ref}$ ) (3.5). Developing  $Area_{ref}$  and  $RF(wt)$  terms respectively from (3.6) and (3.3), we obtain a new mass fraction expression (3.7), expressed as function of pre-calculated terms. As both structural information and Molecular Weights are obtained through GC-MS analyses, all identified products can be easily quantified with the GC-FID once the DR of the reference compound ( $DR_{ref}$ ) is calibrated with the device.

As an example, Figure 3.7 presents how to use the coefficients defined in Table 3.3 with the 5-hydroxymethyl-2furaldehyde (HMF) to calculate its DR ( $DR_{HMF}$ ). Thus, the HMF or any other identified compound can be quantified once the external calibration of the reference compound is performed.

$$RF(mol) = \frac{ECN_{ref}}{ECN_{comp}} \quad \text{or,} \quad RF(wt) = \frac{ECN_{ref} \cdot MW_{comp}}{ECN_{comp} \cdot MW_{ref}} \quad (3.3)$$

$$RF(wt) = \frac{Area_{ref} \cdot w_{comp}}{Area_{comp} \cdot w_{ref}} \quad (3.4)$$

$$w_{comp} = \frac{Area_{comp} \cdot w_{ref} \cdot RF(wt)}{Area_{ref}} \quad (3.5)$$

$$Area_{ref} = DR_{ref} \cdot w_{ref} \quad (3.6)$$

$$\text{Using (3.3) and (3.6) in (3.5), } w_{comp} = \frac{Area_{comp} \cdot ECN_{ref} \cdot MW_{comp}}{DR_{ref} \cdot ECN_{comp} \cdot MW_{ref}} \quad (3.7)$$

$$\text{Or, similarly to (3.6) } w_{comp} = \frac{Area_{comp}}{DR_{comp}} \quad \text{with} \quad DR_{comp} = \frac{DR_{ref}}{RF(wt)} \quad (3.8)$$

**Table 3.3:** The value of carbons and chemical functions penalties used in the ECN model.

	"C" in aliphatic or aromatic	"C" in carbonyl	"C" in olefinic	"O" in ethers	"O" in primary alcohol	"O" in secondary alcohol	"O" in esters or tertiary alcohols
<u>Coeff.</u>	1	0	0.95	-1	-0.6	-0.75	-0.25

Assuming *n*-C8 as the reference compound with an arbitrary  $DR_{ref} = 10000$  a.u.

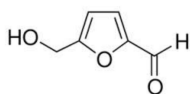
$$ECN_{ref} = 8C_{aliph.} = 8$$

$$ECN_{HMF} = 4C_{olef.} + 1C_{carbon.} + 1C_{aliph.} + 1O_{prim.OH} + 1O_{ether}$$

$$ECN_{HMF} = 4 \times 0.95 + 0 + 1 - 0.6 - 1 = 3.2$$

$$MW_{ref} = 114.2 \text{ g/mol}$$

$$MW_{HMF} = 126.1 \text{ g/mol}$$



HMF

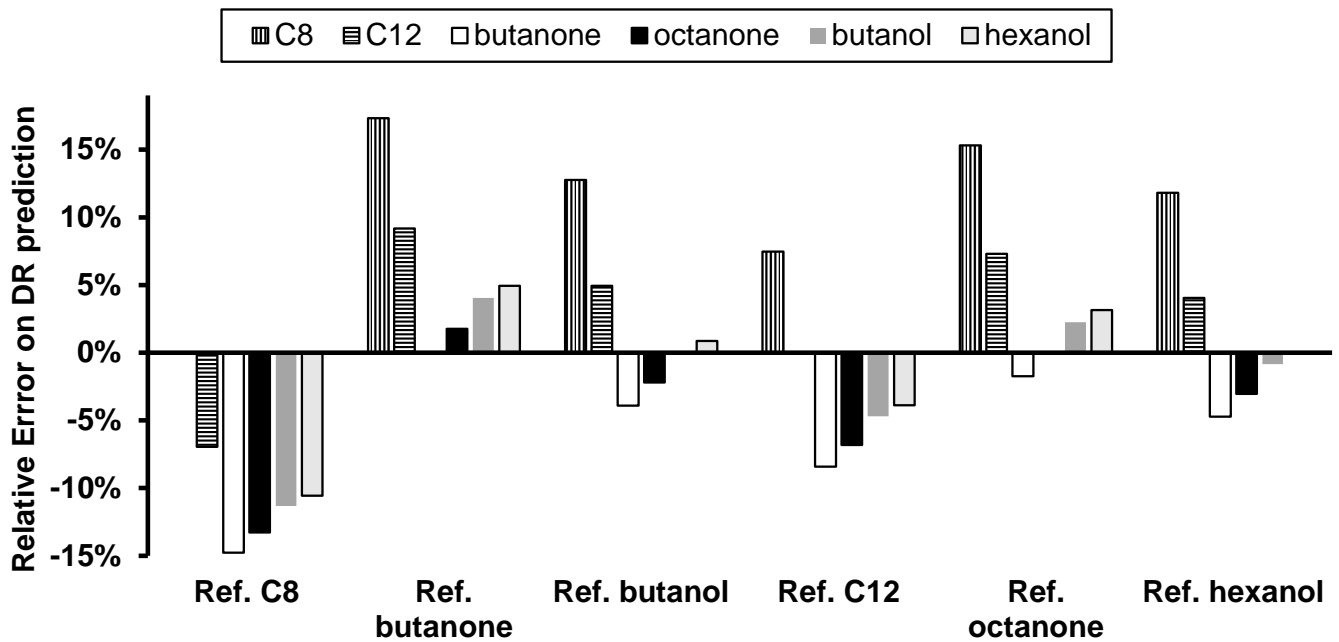
$$\text{Using (3.3), } RF(wt) = \frac{8 \times 126.1}{3.2 \times 114.2} = 2.76 \quad \text{and} \quad D.R._{HMF} \approx 3623.2 \text{ a.u.}$$

**Figure 3.7:** Example of Detector Response calculation using the ECN model. a.u stands for area units. HMF stands for 5-Hydroxymethyl-2-furaldehyde.

### ECN limitations and calibrations validation

As presented in Figure 3.7 and (3.8),  $DR_{comp}$  predictions may deviate according to the ratio  $(\frac{DR_{ref} \times MW_{ref}}{ECN_{ref}})$  which means that the selected reference affects ECN model performance. Hence, the ECN method was evaluated according to a set of oxygenated compounds relevant to the major families of oxidation products: octane, dodecane, butanone, 2-octanone, 2-butanol and 1-hexanol. External calibrations are obtained for each of them and then compared to the ECN model predictions. Calibration mixtures are prepared with a high precision scale (< 0.2 mg) and high purity products (> 99 %) to limit composition uncertainties. As presented in Figure 3.8 and with S1 parameter in Table 3.4, relative errors on DRs predictions are higher when the reference compound is an alkane (C<sub>8</sub> or C<sub>12</sub>) or the butanone. However, as observed in Table 3.4 with S2 parameter, butanone  $\sum |Rel.Errors|$  is much lower omitting errors from alkanes DRs which also means ECN model prediction is not suitable for alkanes DRs. While ECN method prediction is still not satisfactory when alkanes are set as a reference, all other references give satisfying results with a highest  $\sum |Rel.Errors|$  of 11% for butanone.

To conclude, as ECN model deviates for light oxygenated molecules and polyoxygenated compounds [101], octanone was selected as a reference compound for all oxygenated DRs estimation. Due to the linear response of FID with carbon weight, alkanes DRs are estimated according to this method. The gain obtained

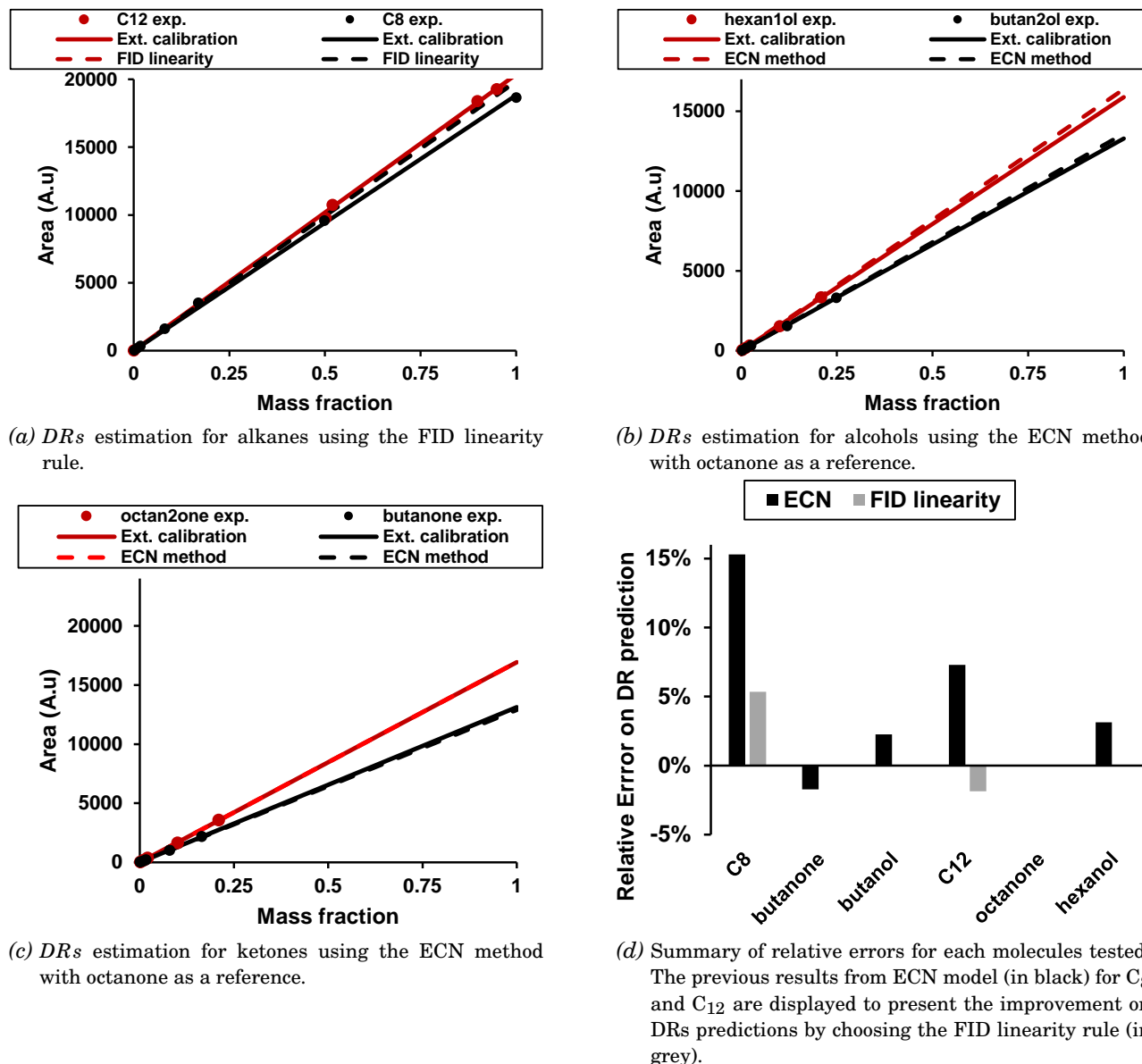


**Figure 3.8:** Relative Errors ( $RE = \Delta(D.R._{ECN,i} - D.R._{Exp,i})/D.R._{Exp,i}$ ) on DR prediction over the 6 molecules tested for a given ECN reference compound. "Ref. C8" means octane is selected as a reference compound ( $DR_{ref}$ ) in the ECN model

**Table 3.4:** Summary of ECN model deviation on predicting  $D.R._{comp}$  from a given reference compound. S1 corresponds to the sum of the absolute relative errors obtained over the 6 molecules tested for a given reference compound, with  $RE = \Delta(D.R._{ECN,i} - D.R._{Exp,i})/D.R._{Exp,i}$ . S2 represents the sum of the absolute relative errors for oxygenated molecules only.

Reference	$S1 = \sum_i  RE $	$S2 = S1 - RE_{C_8} - RE_{C_{12}}$
C <sub>8</sub>	57%	50%
2-butanone	37%	11%
2-butanol	25%	7%
C <sub>12</sub>	31%	24%
2-octanone	30%	7%
1-hexanol	24%	9%

by selecting this method is represented in [Figure 3.9d](#). Finally, as a few percentages error on DRs is not admissible for fuel quantification (especially when  $w_{fuel} \approx 1$ ), an external calibration is performed for each of them. As presented in [Figure 3.9](#), this method gives satisfying results with a maximum relative errors of 7% for all the oxidation products tested.



**Figure 3.9:** Final predictions on the detector response according to typical chemical families of oxidation products. C<sub>8</sub> and C<sub>12</sub> predictions are obtained according to FID linearity rule and oxygenated molecules predictions are obtained according to the ECN models.

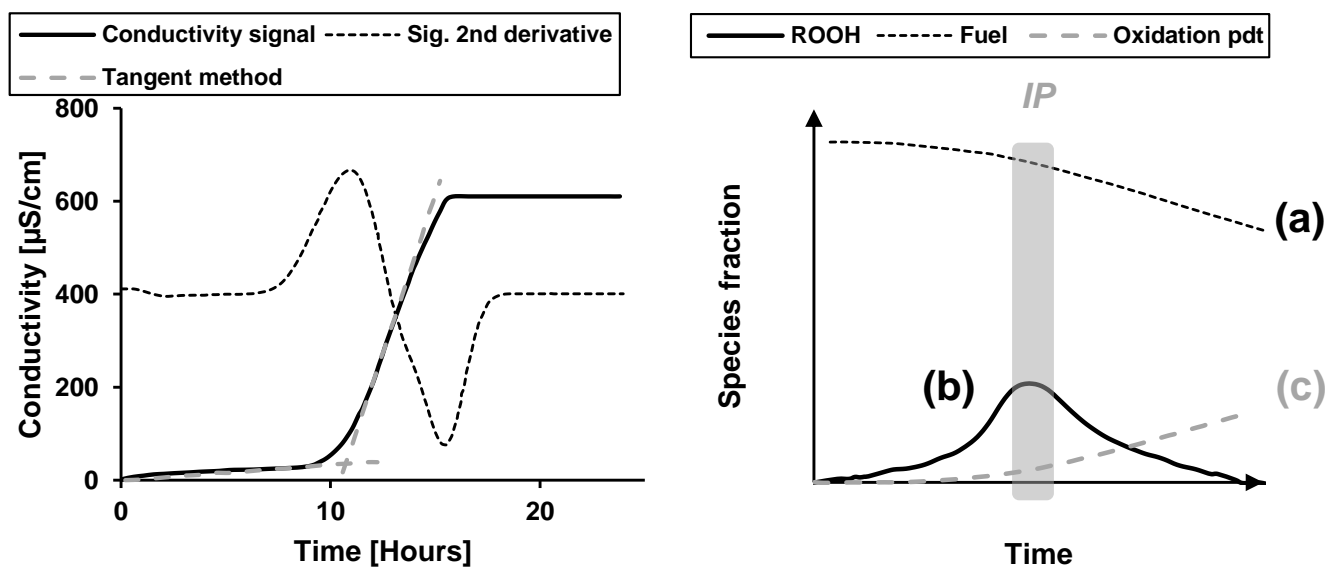
### 3.1.5 Induction Period definitions

This section is devoted to the introduction of the term "IP" and how this macroscopic criterion can be extracted from experimental results. IP refers to a delay from which the autoxidation kinetics accelerates and the branching steps becomes predominant. For this reason, it has been widely used in the present work as a validation parameter for the modeling.

The IP can be extracted from macroscopic descriptors, like a pressure drop monitoring like in the PetroOxy experiment (Figure 3.1b), a conductivity drift induced by volatile compounds formation as presented in Figure 3.10a or in some cases accessible from acidity level measurements [45].

Using more precise data, the IP can be obtained from several types of species profile as presented in Figure 3.10b. In the most simple case (a), when fuel consumption is recorded, a 5 % consumption can be assumed to correspond to IP as it is commonly performed in literature [46]. In conditions (b), when species profiles has a peak shape, like for mono-hydroperoxides, the IP is extracted from its peak maximum. Then

in (c), when a product accumulates, 2 methods can be used to extract IP. The first is to detect the second derivatives maximum as performed for the conductivity signal in Figure 3.10a. The second one, applicable only for experiments with a good carbon balance, is to sum all products mole fraction and detect when this value passes a threshold value of the total mixture.



(a) Typical IP extraction from conductivity monitoring during autoxidation in a Rancimat experiment. The IP can be determined according to the second derivative method or the tangent method as presented in [46].

(b) Typical IP extraction from several species profiles measurements.

**Figure 3.10:** Techniques used to extract IP from experimental data containing different type of data: Species profiles, macroscopic measurements.

Results presented in Figure 3.10 are in ideal conditions and species profiles shapes change due to the experimental vessel design. As an example, oxidation products profiles differ between a vessel operated with a constant oxygen flow and one with a finished oxygen amount. Nonetheless, those examples give an overview of all possibilities to interpret experimental data available to determine an approximate IP.

## 3.2 Molecular modeling approach

As presented in section 2.2.3, the solvent effects imply corrections on both kinetic data and thermochemistry. Each reactive system requires specific corrections and only few solvent-reactant systems were investigated. Therefore, a MSA is proposed here to develop liquid phase mechanisms including relevant species thermochemistry and kinetic rates for the study of new chemical systems. The MSA is part of a general modeling methodology presented in Figure 3.11. It aims to cover multiple steps from fuel identification to stability prediction for given conditions. The goal of the MSA is to reduce mechanism generation time.

Based on a feedback loop, the quality of the mechanisms obtained with the MSA improves along with the number of iterations. This improvement cycle is illustrated in Figure 3.12 where forward and backward connections between each scale levels are respectively illustrated with green and yellow arrows. In this section, the general idea of the methodology is presented first. Then, each scale and their associated tools are detailed. Finally, important features and key steps of this methodology are highlighted.

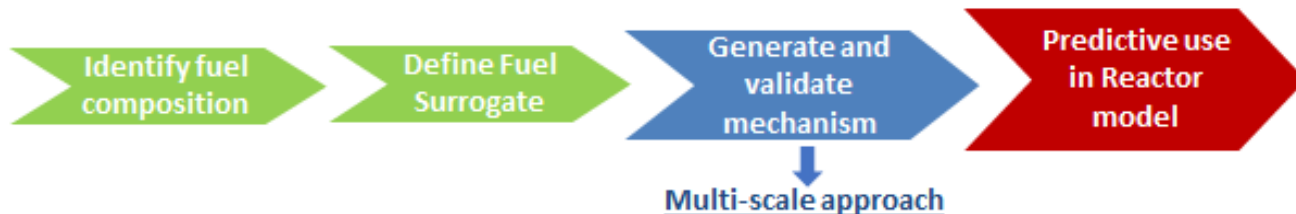


Figure 3.11: General modeling chain from fuel to reactor

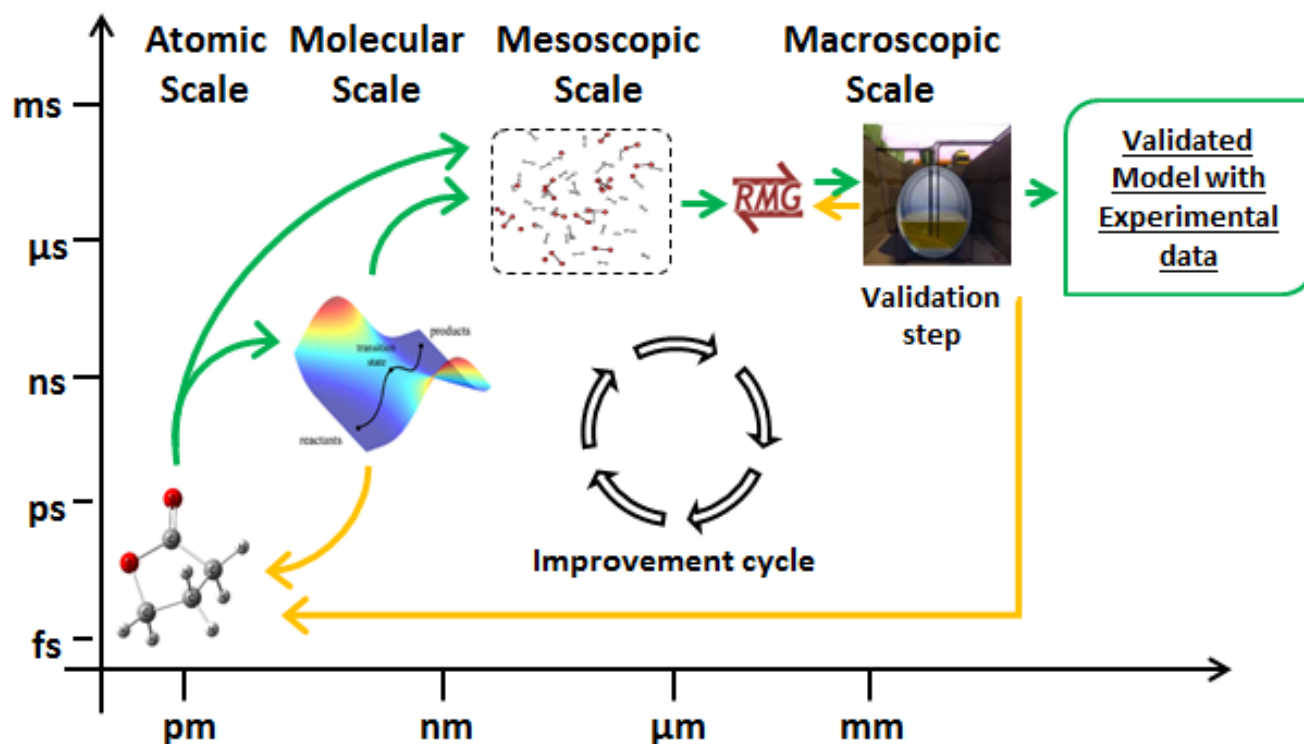


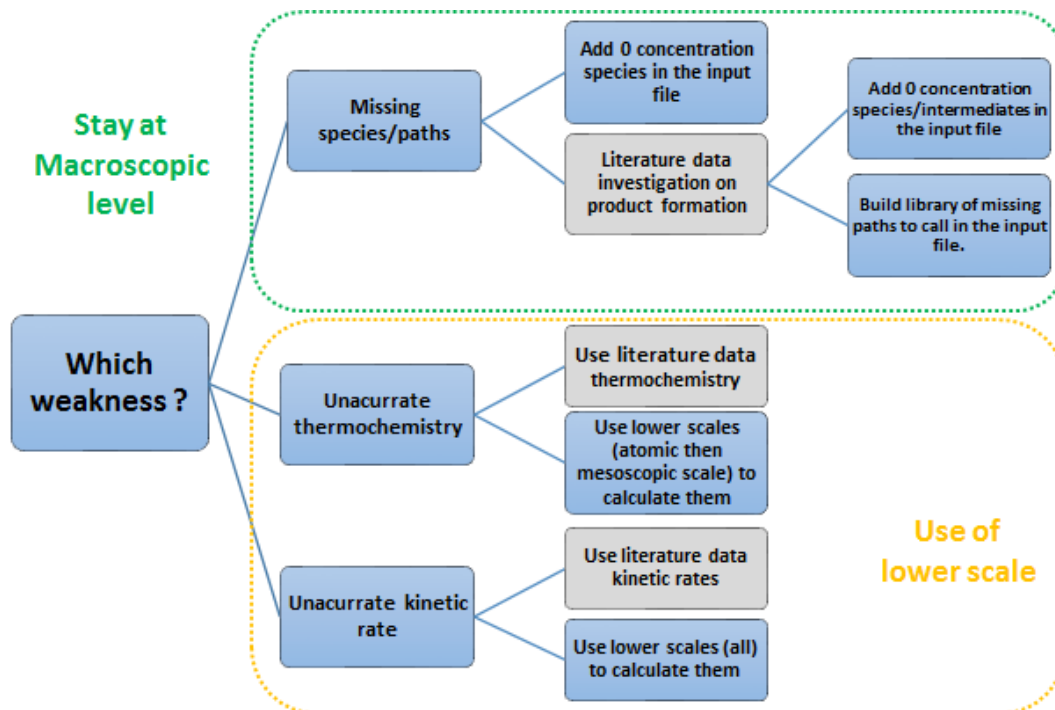
Figure 3.12: MSA presentation.

### 3.2.1 Description of the methodology

Each scale of the methodology can be classified into two different steps: mechanism generation (macroscopic scale) or mechanism improvement (atomic, molecular and microscopic scale). Before going into the details of each scales, those two steps are presented. While kinetic mechanisms from literature may be used as a first guess or to complete sub-mechanisms, only the case that are not available in literature are treated.

#### Mechanism generation

The methodology starts at the macroscopic scale with the selected mechanism generator, RMG, and a kinetic solver. This step aims to generate a first mechanism for a specific system (species composition, temperature, pressure, contact time...) and confront it to experimental results. The mechanism generation requires commonly several iterations to get a relevant mechanism. Experimental data comparison enables to target important discrepancies such as missing species or inaccurate species profiles. Missing species and paths is the first problem to address as presented on the decision diagram in Figure 3.13. Then, analysis of the mechanism with RoP and sensitivity analyses using Chemkin-package [102] is required to identify the



**Figure 3.13:** Decision diagram presentation

species thermochemistry or reactions that have to be updated.

### Improvement of the first mechanism

From the previous step, several possibilities exist. The decision diagram (Figure 3.13) summarizes the options considered to improve the model. As presented in Figure 3.13, the process requires either literature data collections (green filled block) or numerical data from lower scales. Lower scales tools using ESC permit to calculate data species or reaction with insufficient/non-accurate data is available in the literature. Improvement cycle (Cf. Figure 3.12) can be reproduced as many times as required in order to obtain a validated chemical mechanism. Finally, once the mechanism is validated, it can be used for predictive applications, as presented in Figure 3.11.

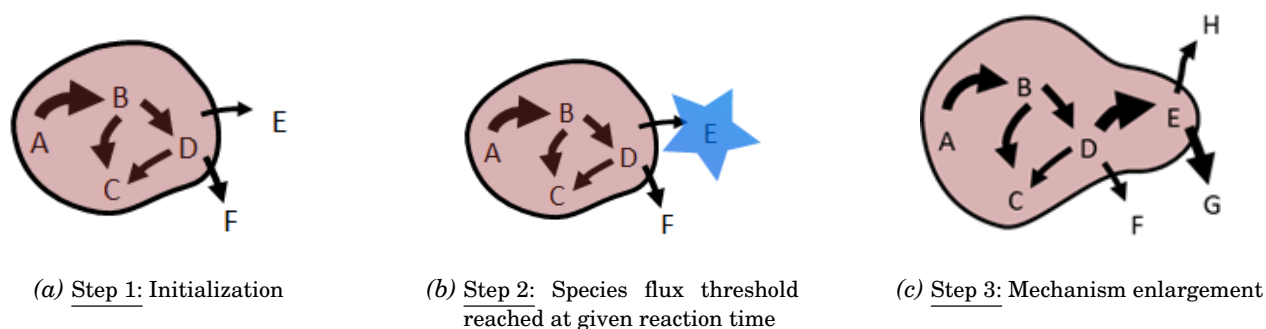
### 3.2.2 Models coupling

All combined, MSA steps aim at calculating liquid phase thermochemical data and kinetic rates for a given species. Atomic and molecular scale levels respectively are intended to calculate geometries, frequencies and species energies in gas phase. Then liquid phase data are obtained applying solvation models on gas phase data in the microscopic scale. Before going more into the details of each scale, the two software used here are presented.



## Mechanism generator software

RMG [103] is an open source automated gas phase chemical mechanism generator developed by Pr. Green's Group<sup>4</sup> and Pr. West's group<sup>5</sup>. The algorithm is based on the estimation rules of both thermochemistry and kinetics rate providing parameters for all species including radicals. In order to establish a correct group contribution method, each molecule used in RMG is represented using bond graph (also called adjacency list). Using this formalism all atoms, bonds and radical positions in each molecules are clearly identified. From this bond graph representation, groups representing the most the molecule are identified and used to estimate the thermochemistry and the kinetic rates using Benson's group additivity. Further information on the adjacency list and the group identification are available in appendices (section .2.4). To improve the thermochemistry and kinetic rate results, libraries can be built to override RMG's estimations. The use of these libraries enhances the capabilities of such automatic mechanism generators by providing the option to implement specific data set. RMG generates a chemical kinetic model for a given set of reactants and for precise conditions (concentrations, temperature, pressure). All species in the code are classified as a core (which is the final mechanism) or an edge species. Species present at the initialization step are automatically included in the core. Then reactions matching core species only are added as a core reaction. If core species react and give new products and new reaction paths, they are added to the edge until reaching the termination criterion (reaction time or conversion of a species). During this enlargement process, species passing a flux threshold (based on the user specified tolerance criterion) are added into the core model. This mechanism enlargement process is illustrated in Figure 3.14.



**Figure 3.14:** RMG generation process illustration. Species A, B, C and D are reactants. During the initialization step, the algorithm is finding reactions matching those species. After a given reaction time, Species E is passing the tolerance threshold and is added to the core mechanisms. Then new paths are investigated with species E in the core mechanism. Illustration was extracted from a RMG study group presentation [14].

RMG has been evaluated for several gas phase applications [104, 105]. Thanks to recent work from Jalan et al. [15, 12], RMG was upgraded with a liquid-phase module including a constant concentration option in the reactor model (mostly to maintain oxygen concentration in liquid) and solvent effect corrections on both species thermochemistry and diffusive limits on reaction rates. As presented on equations (2.5) - (2.15), species thermochemistry are corrected individually depending on a pair of solute/solvent descriptors. Solute descriptors are given in RMG database for approximately 200 components. For intermediates and products not provided in this database, a group contribution method is implemented to estimate the descriptors. Unlike solutes, few solvents descriptors are provided (26 in total). The extension of the solvent database is still on-going at the moment of writing. Liquid and gas phase RMG input files are very

<sup>4</sup>Department of Chemical Engineering, Massachusetts Institute of Technology (MIT), Cambridge MA

<sup>5</sup>Computational Modeling in Chemical Engineering group (CoMoChEng), Department of Chemical Engineering, Northeastern University, Boston MA

similar (liquid phase example is available as a supplementary material in [subsection .2.3](#)). Few additional keywords are required for the liquid phase: "Equation of state: Liquid", "solvent name:" (to identify which solvent descriptor to use), the viscosity in Pa.s-1 (to calculate the diffusion limit from Stokes-Einstein equation (2.14) - (2.15)). All other parts of the input file are similar.

Due to unexpected behaviour of the latest version of RMG-Java 4.0.1 (Cf appendices .2.1), an hybrid version of RMG (RMG-Hybrid) was build based on an updated RMG-Java 3.2.1 for the kinetic rates estimation and the use of the latest RMG 4.0.1 for the thermochemistry estimation. The term updated just means that the RMG-3.2.1 databases was updated with all new reaction families of RMG-4.0.1. Thus, benefits from the most recent version like the Korcek's reaction family and a corrected estimation of the free energy of solvation (Cf appendices .2.2).

Thus, for the consistency of the present work, all mechanisms are generated with RMG-Hybrid version if no specific mentions is given. In addition, typical mechanisms generation is performed with all reaction families except the sulfur-specific ones. Then thermochemical and transport libraries from the GRI 3.0 mechanism were selected and all other libraries were kept empty: primary kinetics library, kinetic library, seed mechanism.

### **Electronic structure calculations softwares**

As introduced in the literature section, many softwares are available in literature to perform ESC. Due to the list of solvent models already implemented in it [106] and its availability, Gaussian 09, was selected to perform all low theory levels calculations. In addition, when post HF calculations are required, MolPro is selected to perform those calculation and reduce computational time. Due to the computational cost of the liquid phase and the use of the SCRF models, only gas phase calculations can be performed at post HF theory level.

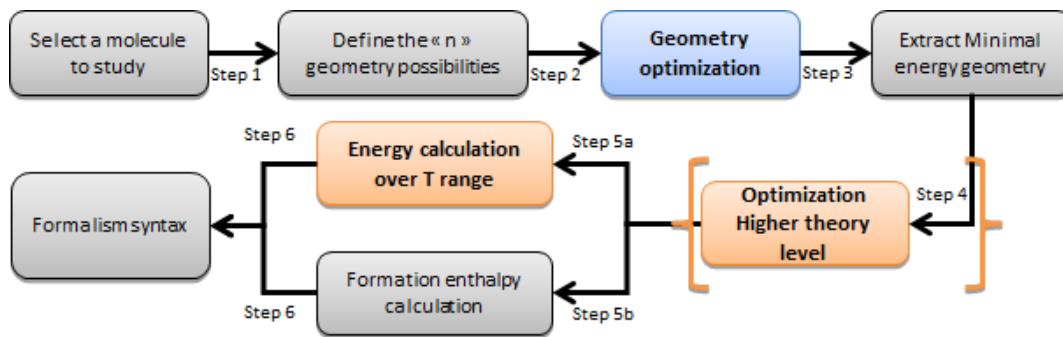
### **Atomic scale presentation**

As presented in [Figure 3.13](#), this step is mandatory for both molecular and microscopic scale levels. In order to obtain accurate gas phase thermochemistry and kinetic, energy calculations of optimized geometries are required. To reduce computational cost, a two-step approach is commonly assumed [107, 69, 108], with a low theory level for geometry investigation and then a higher theory calculation once an optimized geometry has been identified. Finally, energies are calculated over a temperature range and standard formation enthalpy are calculated to reconstruct thermochemical data in a given formalism (NASA, Wilhoit, ... ). Several methods exist in the literature to calculate the formation enthalpy: the reference atomization method, Homodesmotic approach [107, 17] or corrected atomization coefficient method [109, 110, 111, 112]. The whole molecule energy calculation process is summarized in [Figure 3.13](#).

### **Molecular scale presentation**

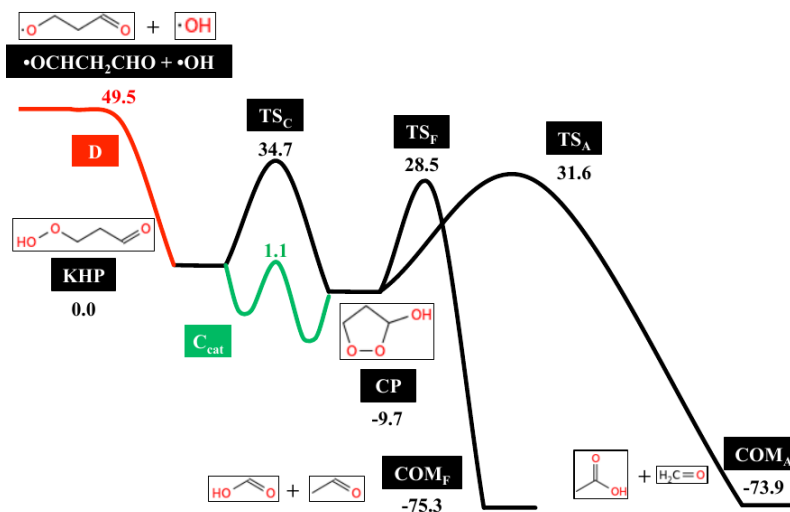
Once geometries, frequencies and electronic energies of all molecules involved in a given reaction are obtained, the PES linking reactants to products can be obtained. Low energy barriers reactions, as presented in [Figure 3.16](#), require specific treatments (based on the Multi Path Transition State Theory (MP-TST) and Multi Structural Transition State Theory (MS-TST) [113, 114, 115] to get accurate PES.

Results from this step can be used either to refine gas phase kinetic database that may be corrected by



**Figure 3.15:** Geometry optimisation process

RMG code or can be used directly as a liquid phase kinetic database after the solvent effect treatment from the mesoscopic scale.



**Figure 3.16:** PES with low energy barrier (D step) obtained by Jalan et al. [15] for the Korcek's reaction

### Mesoscopic scale presentation

Mesoscopic scale calculations can be used in: thermochemical and kinetic rate calculations in liquid phase. In those calculations, gas phase data are corrected applying a given SCRF model ( Figure 2.22 in section subsection 2.2.3) to include solute-solvent interactions.

While in some conditions, the gas phase geometries may correspond to the lowest energy geometry, in some other conditions, the stabilizing effect of solvent may change the energy level order of the geometries. For this reason, a consistent approach is to reconsider all initial geometries of the gas phase step to identify a possible lower energy conformer. This was presented with Figure 2.23 and Figure 2.23b, where energy barrier height may be affected specifically according to solute-solvent interactions. As a results, a higher energy barrier trajectory may become more relevant in liquid phase due to the stabilising effects of the solvent. In addition to the barrier energy height changes, the partition function may also be affected by the solvent effect, as presented in literature review chapter.

Results from this step is either used as an input of RMG generation or used to correct the generated mechanism (without re-generation).

## Macroscopic scale presentation

Because the MSA starts and ends at this scale level, it is important to identify two main components and their goal. At this level, mechanisms are generated with RMG for the first time or improved from the data available in the literature or from PES calculations. Then the second goal is to validate the obtained mechanism against experimental data using a 0D reactor model (IFP-kinetics) based on Chemkin formalism. According to the agreement with literature data, mechanisms can be either validated or improved by regenerating mechanism with new conditions or using the improvement cycle (Cf. [Figure 3.12](#)). Then, when the agreement is satisfactory, the generated model can be used for predictive purposes as presented in [Figure 3.11](#).

### 3.2.3 Key steps of the multi-scale approach

#### Mechanism generation

As a first step of the MSA, the first mechanism has to contain enough species and relevant reactions for the system of interest before improving it. But some paths or species may not be formed by the generator because of missing reaction families or a too low species flux. To identify it, several RMG tools can be used to identify which paths are missing or which reaction are involved to form a given product. Then, if no reactions are found, the expected reaction should be calculated through PES or specific kinetic libraries can be build by user from literature data. Focusing on the thermo libraries treatment in RMG-Java, the use of thermo libraries (in liquid phase generation) concerns only gas phase thermochemistry. Species matching a thermo library is then corrected through the LSER method to obtain liquid phase values in the final mechanism. Thus, liquid phase thermochemical library cannot be used directly without applying a second correction on it.<sup>6</sup> Thanks to this "auto-correction", accurate gas phase thermochemistry can be used in liquid phase mechanism generation.

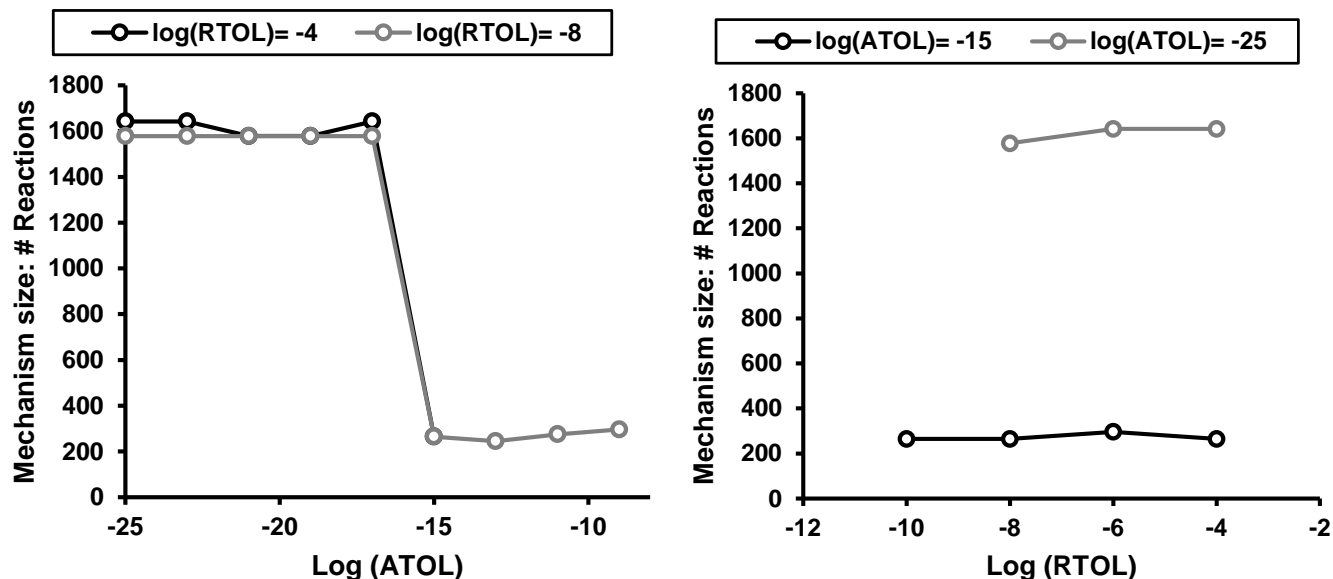
In addition, specific input parameters like ones from the solver, ATOL and RTOL, should be set with care. This is even more true for a rate based algorithm like RMG. To assess their impacts on the generation, a subsequent variation of one parameter with the second fixed is performed. While RTOL values seem non sensitive over the range  $10^{-10}$ - $10^{-4}$ , a critical value for ATOL is identified as respectively presented in [Figure 3.17b](#) and [Figure 3.17a](#). This illustrates that for a given input file the size of the final mechanism may diverge by setting too low solver parameters. According to those results, the ATOL and RTOL parameters has to be respectively set below  $10^{-16}$  and  $10^{-6}$ . In all generations presented within this work, conservatives values of  $10^{-18}$  and  $10^{-8}$  respectively for ATOL and RTOL values.

#### Electronic structure calculations

In ESC, an important step is to minimize the energy of structures from initial structure calculation of during trajectories calculations within a PES. As molecules may contain several rotors, as presented on [Figure 7](#), many geometries should be guessed based on chemical knowledge (hydrogen bonding tendency, bond length, angles, ...). Although all those structures may be pre-processed by hand, a more systemic

---

<sup>6</sup>On the new RMG version this was improved as mentioned in [3.2.3](#)



(a) Mechanism size impact of an ATOL variation for 2 fixed RTOL values

(b) Mechanism size impact of an RTOL variation for 2 fixed ATOL values

**Figure 3.17:** Impact of the ATOL and RTOL parameters on the mechanism size.

approach is possible using the *confgen* module from *MSTOR* [116, 117]. With this tool, the input file is a molecule with its cartesian coordinate representation added to a list of dihedrals on which rotations should be applied. As an output, this tool gives a list of Gaussian input files omitting configurations with a too small interatomic distance<sup>7</sup>. Illustrations of these rotors and typical number of conformers to consider are presented in [section .1](#).

### Mechanism generator upgrades

A new RMG version (RMG-Py), written in python, includes a lot of new features that may improve the generation process and the consistency of liquid phase mechanism. One of the most relevant is the implementation of the New-Style Adjacency list which better describes the molecule structure with paired and unpaired electrons, ions formations and allows proper representation of nitrogen containing molecules with hypervalency. This new style adjacency list has been discussed in literature[95], [Figure 3.18](#) presents an example of the changes. Further explanation on those developments are available in literature[95, 118, 119]. Finally, it allows to use thermochemical or kinetic liquid phase libraries [118]<sup>8</sup>. This highly accurate ESC calculations can be used as an input of a generation as long as they are in the same solvent.<sup>9</sup>

## 3.3 Conclusion

The two main approaches used in this work to obtain experimental autoxidation data have been presented in details. A first exploratory approach aims to assess system reactivity and provide limited information on the kinetics using Petroxy and appropriated analytical devices. The second approach using the autoclave

<sup>7</sup>This threshold is set to 5 Å and can be adjusted.

<sup>8</sup>Work performed during the Visiting Program at MIT, RMG-Py was upgraded to make differences between gas phase and liquid phase libraries for both thermochemistry and kinetics. Thus, highly accurate liquid phase thermo and kinetic libraries may be used to directly improve the generation

<sup>9</sup>Corresponding checks are implemented in the code

1 C 0 {2,S} {6,S} {7,S} {8,S}	1 C u0 p0 c0 {2,S} {6,S} {7,S} {8,S}	
2 C 0 {1,S} {3,S} {5,D}	2 C u0 p0 c0 {1,S} {3,S} {9,S} {10,S}	
3 C 0 {2,S} {4,S} {9,S} {10,S}	3 C u0 p0 c0 {2,S} {4,S} {5,D}	
4 C 0 {3,S} {11,S} {12,S} {13,S}	4 C u0 p0 c0 {3,S} {11,S} {12,S} {13,S}	
5 O 0 {2,D}	5 O u0 p2 c0 {3,D}	
6 H 0 {1,S}	6 H u0 p0 c0 {1,S}	
7 H 0 {1,S}	7 H u0 p0 c0 {1,S}	
8 H 0 {1,S}	8 H u0 p0 c0 {1,S}	
9 H 0 {3,S}	9 H u0 p0 c0 {2,S}	
10 H 0 {3,S}	10 H u0 p0 c0 {2,S}	
11 H 0 {4,S}	11 H u0 p0 c0 {4,S}	
12 H 0 {4,S}	12 H u0 p0 c0 {4,S}	
13 H 0 {4,S}	13 H u0 p0 c0 {4,S}	
<u>Old adjacency list*</u>	<u>New style adjacency list</u>	

**Figure 3.18:** Adjacency lists illustration. \* means this adjacency list contains explanatory H atoms, whereas they are not mandatory. The very first number represents the position of atoms. Then, C and O represent the atoms, then the number stand for the number of radical on the atom, then the list of connection of this atoms are presented between brackets: first number is referring to the atom number and then the letter to the bound type (S: single, D:double)

and its associated analytical devices, is complementary to the Petroxy studies and gives detailed information with both gas and liquid phase species profiles.

From the modeling side, the molecular modeling approach is presented in details with the MSA. It involves a hybrid version of RMG-Java to generate a first mechanism that may be improved by either user knowledge or literature data, ESC or a combination of both. As ESC steps are very long and complex, they were not evaluated during the framework of this thesis.



# Chapter 4

## Results and Discussions

Studies conducted within the framework of this thesis aims to reduce the gap between chemical knowledge and autoxidation phenomenon. To do so, the autoxidation of two chemical systems, the n-paraffins and the iso-paraffins, are subsequently investigated with the PetroOxy and the autoclave device. With the first device, preliminary study is performed in order (i) to assess the overall reactivity of the system, (ii) to identify major oxidation products and (iii) to build and analyse the chemical mechanisms obtained with the MSA. With the second device, detailed species profile of both gas and liquid phase are obtained in order to complete the first study with the dynamics of autoxidation.

Finally the discussion section presents three axis, the structure reactivity relation, experimental results consistency and finally models validation with improvements perspectives.

### 4.1 N-paraffins studies

#### 4.1.1 Preliminary study with PetroOxy

In the bulk of a homogeneous liquid phase, autoxidation kinetics of pure n-alkane or their blends depends on both oxygen pressure and temperature. The influence of those parameters on autoxidation is investigated hereafter for C<sub>8</sub>-C<sub>16</sub> n-alkanes.

#### Material and methods

**Experimental devices** High purity liquid n-alkanes 99% and 99.8% and dioxygen 99.9% were selected to reduce the catalytic effect of trace species during experiments which may influence initiation reaction. Thus, pure liquid reactants were analyzed with a Gas Chromatograph coupled to a mass spectrometer (GC-MS) fully described in chapter 3. N-Alkanes and iso-alkanes with close numbers of carbon and no oxygenates were identified among the 1% impurities, which may suggest a limited influence on IP measurements. Experiments were performed with a PetroOxy apparatus presented in the previous chapter chapter 3.

From this experiment, we can extract the IP, which corresponds to the time required to reach a 10% pressure decrease  $\left(\frac{P_{IP}}{P_{max}} = 0.9\right)$ , [99, 96] as presented in Figure 4.1a. This criterion commonly corresponds to 5% of fuel consumption [46] and corresponds to the hydroperoxide build up and first deposit precursors formation. A typical experimental result is presented in Figure 4.1a, which shows that the time to reach the requested temperature is included in the IP. This delay is below 4 min in all experiments and is therefore

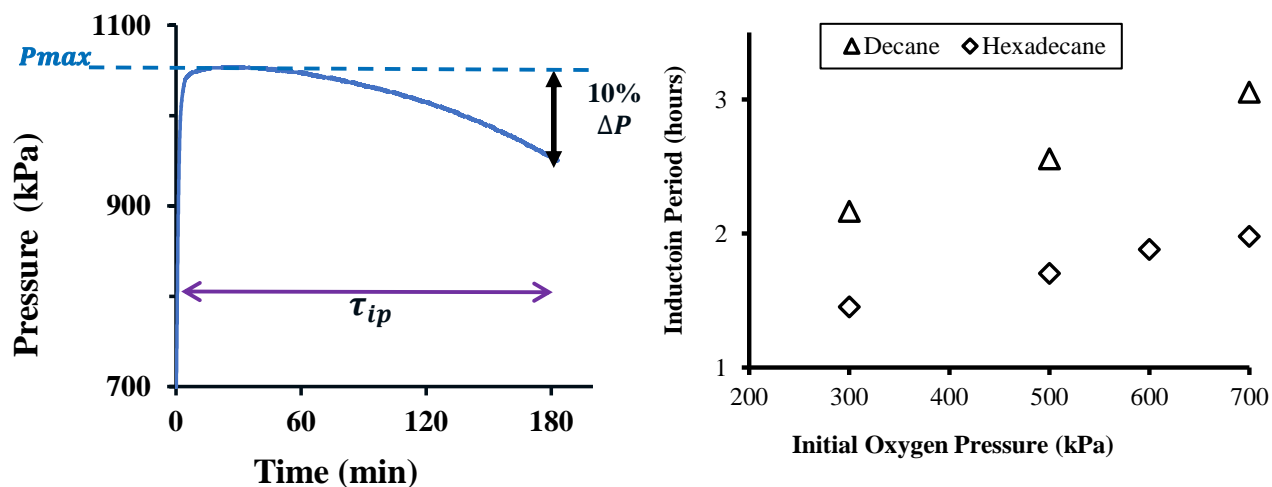


negligible compared to IP.

**Modeling approach** Mechanisms presented in this section are obtained with the Hybrid version of RMG liquid phase presented in chapter 3. Most of solvent parameters were already available in the RMG libraries (n-octane, n-decane, n-dodecane and n-hexadecane) and directly used for mechanism generations. However, Abraham and Mintz parameters for n-tetradecane were interpolated from the corresponding n-dodecane and n-hexadecane parameters. Initial conditions such as concentrations, viscosities, oxygen solubility were computed for each system from data available in literature [120, 121]. For each n-alkane, the mechanisms presented herein were subsequently enlarged by including more intermediates and oxidation products. The final termination criterion selected for the detailed models corresponds to 50% conversion to (1) keep the initial n-alkane as a major constituent throughout the generation condition, (2) let generation proceed until the second stage of oxidation and get relevant reactions paths for deposit precursors. In this manner, solvent effects would rely mainly on the nature of the fuel while oxygenated products contribution may be considered as negligible. The generated mechanisms were coupled to a previously developed zero-dimensional reactor model already used in literature [46]. Note that Hatta number calculated in our conditions was significantly lower than 1 (over a wide range of characteristic chemical time greater than 10 s with  $O_2$  diffusivity around  $10^{-9}$  m<sup>2</sup>/s, mass transfer coefficient in the order of  $10^{-5}$  m/s). This confirms the absence of concentration gradient at the gas-liquid interface.

## Experimental results

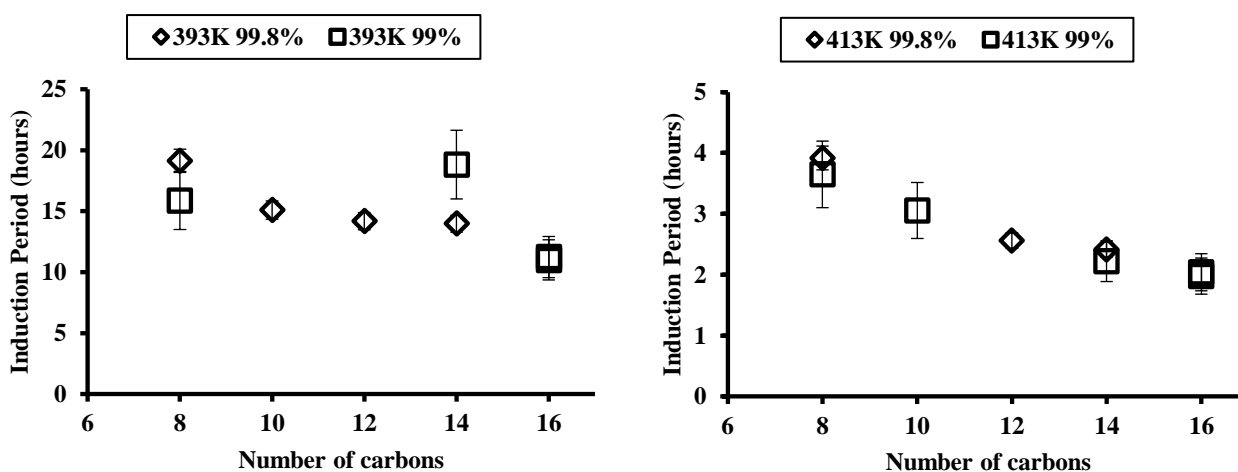
**Impact of oxygen partial pressure** Tests were performed to determine the influence of gas diffusion on autoxidation kinetics in the PetroOxy and evaluate if autoxidation is controlled by kinetics or diffusion during the IP. Results of pressure variation are presented in Figure 4.1b. The IP increases slightly with oxygen availability in the PetroOxy which means oxygen is not limiting the reactivity and oxidation proceeds on the kinetic regime which is in agreement with the Hatta number calculated previously. In addition, IP seems to reach a plateau over 600 kPa of pure oxygen pressure for n-hexadecane. To confirm this reactivity plateau, further experimental results are required. For the next results, initial oxygen pressure is set to 700 kPa in order to limit n-alkanes evaporation.



(a) Typical pressure signal obtained with PetroOxy experiment. Results correspond to n-decane at 413 K and 700 kPa of cold molecular oxygen. (b) Effect of initial oxygen pressure on n-decane and n-hexadecane autoxidation at 413 K.

**Figure 4.1:** Typical experimental results and initial oxygen pressure effect on IP measurements

**Chain length impact on autoxidation** To ensure high quality measurements, a preliminary purity study was performed. The IP of samples having both 99% and 99.8% purity were evaluated as presented in Figure 4.2. Those results demonstrate a systematic error induced by the purity difference. This error can be either positive or negative as impurities may promote or inhibit oxidation. Interestingly, longer reaction times are impacted the most by impurities. In order to get acceptable accuracy on IP measurements, analytical grade (99.8%) n-alkanes were used for autoxidation at 393 K. On runs using 99% grade, an average absolute deviation resulting from the 0.8% purity difference ( $\Delta IP_{99 \rightarrow 99.8}$ ) was calculated. A linear dependency was evidenced on the measured IP ( $\Delta IP_{99 \rightarrow 99.8}$  [hours] =  $0.13 \times IP_{99\%}$  [hours]). This IP variation is applied on 99% grade as measurement uncertainties. All other plots only consider PetroOxy reproducibility ( $\Delta IP$  [hours] =  $0.015 \times IP_{measured}$  [hours]) as measurement uncertainty. Figure 4.3, respectively, presents IPs variation for n-alkanes at 393 K and 413-433 K. For the three temperatures investigated, a non linear dependency of the IP to n-alkane chain length is observed. This trend is more marked at low temperature. Interestingly, Figure 4.3a additionally presents n-hexane IP at 99% purity confirming the non-linear trend obtained with C<sub>8</sub>-C<sub>16</sub> n-alkanes, this trend is even more marked for n-alkanes lighter than C<sub>8</sub>. This sharp reactivity increase between C<sub>6</sub> and C<sub>8</sub> observed at 393 K is in agreement with C<sub>7</sub>-C<sub>8</sub> experimental data from previous work [57] obtained at 413 K.

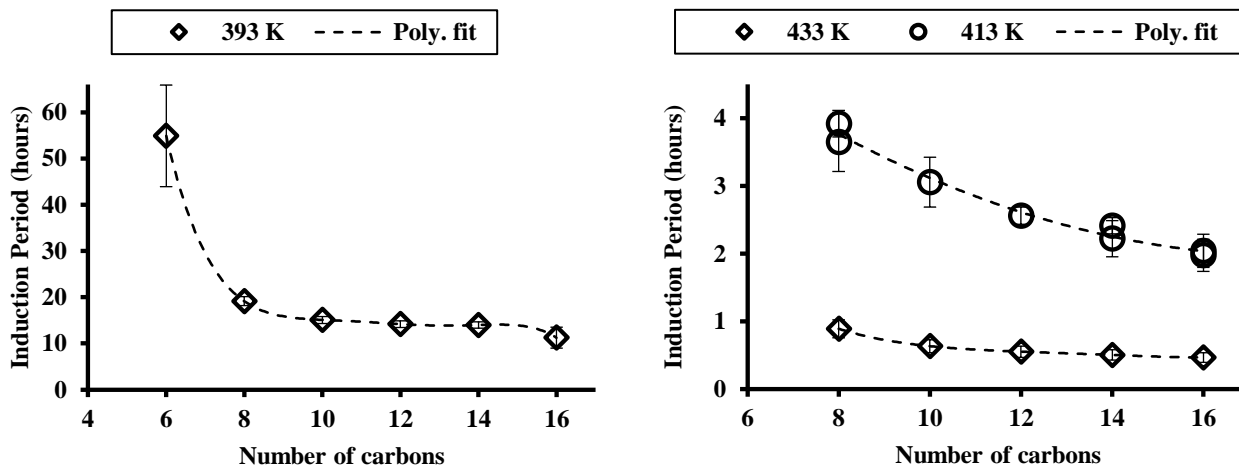


(a) Effect of 0.8% impurity on C<sub>8</sub>-C<sub>16</sub> n-alkanes autoxidation obtained at 393 K with 700 kPa of molecular oxygen at room temperature (RT).

(b) Effect of 0.8% impurity on C<sub>8</sub>-C<sub>16</sub> n-alkanes autoxidation obtained at 413 K with 700 kPa of molecular oxygen at room temperature (RT).

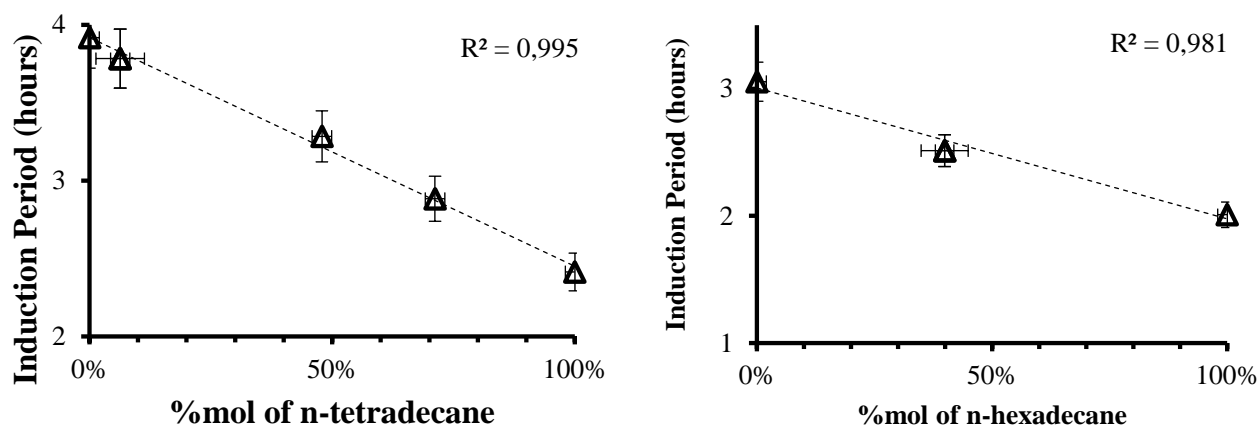
**Figure 4.2:** Measurements uncertainties induced by purity levels

**Blending effect on n-alkanes autoxidation** Experiments were subsequently focused on the impact of n-alkanes blending on autoxidation kinetics. The first mixture investigated is n-octane/ n-tetradecane at 0, 6, 50, 75 and 100% mol of n-tetradecane tested at 413 K. The second mixture is n-decane/n-hexadecane mixture at 0, 40, 100% of n-hexadecane obtained at 413 K. Figure 4.4 summarizes IP results as a function of composition. A relatively good linear fit is obtained in both cases ( $R^2 > 0.98$ ). These results tend to indicate that the IP for n-alkane mixtures varies linearly with the mole, mass or volume fraction. While Figure 4.4 presents only results with mole fractions, similar trends are observed according to both volume and mass fractions. This demonstrate the absence of promoting effects of a more reacting n-alkanes on autoxidation of blends in our tested conditions. This finding should contribute to facilitate the establishment of engineering rules for fuel stability.



(a) Chain length impact on n-alkanes autoxidation at 393 K. Uncertainties were calculated according to reactant purities and PetroOxy reproducibility. (b) Impact of chain length on n-alkanes autoxidation at 413 and 433 K. Uncertainties were calculated according to reactant purities and PetroOxy reproducibility.

**Figure 4.3:** Impact of the chain length on n-alkanes autoxidation within the 393-433 K temperature range.



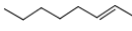
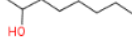
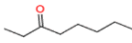
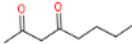
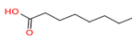
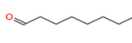
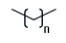
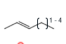
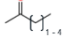
(a) IP for several n-tetradecane/n-octane mixtures. The fit presents the linear effect of the two n-alkanes mix on IP. Uncertainties were calculated according to reactant purities, PetroOxy reproducibility, and composition uncertainties. (b) IP for several n-hexadecane/n-decane mixtures. The fit presents the linear effect of the two n-alkanes mix on IP. Uncertainties were calculated according to reactant purities, PetroOxy reproducibility, and composition uncertainties.

**Figure 4.4:** Impact of the blending on n-paraffins autoxidation using two blends

**Speciation analysis** To identify major oxidation products relevant to n-alkanes, liquid residuals remaining in the PetroOxy apparatus at the end of the experiment are collected for off-line analysis. From the identified oxidation products listed above, comparison of residuals obtained with 393 K runs did not reveal any specific product formation. Over the small temperature range of interest, none of the identified products have a temperature dependent formation. In addition, similar oxidation products are identified across n-alkanes with a major distribution on initial fuel chain products. For lighter oxidation compounds a distribution around half of the initial alkane length is observed qualitatively. Thus, results may be summarized and presented according to chemical family. As presented in Table 4.1, analytical results obtained in this study consolidate literature results and allow refinement and extension of the range of isomer identified under our conditions tested: many C-C bond-breakings occur during low temperature oxidation and lead to several alkanes and alkenes being formed from the initial fuel chain length ( $C_{ini}$ ) to the shortest one ( $C_1$ ) with isomers distinction. However, n-alkanes and n-alkenes below  $C_5$  are gaseous under Standard

Ambient Temperature and Pressure (SATP) conditions, and only the soluble fractions were collected in the liquid sample. All alcohol isomers of  $C_{ini}$  are formed during low temperature oxidation. Lower chain-length alcohols observed in literature are certainly formed but are below detection limits in those conditions. Similarly, all ketone isomers of  $C_{ini}$  are formed and also all 2-ketones (from  $C_3$  to  $C_{ini}$ ). According to our results, the 2-ketones with  $C_{ini-1}$  are disfavored, in line with literature [67].  $C_{ini}$  ketones are qualitatively more produced than lighter ones. All aldehydes from  $C_1$  to  $C_{ini}$  are formed during n-alkanes autoxidation as well. Furanones and branched TetraHydroFurans (THFs), which constitute secondary products are formed in small amounts during the IP time step. Thus, a higher conversion is required for in depth observation of all isomers of these species. As noticed earlier, light n-alkanes and oxygenates are highly underestimated or may not be identified due to the collection at atmospheric pressure. Thus, for those species, standard states are either gas or liquid with high volatility.

**Table 4.1:** Identified products in n-alkanes autoxidation in the present study and literature. Lines starting with asterisks correspond to chemical families for which previous studies may not present the full isomer distinction.

Chemical structure	Structure examples	References
<b>Initial length</b>		
*n-alkenes		This study, [122, 44]
*Alcohols		This study, [122, 67, 73]
*Ketones		This study, [122, 67, 30, 73]
*diones		This study
Acids		This study, [56, 30]
Aldehydes		This study, [122, 67]
<b>Lower products</b>		
n-alkanes		This study, [56, 122]
*n-alkenes		This study
2-Ketones		This study, [67, 56]

## Modeling results

Mechanisms generated for various n-alkanes are presented in Table 4.2. Additional IP data were reconstructed from literature data with the reconstruction techniques presented previously chapter 3. Table 4.3 summarizes literature data and the associated detection techniques used for IP validation. Disparity in detection techniques, apparatus and operating conditions lead to high uncertainty of the experimental data. To minimize this error, a least-squares regression on our experimental data was performed to assess model performance. The fair quality of regression obtained indicates that autoxidation may be represented to some extent as a global process with a constant apparent  $E_a$  over the temperatures and residence times investigated. The  $E_a$  increases roughly linearly with the number of carbons (slope of  $0.63 \text{ kcal.mol}^{-1}.\text{carbon}^{-1}$ ), whereas the Preexponential factor (A) factor in IP decreases with the number of carbons, indicating an enthalpy-entropy[123] compensation effect ( $\ln A [\text{h}] = -1.297 E_a [\text{kcal}] + 3.238$ ). Furthermore discussions on both variations are performed in section 4.3.1. Figure 4.5 presents IP model predictions obtained either in pure oxygen or in air. Model predictions for hydrocarbons-pure  $O_2$  mixtures follow similar trends, underestimating reactivity in general. At low temperature (below 313 K), agreements are not satisfactory with IP prediction lying about 1 order of magnitude above experimental values. How-

ever, at higher temperature ( $> 313$  K), IP predictions remain within a factor of 2 in most cases. On the other hand, IP predictions for experimental data obtained in hydrocarbon-air systems are even more satisfactory and remain within a factor of 2 with respect to experiment, slightly overestimating overall reactivity.

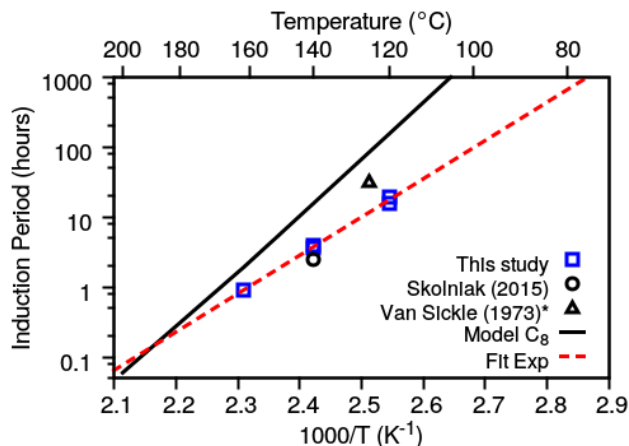
**Table 4.2:** Mechanisms obtained with four n-alkanes

Model	Termination criterion	Tolerance	# of Reactions	# of species
$C_8$	n-octane: 0.5	0.1	8566	254
$C_{10}$	n-decane: 0.5	0.1	13909	324
$C_{12}$	n-dodecane: 0.5	0.1	20276	396
$C_{14}$	n-tetradecane: 0.5	0.1	26669	440

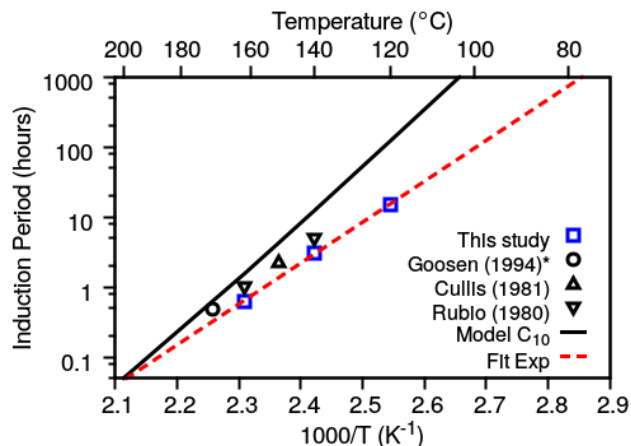
**Table 4.3:** Summary of Literature Data Used for Validation. Operating conditions and reconstruction techniques are given to make comparison easier between experimental data. "5% sum of products" means that IP is obtained when the products concentrations sum reaches 5% of initial fuel concentration. PMC stands for Partially Mixed and Closed. "\*" means the experimental device has a bubbling system.

Reference	Reactor	Mixture	Pressure (kPa)	IP definition
<b><u>Octane</u></b>				
This study	PetroOxy	$C_8 + O_2$	1000	10% $O_2$ consumption
Skolniak (2015)[57]	PetroOxy	$C_8 + O_2$	800	10% $O_2$ consumption
Van Sickle (1973)[29]	PMC reactor	$C_8 + O_2$	$>P_{atm}$	5% Fuel conversion
<b><u>Decane</u></b>				
This study	PetroOxy	$C_{10} + O_2$	1000	10% $O_2$ consumption
Goosen (1994) [124]	Reflux reactor*	$C_{10} + O_2$	100	5% sum of products
Cullis (1981)[67]	Reflux reactor*	$C_{10} + O_2$	100	5% sum of products
Rubio (1980) [32]	Reflux reactor*	$C_{10} + O_2$	100	Max Acid & ROOH
<b><u>Dodecane</u></b>				
This study	PetroOxy	$C_{12} + O_2$	1000	10% $O_2$ consumption
Ben Amara (2013)[46]	Rancimat*	$C_{12} + air$	100	2 <sup>nd</sup> deriv. conductivity
Sicard (2013) [44]	PetroOxy	$C_{12} + O_2$	1000	10% $O_2$ consumption
Rubio (1980) [32]	Reflux reactor*	$C_{12} + O_2$	100	Max. Acid peak
Boss et al. (1975)[71]	Reflux reactor*	$C_{12} + O_2$	100	5% fuel consumption
<b><u>Tetradecane</u></b>				
This study	PetroOxy	$C_{14} + O_2$	1000	10% $O_2$ consumption

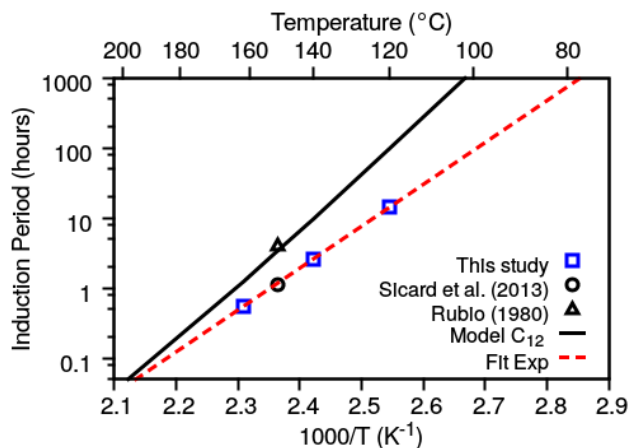
**Speciation analysis** Modeling and experiment speciation comparison was restricted to the major stable autoxidation products, namely alkyl-mono-hydroperoxide (ROOH). In fact, model predictions for ketones and alcohols concentration lie outside the scope of the present study. As presented in Figure 4.6, hydroperoxides formation is quite well reproduced by both models, as modeled concentrations remain within the correct order of magnitude of experimental data. The  $E_a$  of hydroperoxide formation from ROO°s appear to be overestimated by 1 kcal compared to literature data [59]. As IP predictions are sensitive to this reaction, additional experimental data would be required to further adjust this rate constant. As solvation corrections on  $E_a$  is not implemented in RMG, specific ESC should be conducted to confirm the correct value of  $E_a$  and a possible chain length impact on the  $E_a$  as it was observed by Câmara et al. [125].



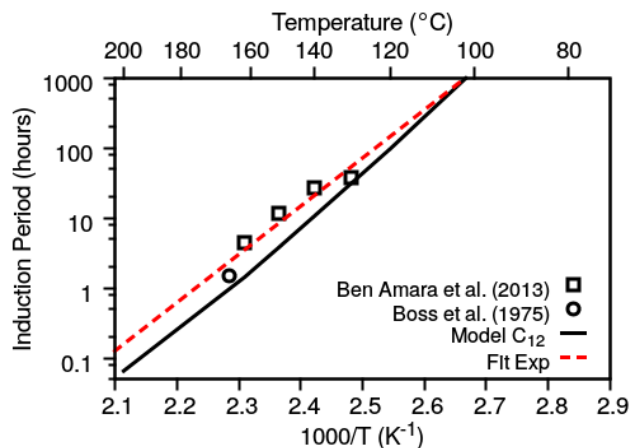
(a) Validation of n-octane model on IP prediction with pure O<sub>2</sub>.



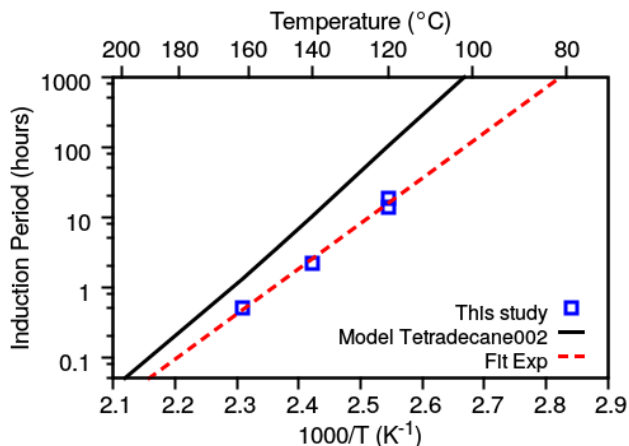
(b) Validation of n-decane model on IP prediction with pure O<sub>2</sub>.



(c) Validation of n-dodecane model on IP prediction with pure O<sub>2</sub>.



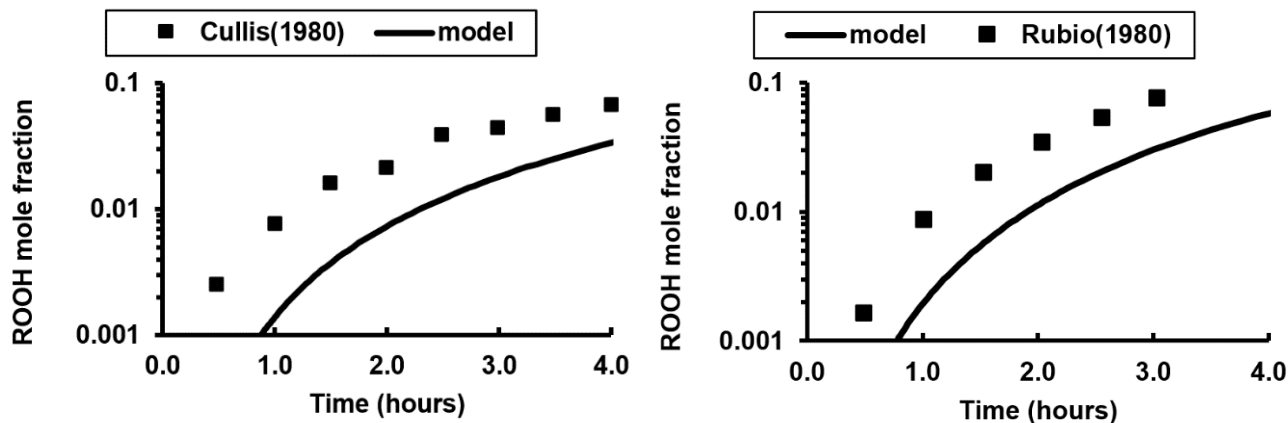
(d) Validation of n-dodecane model on IP prediction with air.



(e) Validation of n-tetradecane model on IP prediction with pure O<sub>2</sub>.

**Figure 4.5:** Model validation with current and literature data. Blue and black symbols respectively stand for present study and literature data results. Red dashed and black solid lines respectively stand for fit of experimental data and model predictions. Data are available as a supplementary material.

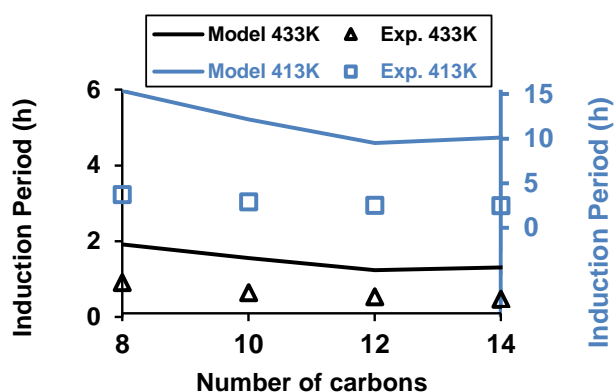
**Chain length impact** Figure 4.7 presents model predictions on IP for the autoxidation of C<sub>8</sub>-C<sub>14</sub> n-alkanes. For clarity's sake, only fits on experimental results are presented. It can be noticed that the model reproduces well the reactivity increase with chain length for the lightest n-alkanes (< C<sub>12</sub>). In the case of n-tetradecane, the reactivity plateau observed for heavier n-alkanes in Figure 4.3 is also well reproduced.



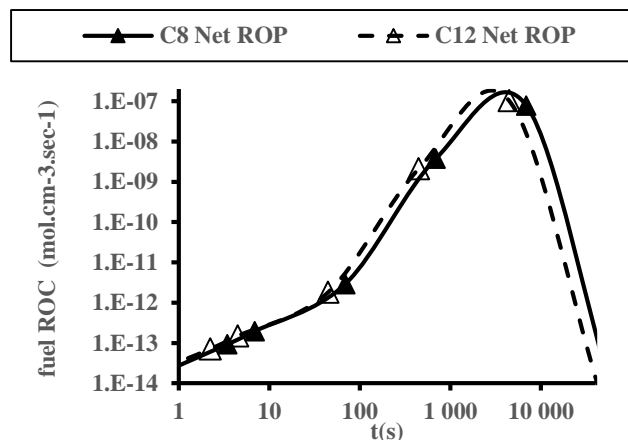
(a) Sum of hydroperoxides species profile validation for decane at 423 K with data from Cullis et al. [67]. (b) Sum of hydroperoxide species profile validation for dodecane at 423 K. data are from Camacho Rubio et al. [32]

**Figure 4.6:** Species profile validation of n-decane and n-dodecane mechanisms with literature data.

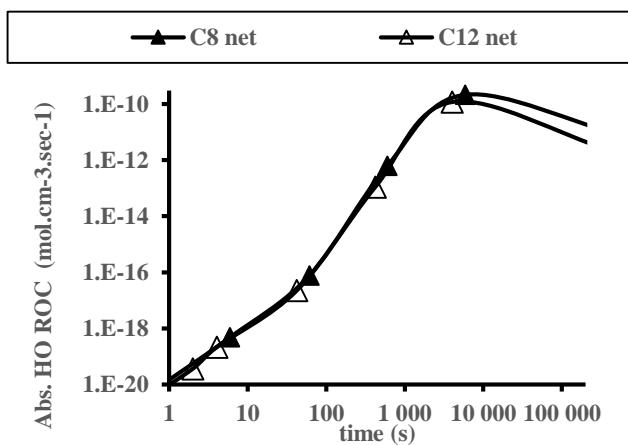
As expressed earlier, models agreement at temperature lower than 413 K (not represented here) is not satisfactory. In all conditions presented here, the prediction of chain length impact lie within a factor of 3, except for n-tetradecane at 413 K. As the generated mechanisms were shown to predict IPs and ROOH concentration quite well, they were subsequently used to perform RoP and RoC analyses on fuel and majors radicals (OH and HO<sub>2</sub>) at 433 K to better understand the chain length impact. Figure 4.8 shows that fuel is consumed at the same rate for both n-C<sub>8</sub> and n-C<sub>12</sub> mechanisms during the first 100 s ( $\frac{t}{IP} < 0.1$ ). At longer reaction times, fuel is consumed faster for C<sub>12</sub>. While no significant distribution change can be detected between the two mechanisms, an earlier contribution of ROO° and  $\gamma$ -peroxy-alkylhydroperoxy radicals (HOOQOO°s) on the C<sub>8</sub> model and a higher contribution of HO<sub>2</sub> on the C<sub>12</sub> model to consume the fuel can be noticed (Figure 4.10). Table 4.4 gives an overview of the main paths involved in n-alkane consumption and summarizes reactions regrouped under each label (namely O<sub>2</sub>, ROO°, HOOQOO°, HO<sub>2</sub>) with corresponding reaction examples for C<sub>8</sub> models. Focusing on HO radicals net RoC, a slight consumption increase by a factor of 2 is observed for the C<sub>8</sub> model at t = IP (Figure 4.9a). Concerning HO<sub>2</sub> radicals, a reactivity difference is observed at t = 100 s (Figure 4.9b). This higher consumption rate of HO<sub>2</sub> on the C<sub>8</sub> model might account for the different reactivities of the n-alkanes models. Focusing on fuel RoC distribution, presented in Figure 4.10, three main oxidation stages are identified: the initiation stage ( $\frac{t}{IP} < 10^{-5}$ ), where only O<sub>2</sub> contributes to RoC, the early oxidation stage, where ROO°s contribute mostly to fuel consumption (t < IP), and then late oxidation, where fuel is consumed by HOOQOO° (t > IP). Although the ROO° and HOOQOO° pathways remain the quasi exclusive consumption pathways for both mechanisms, the HOOQOO° path contribution increases over time, accounting for nearly 30% of fuel consumption at the IP, which is in agreement with previous experimental studies identifying first monohydroperoxides and then polyhydroperoxides[31]. The same trends were noticed for all n-alkanes models.



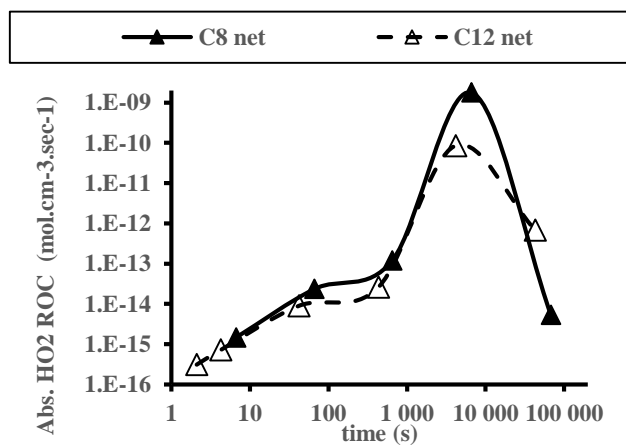
**Figure 4.7:** Comparison of predicted and experimental IPs for the n-alkanes range. Symbols represent values from the above-mentioned fit of our experimental data. Solid lines correspond to model predictions.



**Figure 4.8:** Fuel RoC analysis performed on  $C_8$  and  $C_{12}$  mechanisms. IPs are respectively reached at  $t = 6890$  s and  $t = 4460$  s for  $C_8$  and  $C_{12}$  models.



(a) RoC between  $C_8$  and  $C_{12}$  mechanisms of HO radicals over the reacting time. IPs are respectively reached at  $t = 6890$  s and  $t = 4460$  s for  $C_8$  and  $C_{12}$  models.



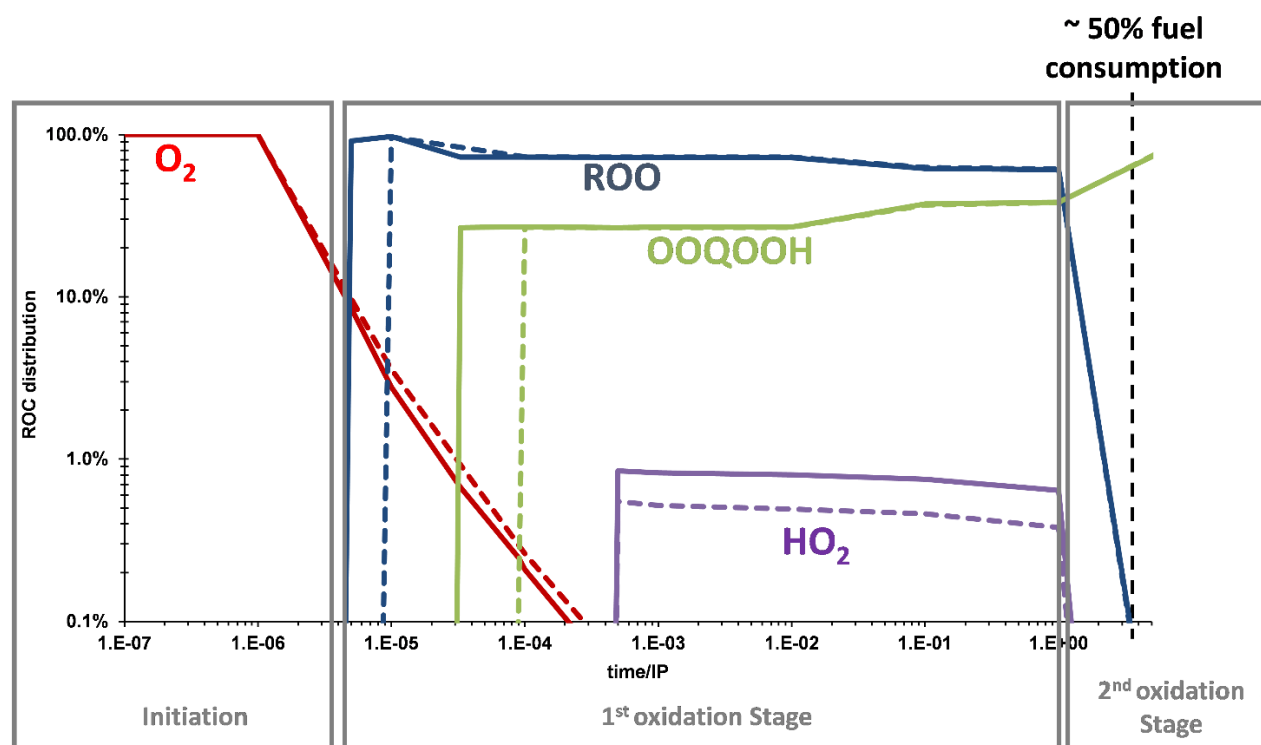
(b)  $HO_2$  radicals RoC between  $C_8$  and  $C_{12}$  mechanisms. IPs are respectively obtained at  $t = 6890$  s and  $t = 4460$  s for  $C_8$  and  $C_{12}$  models.

**Figure 4.9:** RoC analysis of both HO and  $HO_2$  radicals between  $C_8$  and  $C_{12}$  mechanisms



**Table 4.4:** Summary of reactions involved in the RoC analysis of fuel with reaction examples for the octane model with typical kinetic parameters

Reaction label and examples of corresponding examples in C <sub>8</sub> model	A [cm <sup>-3</sup> .mol <sup>-1</sup> .s <sup>-1</sup> ]	n	E <sub>a</sub> [kcal.mol <sup>-1</sup> ]
<b>O<sub>2</sub>:</b> R <sup>o</sup> + HO <sub>2</sub> <sup>o</sup> ⇌ RH + O <sub>2</sub>			
Rxn 1:	1.75 . 10 <sup>10</sup>	0	-3.28
Rxn 2:	1.75 . 10 <sup>10</sup>	0	-3.28
<b>HO<sub>2</sub>:</b> R <sup>o</sup> + H <sub>2</sub> O <sub>2</sub> ⇌ RH + HO <sub>2</sub> <sup>o</sup>			
Rxn 283:	2.030 . 10 <sup>0</sup>	3.29	1.07
Rxn 284:	1.141 . 10 <sup>0</sup>	3.28	0.88
<b>ROO:</b> R <sup>o</sup> + RO <sub>2</sub> H ⇌ RH + RO <sub>2</sub> <sup>o</sup>			
Rxn 5:	1.015 . 10 <sup>0</sup>	3.29	1.07
Rxn 6:	9.205 . 10 <sup>0</sup>	3.34	1.14
<b>OOQOOH:</b> R <sup>o</sup> + HO <sub>2</sub> QO <sub>2</sub> H ⇌ RH + HO <sub>2</sub> QO <sub>2</sub> <sup>o</sup>			
Rxn 183:	1.015 . 10 <sup>0</sup>	3.29	1.14
Rxn 184:	9.205 . 10 <sup>0</sup>	3.34	1.14



**Figure 4.10:** Reaction families involved in the fuel rate of consumption between C<sub>8</sub> and C<sub>12</sub> mechanisms. Solid and dashed lines, respectively, represent C<sub>8</sub> and C<sub>12</sub> models.

## 4.1.2 Detailed results with autoclave

In order to get more information of n-octane oxidation, experiments are now conducted in the autoclave to obtain products formation in both liquid and gas phase over time. In order to obtain results as PetroOxy ones, experiments are conducted with both similar amount of oxygen and sample to reactor volume ratio ( $\frac{V_{sample}}{V_{reactor}} = 0.2$ )

### Material and methods

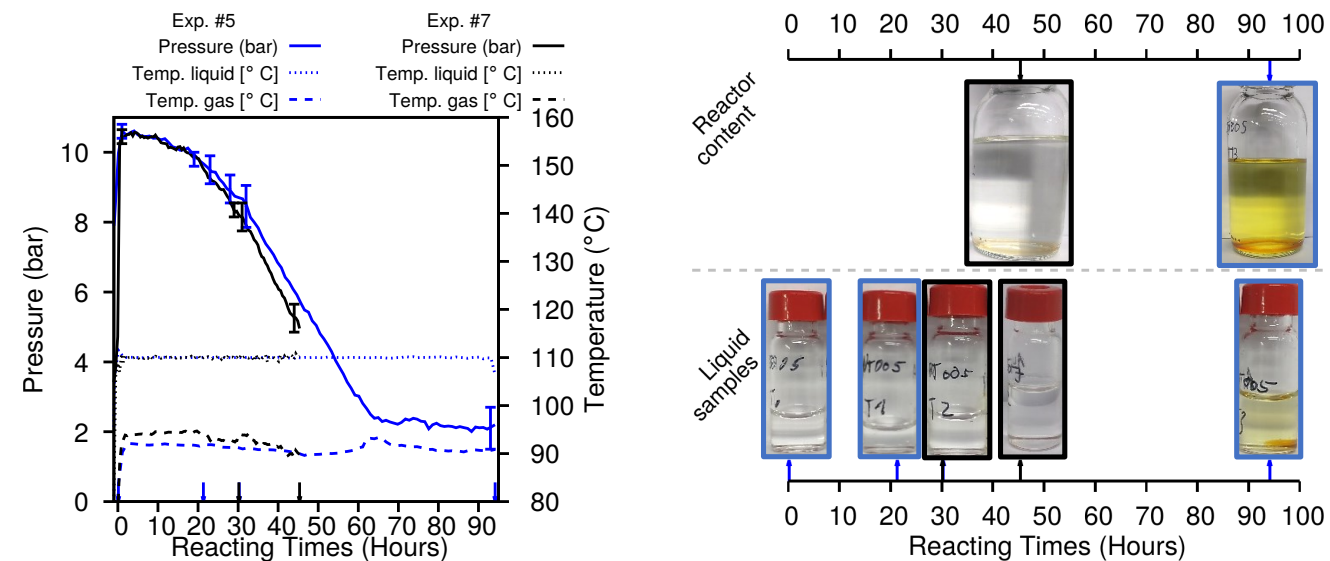
As autoclave experiments and its associated analytical devices were already presented (chapter 3), no further description is performed here.

Experiments are conducted twice at 383 K and 1000 kPa of total pressure with 50mL of reactant. This repeatability point aims to cover most of the oxidation regime and to validate oxidation rates. As the sampling technique presented in (chapter 3) modifies gas phase composition, one of the two experiment is limited to one intermediate sample. Thus, the repeatability point aims to confirm the absence of sampling effect on the oxidation rate. Each intermediate sample is about 1mL and final content of the autoclave is also collected for visual inspections.

### Experimental results

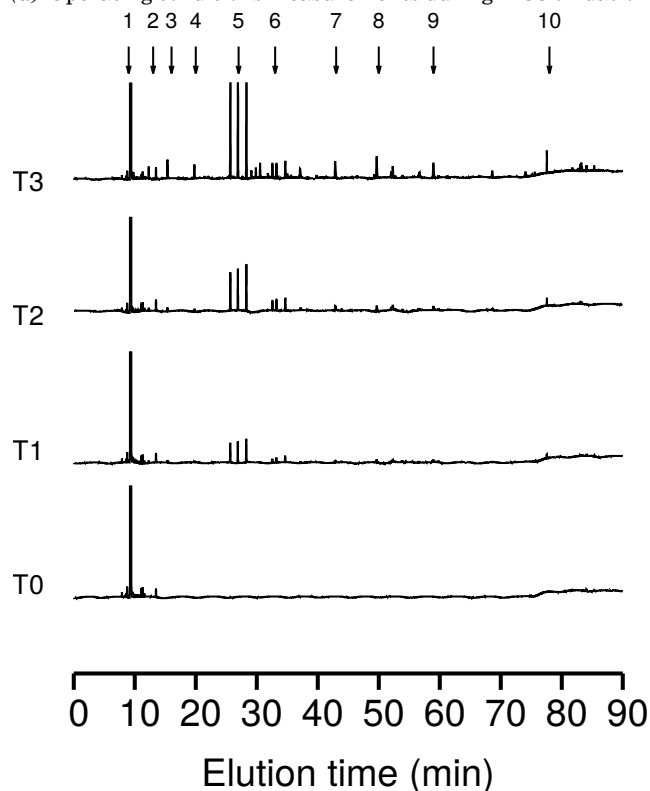
**Macroscopic reactivity** Results summarizing n-C8 oxidation over time are presented in [Figure 4.11](#). [Figure 4.11a](#) presents pressure and temperature evolution over the reaction time of the two experiments. Surprisingly, a high temperature gradient is observed between gas and liquid phase, around 15-20°C and reproduced on both experiments. Pressure uncertainties are calculated according to this equation  $\Delta(P)_t = P_{Uncert.} \times (1 + n_{spl.,t}) + (P_{spl.,t+c} - P_{spl.,t-c})$  to consider both measurements errors and potential pressure addition after the sampling. Considering this uncertainty, the fair reproducibility of pressure and temperature profiles demonstrates the absence of any sampling effect on the autoxidation. Sampling times are represented in [Figure 4.11a](#) with arrows and their corresponding pictures is presented in [Figure 4.11b](#) over reaction time. As observed on those pictures, the starting fuel which was colourless turns into a coloured two phases system at the end of the experiment. From the second reactor content picture, the formation of such two phases system seems to occur below 45 hours. The absence of such two phases system in the corresponding vial tends to prove slight inhomogeneities in the sampling process. The composition of the two phases is discussed later (section 4.3.2). Finally, [Figure 4.11c](#) and [Figure 4.11d](#) respectively illustrate the formation of liquid and gas phase products over time. Liquid and gas phase results are respectively from a GC-FID and from both a GC-FID and a GC-TCD. For clarity sake, only n-C8 and O<sub>2</sub> signals are cut off to observe oxidation products formation.

**Products identification** [Figure 4.12](#) summarizes the identification of both ketones and acids chemical families with the GC-MS. In both figures, the full scan spectrum was filtered with majors ions of the presented chemical families. As concluded with petroxy residual analyses, C<sub>7</sub> acids and ketones formation are disfavoured compared to all others possible lengths. In order to confirm major products formation, the most oxidized samples were analysed with FTIR and the resulting spectrum is presented in [Figure 4.13](#). Absorption bands 1 and 3 are relevant to C-H bond stretch respectively from CH<sub>3</sub> and CH<sub>2</sub> groups. In addition the absorption band 2 is relevant to C=O bond stretch n-C8 spectrum from species containing ketones. Those results validated GCs conclusions with majors species identification as n-C8 and octanone isomers.

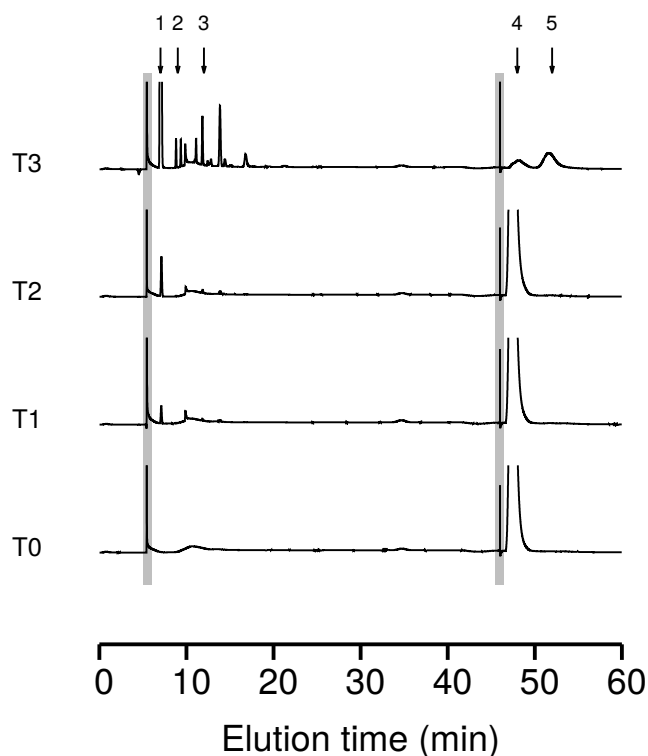


(a) Operating conditions measurements during n-C8 oxidation

(b) Samples and autoclave content pictures



(c) GC-FID signals for liquid samples obtained at different oxidation times from Exp #5. Identified peaks are 1: n-octane, 2: 2-propanone/acetone & 2-butanone, 3: pentanone, 4: 2-hexanone, 5: 2-octanone & 3-octanone & 4-octanone, 6: 4-octanol & 3-octanol & 2-octanol & 1-octanol, 7: butanoic acid, 8: pentanoic acid, 9: hexanoic acid, 10: octanoic acid.

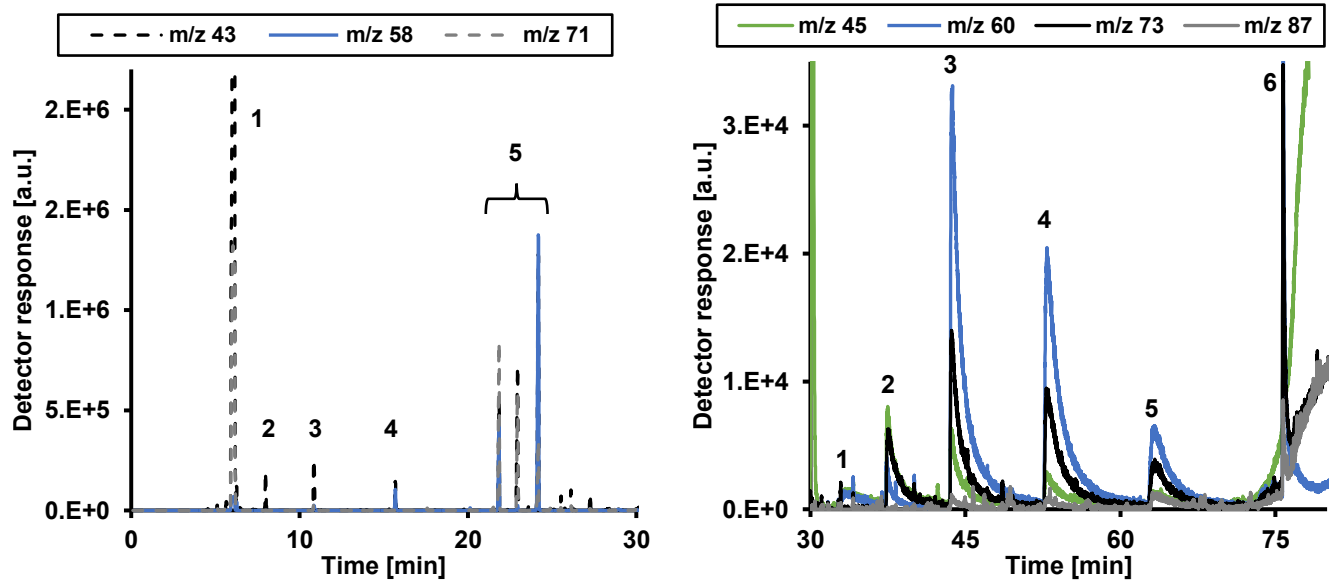


(d) GC-TCD signals for liquid samples obtained at different oxidation times from Exp #5. Identified peaks are 1: CO<sub>2</sub>, 2: ethane & others, 3: propane & others & iso-butane, 4: O<sub>2</sub>, 5: others & methane. Grey areas correspond to valve switch timing.

**Figure 4.11:** Macroscopic results for n-C8 oxidation at 383 K and 1000 kPa in autoclave

**Experimentals species profiles** Liquid phase species are quantified using either external calibration or the ECN model to reconstruct DR coefficient according to the chemical structure identified from the GC-MS. External calibration are only used for the n-C8 and ECN model reference compound.

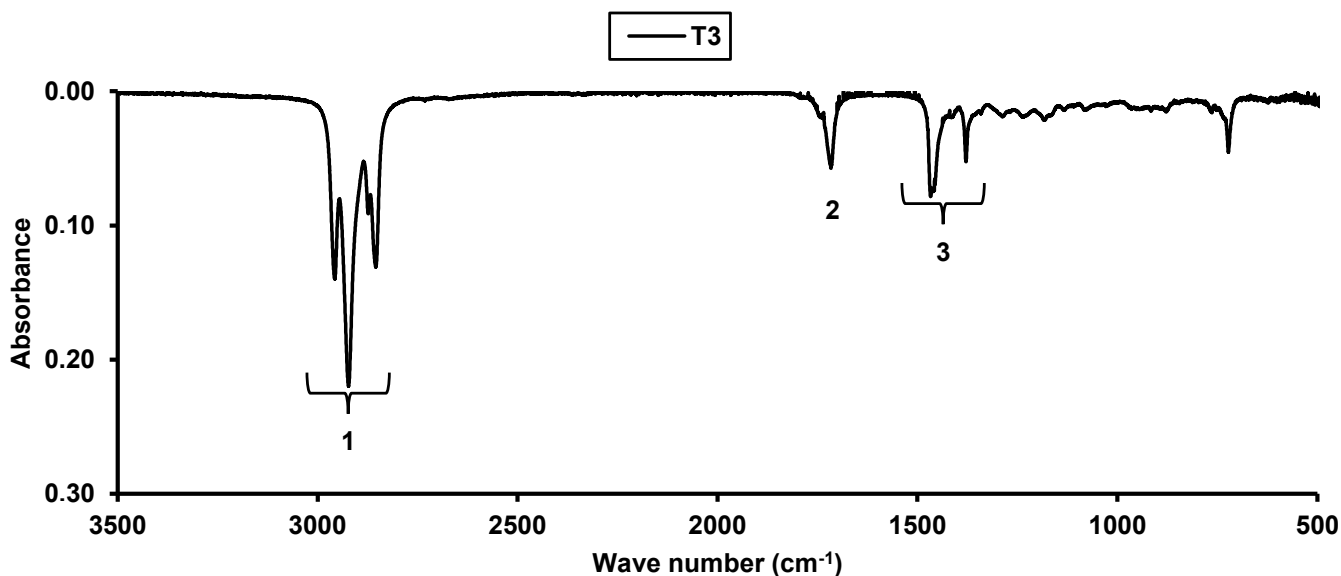
Species profiles for the major products of both liquid and gas phase are presented in [Figure 4.14](#). Based on pressures profile evolution from [Figure 4.11a](#), dashed line curves aim to suggest the species profile



(a) Full scan spectrum filtered with the three major ions of both all 2-ketones species and all n-C8-ketones. Products identified are: 1: 2-propanone/acetone, 2: 2-butanone, 3: 2-pentanone, 4: 2-hexanone, 5: the same order 2-octanone, 3-octanone and 4-octanone

(b) Full scan spectrum filtered with the 4 major ions of aliphatic acids. Products identified are: 1:ethanoic acid/acetic acid, 2: propanoic acid, 3: butanoic acid, 4: pentanoic acid, 5: hexanoic acid, 8: octanoic acid.

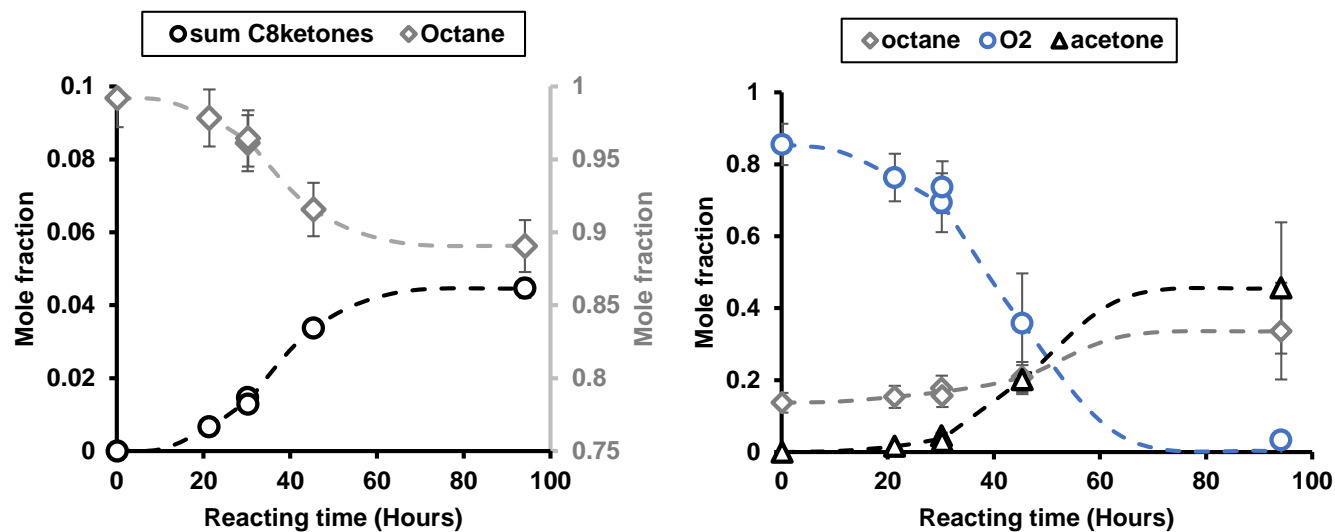
**Figure 4.12:** TIC MS spectrum for oxidized n-C8 sample filtered with specific m/z ions.



**Figure 4.13:** FTIR-ATR analysis of n-C8 sample after 94 h oxidation. Absorption bands 1 and 3 are relevant to C-H bond stretch respectively from CH<sub>3</sub> and CH<sub>2</sub> groups. The absorption band 2 is relevant to C=O bond stretch from n-C8 ketones isomers formed during autoxidation

evolution. From those products formation, three different oxidation regimes may be identified. During the initiation regime ( $\lesssim 20h$ ), the total pressure decreases slowly due to small oxidation rate with both a small consumption of oxygen and fuel. A propagation regime ( $20 \lesssim t \lesssim 60h$ ) with a higher oxidation rate where oxygen is consumed quickly by the fuel and induces a pressure drop. A last regime which could be assimilated to a termination regime, where oxidation rate slow down progressively due to oxygen depletion in the liquid. At the end of the experiment, the liquid phase is still mainly composed of n-C8 (90 %) and the three major products are: [2-4]-octanones ( $\approx 5\%$ ) and all C<sub>2</sub>-C<sub>8</sub> acids ( $\approx 2\%$ ). While in the gas phase, oxygen is fully consumed, n-C8 and 2-propanone are majors components (their sum is close to 70 %). The

fuel fraction increase in the gas phase is discussed later in this chapter (Section 4.3.2)



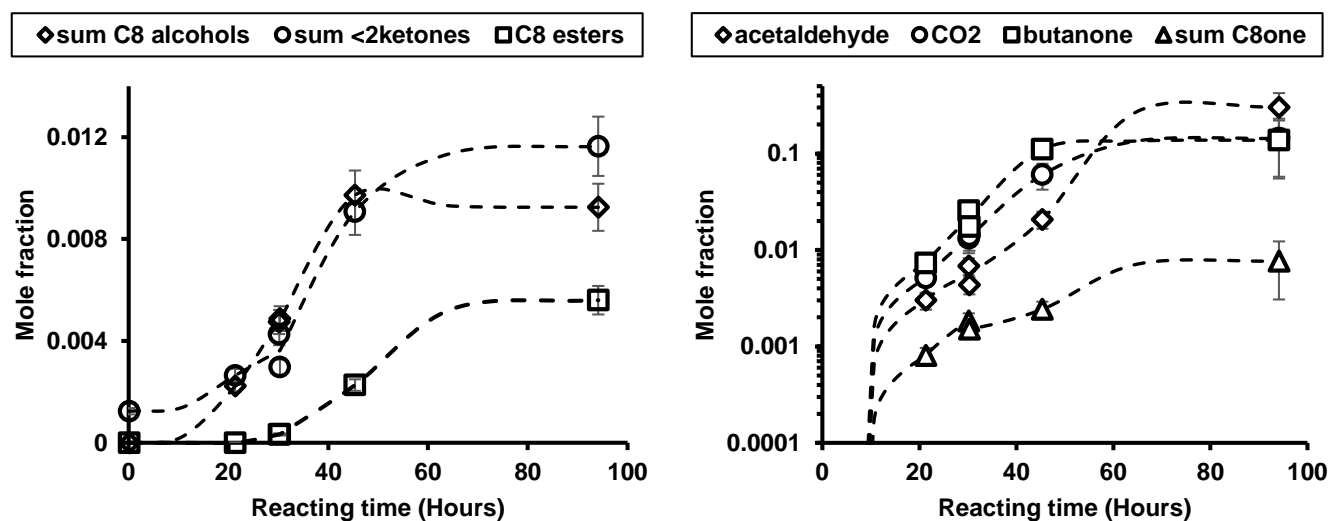
(a) Species profiles of the major products identified in the liquid phase during autoxidation of n-C8 at 383 K. Dashed lines represent the hypothetical species profile trend based on the pressure profile drop.

(b) Species profiles of the major products identified in the gas phase during autoxidation of n-C8 at 383 K. Dashed lines represent the hypothetical species profile trend based on the pressure profile drop.

**Figure 4.14:** Species profiles of major species identified during n-C8 oxidation at 383 K.

Then, the species profiles of minor products are presented in Figure 4.15 for both liquid and gas phases. At the end of the experiments, minors products in the liquid phase are mostly all the [1-4]-octanols ( $\approx 1\%$ ), all the low 2-ketones ( $\approx 1\%$ ) from C<sub>3</sub> to C<sub>6</sub> and several octyl-esters. Based on the products identification and the reaction mechanism presented in Figure 4.16, esters formations seems due to combinatorial reactions between every acids and octanols isomers. Most of the octyl ethanoate, octyl-butanoate and octyl pentanoate esters isomers are distinguished with the GC-MS which corroborate the existence of such mechanism.

Except for CO<sub>2</sub> and acetaldehyde which are gaseous, gas phase composition is mostly due the volatility difference between all liquid phase products (acetone, butanone and octanones).



(a) Species profiles of the minor products identified in the liquid phase during autoxidation of n-C8 at 383 K

(b) Species profiles of the minor products identified in the gas phase during autoxidation of n-C8 at 383 K

**Figure 4.15:** Species profiles of minor species identified during n-C8 oxidation at 383 K.



**Figure 4.16:** Example of an esterification reaction [16]

## 4.2 Iso-paraffins studies

The present section aims at presenting an in-depth understanding of the branching level impact on paraffins autoxidation. To better understand those phenomena, C<sub>8</sub> iso-paraffins reactivity are compared with its corresponding normal paraffins reference, n-octane. The branching effect on reactivity is treated both from experimental and modeling point of view.

### 4.2.1 Preliminary study with PetroOxy

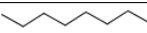

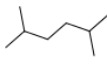
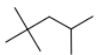
This preliminary study provides new experimental data describing the autoxidation of n-C<sub>8</sub>, MH, 2,5-dimethylheptane (DMH) and TMP over a wide range of temperature, 373-433 K, in a PetroOxy device initially at 700 kPa and 293 K. In addition, four liquid phase kinetic mechanisms relevant to the autoxidation of each compound are proposed and discussed.

#### Material and methods

**Experimental devices** High purity liquid n-alkanes (>99%) and dioxygen (> 99.9%) were selected to reduce the catalytic effect of trace species during experiments which may influence initiation reaction [26]. Thus, pure liquid reactants were analyzed with a Gas Chromatograph coupled to a mass spectrometer (GC/MS) fully described in section 3. N-Alkanes and iso-alkanes with close numbers of carbon and no oxygenates were identified among the 1% impurities, which may suggest a limited influence on IP measurements. Full description of both experimental apparatus and analytical devices is available on previous chapter (Section 3) and no further description is performed in this section. .

Table 4.5 presents the molecules tested within the present study and the experimental conditions investigated with the PetroOxy device. From previous study results (subsection 4.1.1), the initial oxygen pressure is set to 700 kPa for all molecules to limit their evaporation.

**Table 4.5:** Summary of experimental conditions tested in the present work.

Compound	Purity	Formula / # of ramification	Temperature range (K)	Initial O <sub>2</sub> pressure (kPa)
n-octane 	≥ 99 %	C <sub>8</sub> H <sub>18</sub> / 0	373-433	700
MH 	≥ 99 %	C <sub>8</sub> H <sub>18</sub> / 1	373-413	700
DMH 	≥ 99 %	C <sub>8</sub> H <sub>18</sub> / 2	373-413	700
TMP 	≥ 99 %	C <sub>8</sub> H <sub>18</sub> / 3	393-433	700

**Modeling approach** Mechanisms presented in this section are obtained with the hybrid version of RMG liquid phase presented in chapter 3. Most of solvent parameters were already available in the RMG li-

braries (n-octane, iso-octane). As MH, DMH and TMP are all iso-octane, isooctane solvation parameter was applied on them. Initial conditions such as concentrations, viscosities, oxygen solubility were computed for each system from data available in literature [120, 121]. Table 4.6 summarizes the four mechanisms obtained with RMG-Hybrid in best agreement with IPs. Mechanisms generation was established based on the oxidation pathways comprehension from Section 4.1. Thus, all mechanisms are constructed to involve specific products formation: ROOH, C<sub>8</sub>-ketones, C<sub>8</sub>-alcohols, alkyl-di-hydroperoxide (HOOQOOH), KHP, cyclic Korcek intermediates, lighter acids and carbonyls either from Korcek’s reactions or  $\alpha/\beta$ -scissions, lighter Hydrocarbon (HC) from either direct C-C bond breaking or  $\alpha/\beta$ -scissions. In agreement with experimental observations from section 4.1, the formation of both lighter alcohols and peracids is removed to limit mechanisms size increase. The n-C8-v2 mechanism presented in Table 4.6 is an upgraded version of the n-C8 mechanisms from section 4.1. Thus, the remove of all negligible pathways explain why it is smaller than its original version from section 4.1. For a sake of clarity, in the next figures the mechanism n-C8-v2 is called n-C8. The high tolerance value used for both MH and DMH generations, means those mechanism are closely linked to the user specified reaction paths. While in the case of TMP, this criteria was not self consistent and a lower tolerance value was required to add more termination paths (RO<sub>4</sub>R, RO<sub>3</sub>R) and more stable species formation with mostly  $\beta$ -alkene formation.

The generated mechanisms were coupled to a previously developed zero-dimensional reactor model already used in literature [46].

**Table 4.6:** Mechanisms obtained with the four C<sub>8</sub>-alkanes.

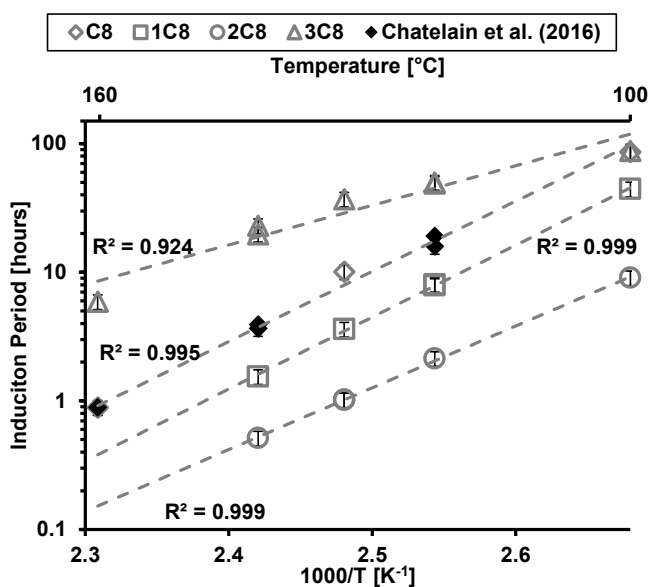
Model	Termination criterion	Solvent selected	Tolerance	# of Reactions	# of species
n-C8-v2:	n-octane: 0.5	octane	0.1	201	7324
MH:	2-methylheptane: 0.5	iso-octane	0.9	191	7004
DMH:	2,5-dimethylhexane: 0.5	iso-octane	0.9	91	1436
TMP:	2,2,4-trimethylpentane: 0.5	iso-octane	0.1	193	5556

## Experimental results

To identify the effect of the branching on alkanes reactivity, wide temperature range (373-433 K) experiments were conducted on the four C<sub>8</sub> alkanes at 700 kPa of initial oxygen. To obtain meaningful data, acquisition of IP below 0.5 hours is not considered due to the  $\frac{\text{heatingtime}}{IP}$  ratio. As purity impact was not studied within this work, previous results (Section 4.1.1) obtained in similar conditions (99% compound purity, similar temperature range, oxygen pressure) with n-alkanes are considered ( $\Delta IP_{99-99.8}(\text{hrs}) = 0.13 \times IP_{99\%}(\text{hrs})$ ).

**Temperature impact** Figure 4.17 presents the evolution of IP with temperature reciprocal for all molecules tested. Whereas additional data would be required for temperature below 393 K, IP seems to decrease exponentially with the temperature reciprocal for n-C8, MH, DMH and TMP. The fair quality of the regression for n-C8, MH, DMH indicates that their autoxidation may be assimilated to a global process with an apparent A’ and Ea’ presented in Figure 4.17b. While a fair regression is presented for TMP, two distinct oxidation regime are observable for temperature above and lower 403 K. In addition, the comparison of apparent Ea’ emphasizes a specific oxidation behaviour of the TMP which has a much smaller

activation energy compared to n-C8, MH and DMH. Further discussions on both variations are performed in section 4.3.1.



(a) IP measurements obtained with the four molecules obtained between 373-433 K at 700 kPa of initial oxygen. Uncertainties are calculated including peroxy repeatability and compound purity. C8, 1C8, 2C8 and 3C8 respectively stands for n-C8, MH, DMH and TMP

Compound	$A'$	$Ea'$
C8	$2.3 \times 10^{-13}$	12.6
1C8	$4.72 \times 10^{-14}$	12.9
2C8	$1.24 \times 10^{-12}$	11.1
3C8	$6.65 \times 10^{-7}$	7.09

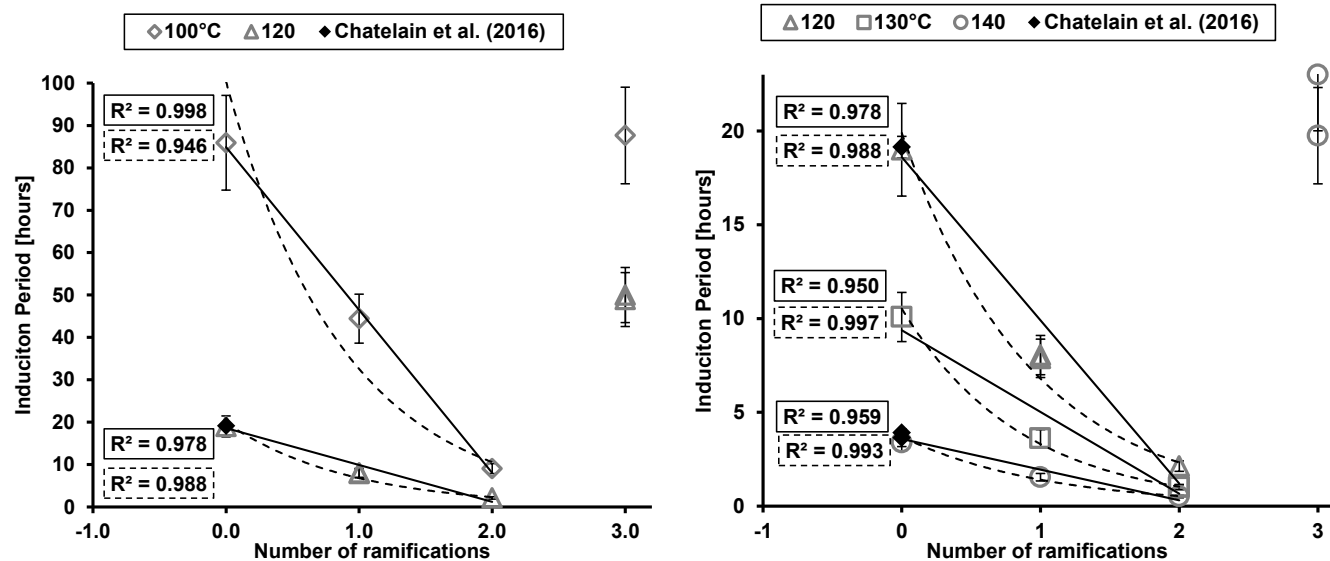
(b) Parameters of the fits plotted on the graph following the expression  $IP = A \times \exp(Ea \times \frac{1000}{T})$

**Figure 4.17:**  $IP=f(1/T)$  for the four molecules investigated.

**Branching impact** Figure 4.18 presents the evolution of IP over ramifications number for several temperatures. From those results, the IP decreases with the increase of ramifications number between the range 0-2 (n-C8, MH and DMH) then increases with the third ramification (TMP). To better characterise this decreasing trend within the 0-2 range, both linear and exponential regressions are presented in solid and dashed lines. In addition to their coefficients identified for each temperatures, an hypothetical general form is proposed in Table 4.7. The accuracy of each regression type is assessed in Figure 4.19 by comparing their error to experimental results uncertainties. Thus, except for the 100°C case, the exponential regression gives better agreement with an error below the experimental uncertainties in most conditions. As pointed out in Figure 4.17 with the temperature effect, a specific behaviour of the TMP is also observed on the branching number. While the BDE of C-H bonds explains the reactivity increase within the 0-2 range, the TMP which also has a tertiary carbon has a slower reactivity than all others molecules tested. Or, as presented in Table 4.5, the TMP is the only compound with a quaternary carbon on which there is no more H to abstract. This demonstrates that more descriptors than just the ramifications number are required to classify all paraffins oxidability. Further discussions are performed in section 4.3.1 with new criteria: number of tertiary and quaternary carbons.

**Species identification** To identify major oxidation products, liquid residuals remaining at the end of the experiment are collected for off-line analysis. Table 4.8 presents products identified by chemical family for all C<sub>8</sub> alkanes studied in the present work. Except for the TMP, all similar oxidation products were identified over the temperature range 373-433K. TMP analyses did not reveal a significant amount of oxygenated species for the low temperature range ( $\leq 393$  K), while both C<sub>8</sub> ketones and alcohols were





(a)  $C_8$  alkanes IP changes as function of temperature and branching level obtained at 373-393 K and 700 kPa of initial oxygen. Uncertainties are calculated including petroxy repeatability and compound purity. Linear and exponential regression are respectively in solid and dashed lines.

(b)  $C_8$  alkanes IP changes as function of temperature and branching level obtained at 403-443 K and 700 kPa of initial oxygen. Uncertainties are calculated including petroxy repeatability and compound purity. Linear and exponential regression are respectively in solid and dashed lines.

**Figure 4.18:** IP evolution with the number of ramification on  $C_8$  alkanes at several temperature

**Table 4.7:** Coefficients of both linear and exponential regressions

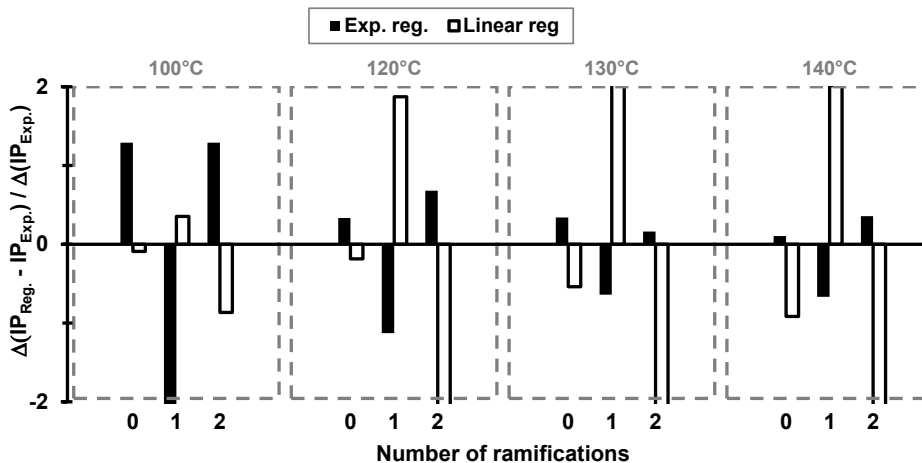
Temperature °C	Linear regression		Exponential regression	
	$IP_{T,Nb} = \alpha_T \times Nb_{ramification} + \beta_T$		$IP_{T,Nb} = \beta_T \exp(\alpha_T \times Nb_{ramification})$	
	$\alpha$	$\beta$	$\alpha$	$\beta$
100	-38.4	84.9	-1.12	100.3
120	-8.7	18.6	-1.07	19.9
130	-4.4	9.4	-1.16	10.5
140	-1.6	3.6	-0.96	3.7
Possible expression	$\approx -\frac{IP_{n-para,T}}{2}$	$IP_{n-para,T}$	$-1.06 \pm 0.1$	$\approx IP_{n-para,T}$

observed at higher temperature ( $\geq 403$  K). This demonstrates two oxidation regimes of TMP respectively below 393 K and above 393 K. The more branching ratio the reactant has, the less the number of oxidation products are numerous. This conclusion can be argued (i) there are less and less isomers distinction with an increasing number of branching, (ii) the small number of products formed are highly concentrated compared to the minors, (iii) the MS spectrum is more complicated to analyse with an increasing ramifications number<sup>1</sup> and (iv) the formation of more volatile compounds with ramification increases (like  $CO_2$ ,  $H_2$ , and light hydrocarbons below  $C_4$ ).

## Modeling results

**Temperature effect validation** Data from the literature and the present study were used for the validation of the model. Table 4.9 with associated methods to reconstruct IPs. Figure 4.20 presents the agreement of models prediction (black solid lines) with IP criterion for all molecules tested. To assess models perfor-

<sup>1</sup>due to both uncertain fragmentation schemes and small signal to noise ratio for minor oxidation products



**Figure 4.19:** Assessment of regressions performance with the ratio of the regression error ( $\Delta(IP_{Reg.} - IP_{Exp.})$ ) over experimental errors ( $\Delta(IP_{Exp.})$ ). When  $|Ratio| < 1$ , the error from the regression ( $\Delta(IP_{Reg.} - IP_{Exp.})$ ) is lower than experimental uncertainties.

**Table 4.8:** Similarities and differences of oxidation products formed between the tested isomers of C<sub>8</sub>. ✓, - and ~ signs respectively mean compounds identified, not identified and traces suspected.

Chemical structure	n-C8 results	MH results	DMH results	TMP results
<b>Initial length</b>				
*n-alkenes	✓, [122, 44]	-	-	-
*Alcohols	✓, [122, 67, 73]	✓	✓	✓
*Ketones	✓, [122, 67, 30, 73]	✓	✓	✓
*diones	✓	-	-	-
Acids	✓, [56, 30]	-	-	-
Aldehydes	✓, [122, 67]	~	~	~
<b>Lower products</b>				
n-alkanes	✓, [56, 122]	✓	-	-
*n-alkenes	✓	-	-	-
2-Ketones	✓, [67, 56]	-	-	-

mance, least-squares regressions (dashed blue lines) are performed on present study data (blue symbols). As presented in Figure 4.20a and Figure 4.20d, the new experimental data are in agreement with literature data [126, 57] and emphasizes the good reproducibility of PetroOxy experiments. To assess models prediction sensibility on the liquid oxygen concentration, an O<sub>2</sub> fraction was varied between 50-20000 ppm<sup>2</sup>. Thus, models presented in Figure 4.20a correspond to the average value and the error bars corresponds to the IPs variations induced by the concentration changes. Surprisingly, two distinct effects of O<sub>2</sub> fractions are observed, on both n-C8 and TMP the relative error is increasing with temperature while it is almost constant in both MH and DMH.

Focusing on model predictions, MH mechanism has the best agreement with experimental data over the range 373-453 K, predicting IPs below a factor of 2. While, MH and DMH mechanisms are able to predict IP below a factor of 3 for high temperature only (T > 403 K), similar agreement is obtained at higher temperature (T > 423 K). For the low temperature range (T < 373 K), models overpredict IP by higher than a factor of 5 and 10 respectively for DMH and both n-C8 and TMP.

<sup>2</sup>Defined applying a 20 factor on the common oxygen solubility for standard conditions (1000 ppm)

**Table 4.9:** Literature data used for validation with their associated detection technique.\* Due to the possible existence of two oxidation regimes, data below 393 K are not conserved for the validation of TMP .

Reference	Reactor	Mixture	Pressure (kPa)	IP definition
<b><u>n-C8</u></b>				
This study	PetroOxy	n-C8 + O <sub>2</sub>	1000	10% O <sub>2</sub> consumption
Chatelain (2016)[126]	PetroOxy	n-C8 + O <sub>2</sub>	1000	10% O <sub>2</sub> consumption
Skolniak (2015)[57]	PetroOxy	n-C8 + O <sub>2</sub>	800	10% O <sub>2</sub> consumption
Van Sickle (1973)[29]	PMC reactor	n-C8 + O <sub>2</sub>	>Patm	5% Fuel conversion
<b><u>MH</u></b>				
This study	PetroOxy	MH + O <sub>2</sub>	1000	10% O <sub>2</sub> consumption
<b><u>DMH</u></b>				
This study	PetroOxy	DMH + O <sub>2</sub>	1000	10% O <sub>2</sub> consumption
<b><u>TMP</u></b>				
This study*	PetroOxy	TMP + O <sub>2</sub>	1000	10% O <sub>2</sub> consumption
Skolniak (2015)[57]	PetroOxy	TMP + O <sub>2</sub>	800	10% O <sub>2</sub> consumption

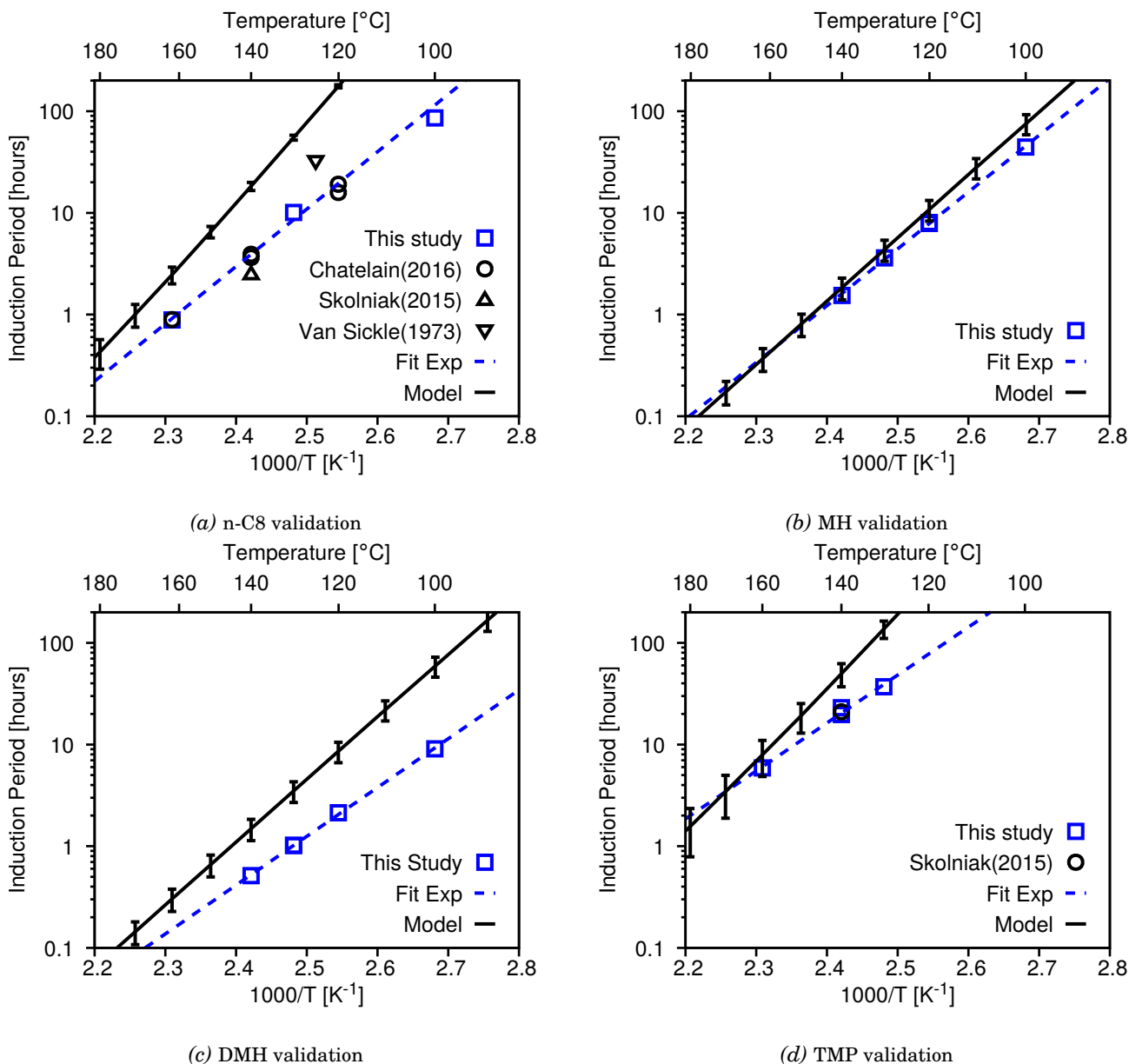
**Branching effects validation** Figure 4.21 presents models capabilities to reproduce the branching effect observed over the molecule tested at 393 K and 413 K. While models prediction can be improved quantitatively, they qualitatively well capture the branching effect<sup>3</sup> over all the conditions tested. While first ramification addition is well predicted by models, the second ramification effect is highly underestimated compared to experimental data. To summarize the overall agreement, Figure 4.22 presents the RE on predicting IPs at several temperatures. Surprisingly, n-C8 mechanism presented in 4.1 has a better agreement than its extended version presented in this section. In addition, Figure 4.22 well represents previous conclusions identifying (i) MH models with the best predictions and (ii) all others models overestimates IPs below a factor of 4 for high temperature (T > 403 K and 423 K for n-C8). RoP and RoC analysis is required to emphasis how the branching is considered in the mechanisms.

**Mechanisms analyses** To better characterize each mechanism, analyses are performed with two oxygen concentrations according to (i) global reactivity, (ii) RoP/RoC distribution and (iii) major species profiles as respectively presented in Figure 4.23, Figure 4.24 and Figure 4.25. Each reaction family under each labels are summarized and presented in Table 4.10 with their corresponding kinetics parameters.

The two oxygen concentrations selected aim at representing the reactivity difference between highly and poorly oxygenated media ( $\times 20$  on O<sub>2</sub> concentration) respectively presented in dashed and solid lines. In addition to the oxygen effect presented in Figure 4.23, the increase of temperature induces both an increase of the RoC/RoP maximum values and a decrease of the delay before reaching it. This is in agreement with experimental conclusions that presented a decreasing IP with temperature. Then, focusing on the sum of both RoC and RoP trends presented in Figure 4.23, a limited influence of oxygen is observed before IP. With n-C8 and TMP mechanisms, this slight reactivity difference is limited to the initiation step while it is constant until IP for MH and DMH. For  $t > IP$ , a larger impact of oxygen concentration is observed with a difference of several orders of magnitude on the sum of both RoC and RoP. This effect of oxygen concentration is also confirmed with the sum of both OH° and HO<sub>2</sub> radicals presented in section 3.

As there is more than 5 orders of magnitude difference between the RoC and RoP, Figure 4.24 presents only the effect of oxygen on the RoC distribution. In addition, as no specific effect of temperature

<sup>3</sup>Illustrated by the IP decrease between 0 and 2 ramifications and then the reactivity increase with TMP



**Figure 4.20:** Models prediction on IP against present study (blue symbols) and literature data (black symbols). For clarity sake, a regression on present study data (dashed blue line) is performed to assess models (solid black lines) performance. Uncertainties on models prediction correspond to IPs variations between 50-20000 ppm initial Oxygen concentration.

is observed on [Figure 4.23](#), RoC analyses are performed at 423 K only. Except the early stage of oxidation ( $\frac{t}{IP} < 10^{-6}$ ) where  $O_2$  and  $HO_2$  mostly contribute to consume the fuel, the main consumption pathways ( $> 95\%$ ) involve the  $ROO^\circ$  and  $HOOQOO^\circ$  radicals until the full consumption of fuel ( $\sim 1.5 - 2 \times IP$ ).

Focusing on smaller changes, the  $HO_2$  contribution trend is different between n-C8 & TMP and MH & DMH. In MH and DMH mechanisms,  $HO_2$  contribution follows oxygen's one by dropping rapidly after initiation, while its contribution remains at a few percentage level during all the propagation step for n-C8 & TMP. Similarly, OH contribution is increasing rapidly close to IP ( $\frac{t}{IP} > 0.1$ ) for both n-C8 & TMP until reaching a fraction of 0.1, while in MH and DMH, OH contribution reaches a peak after IP and represents less than 1%.

Similarly to the sum of rates, a limited influence of oxygen concentration is observed on the RoC distribution for MH and DMH while n-C8 and TMP mechanisms are almost the same. In contrary, in MH and

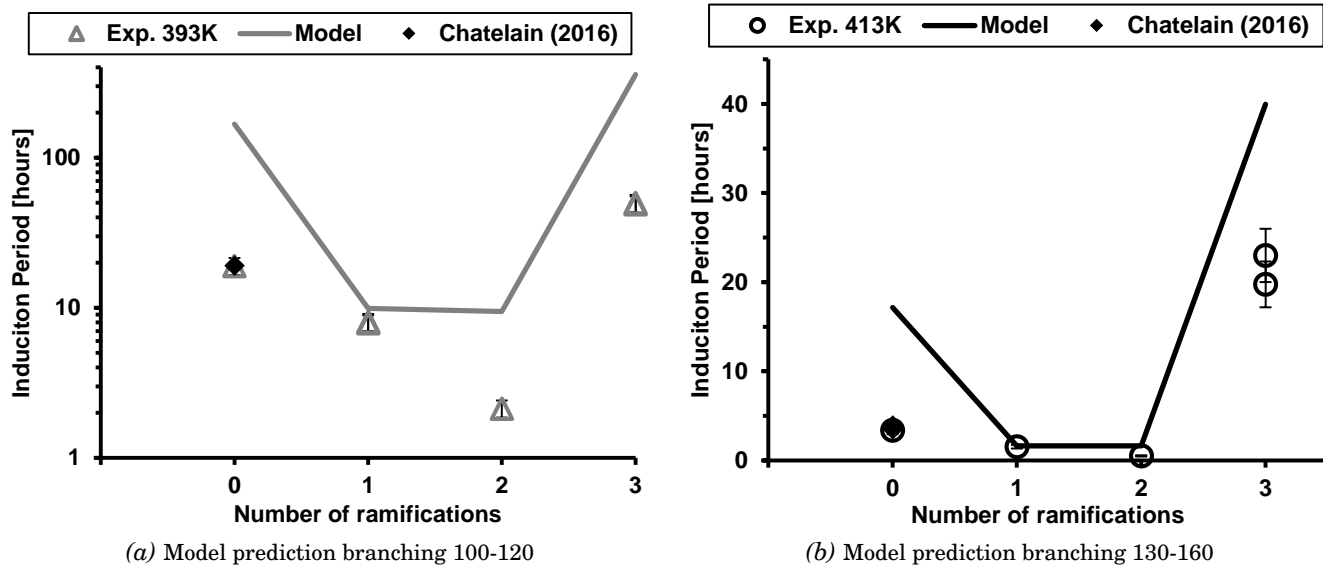


Figure 4.21: Model prediction of the branching impact on paraffins oxidation kinetics

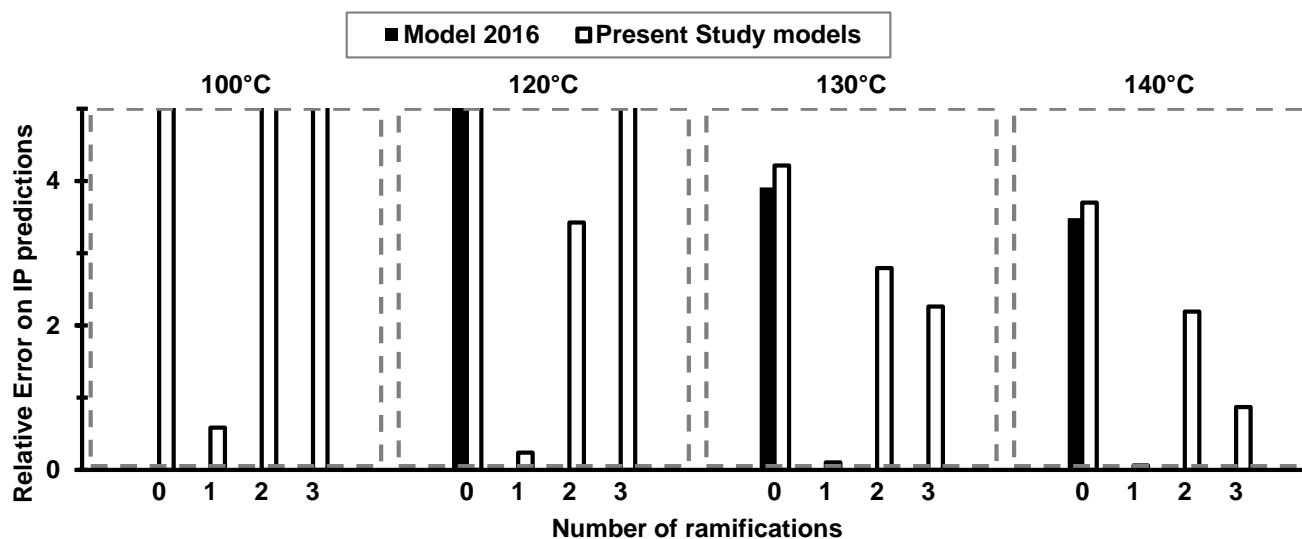


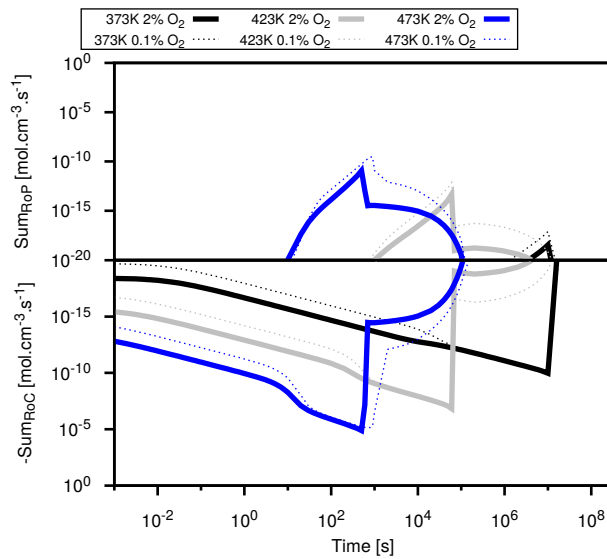
Figure 4.22: RE calculations on both present and literature data models to predict IP at several temperatures.

DMH, the oxygen induces a contribution change between  $\text{HOOQOO}^\circ$  and  $\text{ROO}^\circ$ . They respectively increase and decrease to reach  $\approx 50\%$  of the total rate during the propagation step ( $10^{-6} \lesssim \frac{t}{IP} \lesssim 10^{-2}$ ).

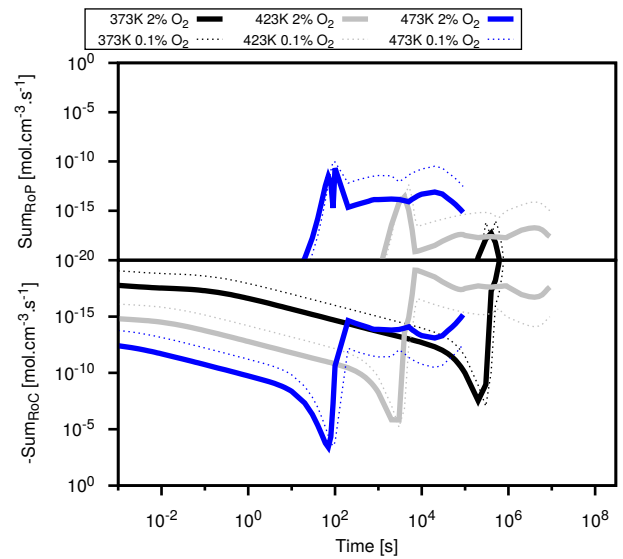
Finally, a last observation is the very specific reactivity of the TMP, for which (i) secondary hydroperoxides seem to contribute only at IP, (ii) peroxy radicals is the main consumption path and (iii) a new reaction family seems to slightly contribute ( $< 1\%$ ) within a very sharp reactivity range ( $0.1 < \frac{t}{IP} < 1$ ). This specific  $\text{HOOQOO}^\circ$  contribution is explainable by the small number of possible  $\text{HOOQOO}^\circ$  isomers on TMP compared with the possible  $\text{ROO}^\circ$ .

**Table 4.10:** Summary of reactions involved in the RoC analysis of fuel with corresponding kinetic parameters within each label. \* Means parameters are identical on each mechanisms. I, II and III mean there is no rate constant distinction if the radical is respectively on a primary, secondary and tertiary carbon.

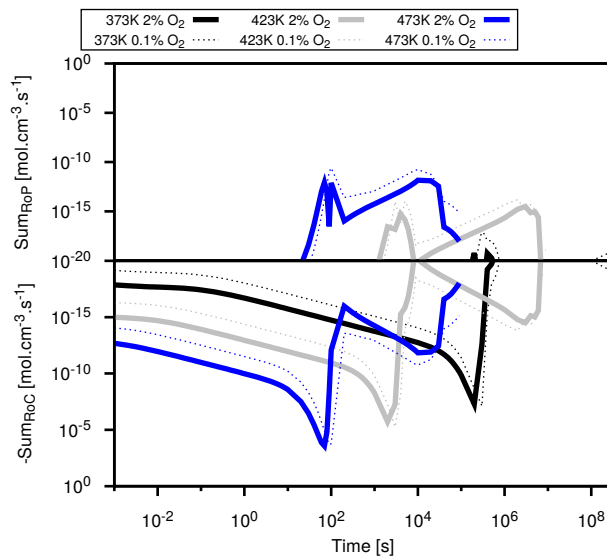
<b>Reaction label and examples of corresponding examples in C<sub>8</sub> model</b>	<b>A</b> [cm <sup>-3</sup> .mol <sup>-1</sup> .s <sup>-1</sup> ]	<b>n</b>	<b>Ea</b> [kcal.mol <sup>-1</sup> ]
<u>O<sub>2</sub>: R° + HO<sub>2</sub>° ⇌ RH + O<sub>2</sub></u>			
(I)*	1.75 . 10 <sup>10</sup>	0	-3.28
(II)*	1.75 . 10 <sup>10</sup>	0	-3.28
(III)*	1.75 . 10 <sup>10</sup>	0	-3.28
<u>OH°: RH + OH° ⇌ R° + H<sub>2</sub>O</u>			
(I): n-C8 & MH & TMP	7.200 . 10 <sup>6</sup>	2	0.86
(I): MH	3.600 . 10 <sup>6</sup>	2	0.86
(I): DMH	14.400 . 10 <sup>6</sup>	2	0.86
(I): TMP	10.8 . 10 <sup>6</sup>	2	0.86
(II): n-C8 & DMH	1.580 . 10 <sup>6</sup>	1.9	0.16
(II): MH & TMP	7.900 . 10 <sup>6</sup>	1.9	0.16
(III): DMH	5.140 . 10 <sup>6</sup>	1.9	1.45
(III): TMP	2.570 . 10 <sup>6</sup>	1.9	1.45
<u>HO<sub>2</sub>: R° + H<sub>2</sub>O<sub>2</sub> ⇌ RH + HO<sub>2</sub>°</u>			
(I)*	2.030 . 10 <sup>0</sup>	3.29	1.07
(II)*	1.141 10 <sup>0</sup>	3.28	0.88
(III)*	3.460 10 <sup>1</sup>	3.050	1.020
<u>ROO (I,II,III): R° + RO<sub>2</sub>H ⇌ RH + RO<sub>2</sub>°</u>			
(I)*	1.015 . 10 <sup>0</sup>	3.290	1.070
(II)*	9.205 . 10 <sup>-1</sup>	3.340	1.140
(III)*	1.73 . 10 <sup>1</sup>	3.050	1.020
<u>OOQOOH (I,II,III): R° + HO<sub>2</sub>QO<sub>2</sub>H ⇌ RH + HO<sub>2</sub>QO<sub>2</sub>°</u>			
(I)*	1.015 . 10 <sup>0</sup>	3.290	1.070
(II)*	9.205 . 10 <sup>-1</sup>	3.340	1.140
(III)*	1.73 . 10 <sup>1</sup>	3.050	1.020



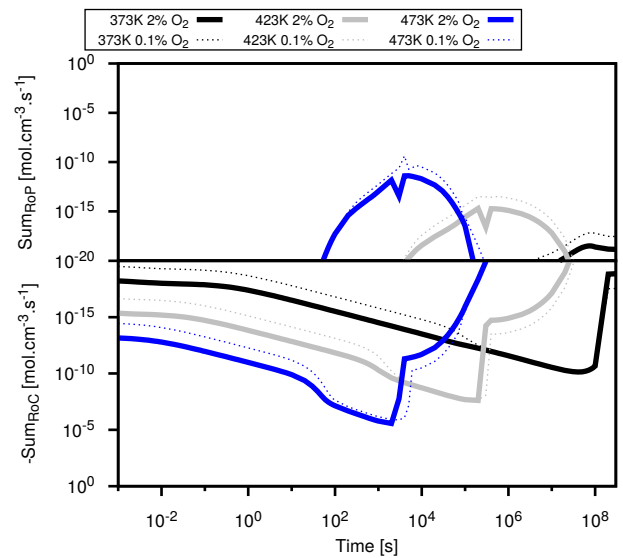
(a) Sensibility analysis with n-C8 mechanism



(b) Sensibility analysis with MH mechanism

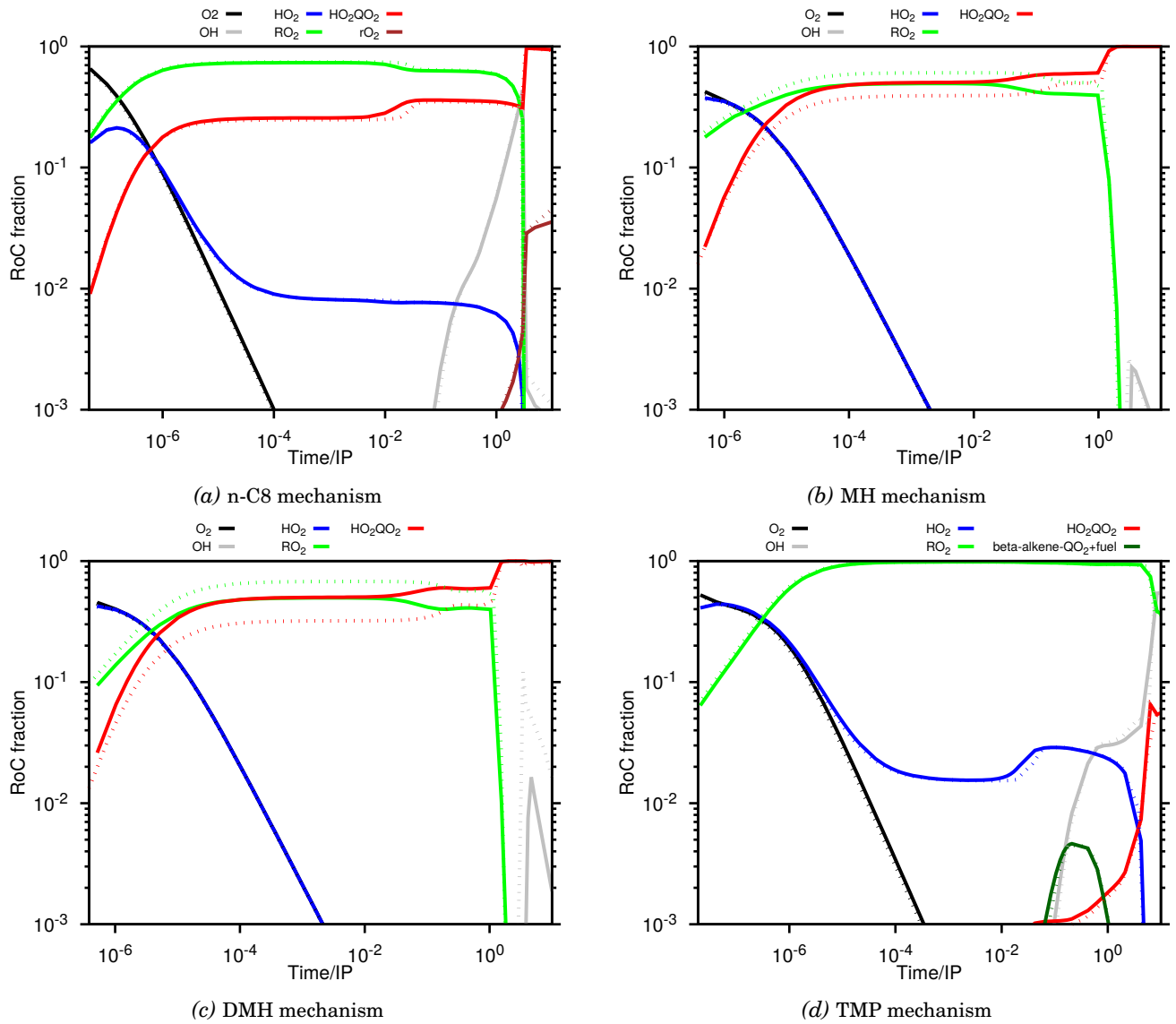


(c) Sensibility analysis with DMH mechanism



(d) Sensibility analysis with TMP mechanism

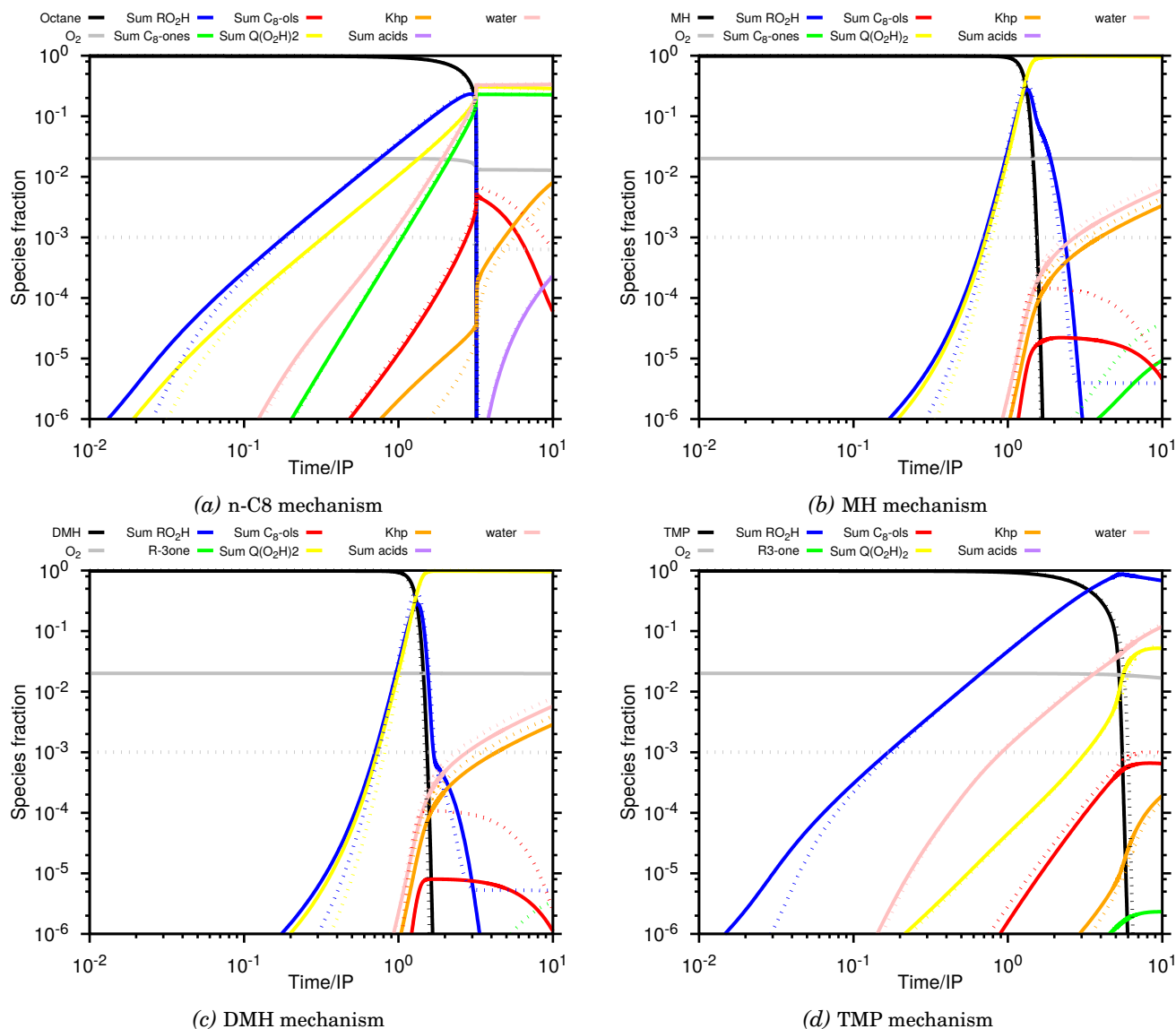
**Figure 4.23:** Effect of both oxygen concentration and temperature on the sum of fuel RoP and RoC respectively presented on the upper and lower parts of each chart. Analysis was conducted at 423 K with 20000 ppm and 1000 ppm of oxygen respectively in solid and dashed lines.



**Figure 4.24:** Effect of oxygen concentration on fuel RoC distribution. Analysis was conducted at 423 K with 20000 ppm and 1000 ppm of oxygen respectively in solid and dashed lines.  $rOO^\circ$  stands for the sum of light hydroperoxides from  $C_1$  to  $C_7$



Figure 4.25 presents the major products formed with the four mechanisms at two different oxygen concentration. Except for the fuel, which is the major product until several IPs ( $t = x \times IP$ ), the products distribution emphasize similar conclusions as the RoC analyses. Thus, single and poly hydroperoxides are the major oxidation products in all the mechanisms, except for the TMP where the concentration of polyhydroperoxide is very low concentration ( $1 \text{ ppm} < x_{HO_2QO_2H} < 100 \text{ ppm}$ ) and only close to IP ( $0.1 < \frac{t}{IP} < 1$ ). Focusing on the effect of oxygen, a limited influence is observed during the species onset of single and polyhydroperoxides for time below IP. While after IP, alcohols and ROOH are an order of magnitude higher difference between the two conditions.



**Figure 4.25:** Effect of oxygen concentration on major species formation. Analysis was conducted at 423 K with 20000 ppm and 1000 ppm of oxygen respectively in solid and dashed lines.

Figure 4.26 and Figure 4.27 both compare by pair the fuel RoP and RoC in mechanisms to identify the branching effect captured by models. Figure 4.26 presents the evolution of the sum of RoP and RoC according to different mechanisms pairs at three temperature. RoPs maximum peaks are correlated with the RoC maximum over the four mechanisms in all conditions tested. In addition, the value of the RoPs in all mechanisms are negligible compared to the RoC until the full consumption of the fuel<sup>4</sup>.

Interestingly, by comparing reactivity of both MH and DMH with n-C8 (Figure 4.26a and Figure 4.26b), a similar initiation phase is observed with very close RoC values. In addition, the RoC rates is increasing faster during the propagation step for both MH and DMH than for n-C8. This reactivity increase induces both a shorter delay to reach RoC maximum peak and a higher value of RoC maximum. This demonstrates that the branching effect of mono-branched carbons<sup>5</sup> is caused by an equilibrium or a reactivity promoter in this propagation step.

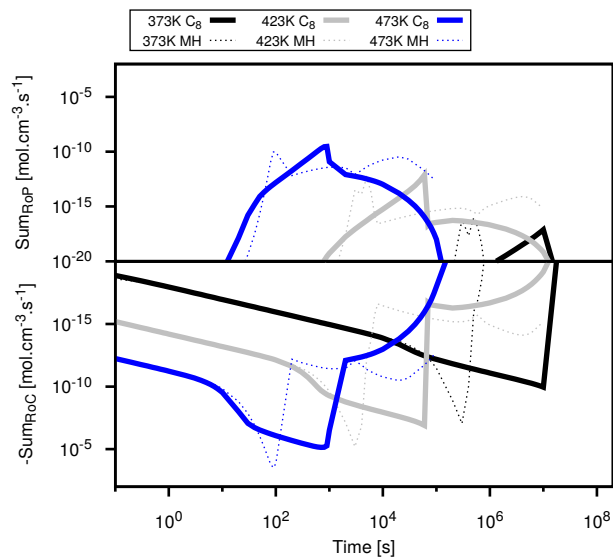
In the other hand, the TMP RoC is slower in all conditions tested than both n-C8 and MH respectively in Figure 4.26c and Figure 4.26d. As a consequence, the delay to reach RoC maximum peak is longer and its value is lower for TMP than for both n-C8 and MH. Those conclusions are in agreement with the experimental observations that the IP of TMP is longer than the three others compounds.

Using the same pair of mechanisms, Figure 4.27 presents the major chemical families contributing to the RoC values at 423 K. Thus, as expected from Figure 4.24 results, the single and poly-hydroperoxi radicals cause the reactivity increase identified in the propagation step for both MH and DMH. While the RoC of TMP involve similar reaction families between both MH and n-C8, the absolute value of the rate is lower for the TMP in all conditions presented. However, as presented in Table 4.10, kinetic rates for single and poly-hydroperoxides are identical are identical between all mechanisms. Thus, the reactivity difference comes from the structure change between TMP and other compounds. This structural changes induce an increase of primary carbons inside the molecule whose the H-abstraction the kinetic rate is much slower than secondary carbons.

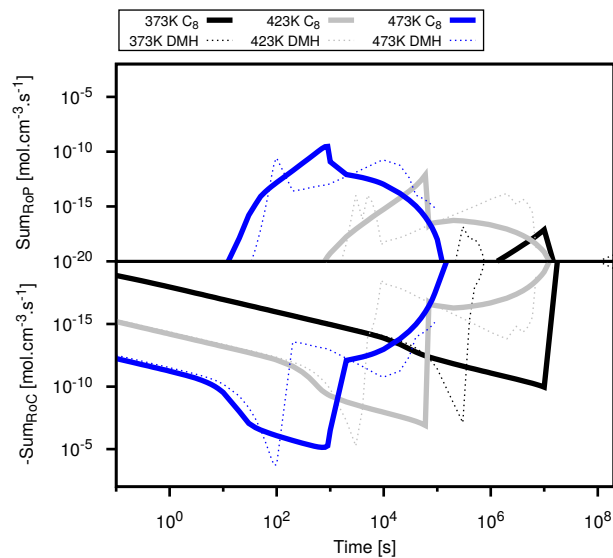
---

<sup>4</sup>As mentioned earlier, this typically corresponds to  $\sim 2 - 3 \times IP$  in all mechanisms

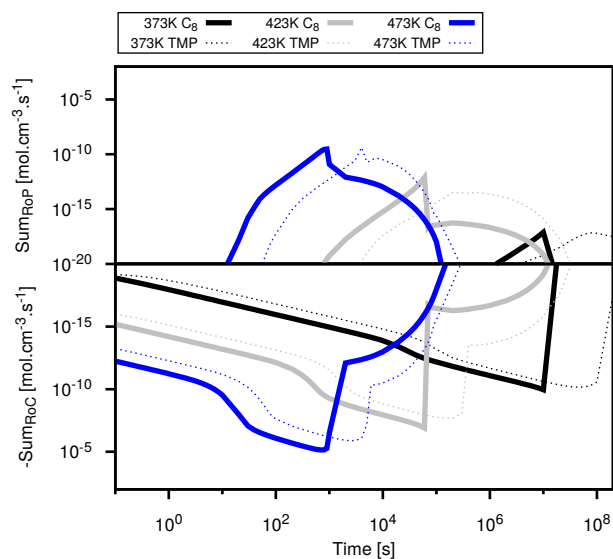
<sup>5</sup>In this case mono-branched should means only one branching per carbon and not one branching on the overall molecule. This could be assimilated to all branched compounds except quaternary carbon containing molecules



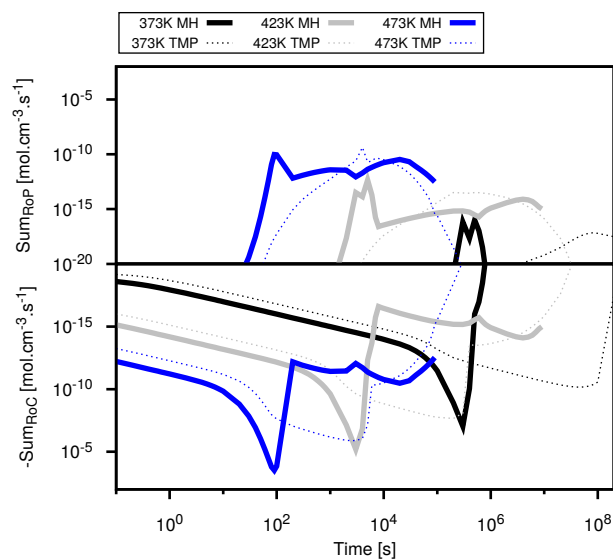
(a) n-C8 (solid lines) and MH (dashed lines)



(b) n-C8 (solid lines) and DMH (dashed lines)

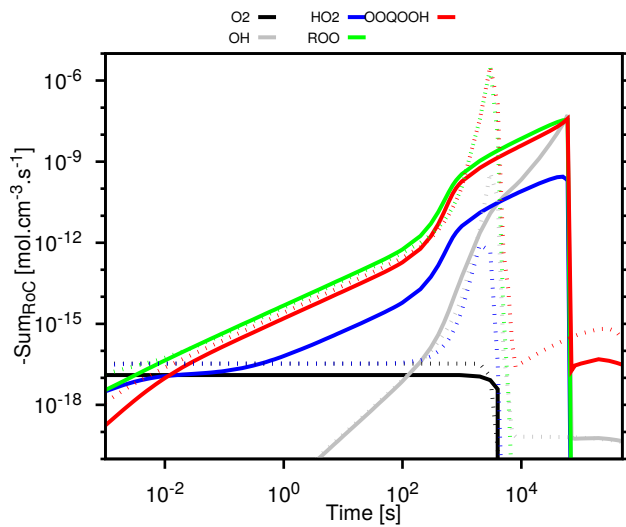


(c) n-C8 (solid lines) and TMP (dashed lines)

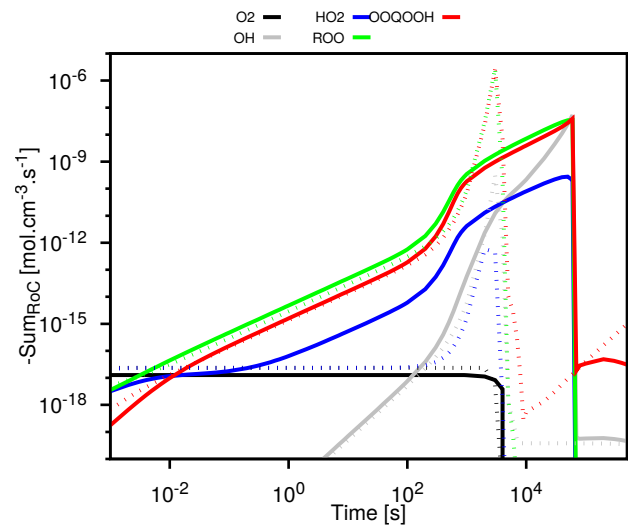


(d) MH (solid lines) and TMP (dashed lines)

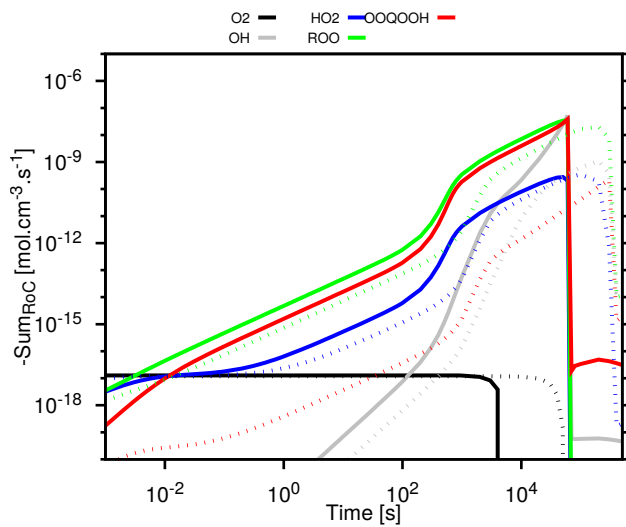
**Figure 4.26:** Temporal evolution of the sum of RoC and RoP with two different pairs of mechanisms.



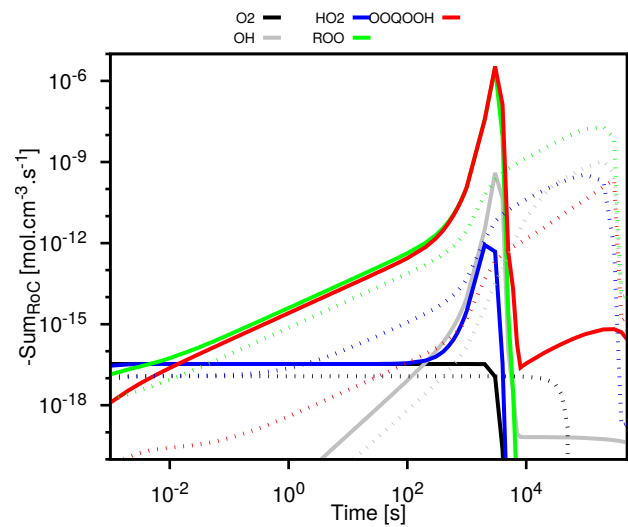
(a) n-C8 (solid lines) and MH (dashed lines)



(b) n-C8 (solid lines) and DMH (dashed lines)



(c) n-C8 (solid lines) and TMP (dashed lines)



(d) MH (solid lines) and TMP (dashed lines)

**Figure 4.27:** Temporal evolution of the RoC distribution with different pairs of mechanisms.

## 4.2.2 Detailed results with autoclave

In order to get more information of MH oxidation, experiments are now conducted in the autoclave to obtain products formation in both liquid and gas phases over time. In order to obtain similar results as PetroOxy, experiments are conducted with similar amount of oxygen and similar sample to reactor volume ratio ( $\frac{V_{sample}}{V_{reactor}} = 0.2$ ). Further discussions on the differences between autoclave and PetroOxy experiments is performed [subsection 4.3.2](#).

### Material and methods

As autoclave experiments and its associated analytical devices were already presented (chapter 3), no further description is performed here.

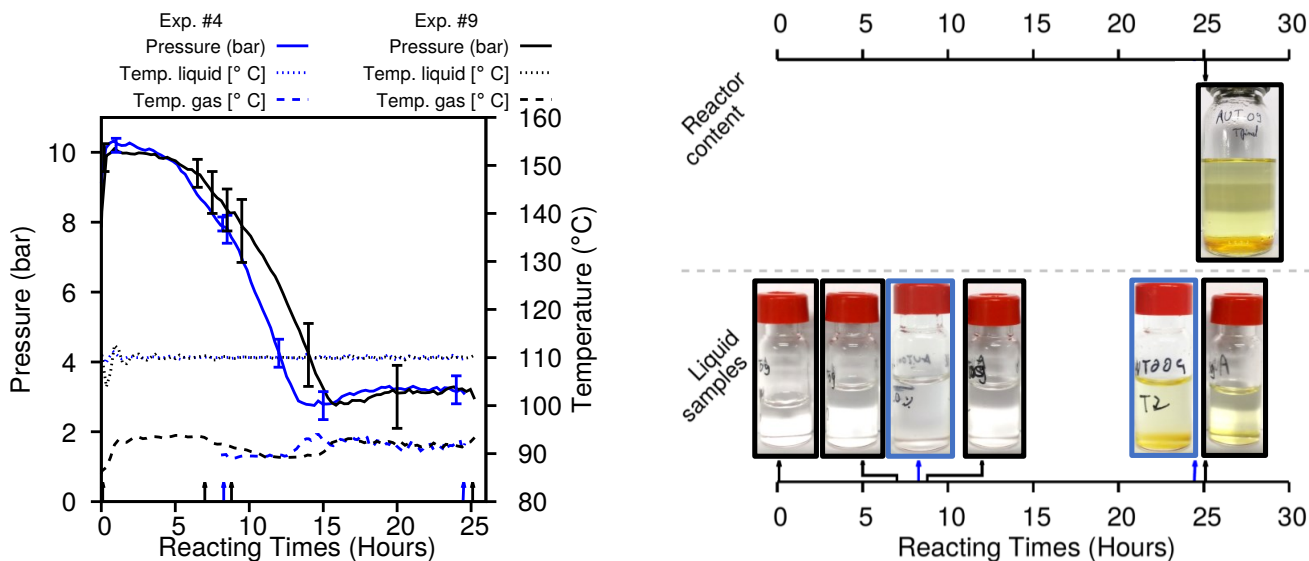
Experiments are conducted twice at 383 K and 1000 kPa of total pressure with 50mL of reactant. This repeatability point aims to cover most of the oxidation regime and to validate oxidation rates. As the sampling technique presented in (chapter 3) modifies gas phase composition, one of the two experiment is limited to one intermediate sample. Thus, the repeatability point aims to confirm the absence of sampling effect on the oxidation rate. Each intermediate sample is about 1mL and final content of the autoclave is also collected for visual inspections.

### Experimental results

**Macroscopic reactivity** Results summarizing MH oxidation over time are presented in [Figure 4.28](#). [Figure 4.28a](#) presents pressure and temperature evolution over reacting time between the 2 experiments. As observed for n-C8 experiments, a high temperature gradient is observed between the gas and the liquid phase, around 15-20°C and is also reproduced on both experiments. Pressure uncertainties are calculated according to this equation  $\Delta(P)_t = P_{Uncert.} \times (1 + n_{spl.,t}) + (P_{spl.,t+\epsilon} - P_{spl.,t-\epsilon})$  to consider both measurements errors and potential pressure addition after the sampling. Compared to n-C8 results, experiments reproducibility seems weaker due to the pressure variation before and after the third sampling. This pressure variation also explains why pressure uncertainties are higher in MH experiments. Considering this uncertainty, the fair reproducibility of pressure and temperature profiles demonstrates the absence of any sampling effect on the autoxidation.

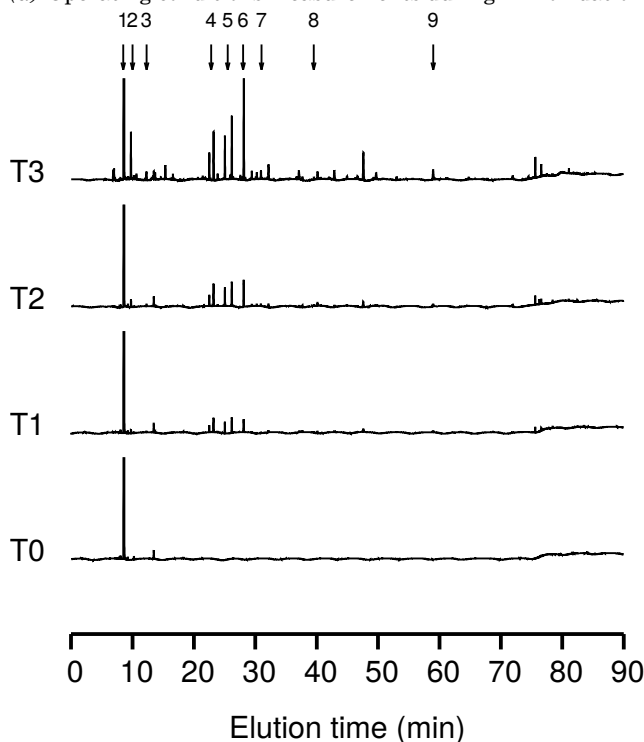
Sampling times are represented in [Figure 4.28a](#) with arrows and pictures of each sample are represented over time in [Figure 4.28b](#). As observed on those pictures, the starting fuel which was colourless turns into a coloured binary liquid phase system at the end of the experiment. From the picture of the reactor content, the formation of such two phases system seems to occur below the 25<sup>th</sup> reacting hour. Finally, [Figure 4.28c](#) and [Figure 4.28d](#) respectively illustrate liquid and gas phase products formation over time. Liquid and gas phase results are respectively from the GC-FID and from the GC-TCD. For clarity sake, chromatograms are cut off to observe oxidation products formation.

**Product identification** [Figure 4.29](#) aims to justify the products identification performed with the GC-MS for ketones and acids chemical families. In both figures, the full scan spectrum was filtered with majors ions of the involved chemical families. As concluded with PetroOxy residual analyses, majors products identified are all the MH ketones and the tertiary alcohol, the 2-methyl-2-heptanol. Minor products observed are both aliphatic and branched 2-ketones and acids with a disfavoured chain lengths for 6 carbons. Even with the most oxidized sample, the FTIR spectrum presented in [Figure 4.30](#) does not reveal any OH

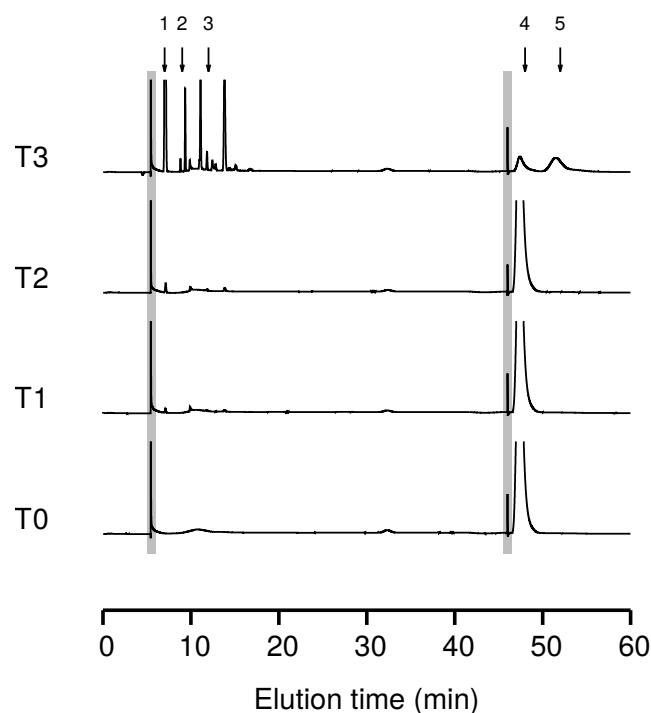


(a) Operating conditions measurements during MH oxidation

(b) Samples and autoclave content pictures



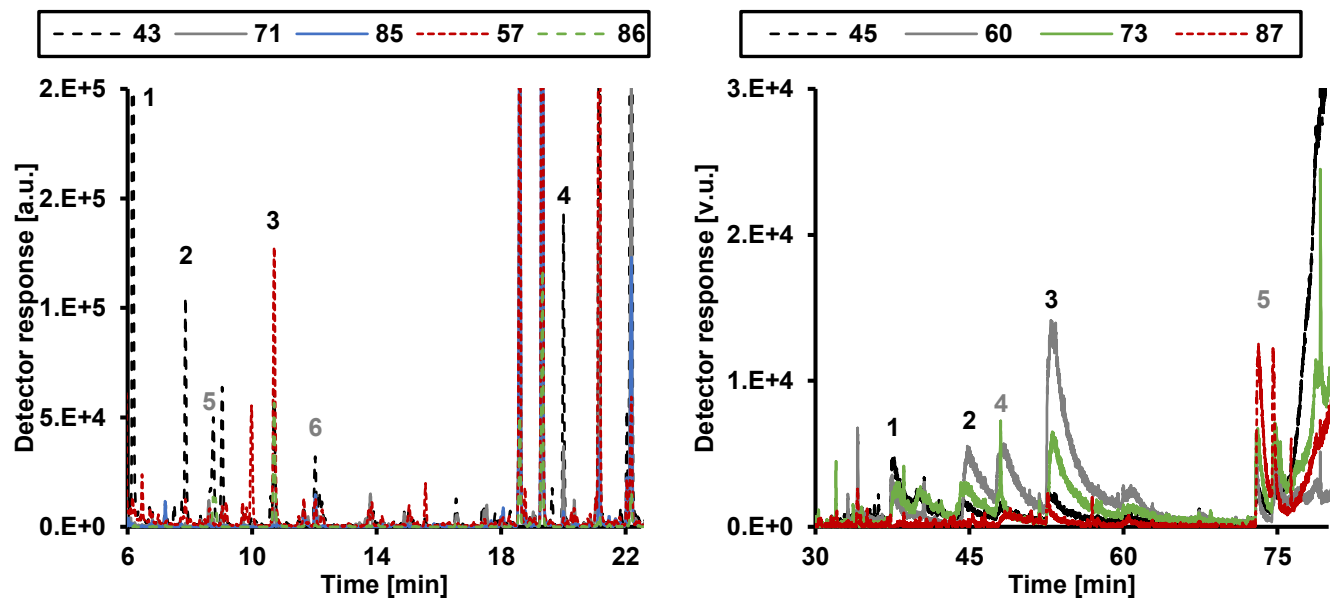
(c) GC-FID signals for liquid samples obtained at different oxidation times from Exp #9. Identified peaks are 1:MH, 2: Acetone/2-propanone, 3: 2-butanone, 4 & 5: 2-methylheptanones 6: 2-methylheptan2ol, 7: others 2-methylheptanols 8: butanoic acid, 9: hexanoic acid.



(d) GC-TCD signals for liquid samples obtained at different oxidation times from Exp #9. Identified peaks are 1:CO<sub>2</sub>, 2: ethane & others, 3: propane & others & iso-butane, 4: O<sub>2</sub>, 5: others & methane. Grey areas correspond to valve switch timing.

**Figure 4.28:** Macroscopic results for MH oxidation at 383 K and 1000 kPa in autoclave

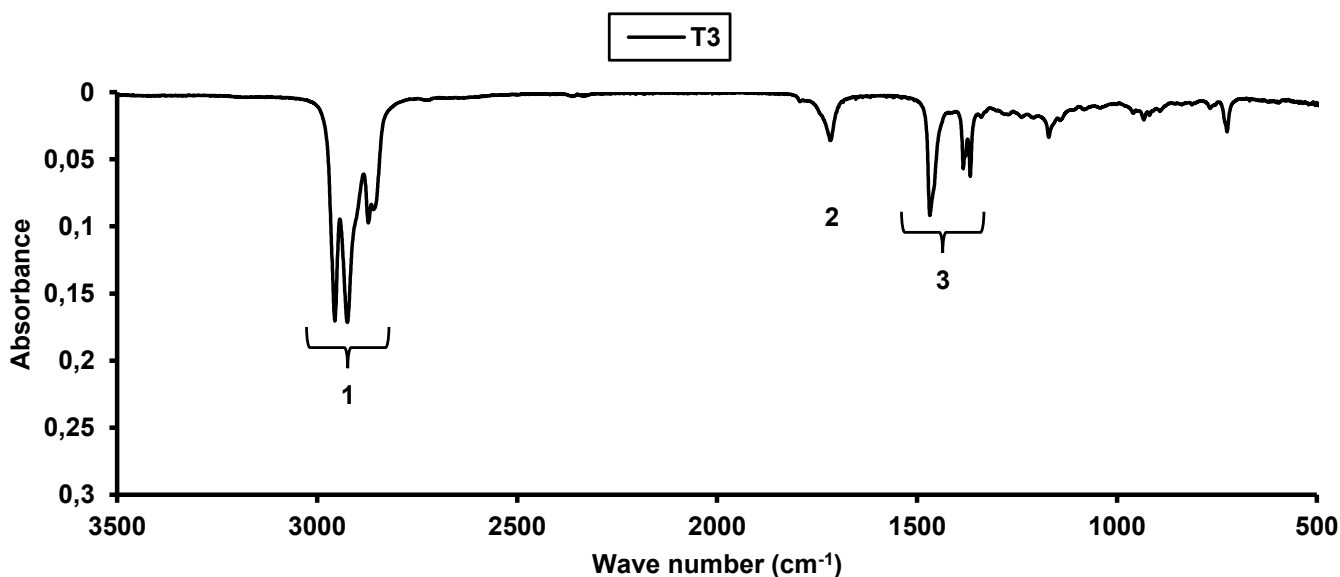
absorption band due to both a too small concentration of 2-methylheptanol and a weak absorption band compared to both CH and C=O bands. As presented in the theoretical spectrum of pure 2-methylheptanol, the maximum absorbance for the OH band is 10 times smaller compared to CH bands. Absorption bands 1 and 3 are relevant to C-H bond stretch respectively from CH<sub>3</sub> and CH<sub>2</sub> groups. In addition the absorption band 2 is relevant to C=O bond stretch MH spectrum from species containing ketones. Those results are in line with both GC-MS identification and GC-FID quantification presented in the next section and presenting major species, in the liquid phase, such as MH and octanone isomers.



(a) Full scan spectrum filtered with the major ions of all ketones species identified in MH. Products identified are: 1: 2-propanone/acetone, 2: 2-butanone, 3: 2-pentanone, 4: 2-heptanone, 5: 3-methyl-2-butanone, 6: 4-methyl-2-pentanone. Chromatographic settings are similar to the previous studies and common compounds have identical retention times (Figure 4.29a)

(b) Full scan spectrum filtered with the major ions of aliphatic acids. Products identified are: 1: propanoic, 2: butanoic acid, 3: pentanoic acid, 4: 3-methylbutanoic acid, 5: methylheptanoic acids isomers. Chromatographic settings are similar to the previous studies and common compounds have identical retention times (Figure 4.29a)

**Figure 4.29:** TIC MH spectrum for oxidized octane sample filtered with specific  $m/z$  ions.

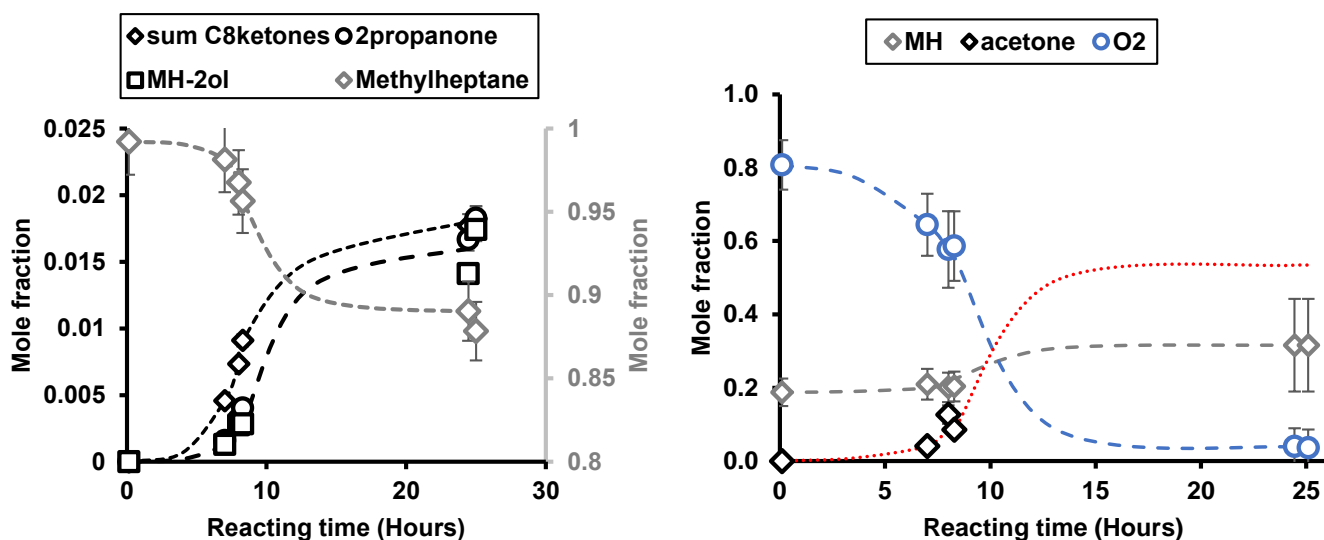


**Figure 4.30:** FTIR-ATR analysis of MH sample after 24 h oxidation. Absorption bands 1 and 3 are relevant to C-H bond stretch respectively from  $\text{CH}_3$  and  $\text{CH}_2$  groups. The absorption band 2 is relevant to C=O bond stretch from MH ketones isomers formed during autoxidation.

**Species profiles** Liquid phase species are quantified using either external calibration or the ECN model to reconstruct DR coefficient according to the chemical structure identified with the GC-MS. External calibration are only used for the MH and ECN model reference compound.

Species profiles for both liquid and gas phase major products are presented in Figure 4.31. Based on pressure profile evolution from Figure 4.28a, dashed line curves aim to suggest the species profile evolution. From those products formation, three different oxidation regimes may be identified. A first initiation

regime ( $\lesssim 4h$ ), where the total pressure decreases slowly due to small oxidation rate with both a small consumption of oxygen and fuel. A propagation regime ( $4 \lesssim t \lesssim 12h$ ) with a higher oxidation rate where the oxygen is consumed quickly by the fuel and induces a pressure drop. A last regime regime which could be assimilated to a termination regime, where oxidation rate slows down due to first the oxygen diffusive limitation into the liquid and then its full consumption at the end of the experiment. At the end of the experiment, the liquid phase is still mainly composed of MH (90 %) and the three major products are: methyl-heptanones isomers, 2-propanone/acetone and the 2-methyl-2heptan-2-ol. While in the gas phase, oxygen is fully consumed, MH seems to be the major component ( $\approx 30\%$ ). From Figure 4.31b, the final 2-propanone fraction is not presented due to meaningless results with a fraction higher than 1. As this error is repeated and was not observed for n-C8 experiments, others oxidation products specific to MH at heavy oxidation stage certainly contribute to the signal. Thus, the red dotted line presented in Figure 4.31b is based on both the 2-propanone data available and theoretical partial pressure in final conditions.



(a) Dashed lines represent the hypothetical species profiles trends between two samples based on the pressure profile drop. Due to very close species profiles trend 2-propanone and 2-methylpropanol are represented with the same black dashed line.

(b) Dashed lines represent the hypothetical species profiles trends between two samples based on the pressure profile drop. The red dotted line present theoretical fraction of 2-propanone based on its partial pressure in those conditions.

**Figure 4.31:** Species profiles of major species identified during MH oxidation at 383 K.

Then, the species profiles of minor products are presented in Figure 4.32 for both liquid and gas phases. At the end of the experiments, minors products in the liquid phase are mostly all the [1-4]-octanols ( $\approx 1\%$ ), all the low 2-ketones ( $\approx 1\%$ ) from C<sub>3</sub> to C<sub>6</sub>. Except for CO<sub>2</sub> and acetaldehyde which are gaseous, the composition of minor products is mostly due the volatility of liquid phase products like for butanone and octanones.

## 4.3 Discussions

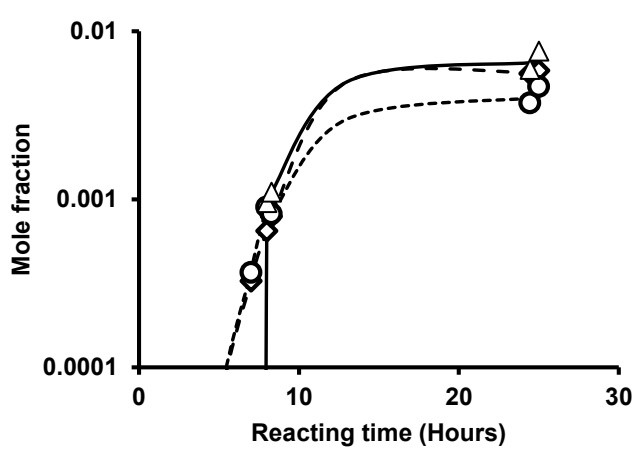
### 4.3.1 Structure reactivity impact on paraffins autoxidation

Based on experimental reactivity trends observed previously, an empirical formula may be used to describe paraffins reactivity according to temperature, number of carbons and carbons types. Empirical models are developed subsequently for n-paraffins and iso-paraffins.

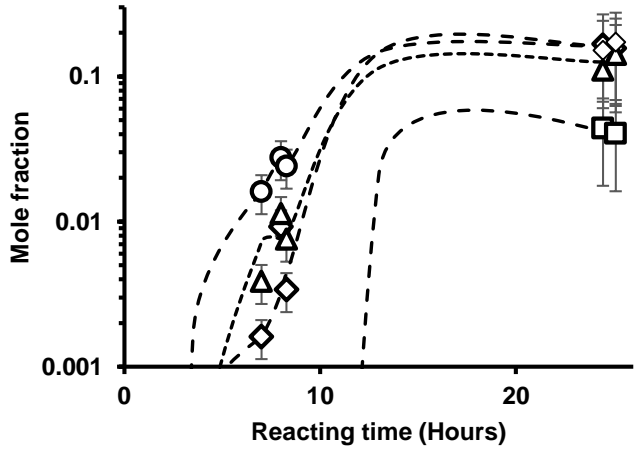


◆Others <2ketones ○Others C8ol △sum acids

◆C02 ○acetaldehyde △butanone □sum C1-C3



(a) Dashed lines represent the hypothetical species profiles trends between two samples based on the pressure profile drop.



(b) Dashed lines represent the hypothetical species profiles trends between two samples based on the pressure profile drop.

**Figure 4.32:** Species profiles of minors species identified during MH oxidation at 383 K.

**n-paraffins empirical model** As concluded in section 4.1, n-paraffins oxidability increases according to both chain length and temperature. Combining n-paraffins results from both section 4.1 and section 4.2, the n-paraffins dataset represents 21 individual IP measurements between 393 and 433K<sup>6</sup>. Their stabilities can be expressed as function of an apparent kinetic rate with a A' and Ea'. The monotonic linear variation of both ln(A) and Ea with respect to the number of carbons, presented in Figure 4.33, tends to demonstrate the existence of the relation. Thus, the two expressions of ln(A) and Ea can be used to reconstruct  $IP_{n-para}$  as presented in Equation 4.1.

$$IP_{n-para,T} = A'_{n-para} \times \exp\left(Ea'_{n-para} \times \frac{1000}{T}\right)$$

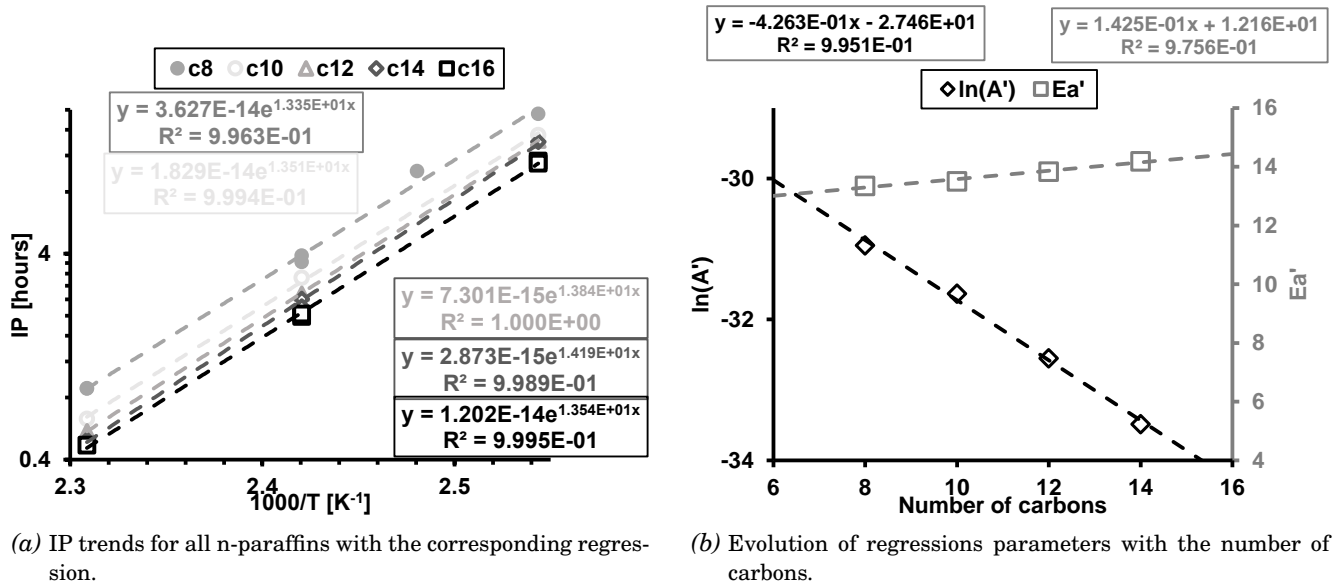
With,  $\ln(A'_{n-para}) = -0.426 \times Nb_{carbons} - 27.5$  (4.1)

And,  $Ea'_{n-para} = 0.1425 \times Nb_{carbons} - 12.155$

**Iso paraffins empirical model** From results presented in section 4.2, a simple empirical model for C<sub>8</sub> iso-paraffins presented a fair agreement with experimental data. This exponential regression, Figure 4.19 and Table 4.7, pointed out empirical correlation linking both iso and normal paraffin IPs at a given temperature with the number of tertiary carbons inside the molecule ( $IP_{iso-C_8,T,Nb} = IP_{n-C_8,T} \exp(\alpha_T \times Nb_{ramification})$ ).

Using the same experimental data, another approach is proposed here based on the apparent Ea' and A' as performed in the previous section. Figure 4.34 illustrates the variation of those parameters across iso-alkanes with a non monotonic dependence with the number of tertiary carbons ( $Nb_{Tert.}$ ). Assuming a linear dependence of the number of quaternary on both Ea' and A', a last term must be added to consider TMP results. Thus, two expressions of ln(A) and Ea are proposed to reconstructs  $IP_{iso-para}$  as presented in

<sup>6</sup>As only one experiment is available at 373 K and only for n-C8, this temperature range is omitted from the regression



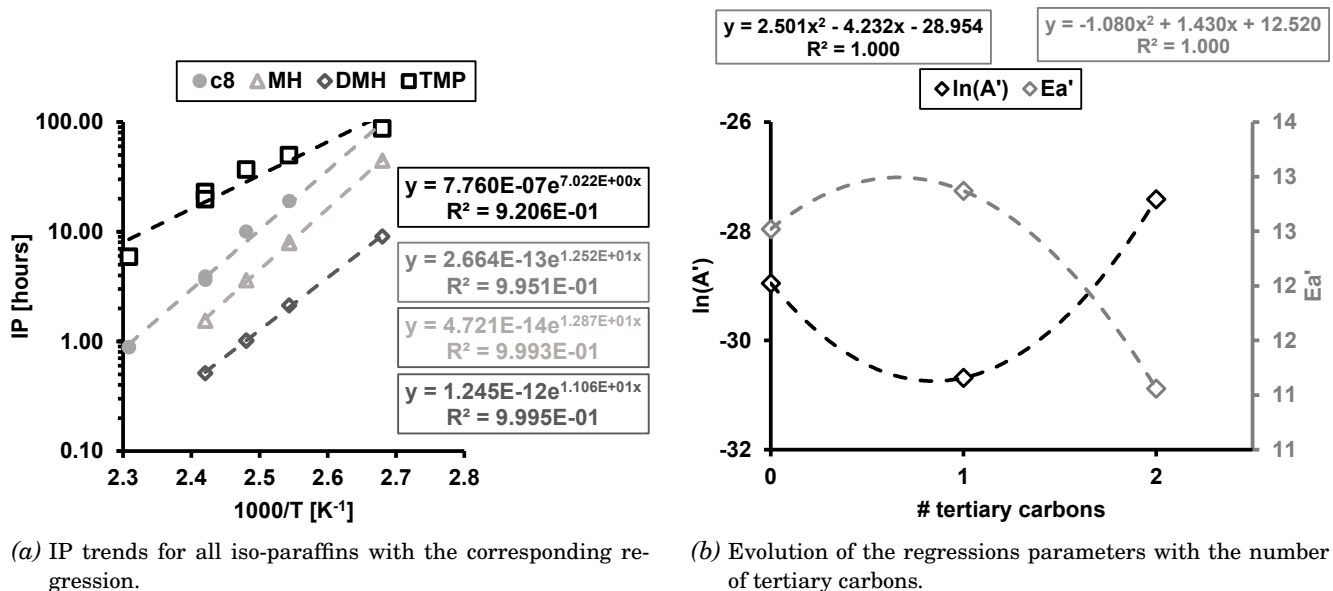
**Figure 4.33:** Evolution of both IPs and regression parameters as function of the number of carbons of all n-paraffins studied.

#### Equation 4.2.

$$IP_{iso-para,T} = A'_{iso-para} \times \exp(Ea'_{iso-para} \times \frac{1000}{T})$$

With,  $\ln(A'_{iso-para}) = Nb_{Tert.} \times (2.501 \times Nb_{Tert.} - 4.232) + 13.13 \times Nb_{Quat.} - 28.954$  (4.2)

And,  $Ea'_{iso-para} = Nb_{Tert.} \times (-1.080 \times Nb_{Tert.} + 1.430) - 4.382 \times Nb_{Quat.} + 12.250$



**Figure 4.34:** Evolution of both IPs and regression parameters as function of the number of carbons of all iso-paraffins studied.

**Extended empirical model** Assuming a similar dependence of the branching, across all chain lengths, a generalized empirical model may be proposed for all n/iso-paraffins compounds from Equation 4.2 and Equation 4.1. Its general expression is presented in Equation 4.3 with both expression of  $\ln(A)$  and  $Ea$ . Model agreements with the two data sets are presented in Figure 4.35 and Figure 4.36. The extended

model agreements with both Absolute Error (AE) and RE according to iso/normal chemical families is summarized in Table 4.11. In most of conditions with IPs below 72 hours<sup>7</sup>: this empirical model offers fair results ( $IP_{emp.model} \leq 20\%$ ) comparable to the sum of experimental measurements uncertainties (15%).

$$IP_{alkanes,T} = A'_{alkanes} \times \exp\left(Ea'_{alkanes} \times \frac{1000}{T}\right)$$

With,  $\ln(A'_{alkanes}) = \ln(A'_{iso-para}) + 28.954 + \ln(A'_{n-para})$  (4.3)

And,  $Ea'_{alkanes} = Ea'_{iso-para} - 12.250 + Ea'_{n-para}$

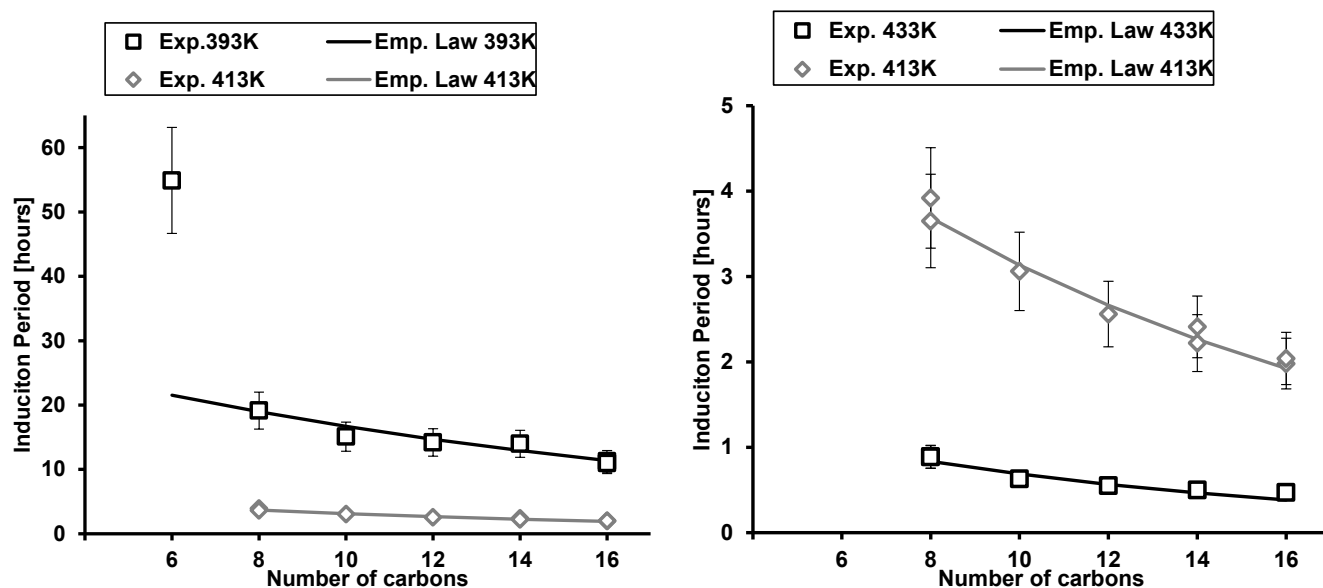


Figure 4.35: Validation of the extended model for n-paraffins chemical families

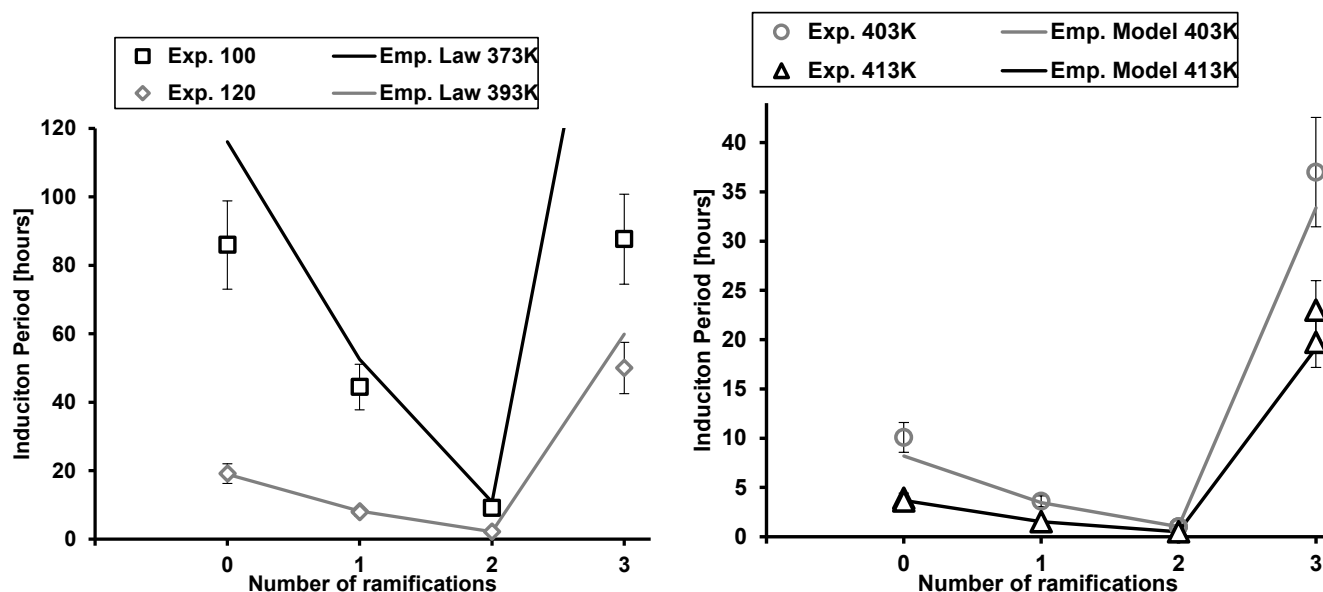


Figure 4.36: Validation of the extended model for iso-paraffins chemical families

While results presented here revealed a fair agreements with experimental data in most conditions. More experimental data are required to both refine and validate the empirical formula for longer branched

<sup>7</sup>Only experimental data of hexane at 393K present higher errors.

**Table 4.11:** Performance of the extended empirical model according to both chemical families and IPs values

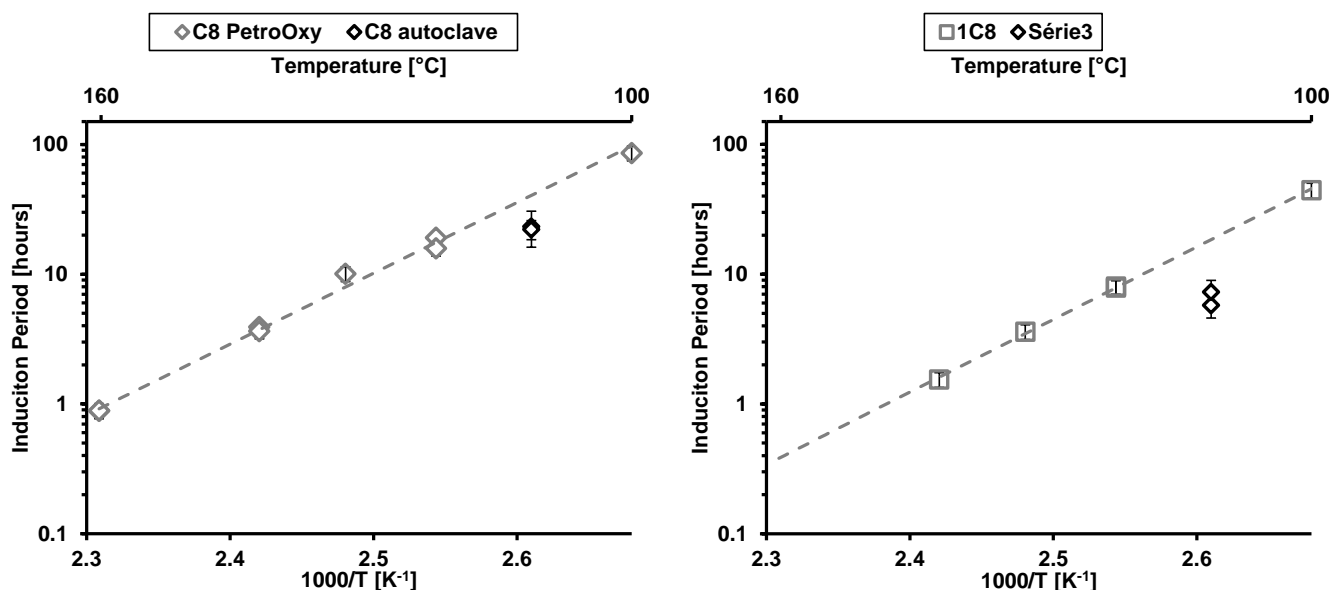
	AE values			RE values		
	Min.	Max.	Average	Min.	Max.	Average
<b>All IPs</b>						
n-paraffins	0.02	33.37	3.06	0%	60%	10%
Iso-paraffins	0.01	124.09	9.59	0%	140%	20%
<b>IPs &lt; 72h</b>						
n-paraffins	0.02	33.37	1.83	0%	60%	10%
Iso-paraffins	0.01	9.89	1.96	0%	20%	10%

compounds. As our dataset only contained one example with a quaternary carbon, the empirical formula should be used with caution for predictive purposes in such conditions.

### 4.3.2 Experimental results discussions

#### PetroOxy-Autoclave comparison

As introduced in the experimental results section, the autoclave experiments aimed at reproducing PetroOxy experiments with detailed species profiles over time on both gas and liquid phase. However, comparing the IPs from autoclave pressure profiles with PetroOxy data (Figure 4.37), IPs values for n-C8 and MH slightly differ and are respectively within a factor of 4 and 5. The differences between experimental apparatus that may cause such reactivity offset are discussed hereafter.



(a) Measured IPs for n-C8 according to both experimental apparatus

(b) Measured IPs for MH according to both experimental apparatus

**Figure 4.37:** Measured IPs for MH according to both experiments

**Oxygen diffusion into the liquid** A first difference is the presence of a bubbling device into the autoclave and is not in the PetroOxy. However, the oxygen availability seems not responsible of this reactivity difference. (1) As presented in models analyses, the predicted IP is not sensitive to the oxygen amount into the liquid within the 50-20000 ppm range. (2) As presented in the section 4.1 with the Hatta number calculation, the system is in kinetic regime and not limited by the oxygen content. The existence of the

bubbling system into the autoclave is due to a less favorable surface over volume ratio  $\left(\frac{Surface}{volume}\right)$  compare to PetroOxy experiment.

**Temperature gradient** While liquid phase temperature is directly monitored in autoclave experiments, this monitoring is not available in the PetroOxy device. Thus, the effective liquid phase temperature might be lowered due to thermal conduction within either the liquid only or both liquid and heating system. Assuming that the autoclave temperature is the correct one, it is possible to calculate the equivalent liquid phase temperature in the Petroxy to obtain similar IP. Using equations from [Figure 4.34](#), the same IP, obtained in autoclave at 383 K, can be identified between the range 388-392 K on both n-C8 and MH experiments.

Thus the reactivity difference between the two experiments seems partially caused by a temperature gradient between the heating surface and the bulk phase. A second error may be linked to the uncertainty on the oxygen quantity introduced into the autoclave. While a temperature gradient seems to cause this reactivity difference, further investigations are required to affirm the origin of this slight reactivity difference.

### **Occurrence of multiphase processes**

As presented with the present experimental results, several equilibria are involved in autoxidation like (i) gas-liquid, (ii) liquid-liquid and finally the (iii) liquid-solid. As the present study is focused on the deposit precursor formation, the oxidation levels are not high enough to allow deposit formation and they cannot be discussed here.

**Gas-liquid equilibrium** Combining both FID and TCD GCs, the three main liquid-gas equilibria occurring in autoxidation processes are confirmed over two different chemical systems. A first equilibrium, governed by Henry's equation, is confirmed with the pressure decrease along oxygen consumption. A second equilibrium with the light and gaseous products formation, like CO<sub>2</sub>, light HCs, acetaldehyde, that migrate from the liquid to the gas phase. For those specific compounds, only their soluble fractions, which is very low, is observable in the liquid phase. A last equilibrium well represented for fuel is the liquid evaporation. As observed in both experiments, fuel fraction increases over the reacting time following other products formation. However, fuel is not produced in the gas phase but remains constant over time, and this fuel fraction increase is only due to the total pressure decrease and is explained by Raoult's equation ( $P_i = x_i \times P_{tot}$ ).

**Liquid-liquid equilibrium** As presented in autoclave results and recalled here in [Figure 4.38](#), a second liquid phase is formed during paraffins autoxidation for long reaction times. Analysis on those two phases are performed with the GC-MS to identify each phase composition. [Figure 4.39](#) and [Figure 4.40](#) respectively corresponds to the two phases analysis for n-C8 and MH. On both compounds tested, two types of products are identified where a first set of compounds is common to both phases whereas some of them appear only on the lower phase.

Focusing on common products in n-C8 results ([Figure 4.39](#)), the fraction of major oxidation products (n-octane, all C8-ketones and alcohols, C<sub>3-6</sub>-2-ketones) are mostly in the upper phase. On the contrary, acids fraction are mostly in the lower phase than in the upper one. Thanks to this, all C<sub>2-6</sub> acids signals are stronger and their identification is confirmed. Similar trends are observed on MH results in [Figure 4.40](#) for

both major products and acids. Focusing on new products apparition, a wide and co-eluted peak is observed at the end of the chromatogram ( $t > 80\text{min}$ ). According to the mass spectrum and the long retention time, it seems mostly oxygenated with high molecular weight. In contrary, water is identified at  $t = 14\text{min}$  on both lower phases. All those identifications are confirmed with the three IR spectrums presented in Figure 4.41. It presents the spectra of both lower phase, upper phase and water<sup>8</sup>. The three areas identified on the figure aim to prove the aqueous and organic nature of the two phases. The area 1 represents the water signal contribution on the lower phase spectrum only and its absence on the upper phase spectrum. The area 2 represents the absence of C-H bonds vibrations on the lower phase spectrum. The area 3 represents contribution of the C=O bands on the lower and the upper phase accounting respectively for acids (major products) and ketones (few % concentration)

Thus the product distribution difference seems due to products solubility in water  $\left(\frac{S_{acids_{water}}}{S_{acids_{HCs}}} > \frac{S_{ketones_{water}}}{S_{ketones_{HCs}}} > \frac{S_{fuel_{water}}}{S_{fuel_{HCs}}}\right)$ . Thus, it means that the total amount of acids quantified by the GC-FID is underestimated due to their re-concentration in lower phase. This products migration may significantly modify the kinetics of some reactions by either the elimination of the reactant/product or either concentrate some products and increase the reactivity. Thus, in the case of the esterification reaction (Figure 4.42) identified in n-C8 experiments, the existence of a "sub-media" concentrated in both acids and alcohols may highly promote ester formation.

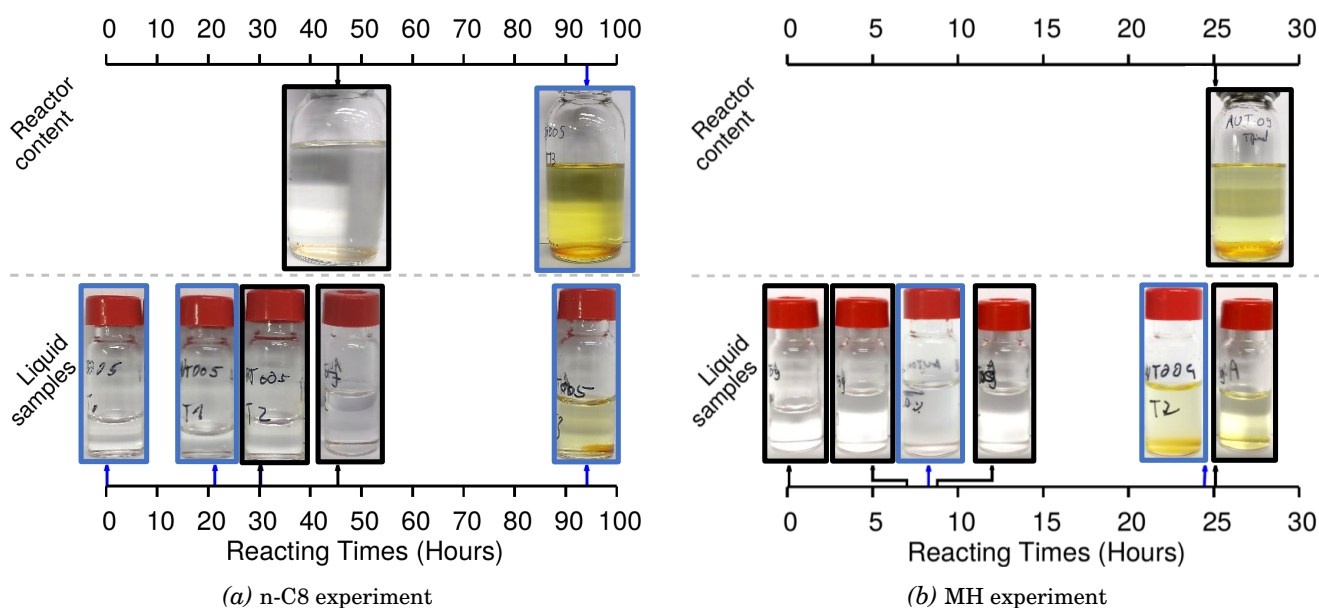


Figure 4.38: Pictures of samples and autoclave content for both n-C8 and MH

### 4.3.3 Modeling results discussions

As presented in Figure 4.20 and Figure 4.21, IPs evolution with both temperature, the chain length and the effects are qualitatively well reproduced with the presented mechanisms. This section aims to (1) assess the species profiles predictions with both n-C8 and MH results, (2) evaluate improvements possibilities based on the mechanisms analyses and (3) illustrate the impacts of the current liquid phase modeling limitations.

<sup>8</sup>Theoretical spectrum from NIST[120]

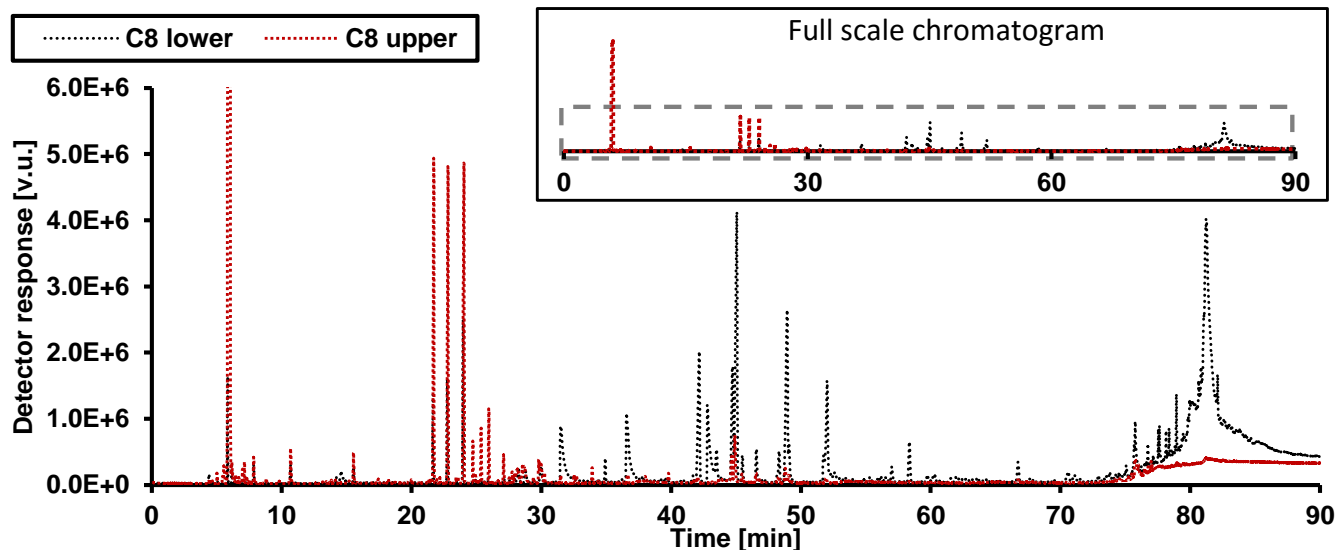


Figure 4.39: Two phases analysis on the most oxidized sample of n-C8 experiment

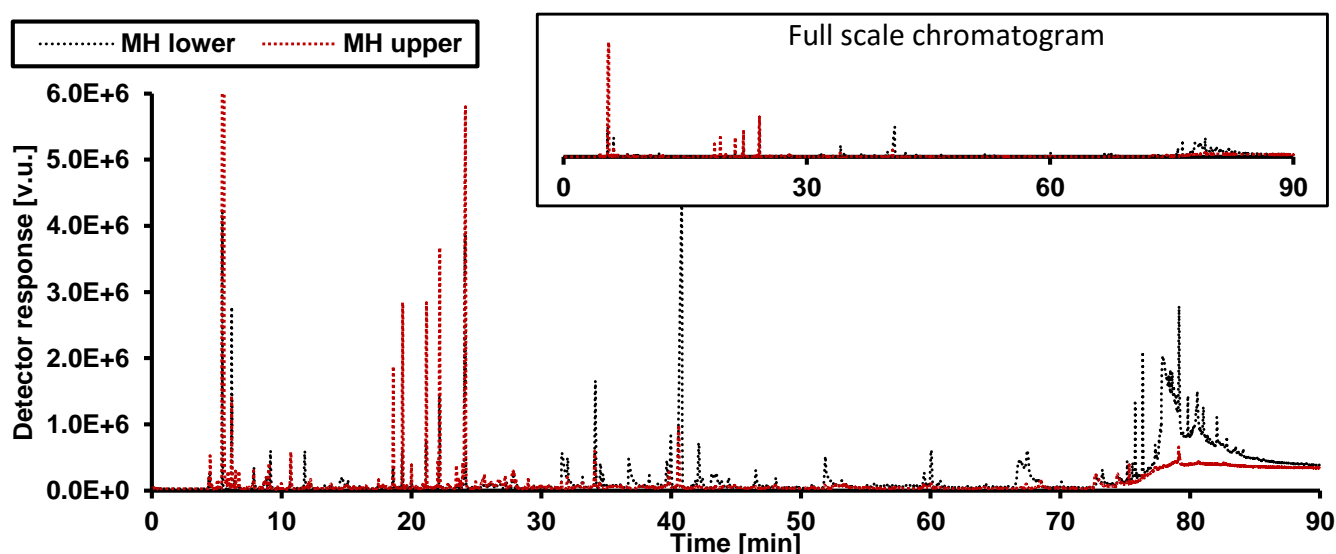


Figure 4.40: Two phases analysis on the most oxidized sample of MH experiment

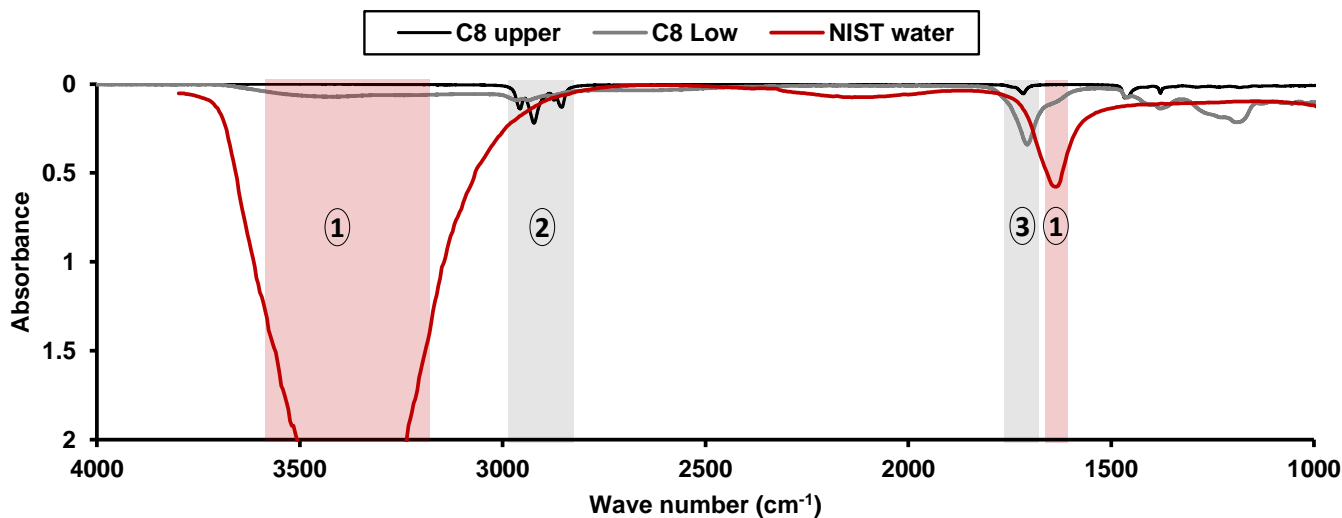
## Experimental data validation

Figure 4.43 and Figure 4.44 presents respectively n-C8 and MH species profiles agreement with experimental results obtained at 383K and 10 bars in autoclave experiments. As presented earlier in Figure 4.21, mechanisms require further work in this low temperature range to better represent the fuel consumption rate. Thus, the time evolution is normalised by 5 % fuel conversion delay (IP) to assess major and minor species production<sup>9</sup>. While ROOH are the major oxidation products, the weak O-O bonds makes their direct quantification impossible due to their thermal decomposition into the GC. Thus, in both figures (Figure 4.43 and Figure 4.44), their fraction was equally splitted between alcohols<sup>10</sup> and ketones<sup>11</sup>. Based on both ketones and alcohols formation during the autoxidation, this split value seems in agreement with literature [67] for a linear molecule. As no species profiles are available for branched molecules, this alcohol to ketone ratio would require further investigations according to the molecule structure. In the present

<sup>9</sup>Figures without the normalized axis are available in appendix, section 4.

<sup>10</sup>For n-C8: R[1-4]OOH and for MH: R[1-7]OOH

<sup>11</sup>For n-C8: R[2-4]OOH and for MH: R[3-6]OOH



**Figure 4.41:** Two phases analysis on the most oxidized sample of n-C8 experiment and theoretical IR spectrum of water from NIST. The area 1 represents the water signal contribution. The area 2 represents the C-H bonds vibrations. The area 3 represents contribution of the C=O bands.



**Figure 4.42:** Example of an esterification reaction [16]

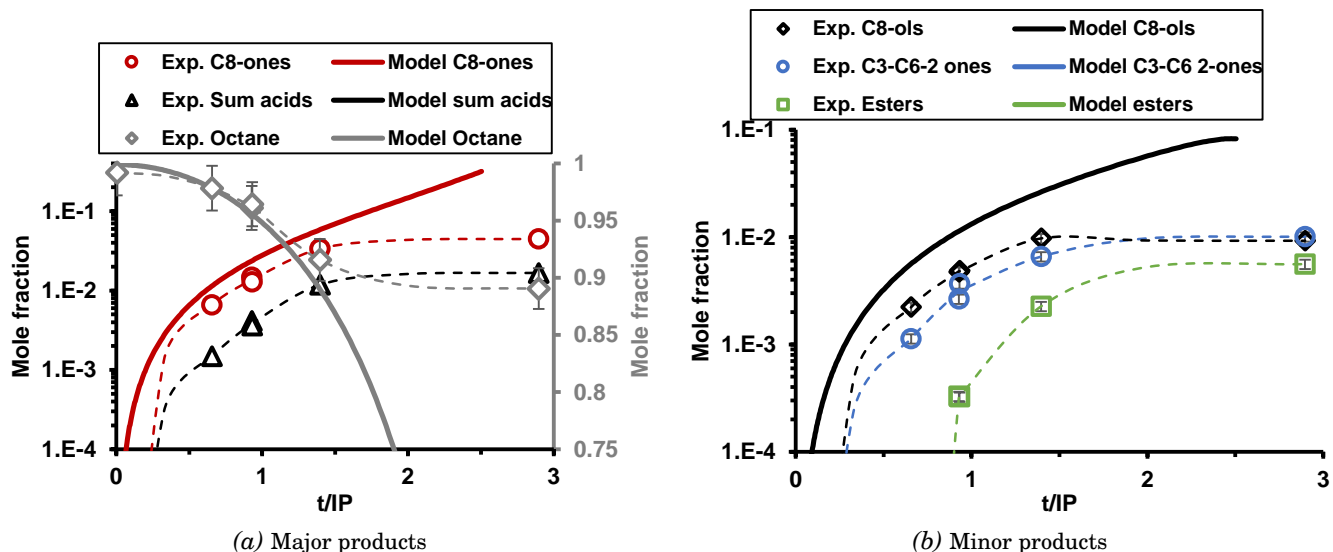
validation, those values are set for tertiary ROOH to form only alcohols ( $\frac{\text{ketones}}{\text{alcohols}} = 0$ ) while for primary and secondary ROOH values are set to form both ( $\frac{\text{aldehydes or ketones}}{\text{alcohols}} = 0.5$ ).

**Quantitatively** Thus, the time profile evolution of major species (Fuel, C8-ketones, C8-alcohols) is well reproduced by both models until reaching the experimental pressure plateau<sup>12</sup>. Then for longer reaction times, the oxidation rate is too fast and the fuel is fully consumed before reaching  $2 - 3 \times IP$ . As both mechanisms were generated with a 50% fuel conversion criteria and the solvent effect from the fuel is not relevant for such conversion, simulations are stopped when fuel fractions are below 0.1. This huge reactivity difference is due to an experimental oxygen limitation at the end of the experiment. On the other hand, some secondary oxidation products are either highly underestimated, like lower acids and ketones, or either not considered in the mechanisms, like esters formation. Focusing specifically on alcohols chemical family, their formation seems overestimated with both mechanisms and even more with the tertiary alcohol (MH). As ester formation consumes alcohols and acids, this overestimation might be corrected by including esters formation paths into the mechanisms. Antagonist trends are identified with both mechanisms on C8-ones formation, it is either slightly overestimated with n-C8 mechanisms and underestimated with MH mechanisms.

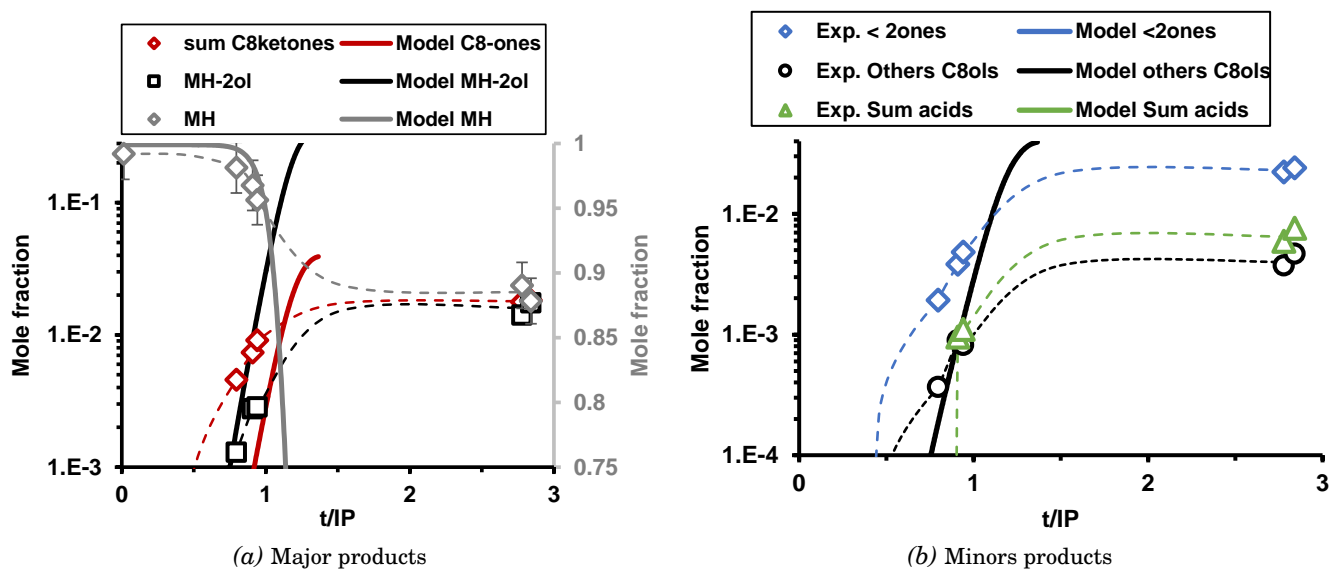
**Qualitatively** The selectivity within a chemical family is well reproduced by models, by disfavouring position 1 compared to other positions for both alcohols and ROOH. Based on either Benton's [127] results or Boss's results [122], none or a slight selectivity is presented for all chemical families from secondary carbons. Those observations are fairly well reproduced by both models where only a 10% variation is observed between all secondary ROOH fractions. In addition, for n-C8 model, chemical function in primary

<sup>12</sup>The pressure plateau is observable with the dashed lines on experimental data points.





**Figure 4.43:** Species profiles agreement between experimental results and model predictions on n-C8 at 383K and 10 bars.



**Figure 4.44:** Species profiles agreement between experimental results and model predictions on MH at 383K and 10 bars.

carbons are also well depreciated by the models ( $\times 15$  factor at  $t/ip = 2$ ) which is in agreement within Benton's proposition with a 10 factor. Similar observations are made omitting the secondary carbon nearby the tertiary carbon on MH.

In addition, significant water production is observed which is in agreement with literature data [122, 128, 56]. On both n-C8 and MH, water fractions are around several percent at  $2 \times IP$ . This is confirmed in our experimental second phase formation mostly composed of water. Except the absence of  $CO_2$  in MH models, most of gaseous products are qualitatively produced in both models including  $CO$ ,  $H_2$ ,  $C_1$  to  $C_4$  HCs and  $C_{1-2}$ -Aldehydes. Furthermore, in n-C8 models, the ratio  $\frac{CO_2}{water} \approx 0.01$  at  $\frac{t}{IP} = 2$  presents an interesting agreement with the experimental data from Boss et al. [122] ( $\approx \frac{3}{256} \approx 0.11$ ) and emphasize the consistency of the presented models.

## Mechanisms improvements

**Global reactivity** Results from [Figure 4.21](#), [Figure 4.7](#) and [section .4](#) illustrate that most of the presented mechanisms require reactivity adjustments on the low temperature range. Based on the analysis performed on both normal and iso-paraffins mechanisms, systematic key reactions paths were identified involving  $\text{ROO}^\circ$  and  $\text{HOOQOO}^\circ$  to consume fuel. Due to the absence of both (i) solvent effect on the current  $E_a$  and specificity between all  $\text{ROO}^\circ$  kinetic rates <sup>13</sup>, specific adjustments seem possible to correct those kinetic rates. In addition, extensive liquid phase ESCs may be proposed to confirm or correct the thermochemistry of major stable and radicals species involved in those reactions.

**Speciation** While majors species prediction presents a fair agreement in both [Figure 4.43](#) and [Figure 4.44](#), minor products formation is highly underestimated or not formed like for esters. The main expected pathway to form lighter products is from  $\alpha/\beta$ -scission and Korcek's reaction families and involve respectively carbonyles compounds and KHP. Further investigations on either the establishment of those kinetic rates or the formation of those products is required to improve the prediction of both lower acids and ketones formation. As presented in [Figure 4.16](#), esters formation is both octanols and lower acids production dependent. Which means, even with appropriate kinetic rates for ester formation [120], acids formation has to be corrected first.

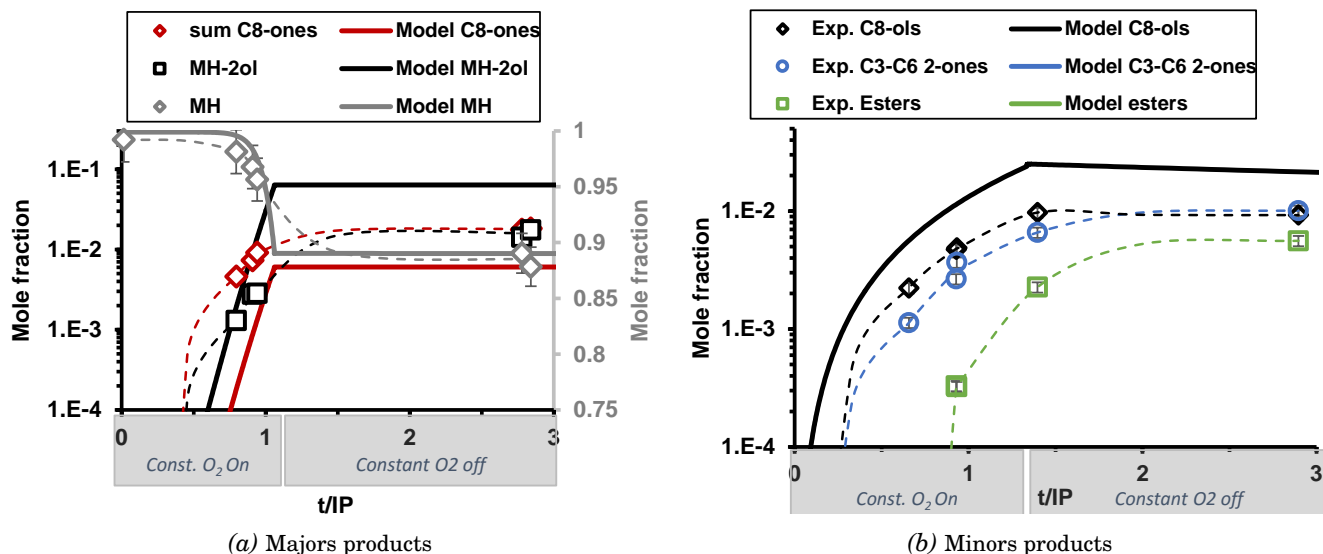
## Modeling limitation

This section aims at presenting the modeling limitations of our current homogeneous liquid phase reactor model and how they can impact the oxidation kinetics. The current reactor model represents only the homogeneous liquid phase part of the system omitting the gas phase. This modeling do not take into account (i) gaseous oxygen diffusion into the liquid and (ii) products migration out of the system.

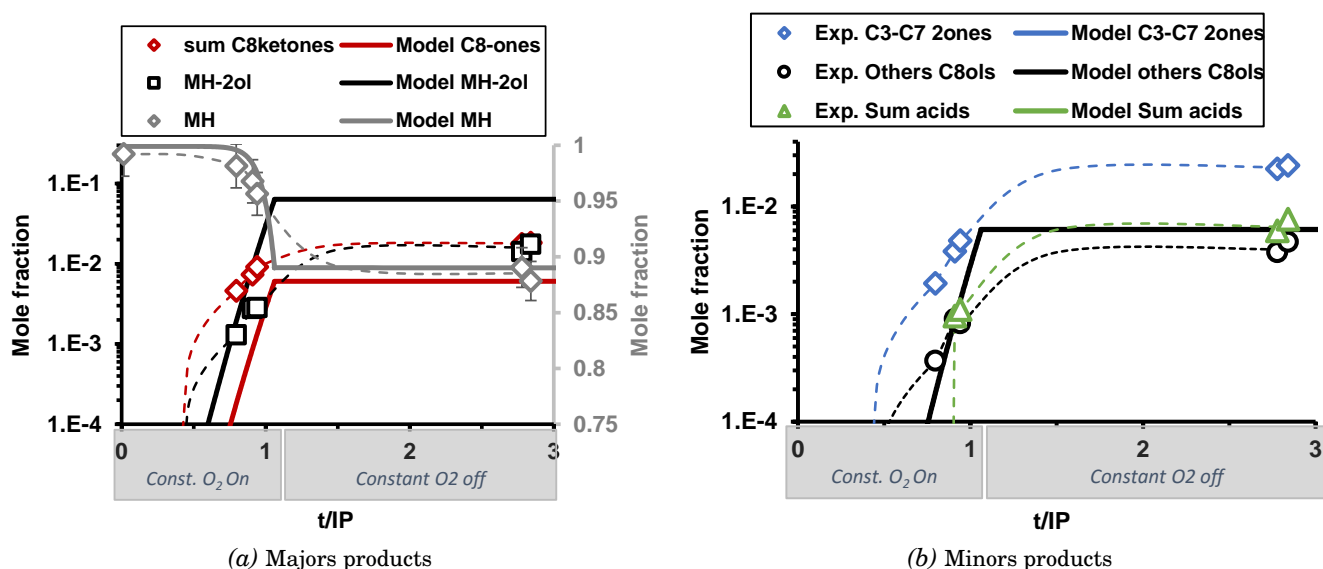
**Oxygen limitation into the liquid** Thus, the constant concentration option is required on  $\text{O}_2$  to properly model liquid phase autoxidation in a non diffusion limited system. However, this hypothesis is not true for long reaction time in the presented autoclave conditions ([Figure 4.43](#) and [Figure 4.44](#)) when oxygen is fully consumed. Thus, additional simulations were conducted without constant concentration option to better represent oxygen limitation into the liquid bulk. The coupling time is defined by the value of the fuel fraction plateau observed experimentally with the suggested curves. [Figure 4.45](#) and [Figure 4.46](#) are the sum of those two simulations and represent hypothetical modeling results with a reactor model including the oxygen limitation. As observed experimentally, mechanisms predictions are in agreement with species profiles and the overall reactivity is slowed down. This underlines the consistency of the mechanisms and highlights the requirement of a more precise reactor model with a well defined oxygen diffusion.

---

<sup>13</sup>Selectivity either between all primary, secondary and tertiary  $\text{RO}_2^\circ$  reaction but also between  $\text{RO}_2^\circ$  and  $\text{HO}_2\text{QO}_2^\circ$  reactions with fuel

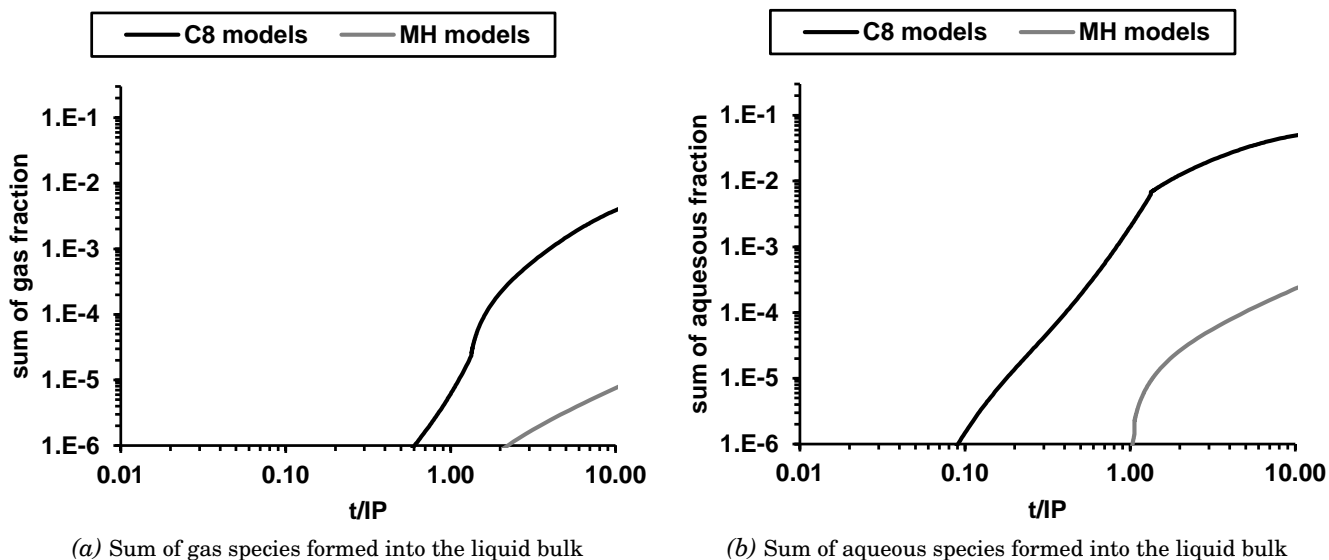


**Figure 4.45:** Species profiles agreement between experimental results and model predictions on n-C8 at 383K and 10 bars with an hypothetical new reactor model.



**Figure 4.46:** Species profiles agreement between experimental results and model predictions on MH at 383K and 10 bars with an hypothetical new reactor model.

**Species migration from liquid bulk** As presented in autoclave results, some products may migrate from the liquid bulk to either the gas phase (Fuel, light HCs) or to a second liquid phase mostly aqueous. This section aims to present the orders of magnitude of those potential products that should not remain in the liquid phase. The first set of compounds considers all gaseous products in their standard states like CO<sub>2</sub>, CO, H<sub>2</sub>, light aldehydes, light HCs. The second set of compounds considers all water, a 50 % fraction of all water soluble products identified in Figure 4.39 and Figure 4.40. The evolution of these two sets of compounds over reaction time is presented in Figure 4.47. Comparing the two evolutions, the sum of aqueous fractions is much greater than the sum of gaseous products. A priori, the migration of the aqueous products will affect more the kinetics than the gaseous products migration. In addition, due to their small fractions, around 1ppm at  $\frac{IP}{10}$  and 1% at IP, their migration should not affect significantly the individual rates. While, specific reactions at chemical equilibrium may still be significantly impacted by reactants or products removal. Thus, first developments on the new reactor model should be focused on the second liquid phase formation to observe strongest effects on the kinetics.



**Figure 4.47:** Representation of the sum of products remained in the liquid phase from both n-C8 and MH models predictions at 383 K.

## 4.4 Conclusion

In this chapter, new experimental data were obtained in order to assess the modeling methodology consistency. As presented in the Material and Method chapter, a complementary approach provides both macroscopic and detailed data, suitable for the comprehension of the autoxidation processes with both normal and iso-paraffins systems.

Considering, all hypotheses of our current modeling, a satisfactory agreement of the predicted IP ( $RE < 3$ ) is observed for high temperature range ( $T > 403K$ ) for most of the paraffins mechanisms (all except n-C8<sup>14</sup>). In addition, species profiles predictions of major species is in agreements with the present experimental data with a consistent branching ratios between isomers. In contrary, minor species formation are highly underestimated either due to either underestimated kinetic rates of Korcek's reactions or due an underestimated formation of Korcek's reactants.

In addition, the detailed results from autoclave experiments evidenced critical multiphases equilibria: Gas-organic bulk and gas-aqueous bulk. Based on the current experimental observations, no deposits are formed before the apparition of this second liquid phase. In order to model the the deposit formation from bulk autoxidation, a new reactor model considering all those equilibria is required. According to the modeling results, the second liquid phase formation seems to include the major part of "moveable" products.

While the generated models does not quantitatively reproduce all experimental conditions, they qualitatively reproduce the overall phenomenology of (i) the temperature, (ii) the chain length and (iii) the branching effect of paraffins autoxidation. Although further mechanisms development is still required, present results underline the consistency of our current modeling methodology and the requirement of a liquid phase reactor to model LPA.

<sup>14</sup>RE of n-C8 mechanism is close to 4.2 at 403K and then decrease below 1 at 433K



## Chapter 5

# General conclusions

Liquid phase stability is a major concern in the transportation and the energy field. A perfect illustration is fuels, lubricants and additives which have to be stable from the refinery to their application (engine, combustors). The fuel and transport field is constantly changing due to recent environmental considerations with the reduction of greenhouse gas emissions and the improvement of local air purity. Those considerations impact fuel compositions with the increasing use of biofuels (E10, B7). In addition, technology improvements on both fuel and combustion lead to a diversification of additive packages whose chemistry and interaction with conventional fuel fractions is poorly assessed.

In a first part, main concepts governing LPA were briefly presented including the state of the art from both experimental and modeling point of view. Thanks to literature review, key parameters influencing LPA were put in evidence: chemical families reactivity, oxygen content and its availability in the liquid phase, trace species such as hydroperoxides, metals and antioxidants. In addition to the impact of solvent effect on thermochemistry and kinetics, important gas-phase interaction was evidenced. Those parameters are critical and must be known accurately for quantitative modeling. From literature, a brief introduction of deposition processes has demonstrated that deposits have specific chemical composition which is induced by deposit precursors composition. Thus, it is of major concern to get detailed modeling of those precursors formation to model deposition processes. As reminded in chapter 2, the present work investigates the deposit precursors based on a bulk autoxidation process. While LPA modeling was previously performed using global mechanisms with lumped species, a more detailed approach seems required to obtain a meaningful representation of the deposit precursors formation.

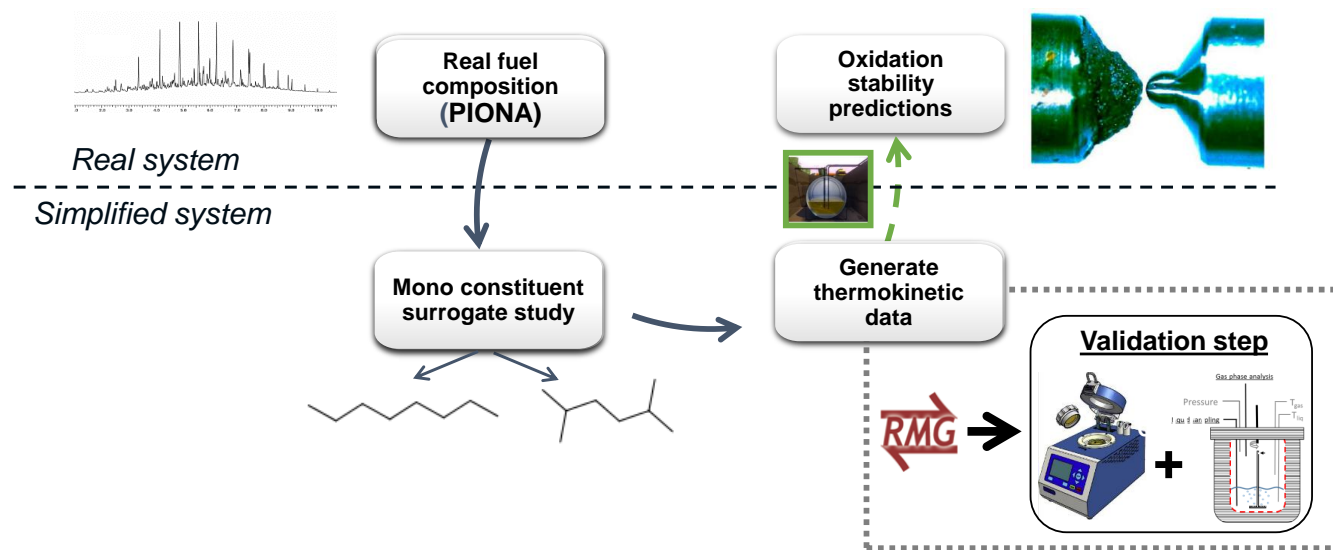
A second part presents the overall methodology developed to study LPA. Experimentally, a complementary approach provides both macroscopic reactivity criteria with the PetroOxy (IP) and detailed species profiles on both gas and liquid phases with autoclave. Numerically, a multi-scale approach is proposed in order to obtain relevant liquid phase kinetic models for a specific fuel surrogates. This multi-scale approach is based on RMG, to generate detailed kinetic mechanisms with structural isomers distinction. An optional step, not performed within the framework of this thesis, involves ESC to confirm and correct specific blocks of the generated mechanisms.

Finally, both experimental and numerical methodologies were validated on two chemical systems relevant to real fuel composition. Thus, the reactivity of both n-paraffins from C<sub>8</sub> to C<sub>16</sub> and several C<sub>8</sub> iso-paraffins were investigated over a wide temperature range (373-433 K) in the PetroOxy device first. Then, n-C8 and MH respectively representative of normal and iso-paraffins were studied in autoclave experiment at 383 K. Structure-reactivity relations were put in evidence thanks to the preliminary study: the IP decreases with an increasing (i) number of carbons inside n-paraffins up to C<sub>12</sub>, (ii) temperature, (iii) number of tertiary

carbons for molecule at constant carbons number. Based on TMP results, a specific reactivity of quaternary carbon containing molecules was evidenced. This reactivity change seems correlated to the modification of the ratio ( $\frac{carbon_{secondary,tertiary}}{carbon_{primary}}$ ). Based on the presented experimental data, an empirical model described in section 4.3.1, was established combining both normal and iso paraffins results on a large temperature range (373-433 K). This empirical model presents satisfactory agreement (RE < 60%) with all presented data and represents a promising tool for the prediction of structure-stability relations.

Numerically, the first step of the multi-scale methodology was investigated on both normal and iso-paraffins. Detailed liquid phase mechanisms were presented for all molecules tested up to C<sub>14</sub>. The presented models well predict IP (RE < 300%) for the high temperature reactivity (T > 403 K). While those mechanisms are quantitatively perfectible, they qualitatively reproduces the overall phenomenology of (i) the temperature, (ii) the chain length and (iii) the branching effect of paraffins autoxidation. As identified from RoP analyses on all mechanisms, the reactivity of alkanes is mostly due to the ROO° and HOOQOO° paths over the 373-473 K temperature range. These similarities are in agreement with the detailed identification of oxidation products performed on both chemical families with autoclave experiments. In addition, autoclave experiments evidenced critical multiphases equilibria between gas-liquid and a second liquid phase formation mostly aqueous. Based on the current experimental observations, no deposits are formed before the apparition of this second liquid phase. In order to model the deposit formation from bulk autoxidation, a new reactor model considering all those equilibria is required (liquid-liquid, gas-liquid and liquid-solid).

As presented in Figure 5.1 with normal and iso-paraffins, the experimental and modeling methodology developed within the framework of this thesis is the first step to the comprehension of LPA processes. Applying the same methodology to new chemical systems will *in fine* enable to reduce the gap of knowledge between surrogates autoxidation and real fuels autoxidation.



**Figure 5.1:** Schematic presenting the overall methodology used here. The framed block and arrow in green aim to emphasize the current modeling limitation pointed during this work.

# Chapter 6

## Perspectives

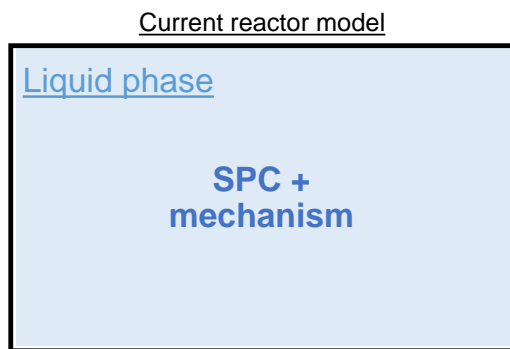
### 6.1 New chemical systems

Real fuel composition is a complex blend of compounds according to macroscopic properties. As the kinetic study of autoxidation of such blend is not realistic, the comprehension of fuel autoxidation remains on the study of individual chemical families. Thus, the study of new chemical systems could be divided into three steps. A first step could extend and refine both oxidation schemes and structure-stability relations identified for paraffins. In addition, the position of the ramification could also be investigated using topological index descriptors (e.g Wiegner index or the Randic index). In addition, the branching effect identified for C<sub>8</sub> iso-alkanes must be confirmed for heavier systems including (i) an increasing number of tertiary carbons, (ii) an increasing number of quaternary carbons and (iii) a mix of both. Using a similar methodology, a second step could consist in the study of new chemical systems according to PIONA composition (olefins, naphthenes and aromatics). Once this full comprehension of individual constituents is performed, a third step corresponding to the multi-surrogate investigation could start. This last step aims to highlight promoting and inhibitors effect of specific chemical families blends, as identified from recent work of Ben Amara et al. [40].

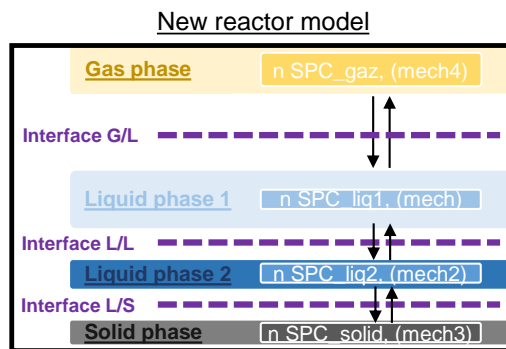
### 6.2 New reactor model

As expressed in chapter 2 and from section 4.3, LPA requires a specific multiphase reactor to model interface exchanges occurring during autoxidation. The improvement of the current liquid phase reactor model, illustrated in Figure 6.1, would consist in defining four homogeneous reactors to consider the coexistence of gas, liquid and solid phases as illustrated in Figure 6.2. As presented in Figure 6.2, depending on both the application and the complexity of the system to model, each phase could consider its proper kinetic model.



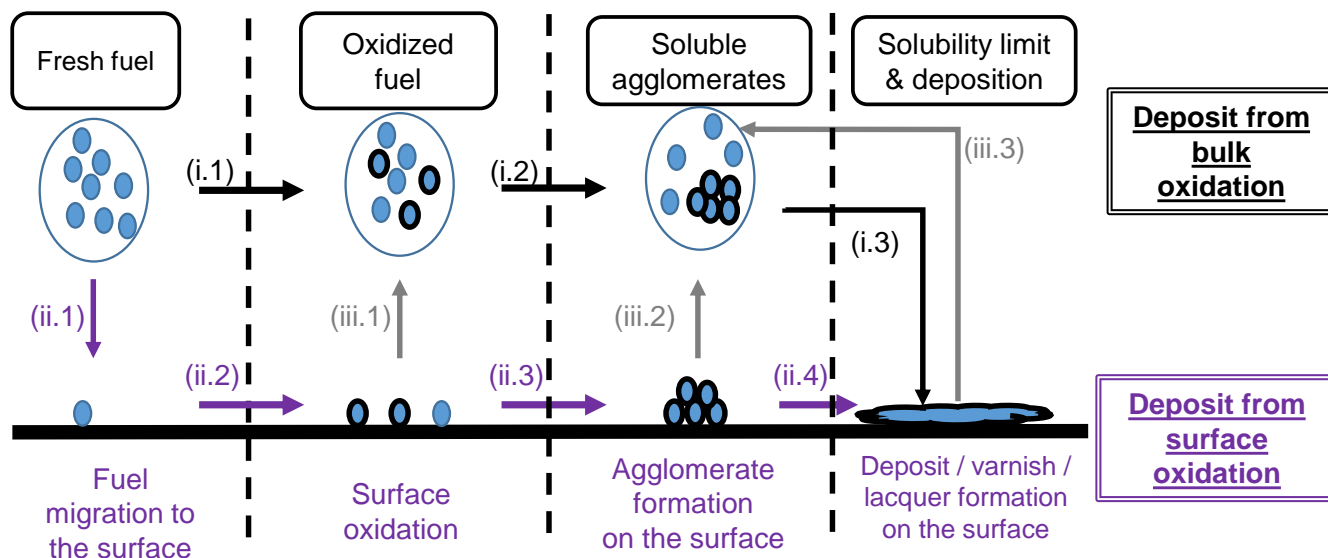


**Figure 6.1:** Current liquid phase reactor model representing an homogeneous liquid phase with a set of species (SPC) and its associated mechanism.



**Figure 6.2:** Hypothetical new reactor model with four distinct phases: *gas*, *liquid1*, *liquid2* and *solid*. Every phase has its own set of species with its own mechanism. Three distinct interfaces are represented in purple to represent the species transport from one phase to another.

A first application of such reactor is bulk autoxidation (as discussed in section 4.3 to better represent the species migration. As discussed, in addition to the concentration change which may affect species rates, new reaction kinetics may control the reactivity in such water based media (like ionic reactions). A second major application, also related to the liquid autoxidation, is to consider the heterogeneous catalysis. As presented in Figure 6.3, both bulk autoxidation and heterogeneous autoxidation are competing paths to deposits formation. The modeling of both autoxidation would greatly increase the comprehension of their relative contributions to form deposits. A third application is for storage safety, as observed in the present study, some light HCs may desorb from the liquid phase and concentrate over time in the gas phase. Thus, the prediction of an explosive phase formation would be useful for storage safety applications.



**Figure 6.3:** Global process for the deposit formation. The bulk reactivity path (i) is represented with black arrows. The catalytic oxidation path (ii) is represented with purple arrows. The solubility of deposit into fresh solvent (iii) is represented with grey arrows.

## 6.3 RMG upgrades

### 6.3.1 Solvent database upgrade

One current limitation of RMG, is the limited number of solvents available to calculate the solvent effect corrections. Beside solvent effects, solvent properties are also of interest<sup>1</sup>. However, the evolution of the mixture composition during autoxidation implies to reconsider the solvation corrections for high fuel conversion values (due to high conversion of the initial fuel sample, formation of wide variety of carbonyl compounds and water). Currently, solvation corrections are not taking into account this composition change and is still using the initial fuel for the solvation correction. For the modeling of systems at low conversion, this assumption is realistic. As the solvent database contains only 26 solvents, an update is required before implementing reacting system calculations

### 6.3.2 Solvent effects on the thermokinetics

In addition to the database upgrade, current RMG calculations are based on some assumptions like the linear temperature dependence on the free energy of solvation (pointed out in Jalan's work). In addition, new developments are in progress in RMG codes to better represent solvation in autoxidation conditions (highly concentrated system and not in SATP). To complete the thermochemistry improvements, new studies [129] are currently in progress to consider on the fly solvent effect correction on the  $E_a$ . Recent discussions with RMG members indicated that both corrections (cage diffusion effect and  $E_a$  corrections) will be directly integrated into the rate constant in the next developments. Thus, the consistency of the generated mechanisms will be improved.

---

<sup>1</sup>Solvent properties do not evolve during the oxidation and is fixed by the input file.



# Bibliography

- [1] L. Russier, "Documents from ifp training course "moteurs - carburants". originally from université de berne."
- [2] L. Russier, "Documents from ifp training course "moteurs - carburants". originally from "air parif".
- [3] K. Bacha, Etude de l'interaction entre le carburant diesel et les composants du système d'injection diesel. PhD thesis, Université Haute-Alsace, IS2M, 2016.
- [4] T. R. Sem, "Investigation of injector tip deposits on transport refrigeration units running on biodiesel fuel," tech. rep., SAE Technical Paper, 2004.
- [5] A. Nicolle, S. Cagnina, and T. de Bruin, "First-principle based modeling of urea decomposition kinetics in aqueous solutions," Chemical Physics Letters, pp. –, 2016.
- [6] W. M. Zongo, Etudes de l'oxydation des huiles de poisson microencapsulées par DSC sous pression. PhD thesis, HES-SO Valais, 2009.
- [7] B. M. Trost and I. Fleming, Comprehensive Organic Synthesis, Selectivity, Strategy and Efficiency in Modern Organic Chemistry, Volume7, ch. 5.1: The Baeyer-villiger Reaction, pp. 671–689. Elsevier, 1991.
- [8] E. T. Denisov and I. B. Afanas' ev, Oxidation and antioxidants in organic chemistry and biology. CRC press, 2005.
- [9] C. Marteau, F. Ruyffelaere, J.-M. Aubry, C. Penverne, D. Favier, and V. Nardello-Rataj, "Oxidative degradation of fragrant aldehydes. autoxidation by molecular oxygen," Tetrahedron, vol. 69, no. 10, pp. 2268–2275, 2013.
- [10] B. Beaver, L. Gao, C. Burgess-Clifford, and M. Sobkowiak, "On the mechanisms of formation of thermal oxidative deposits in jet fuels. are unified mechanisms possible for both storage and thermal oxidative deposit formation for middle distillate fuels?," Energy & Fuels, vol. 19, no. 4, pp. 1574–1579, 2005.
- [11] E. Oganeseva, E. Bordubanova, G. Kuz'mina, V. Bakunin, and O. Parenago, "Influence of the structure of higher paraffin hydrocarbons and their derivatives on the mechanism of high-temperature liquid-phase oxidation," Petroleum Chemistry, vol. 49, no. 4, pp. 311–316, 2009.
- [12] A. Jalan, R. W. Ashcraft, R. H. West, and W. H. Green, "Predicting solvation energies for kinetic modeling," Annual Reports Section "C"(Physical Chemistry), vol. 106, pp. 211–258, 2010.
- [13] T. Lu and C. K. Law, "Toward accommodating realistic fuel chemistry in large-scale computations," Progress in Energy and Combustion Science, vol. 35, no. 2, pp. 192 – 215, 2009.
- [14] Pr. Green's group website: [cheme.scripts.mit.edu/green-group/rmg](http://cheme.scripts.mit.edu/green-group/rmg).
- [15] A. Jalan, I. M. Alecu, R. Meana-Pañeda, J. Aguilera-Iparraguirre, K. R. Yang, S. S. Merchant, D. G. Truhlar, and W. H. Green, "New pathways for formation of acids and carbonyl products in low-temperature oxidation: the korcek decomposition of  $\gamma$ -keto hydroperoxides," Journal of the American Chemical Society, vol. 135, no. 30, pp. 11100–11114, 2013.

- [16] M. Aslam, G. P. Torrence, and E. G. Zey, "Esterification," Kirk-Othmer Encyclopedia of Chemical Technology, 2000.
- [17] S. E. Wheeler, K. N. Houk, P. v. R. Schleyer, and W. D. Allen, "A hierarchy of homodesmotic reactions for thermochemistry," Journal of the American Chemical Society, vol. 131, no. 7, pp. 2547–2560, 2009.
- [18] Z. Yang, B. P. Hollebone, Z. Wang, C. Yang, C. Brown, and M. Landriault, "Storage stability of commercially available biodiesels and their blends under different storage conditions," Fuel, vol. 115, pp. 366–377, 2014.
- [19] G. A. Olah et al., Hydrocarbon chemistry. John Wiley & Sons, 2003.
- [20] S. Matsumoto, K. Date, T. Taguchi, and O. E. Herrmann, "The new denso common rail diesel solenoid injector," MTZ worldwide, vol. 74, no. 2, pp. 44–48, 2013.
- [21] D. Ueda, H. Tanada, A. Utsunomiya, J. Kawamura, and J. Weber, "4th generation diesel piezo injector (realizing enhanced high response injector)," tech. rep., SAE Technical Paper, 2016.
- [22] T. Dounghthip, J. Ervin, S. Zabarnick, and T. Williams, "Simulation of the effect of metal-surface catalysis on the thermal oxidation of jet fuel," Energy & fuels, vol. 18, no. 2, pp. 425–437, 2004.
- [23] J. Ervin and S. Zabarnick, "Computational fluid dynamics simulations of jet fuel oxidation incorporating pseudo-detailed chemical kinetics," Energy & fuels, vol. 12, no. 2, pp. 344–352, 1998.
- [24] L. M. Balster, E. Corporan, M. J. DeWitt, J. T. Edwards, J. S. Ervin, J. L. Graham, S.-Y. Lee, S. Pal, D. K. Phelps, L. R. Rudnick, et al., "Development of an advanced, thermally stable, coal-based jet fuel," Fuel Processing Technology, vol. 89, no. 4, pp. 364–378, 2008.
- [25] L. M. Balster, S. Zabarnick, R. C. Striebich, L. M. Shafer, and Z. J. West, "Analysis of polar species in jet fuel and determination of their role in autoxidative deposit formation," Energy & fuels, vol. 20, no. 6, pp. 2564–2571, 2006.
- [26] N. J. Kuprowicz, S. Zabarnick, Z. J. West, and J. S. Ervin, "Use of Measured Species Class Concentrations with Chemical Kinetic Modeling for the Prediction of Autoxidation and Deposition of Jet Fuels," Energy & Fuels, vol. 21, no. 2, pp. 530–544, 2007.
- [27] S. Jain and M. Sharma, "Stability of biodiesel and its blends: a review," Renewable and Sustainable Energy Reviews, vol. 14, no. 2, pp. 667–678, 2010.
- [28] B. D. Batts and A. Z. Fathoni, "A literature review on fuel stability studies with particular emphasis on diesel oil," Energy & Fuels, vol. 5, no. 1, pp. 2–21, 1991.
- [29] D. E. Van Sickle, T. Mill, F. R. Mayo, H. Richardson, and C. W. Gould, "Intramolecular propagation in the oxidation of n-alkanes. autoxidation of n-pentane and n-octane," The Journal of Organic Chemistry, vol. 38, no. 26, pp. 4435–4440, 1973.
- [30] F. Garcia-Ochoa, A. Romero, and J. Querol, "Modeling of the thermal n-octane oxidation in the liquid phase," Industrial & engineering chemistry research, vol. 28, no. 1, pp. 43–48, 1989.
- [31] R. Jensen, S. Korcek, L. Mahoney, and M. Zinbo, "Liquid-phase autoxidation of organic compounds at elevated temperatures. 1. the stirred flow reactor technique and analysis of primary products from n-hexadecane autoxidation at 120-180. degree. c," Journal of the American Chemical Society, vol. 101, no. 25, pp. 7574–7584, 1979.
- [32] F. Camacho Rubio, F. Diaz-Rodriguez, and J. Fernandez-Gonzalez, "Oxidacion de n-parafinas in fase liquida," Anales de Quimica, vol. 76, p. 375, 1980.
- [33] S. Gernigon, Etude de la stabilité à l'oxydation des carburants liquides hydrocarbonés: Influence et comportement des antioxydants. PhD thesis, Paris 7, 2010.

- [34] N. Blin-Simiand, F. Jorand, K. Keller, M. Fiderer, and K. Sahetchian, "Keto hydroperoxides and ignition delay in internal combustion engines," Combustion and Flame, vol. 112, no. 1-2, pp. 278–282, 1998.
- [35] S. Blaine and P. E. Savage, "Reaction pathways in lubricant degradation. 2. n-Hexadecane autoxidation," Industrial & engineering chemistry research, vol. 30, no. 9, pp. 2185–2191, 1991.
- [36] R. Thompson, L. Druge, and J. Chenicek, "Stability of fuel oils in storage: Effect of sulfur compounds," Industrial & Engineering Chemistry, vol. 41, no. 12, pp. 2715–2721, 1949.
- [37] S. Zabarnick, "Studies of jet fuel thermal stability and oxidation using a quartz crystal microbalance and pressure measurements," Industrial & engineering chemistry research, vol. 33, no. 5, pp. 1348–1354, 1994.
- [38] S. Zabarnick, "Chemical kinetic modeling of jet fuel autoxidation and antioxidant chemistry," Industrial & engineering chemistry research, vol. 32, no. 6, pp. 1012–1017, 1993.
- [39] R. I. Masel, "Chemical Kinetics and Catalysis (Masel, Richard I.)," J. Chem. Educ., vol. 79, pp. 313–, Mar. 2002.
- [40] A. Ben Amara, S. Kaoubi, and L. Starck, "Toward an optimal formulation of alternative jet fuels: Enhanced oxidation and thermal stability by the addition of cyclic molecules," Fuel, 2016.
- [41] B. N. Sundaram, The effects of oxygen on synthetic crude oil fouling. PhD thesis, University of British Columbia, 1998.
- [42] J. Shepherd, C. Nuyt, J. Lee, and J. Woodrow, "Flash point and chemical composition of aviation kerosene (jet a)," 2000.
- [43] F. Adam, F. Bertoncini, V. Coupard, N. Charon, D. Thiébaud, D. Espinat, and M.-C. Hennion, "Using comprehensive two-dimensional gas chromatography for the analysis of oxygenates in middle distillates: I. determination of the nature of biodiesels blend in diesel fuel," Journal of Chromatography A, vol. 1186, no. 1, pp. 236–244, 2008.
- [44] M. Sicard, J. Boulicault, K. Coulon, C. Thomasset, J. Ancelle, B. Raepsaet, and F. Ser, "Oxidation stability of jet fuel model molecules evaluated by rapid small scale oxidation tests.," in The 13th International Conference on Stability, Handling and Use of Liquid Fuels 2013 IASH 2013, 2013.
- [45] A. Ben Amara, B. Lecointe, N. Jeuland, T. Takahashi, Y. Iida, H. Hashimoto, and J. Bouilly, "Experimental study of the impact of diesel/biodiesel blends oxidation on the fuel injection system," tech. rep., SAE Technical Paper, 2014.
- [46] A. Ben Amara, A. Nicolle, M. Alves-Fortunato, and N. Jeuland, "Toward predictive modeling of petroleum and biobased fuel stability: Kinetics of methyl oleate/n-dodecane autoxidation," Energy & Fuels, vol. 27, no. 10, pp. 6125–6133, 2013.
- [47] E. G. Jones and L. M. Balster, "Autoxidation of dilute jet-fuel blends," Energy & Fuels, vol. 13, no. 4, pp. 796–802, 1999.
- [48] L. J. Spadaccini, R. A. Meinzer, and H. Huang, "For removing dissolved oxygen from a liquid fuel in the fuel system of an energy conversion device.," Nov. 13 2001. US Patent 6,315,815.
- [49] S. W. Benson and P. S. Nangia, "Some unresolved problems in oxidation and combustion," Accounts of Chemical Research, vol. 12, no. 7, pp. 223–228, 1979.
- [50] N. Semenov, Some Problems of Chemical Kinetics. Vol. 1 & 2. Pergamon, 1958.
- [51] E. G. Jones, L. M. Balster, and W. J. Balster, "Autoxidation of aviation fuels in heated tubes: Surface effects," Energy & fuels, vol. 10, no. 3, pp. 831–836, 1996.

- [52] S. Zabarnick, "Pseudo-detailed chemical kinetic modeling of antioxidant chemistry for jet fuel applications," Energy & Fuels, vol. 12, no. 3, pp. 547–553, 1998.
- [53] E. G. Jones and L. M. Balster, "Interaction of a synthetic hindered-phenol with natural fuel antioxidants in the autoxidation of paraffins," Energy & fuels, vol. 14, no. 3, pp. 640–645, 2000.
- [54] I. Oil, "Thermal/oxidation storage stability of bio-diesel fuels," 2009.
- [55] B. Grinstead and S. Zabarnick, "Studies of jet fuel thermal stability, oxidation, and additives using an isothermal oxidation apparatus equipped with an oxygen sensor," Energy & Fuels, vol. 13, no. 3, pp. 756–760, 1999.
- [56] L. D. T. Câmara, R. S. Monteiro, A. M. Constantino, D. A. Aranda, and J. C. Afonso, "Oxidative cracking of linear hydrocarbons at low temperatures," Chemical Engineering Communications, vol. 198, no. 3, pp. 416–424, 2010.
- [57] M. Skolniak, P. Bukrejewski, and J. Frydrych, "Analysis of changes in the properties of selected chemical compounds and motor fuels taking place during oxidation processes," Intech, 2015.
- [58] J. Pfaendtner and L. J. Broadbelt, "Mechanistic Modeling of Lubricant Degradation. 2. The Autoxidation of Decane and Octane," Industrial & Engineering Chemistry Research, vol. 47, pp. 2897–2904, Mar. 2008.
- [59] J. Pfaendtner and L. J. Broadbelt, "Mechanistic Modeling of Lubricant Degradation. 1. Structure-Reactivity Relationships for Free-Radical Oxidation," Industrial & Engineering Chemistry Research, vol. 47, pp. 2886–2896, Mar. 2008.
- [60] J. Pfaendtner and L. J. Broadbelt, "Elucidation of structure–reactivity relationships in hindered phenols via quantum chemistry and transition state theory," Chemical Engineering Science, vol. 62, no. 18, pp. 5232–5239, 2007.
- [61] N. Semenov, "Z. physik, 48, 571 (1928)," Z. phys. Chem.,(B), vol. 11, p. 464, 1930.
- [62] J. D. Savee, E. Papajak, B. Rotavera, H. Huang, A. J. Eskola, O. Welz, L. Sheps, C. A. Taatjes, J. Zádor, and D. L. Osborn, "Direct observation and kinetics of a hydroperoxyalkyl radical (qooh)," Science, vol. 347, no. 6222, pp. 643–646, 2015.
- [63] K. T. Reddy, N. P. Cernansky, and R. S. Cohen, "Modified reaction mechanism of aerated n-dodecane liquid flowing over heated metal tubes," Energy & Fuels, vol. 2, no. 2, pp. 205–213, 1988.
- [64] S. Korcek, J. Chenier, J. Howard, and K. Ingold, "Absolute rate constants for hydrocarbon autoxidation. xxi. activation energies for propagation and the correlation of propagation rate constants with carbon-hydrogen bond strengths," Canadian Journal of Chemistry, vol. 50, no. 14, pp. 2285–2297, 1972.
- [65] A. Van Tiggelen, Oxydations et combustions, vol. 2. Editions Technip, 1968.
- [66] J. Bolland, "Kinetic studies in the chemistry of rubber and related materials. i. the thermal oxidation of ethyl linoleate," Proceedings of the Royal Society of London. Series A. Mathematical and Physical Sciences, vol. 186, no. 1005, pp. 218–236, 1946.
- [67] C. Cullis, M. Hirschler, and R. Rogers, "The oxidation of decane in the liquid and gaseous phases," Proceedings of the Royal Society of London. A. Mathematical and Physical Sciences, vol. 375, no. 1763, pp. 543–563, 1981.
- [68] J. Zádor, C. A. Taatjes, and R. X. Fernandes, "Kinetics of elementary reactions in low-temperature autoignition chemistry," Progress in energy and combustion science, vol. 37, no. 4, pp. 371–421, 2011.
- [69] A. Jalan, R. H. West, and W. H. Green, "An Extensible Framework for Capturing Solvent Effects in Computer Generated Kinetic Models," J. Phys. Chem. B, vol. 117, pp. 2955–2970, Jan. 2013.

- [70] R. Larsen, R. Thorpe, and F. Armfield, "Oxidation characteristics of pure hydrocarbons," Industrial & Engineering Chemistry, vol. 34, no. 2, pp. 183–193, 1942.
- [71] B. Boss and R. Hazlett, "n-dodecane oxidation-elucidation by internal reference techniques," Product R&D, vol. 14, no. 2, pp. 135–138, 1975.
- [72] E. Booser and M. Fenske, "Liquid phase hydrocarbon oxidation," Industrial & Engineering Chemistry, vol. 44, no. 8, pp. 1850–1856, 1952.
- [73] A. M. Syroezhko, V. M. Potekhin, and V. A. Proskuryakov, "Composition of the products of the liquid phase oxidation of n-decane," Zhurnal Prikladnoi Khimii, vol. 43, pp. 1791 – 1798, 1970.
- [74] A. Watkinson and D. Wilson, "Chemical reaction fouling: A review," EXPERIMENTAL THERMAL AND FLUID SCIENCE, vol. 14, pp. 361–374, MAY 1997.
- [75] P. Lacey, S. Gail, J. M. Kientz, N. Milovanovic, and C. Gris, "Internal fuel injector deposits," SAE International Journal of Fuels and Lubricants, vol. 5, no. 1, pp. 132–145, 2012.
- [76] O. K. Bhan, D. W. Brinkman, J. B. Green, and B. Carley, "Storage stability of marine diesel fuels," Fuel, vol. 66, no. 9, pp. 1200 – 1214, 1987.
- [77] A. Jalan, Predictive kinetic modeling of low-temperature hydrocarbon oxidation. PhD thesis, Massachusetts Institute of Technology, 2014.
- [78] O. Parenago, G. Kuz'mina, V. Bakunin, and E. Y. Oganeseva, "Nanosized structures in high-temperature oxidation of lubricating oil hydrocarbons," Russian Journal of General Chemistry, vol. 79, no. 6, pp. 1390–1399, 2009.
- [79] O. Kasaikina, Z. Kartasheva, and L. Pisarenko, "Effect of surfactants on liquid-phase oxidation of hydrocarbons and lipids," Russian Journal of General Chemistry, vol. 78, no. 8, pp. 1533–1544, 2008.
- [80] O. Kasaikina, A. Golyavin, D. Krugovov, Z. Kartasheva, and L. Pisarenko, "Micellar catalysis in the oxidation of lipids," Moscow University Chemistry Bulletin, vol. 65, no. 3, pp. 206–209, 2010.
- [81] E. Y. Oganeseva, E. Bordubanova, Z. Popova, V. Bakunin, G. Kuz'Mina, and O. Parenago, "Influence of the conditions of the liquid-phase oxidation of hexadecane on the reaction mechanism," Petroleum Chemistry, vol. 44, no. 2, pp. 99–105, 2004.
- [82] "Detherm database 2015."
- [83] R. Battino, T. R. Rettich, and T. Tominaga, "The solubility of oxygen and ozone in liquids," Journal of physical and chemical reference data, vol. 12, no. 2, pp. 163–178, 1983.
- [84] J. Makranczy, K. Megyery-Balog, L. Rusz, and L. Patyi, "Solubility of gases in normal-alkanes," Hung. J. Ind. Chem., vol. 4, no. 2, pp. 269–280, 1976.
- [85] C. Blanc and M. Batiste, "Solubility coefficient of oxygen in paraffins," Bulletin du Centre de Recherches de Pau, vol. 4, no. 1, pp. 235–241, 1970.
- [86] M. Orozco and F. J. Luque, "Theoretical methods for the description of the solvent effect in biomolecular systems," Chemical reviews, vol. 100, no. 11, pp. 4187–4226, 2000.
- [87] M. H. Abraham, R. E. Smith, R. Luchtefeld, A. J. Boorem, R. Luo, and W. E. Acree, "Prediction of solubility of drugs and other compounds in organic solvents," Journal of pharmaceutical sciences, vol. 99, no. 3, pp. 1500–1515, 2010.
- [88] C. Mintz, J. Gibbs, W. E. Acree, and M. H. Abraham, "Enthalpy of solvation correlations for organic solutes and gases dissolved in acetonitrile and acetone," Thermochimica Acta, vol. 484, no. 1, pp. 65–69, 2009.



- [89] H. Struebing, Z. Ganase, P. G. Karamertzanis, E. Sioungkrou, P. Haycock, P. M. Piccione, A. Armstrong, A. Galindo, and C. S. Adjiman, "Computer-aided molecular design of solvents for accelerated reaction kinetics," Nature Chemistry, vol. 5, pp. 952–957, 2013.
- [90] J. T. Hynes, "Chemical reaction rates and solvent friction," Journal of Statistical Physics, vol. 42, no. 1-2, pp. 149–168, 1986.
- [91] H. S. El-Sheshtawy, U. Pischel, and W. M. Nau, "Solvent polarity affects h atom abstractions from c–h donors," Organic letters, vol. 13, no. 10, pp. 2694–2697, 2011.
- [92] S. A. Rice, Diffusion-limited reactions, ch. 2, pp. 3–45. Elsevier, 1985.
- [93] N. M. Vandewiele, G. R. Magoon, K. M. Van Geem, M.-F. Reyniers, W. H. Green, and G. B. Marin, "Kinetic modeling of jet propellant-10 pyrolysis," Energy & Fuels, vol. 29, no. 1, pp. 413–427, 2014.
- [94] E. Blurock, F. Battin-Leclerc, T. Faravelli, and W. H. Green, "Automatic generation of detailed mechanisms," in Cleaner Combustion, pp. 59–92, Springer, 2013.
- [95] C. W. Gao, J. W. Allen, W. H. Green, and R. H. West, "Reaction mechanism generator: Automatic construction of chemical kinetic mechanisms," Computer Physics Communications, 2016.
- [96] "Astm d7545 - 09 standard test method for oxidation stability of middle distillate fuels-rapid small scale oxidation test (rssot)."
- [97] K. Bacha, A. Ben-Amara, A. Vannier, M. Alves-Fortunato, and M. Nardin, "Oxidation stability of diesel/biodiesel fuels measured by a petrooxy device and characterization of oxidation products," Energy & Fuels, vol. 29, no. 7, pp. 4345–4355, 2015.
- [98] Y. Machado, U. Teles, A. D. Neto, T. Dantas, and J. Fonseca, "Determination of antioxidant depletion kinetics using {ASTMD} 7545 as the accelerated oxidation method," Fuel, vol. 112, no. 0, pp. 172 – 177, 2013.
- [99] "En pren 16091-2010 liquid petroleum products. middle distillates and fatty acid methyl ester fame fuels and blends. determination of oxidation stability by rapid small scale oxidation method," 2010.
- [100] G. Sarau, A. Bochmann, R. Lewandowska, and S. Christiansen, From Micro- to Macro-Raman Spectroscopy: Solar Silicon for a Case Study, Advanced Aspects of Spectroscopy, ch. 3. InTech, 2012.
- [101] S. Drevet, M. Ménard, and S. Souchon, "Internal report ifpen: R0520s vs/sb 074-15," tech. rep., IF-PEn, 2015.
- [102] "Chemkin-pro, 15131, reaction design: San diego, 2013."
- [103] W. H. Green, J. W. Allen, B. A. Buesser, R. W. Ashcraft, G. J. Beran, C. A. Class, C. Gao, C. F. Goldsmith, M. R. Harper, A. Jalan, M. Keceli, G. Magoon, D. M. Matheu, S. S. Merchant, J. A. D. Mo, S. Petway, S. Raman, S. S. J. Song, Y. Suleymanov, K. M. V. Geem, J. Wen, R. H. West, A. Wong, H. Wong, P. Yelvington, N. Yee, and J. Yu, "Rmg - reaction mechanism generator v4.0.1," tech. rep., <http://rmg.sourceforge.net/>, 2013.
- [104] K. M. Van Geem, M.-F. Reyniers, G. B. Marin, J. Song, W. H. Green, and D. M. Matheu, "Automatic reaction network generation using rmg for steam cracking of n-hexane," AIChE journal, vol. 52, no. 2, pp. 718–730, 2006.
- [105] M. R. Harper, K. M. Van Geem, S. P. Pyl, G. B. Marin, and W. H. Green, "Comprehensive reaction mechanism for n-butanol pyrolysis and combustion," Combustion and Flame, vol. 158, no. 1, pp. 16–41, 2011.

- [106] M. J. Frisch, G. W. Trucks, H. B. Schlegel, G. E. Scuseria, M. A. Robb, J. R. Cheeseman, G. Scalmani, V. Barone, B. Mennucci, G. A. Petersson, H. Nakatsuji, M. Caricato, X. Li, H. P. Hratchian, A. F. Izmaylov, J. Bloino, G. Zheng, J. L. Sonnenberg, M. Hada, M. Ehara, K. Toyota, R. Fukuda, J. Hasegawa, M. Ishida, T. Nakajima, Y. Honda, O. Kitao, H. Nakai, T. Vreven, J. A. Montgomery, Jr., J. E. Peralta, F. Ogliaro, M. Bearpark, J. J. Heyd, E. Brothers, K. N. Kudin, V. N. Staroverov, R. Kobayashi, J. Normand, K. Raghavachari, A. Rendell, J. C. Burant, S. S. Iyengar, J. Tomasi, M. Cossi, N. Rega, J. M. Millam, M. Klene, J. E. Knox, J. B. Cross, V. Bakken, C. Adamo, J. Jaramillo, R. Gomperts, R. E. Stratmann, O. Yazyev, A. J. Austin, R. Cammi, C. Pomelli, J. W. Ochterski, R. L. Martin, K. Morokuma, V. G. Zakrzewski, G. A. Voth, P. Salvador, J. J. Dannenberg, S. Dapprich, A. D. Daniels, Á. Farkas, J. B. Foresman, J. V. Ortiz, J. Cioslowski, and D. J. Fox, "Gaussian 09 Revision D.01." Gaussian Inc. Wallingford CT 2009.
- [107] M. S. Contreras, T. De Bruin, P. Mougin, and H. Toulhoat, "Thermochemistry of 1-methylnaphthalene hydroconversion: Comparison of group contribution and ab initio models," *Energy & fuels*, vol. 27, no. 9, pp. 5475–5482, 2013.
- [108] M. H. Keshavarz, M. Zamani, F. Atabaki, and K. Hosseini Monjezi, "Reliable approach for prediction of heats of formation of polycyclic saturated hydrocarbons using recently developed density functionals," *Computational and Theoretical Chemistry*, vol. 1011, pp. 30–36, 2013.
- [109] A. Osmont, L. Catoire, I. Gökalp, and M. T. Swihart, "Thermochemistry of cc and ch bond breaking in fatty acid methyl esters," *Energy & fuels*, vol. 21, no. 4, pp. 2027–2032, 2007.
- [110] L. Catoire, M. Yahyaoui, A. Osmont, I. Gökalp, M. Brothier, H. Lorcet, and D. Guénadou, "Thermochemistry of compounds formed during fast pyrolysis of lignocellulosic biomass," *Energy & Fuels*, vol. 22, no. 6, pp. 4265–4273, 2008.
- [111] A. Osmont, L. Catoire, T. M. Klapötke, G. L. Vaghjiani, and M. T. Swihart, "Thermochemistry of species potentially formed during nto/mmh hypergolic ignition," *Propellants, Explosives, Pyrotechnics*, vol. 33, no. 3, pp. 209–212, 2008.
- [112] A. Osmont, M. Yahyaoui, L. Catoire, I. Gökalp, and M. T. Swihart, "Thermochemistry of co,(co) o, and (co) c bond breaking in fatty acid methyl esters," *Combustion and Flame*, vol. 155, no. 1, pp. 334–342, 2008.
- [113] I. Alecu and D. G. Truhlar, "Computational study of the reactions of methanol with the hydroperoxyl and methyl radicals. 1. accurate thermochemistry and barrier heights," *The Journal of Physical Chemistry A*, vol. 115, no. 13, pp. 2811–2829, 2011.
- [114] I. Alecu and D. G. Truhlar, "Computational study of the reactions of methanol with the hydroperoxyl and methyl radicals. 2. accurate thermal rate constants," *The Journal of Physical Chemistry A*, vol. 115, no. 51, pp. 14599–14611, 2011.
- [115] X. Xu, I. Alecu, and D. G. Truhlar, "How well can modern density functionals predict internuclear distances at transition states?," *Journal of Chemical Theory and Computation*, vol. 7, no. 6, pp. 1667–1676, 2011.
- [116] J. Zheng, R. Meana-Pañeda, and D. G. Truhlar, "Mstov version 2013: A new version of the computer code for the multi-structural torsional anharmonicity, now with a coupled torsional potential," *Computer Physics Communications*, vol. 184, no. 8, pp. 2032–2033, 2013.
- [117] J. Zheng, S. L. Mielke, K. L. Clarkson, and D. G. Truhlar, "Mstov: A program for calculating partition functions, free energies, enthalpies, entropies, and heat capacities of complex molecules including torsional anharmonicity," *Computer Physics Communications*, vol. 183, no. 8, pp. 1803–1812, 2012.
- [118] Online manual of RMG-Py: <http://reactionmechanismgenerator.github.io/RMG-Py/users/rmg/index.html>.
- [119] s. g. RMG, "21- introduction to rmg-py," tech. rep., RMG study group, 2015.

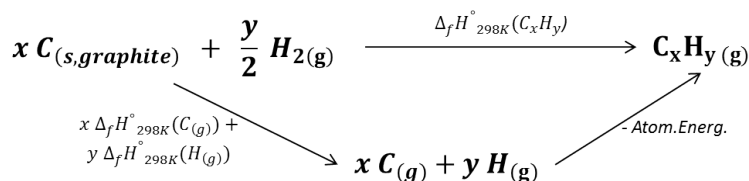
- [120] P. Linstrom and E. W.G. Mallard, "Nist chemistry webbook," NIST Standard Reference Database Number 69, National Institute of Standards and Technology, 2001.
- [121] J. Rowley, W. V. Wilding, J. L. Oscarson, Y. Yang, and N. Giles, "Design institute for physical properties data," (DIPPR-AIChE), 2011.
- [122] B. Boss and R. Hazlett, "Oxidation of hydrocarbons in the liquid phase: n-dodecane in a borosilicate glass chamber at 200c," Canadian Journal of Chemistry, vol. 47, no. 22, pp. 4175–4182, 1969.
- [123] L. Liu and Q.-X. Guo, "Isokinetic relationship, isoequilibrium relationship, and enthalpy-entropy compensation," Chemical reviews, vol. 101, no. 3, pp. 673–696, 2001.
- [124] A. Goosen and D. H. Morgan, "Autoxidation of nonane and decane: a product study," Journal Chemical Society , Perkin Trans. 2, pp. 557–562, 1994.
- [125] L. D. T. Câmara, N. C. Furtado, R. S. Monteiro, D. A. Aranda, and C. Taft, "Molecular orbital approach for investigating the kinetics of cracking hydroperoxides," Journal of Molecular Structure: THEOCHEM, vol. 776, no. 1-3, pp. 41–45, 2006.
- [126] K. Chatelain, A. Nicolle, A. Ben Amara, L. Catoire, and L. Starck, "Wide range experimental and kinetic modeling study of chain length impact on n-alkanes autoxidation," Energy & Fuels, vol. 30, no. 2, pp. 1294–1303, 2016.
- [127] J. Benton and M. Wirth, "Position of radical attack during oxidation of long-chain paraffins," Nature, 1953.
- [128] B. D. Boss, R. N. Hazlett, and R. L. Shepard, "Analysis of normal paraffin oxidation products in the presence of hydroperoxides," Analytical Chemistry, vol. 45, no. 14, pp. 2388–2392, 1973.
- [129] B. Slakman, K. Chatelain, A. B. Amara, L. Starck, M. Matrat, L. Catoire, A. Nicolle, and R. West, "Liquid-phase mechanism generation for application to fuel oxidation," in ISCRE, 2016.

# 1 ESC supplementaries

## Formation enthalpy calculations

Standard formation enthalpy calculations can be performed using different methods: the most standard one is the atomisation approach and more sophisticated one is to use reaction enthalpy approach.

In the first case, a Hess cycle is drawn for each formation enthalpy of interest, as presented in Figure 4 with a general hydrocarbon,  $C_xH_y$ . The first path is the formation enthalpy definition, with the formation of the hydrocarbon from its standard constituents (graphite carbon and molecular hydrogen) and the second path is going through atomic carbon and atomic hydrogen at gas state. According to this cycle formation enthalpy at 298 K can be obtained using Equation 1 and Equation 2. This cycle needs to include molecular oxygen and atomic oxygen for oxygenated hydrocarbons.



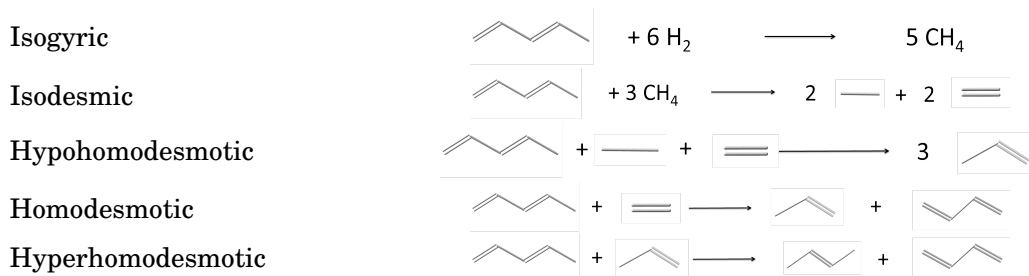
**Figure 4:** Thermodynamic cycle to determine formation enthalpy at 298 K for a given hydrocarbon  $C_xH_y$ . *Atom.Energ.* correspond to atomization energy.

$$\Delta H_f^\circ(298K)C_xH_y = x\Delta H_f^\circ(298K)C_{(g)} + y\Delta H_f^\circ(298K)H_{(g)} - Atom.Energ. \quad (1)$$

$$Atom.Energ. = xE(C_{(g)}) + yE(H_{(g)}) - E(C_xH_{y(g)}) \quad (2)$$

Main drawbacks are the technique accuracy which is dependant to the theory level used for both C, H, O atomization energies and molecule energy calculations. Whereas, using corrected atomisation energies, like the coefficient proposed by Osmont et al [109, 110, 111, 112], results obtained at a B3LYP theory level may have reasonable uncertainties within 1-2 kcal/mol with some higher errors related to specific compounds. This technique was applied for Fatty Acids Methyl Esters (FAME), radicals or energetic materials families and gives the same range of errors. Coefficients need to be set for each molecules family at a given theory level. Uncertainties of the technique seem reasonable regarding the experimental accuracy limitations and the lack of data for those specific compounds.

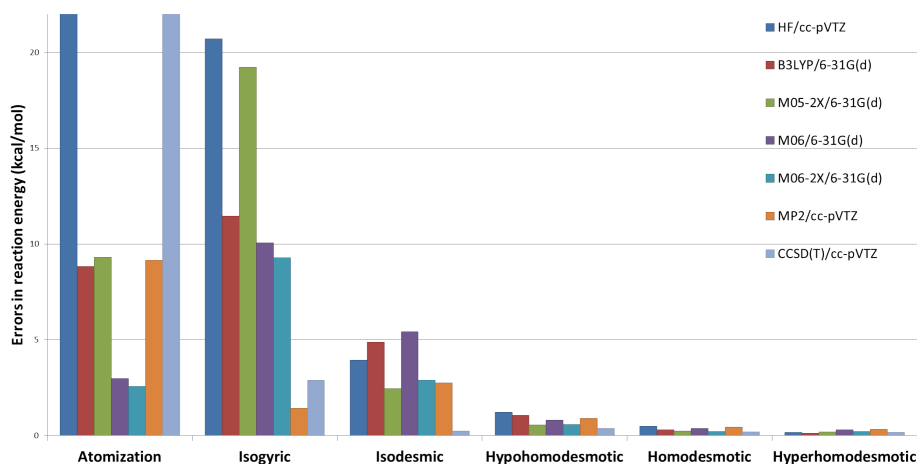
The second method is the Isogyric/Homodesmotic approach [107], summing reaction enthalpies to minimize errors by cancelling them. A new hierarchy in homodesmotic reactions presented by Wheeler et al. [17] defined with five level of reactions for hydrocarbons: Isogyric, Isodesmic, Hypohodesmotic, Homodesmotic, Hyperhomodesmotic where precision in the molecule bond definition is increasing from isogyric to hyperhomodesmotic. A full definition for each level is presented in the publication [17], an overview of level differences is presented in Figure 5.



**Figure 5:** General presentation of each hierarchy defined by Wheeler et al [17].

Considering only homodesmotic and hyperhomodesmotic, enthalpy formation estimations presented by Wheeler et al. [17] for hydrocarbons are barely dependent of theory level as it is presented in Figure 6.

This technique permits formation enthalpy calculations with very low errors ( $\leq 1$  kcal/mol) even with Hartree-Fock level calculations with the presented validation data set.



**Figure 6:** Comparison of average errors using atomization energies and the new homodesmotic hierarchy presented by Wheeler et al. [17] obtained for conjugated hydrocarbons or not against common theory levels. The two cut off values are respectively from left to right 342 and 36 kcal/mol.

## Gaussian input file

Here is presented a typical Gaussian input file for geometry optimization of decane (opt keyword) using M062X method and the aug-cc-pvtz basis set. Freq and nosymm respectively stands for frequency calculation and no symmetry assumptions in the geometry. The line %nprocshared: specify the number of processor to use, %mem specify the physical memory amount to use.

## Rotor consideration for geometry optimisations

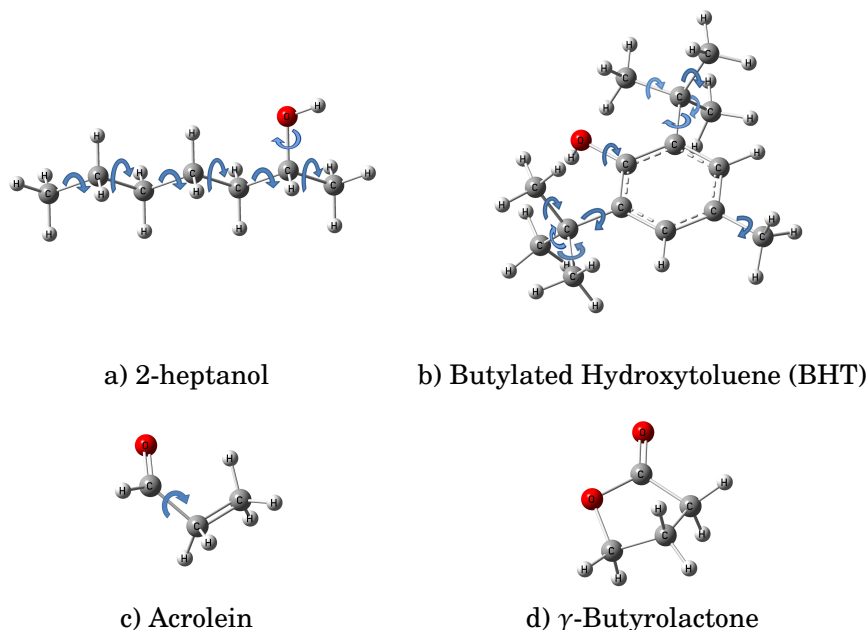
In order to identify the lowest energy conformers. Geometry optimisations must consider multiple dihedral torsion as presented in Figure 7. As presented in Table 2, there is huge number of potential conformers according to the number of rotors considered inside a molecule and according to the number of rotations performed on rotor.

**Table 1:** Gaussian input file example. The effective input file is within the section filled in grey and comments on each line are in parenthesis.

(Number of processor)	%nprocshared=8			
(Memory amount)	%mem=20GB			
(Name of the checkpoint)	%chk=decaneOPT2.chk			
(Route section)	# M062X/aug-cc-pvdz Freq opt nosymm			
(Title)	conformer 1			
(Radicals & Multiplicity)	0 1			
(Cartesian coordinates)	C	-3.167229090347	0.097788855374	0.00184111032
	H	-3.55059478649	1.123385239743	0.0028037597
	H	-3.572144925725	-0.407700684153	-0.882337799736
	H	-3.572607466229	-0.40953118667	0.884759610382
	C	-1.055239899403	-1.349426839871	0.000889151444
	C	0.477596158603	-1.386959108493	0.001289309279
	H	-1.432265701379	-1.89531736006	0.877776213377
	H	-1.431764936103	-1.89348186379	-0.877351495101
	H	0.853733066133	-0.840653830404	-0.875590757985
	H	0.85322646603	-0.842447087499	0.879499892309
	C	1.057493222119	-2.806807989293	0.000005202967
	C	2.590476749388	-2.84416695366	0.000419384509
	H	0.681887121666	-3.35131282287	-0.878179418119
	H	0.681368075225	-3.353105681714	0.876854299033
	C	3.170373815985	-4.264015832712	-0.00086472637
	H	2.966601895555	-2.297869256341	-0.876429708696
	H	2.966082848124	-2.299662118231	0.878604007595
	C	4.703209873717	-4.301548097698	-0.000464568847
	H	2.794236910379	-4.810321113789	0.876015340066
	H	2.794743510141	-4.808527850638	-0.879075309441
	H	5.080235675525	-3.755657575866	-0.877351629222
	H	5.079734909121	-3.757493073241	0.877776080203
	C	5.283863077014	-5.721120807664	-0.001791223201
	H	4.907519850097	-6.266275897915	0.874584312884
	H	4.907982796264	-6.264440733028	-0.879503467189
	C	6.815199068957	-5.748763784858	-0.00141651579
	H	7.198564771561	-6.774360166808	-0.002379153376
	H	7.220577449343	-5.241443744565	-0.884335014013
	H	7.220114894975	-5.243274237931	0.882762397308
	C	-1.635893097964	0.070145871351	0.002215803559
	H	-1.25954987249	0.615300958715	-0.874159734061
	H	-1.260012809794	0.613465794583	0.879928046209

Number of Dihedrals	1	3	5	7	9	11	13	15
2 Rotations per rotor	2	8	32	128	512	2048	8192	32768
3 Rotations per rotor	3	27	243	2187	19683	177147	1594323	14348907

**Table 2:** Number of conformers obtained for C<sub>2</sub>-C<sub>16</sub> paraffins with 2 and 3 rotations per rotor following the expression:  $Rot^{Number\ dihedrals}$ . With  $Rot$  corresponding to the number of twist per rotors and  $Number\ dihedrals = N_{carbons} - 1$  for n-paraffins



**Figure 7:** Free rotors in 2-heptanol, Butylated Hydroxytoluene (BHT), acrolein and  $\gamma$ -Butyrolactone.

## .2 RMG supplementaries

### .2.1 Reactivity difference between RMG3 and RMG4 mechanisms

In [Figure 8](#), significant reactivity differences are presented between RMG-3.2.1 and RMG 4.0.1 mechanisms obtained with identical input files. Those mechanisms were used in IFP-kinetics solvers with identical input conditions. The IP plateau equals to  $10^8$ s is a manual cut off, real values are higher than this value. In all presented plots, IP is considered as a 5 % fuel conversion. In all cases presented here the RMG 4.0.1 mechanisms are almost unreactive (with very slow fuel conversion rate) until reaching a certain temperature. Those results are unexpected according to the correction on free energy of solvation calculation implemented since RMG 4.0.1 and represented in section([Appendix .2.2](#)).

### .2.2 Correction on the Free energy of solvation calculation implemented since RMG4

As written in the RMG-Java manual [[103](#)], the liquid phase corrections implemented for thermochemistry in RMG-Java 3.2.1 contained miscalculations. This section aims to illustrate this problem pointed out in the manual by assessing thermochemistry predictions of species with both versions against experimental data. While Species Free Energy of formation ( $\Delta G_f$ ) are equals with both versions ([Figure 9c](#)), the enthalpy and the entropy of formation are closer to experimental data with RMG 4.0.1 for the 4 alkanes tested ([Figure 9a-Figure 9c](#)). In addition to these significant gaps, the temperature dependance of the  $\Delta G_{solv}$  of 1-decanol is not in agreement with experimental data with RMG 3.2.1 as observed in [Figure 9d](#). Similarly to [Figure 9c](#), both versions predict well the  $\Delta G_{solv}$  and discrepancies are observed at higher temperature.

Thus, the RMG-Hybrid version use RMG-Java 4.0.1 thermochemistry calculation rather than RMG-Java 3.2.1.

### .2.3 RMG input file

This is an RMG input file example for liquid phase generation. The input file is under Java syntax which means `"/"` are commented lines. In this example, two thermo library are provided "GRI- Mech" and the "Primary thermo Library". As the lines with the "seed mechanism" are commented, they are not used.

**Table 3:** RMG input file example. The effective input file is within the section filled in grey and comments on each line are in parenthesis.

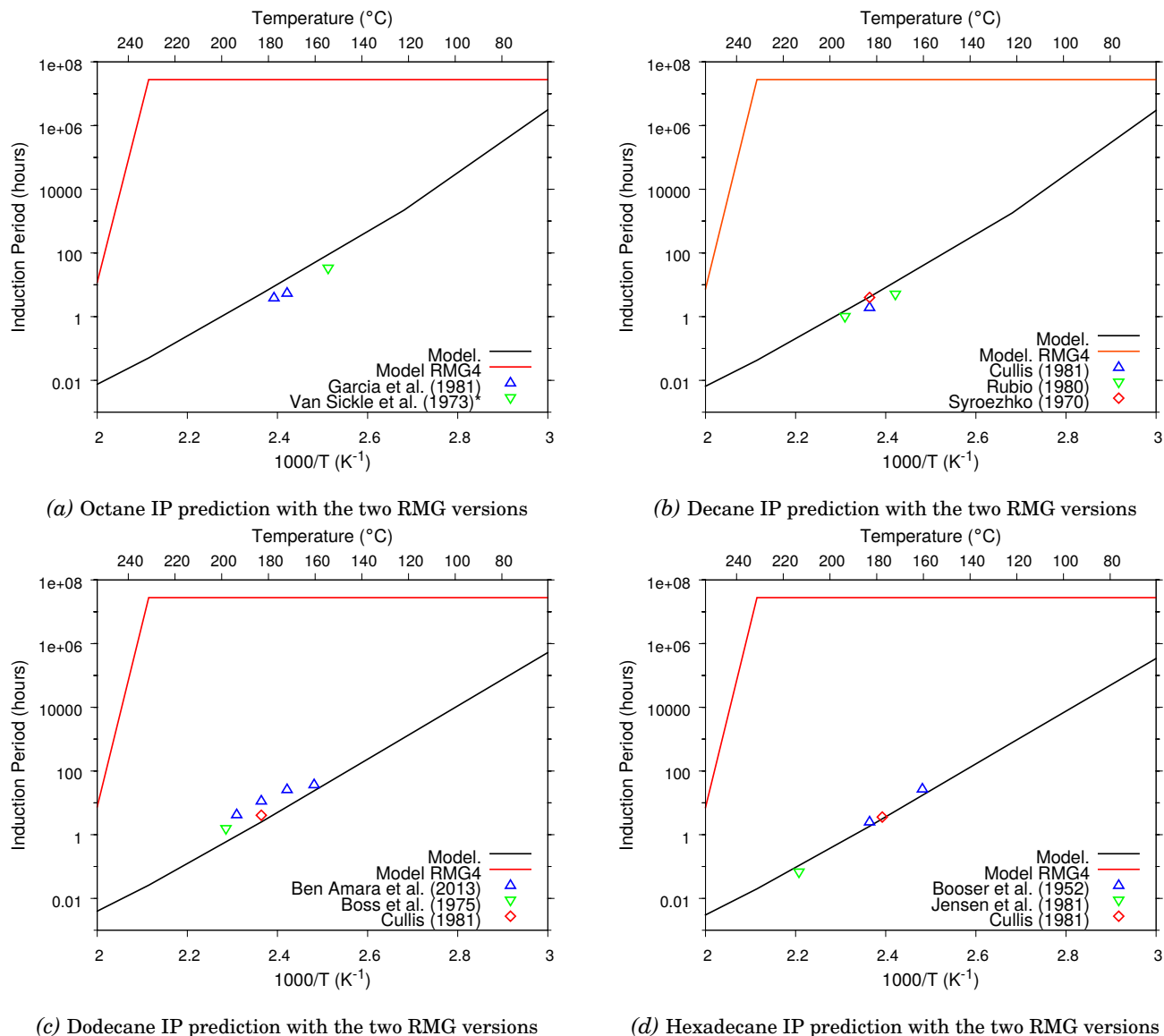
<i>(Name of the database)</i>	Database: RMG_database
<i>(Thermo library section)</i> <i>(1st thermo library)</i>	PrimaryThermoLibrary: Name: GRIMech3.0 Location: GRI-Mech3.0
<i>(2nd thermo library)</i>	Name: RMG-minimal Location: primaryThermoLibrary
<i>(End of section)</i>	END
<i>(Transport library section)</i> <i>(Name of the library)</i>	PrimaryTransportLibrary: Name: GRIMech3.0 Location: GRI-Mech3.0
<i>(End of the section)</i>	END
<i>(Option to read a restart file)</i> <i>(Option to write the restart)</i>	ReadRestart: no WriteRestart: no
<i>(Temperature range)</i> <i>(Pressure range)</i>	TemperatureModel: Constant (K) 500 PressureModel: Constant (atm) 1
<i>(Liquid phase keyword)</i> <i>(Solvent name)</i> <i>(Viscosity in Pa.s-1)</i>	/// THESE ARE THE IMPORTANT PARTS FOR LIQUID SIMULATIONS EquationOfState: Liquid Solvation: on octane Diffusion: on 1.0e-3
<i>(Species list and concentration)</i>	InitialStatus:  Octane (mol/cm3) 6.154e-3 1 C 0 {3,S} 2 C 0 {4,S} 3 C 0 {1,S} {5,S} 4 C 0 {2,S} {6,S} 5 C 0 {3,S} {7,S} 6 C 0 {4,S} {8,S} 7 C 0 {5,S} {8,S} 8 C 0 {6,S} {7,S}
<i>(Species are separated with a blank line)</i>	
<i>(Constant concentration keyword to apply on a specific species)</i>	O2 (mol/cm3) 4.953e-6 ConstantConcentration 1 O 1 {2,S} 2 O 1 {1,S}
<i>(End of species list section)</i>	END
<i>(Inert gas declaration)</i>	InertGas: N2 (mol/cm3) 0.0 Ar (mol/cm3) 0.0 END
<i>(RMG options)</i>	SpectroscopicDataEstimator: off PressureDependence: off
<i>(Termination criteria)</i> <i>(in this case 10 sec. reaction time and the 0.5 error tolerance)</i>	FinishController: (1) Goal ReactionTime: 10 (sec) (2) Error Tolerance: 0.5
<i>(Solver selection)</i> <i>(Output solver time step)</i> <i>(Solver tolerances)</i>	DynamicSimulator: DASSL TimeStep: AUTO Atol: 1e-18 Rtol: 1e-8
<i>(Primary kinetic library)</i>	PrimaryKineticLibrary: END
<i>(Reaction library)</i>	ReactionLibrary: END
<i>(Seed mechanism, in this case not used " / / ")</i>	SeedMechanism: //Name: GRIMech3.0 //Location: GRI-Mech3.0 END
<i>(Mechanism units)</i>	ChemkinUnits: A: moles Ea: cal/mol

## .2.4 Molecule identification and thermo-kinetic calculations

### Group identification

In RMG, molecules are represented using the bond graph representation (called adjacency list). From this identification, molecules are identified according chemical groups defined in RMG database, as presented in





**Figure 8:** IP validation with both RMG Java version: 3.2.1 and 4.0.1

**Figure 3.18.** Thus, the algorithm identifies molecules by chemical groups in order to estimate both thermochemistry and kinetic rates. Each group is represented with individual elements (Table 4) representing atoms and bonds linking it to other atoms. presents elements used to describe each group. Additional information on group identification are available in RMG manual.

Thanks to this tabular, we can identify 3 Cs, 1 CO and 1 Od on the butanone.

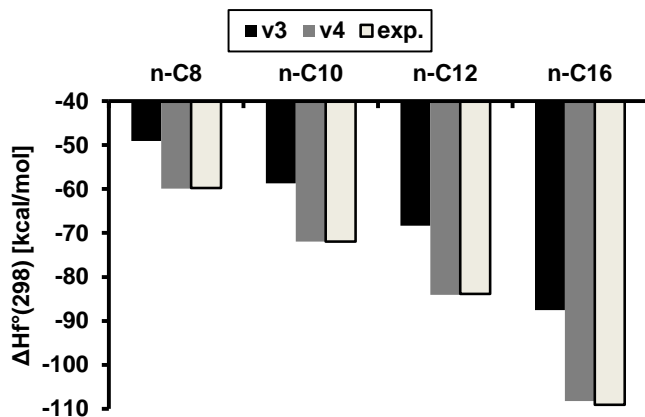
## .2.5 RMG thermochemistry calculation

### Matching thermo libraries

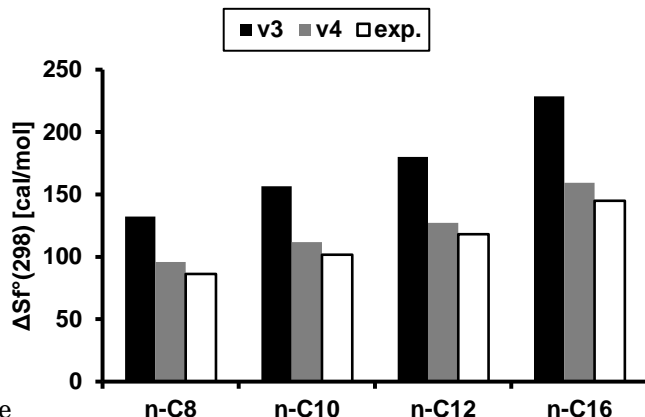
When generating the species, algorithm is trying to find exact species adjacency list in selected libraries mentioned in the input file and return the first match. However if no match is found, the algorithm use as a default the Group Contribution method.

### Group Contribution Method

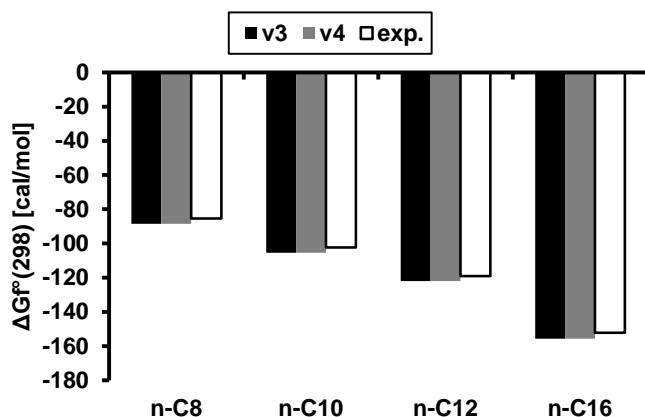
By default, the algorithm use a group identification based on its Elements composition (presented in Table 4) and specify surrounding atoms to calculate thermochemical data. Each group entry contains a value



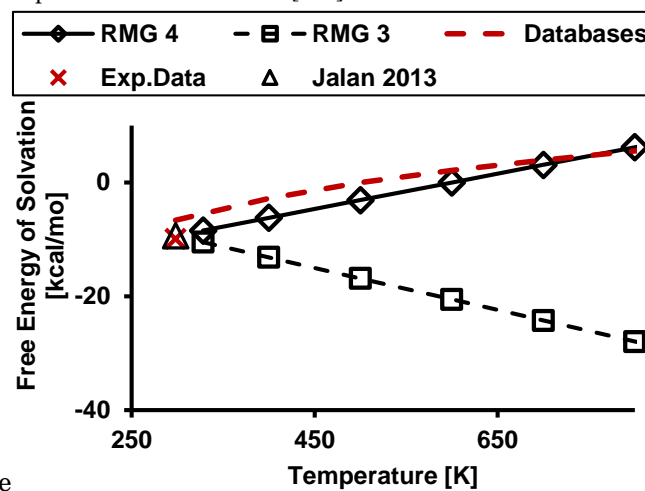
(a) Formation enthalpy predictions of both RMG versions compared to literature data. [120]



(b) Formation entropy predictions of both RMG versions compared to literature data. [120]



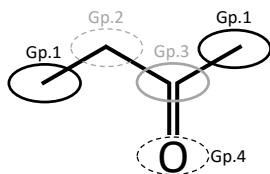
(c) Formation free energy predictions of both RMG versions compared to literature data. [120]



(d) The temperature dependence of  $\Delta G_{solv}$  obtained for 1-decanol with both RMG versions validated against literature results. "Databases result" corresponds to  $\Delta G_{solv}$  reconstructed from liquid and gas phase data[121]. "Exp Data" and "Jalan 2013" are respectively extracted from the validation data of Jalan et al.[15].

**Figure 9:** Accuracy of thermochemistry calculations of RMG 3.2.1 and RMG 4.0.1.

for Cp300, Cp400, Cp500, Cp600, Cp800, Cp1000, Cp1500, H298K, S298K. From the previous Butanone example, four groups are identified. Then, the thermochemistry is calculated summing individual groups values, as presented for formation enthalpy calculation on (3)



- Group 1: 1 Cs linked to 1 carbon
- Group 2: 1 Cs linked to 2 carbons
- Group 3: 1 CO linked to 2 carbons and 1 oxygen
- Group 4: 1 Od linked to a carbon

**Figure 10:** Illustration of the group representation used in RMG

$$\Delta_f H_{298K}^\circ = \sum_i Gp.(i) = 2 \times Gp.1 + Gp.2 + Gp.3 + Gp.4 \quad (3)$$

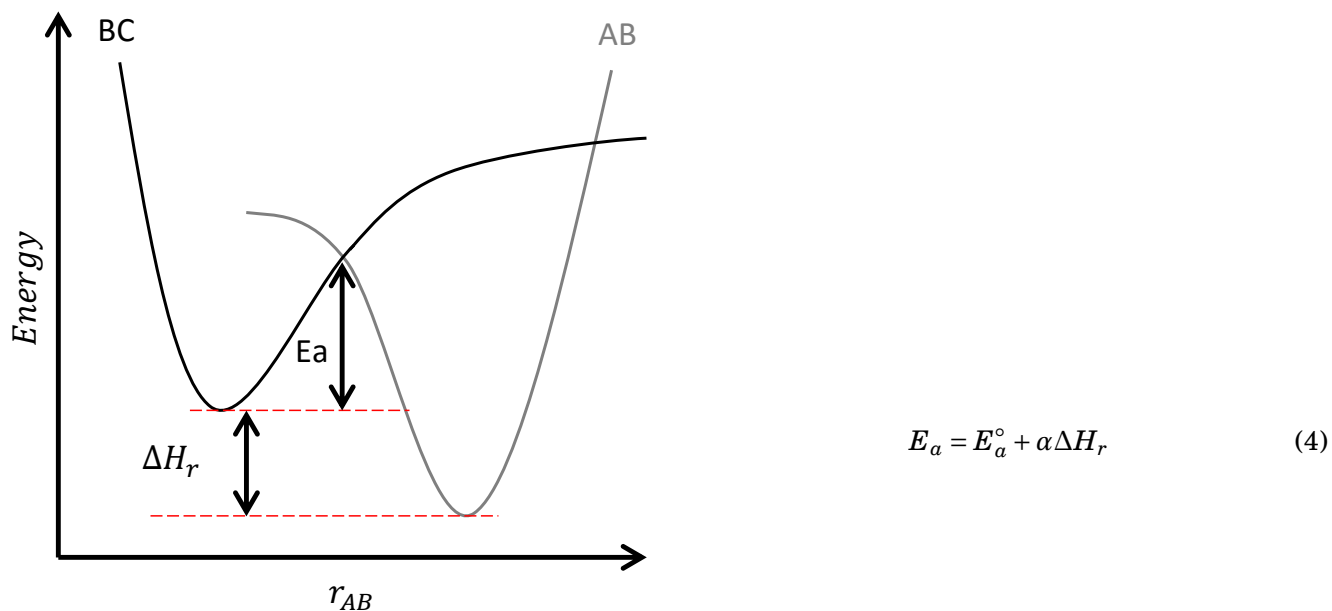
## 2.6 RMG kinetic rate estimation

RMG algorithm estimates kinetics based on groups identifications implemented inside each chemical families. Each chemical family contain its own reaction parameters database ( $A$ ,  $E_a$ ,  $n$ ) for a given group.

**Table 4:** Elements used in the group definition

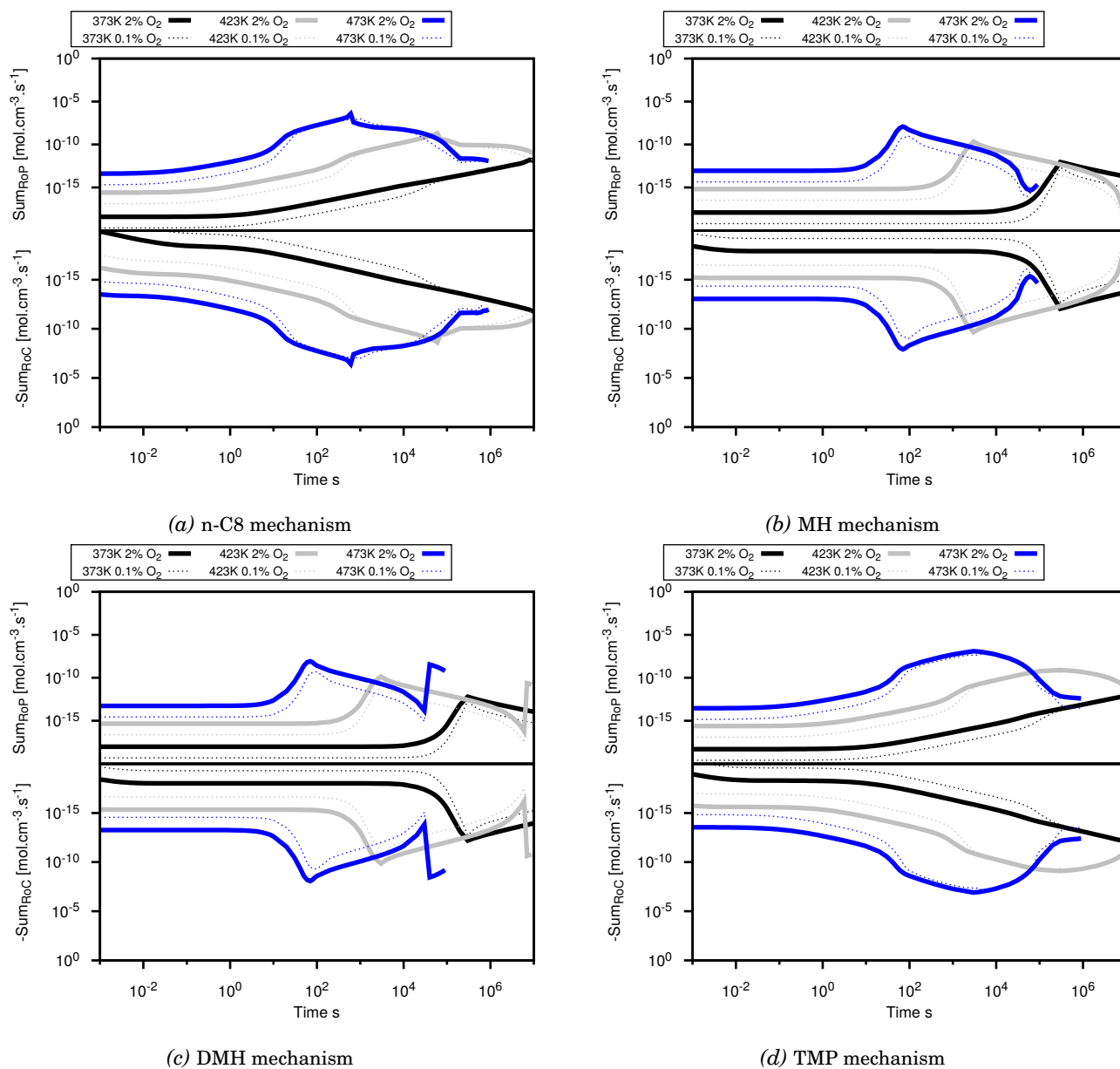
Symbol	Definition
Cs	Carbon bonded to four single bonds
Cd	Carbon bonded to a double bond and two single bonds. (The other end of the double bond is carbon)
Cdd	Carbon bonded to two double bonds
Ct	Carbon bonded to a triple bond and single bond
Cb	Carbon bonded to two benzene bonds and a single bond. (The carbon belongs to only one benzene ring)
Cbf	Carbon bonded to three benzene bonds (the carbon belongs to two or three benzene rings)
CO	Carbon bonded to a double bond and two single bonds. (The other end of the double bond is oxygen)
Os	Oxygen bonded to two single bonds
Od	Oxygen bonded to a double bond
Oa	Oxygen triplet
R	Any atom
R!H	Any non-hydrogen atom

There are three formats for kinetic rates in RMG, Arrhenius ( $E_a$  and  $A$  provided), modified Arrhenius ( $E_a$ ,  $A$  and  $n$  provided) and Evans Polanyi ( $A$ ,  $n$ ,  $E_a^\circ$  and  $\alpha$  provided). The Evans Polanyi calculates  $E_a$  based on empirical corrections ( $E_a^\circ$  and  $\alpha$ ) to the ( $\Delta H_r$ ), as presented in [Figure 11](#) and (4).

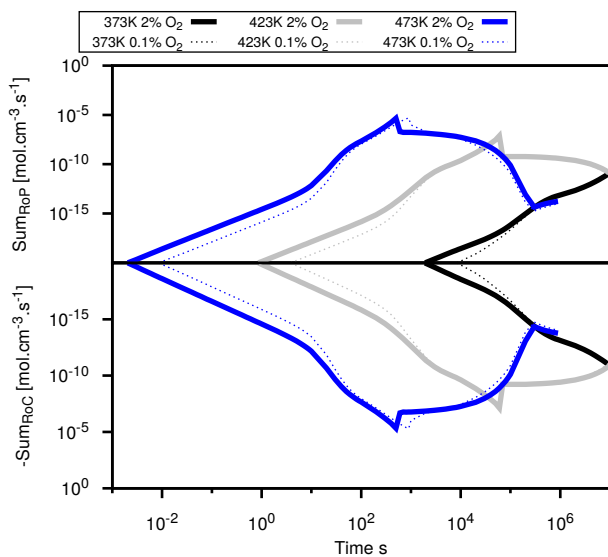
**Figure 11:** Presentation of the Evans-Polanyi expression to obtain  $E_a$  from the empirical law (4).

### 3 Complementary iso-paraffins mechanisms analyses

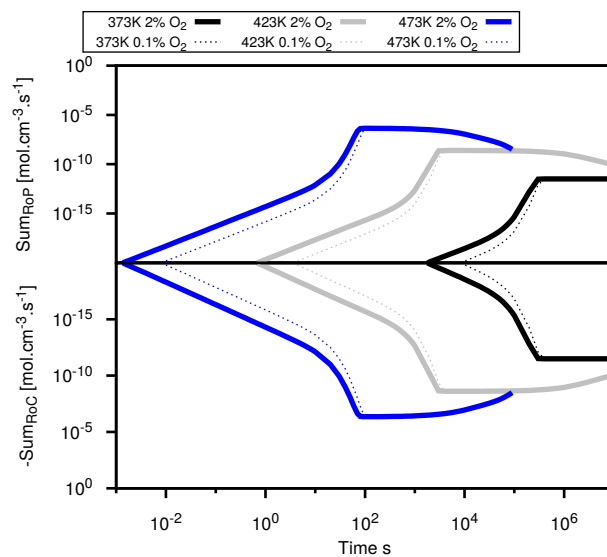
Complementary to results presented in the main text body, Figure 13 and Figure 12 present the sum of RoC and RoP analyses respectively on °OH and HO<sub>2</sub><sup>o</sup>.



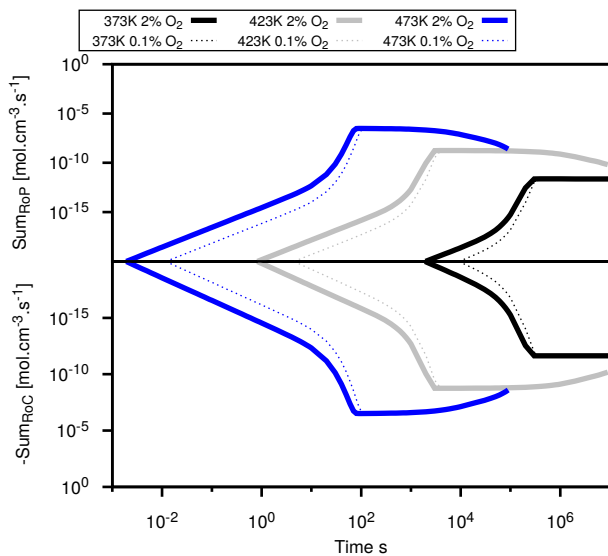
**Figure 12:** Impact of both temperature and oxygen concentration on the sum of HO<sub>2</sub><sup>o</sup> radical RoP and RoC respectively presented on upper and lower part of each chart.



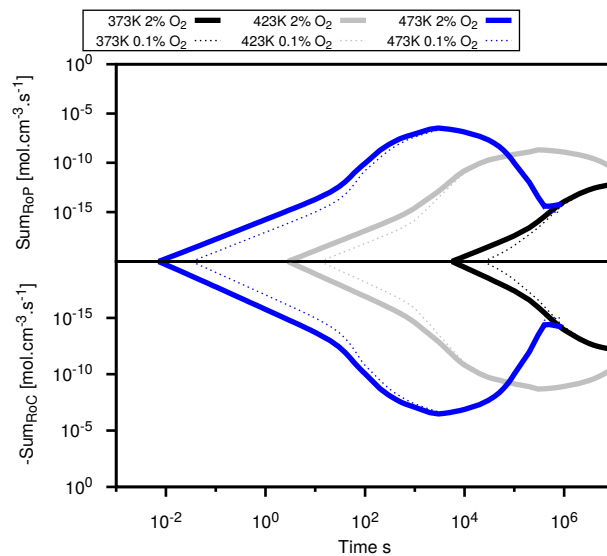
(a) n-C8 mechanism



(b) MH mechanism



(c) DMH mechanism

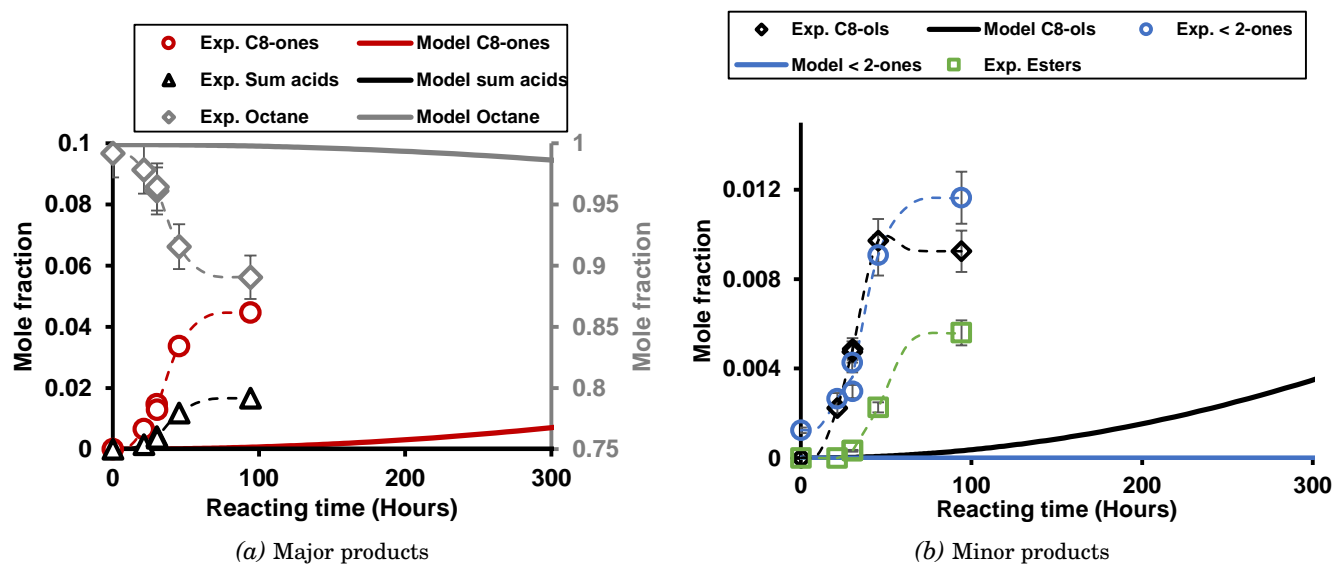


(d) TMP mechanism

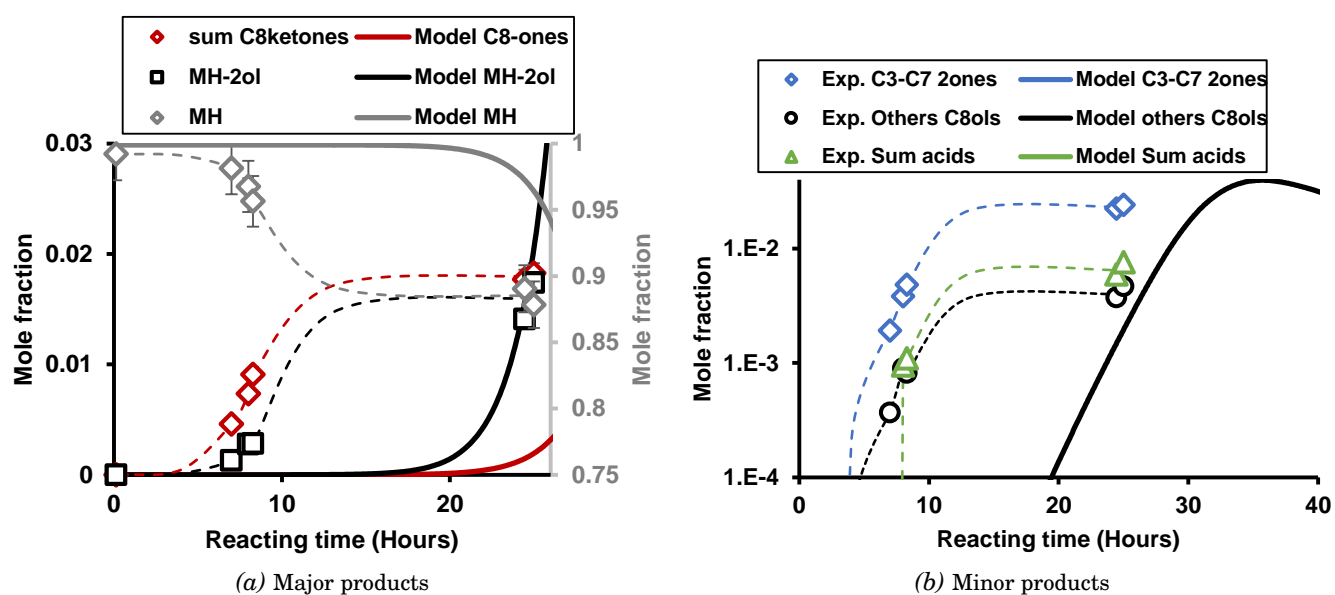
**Figure 13:** Impact of both temperature and oxygen concentration on the sum of  $\text{OH}^\circ$  radical RoP and RoC respectively presented on upper and lower part of each chart.

## 4 Additional figures for species profiles agreements

Identical figures as [Figure 4.43](#) and [Figure 4.44](#) without the IP normalization.



**Figure 14:** Species profiles agreement between experimental results and model predictions on n-C8 at 383K and 10 bars.



**Figure 15:** Species profiles agreement between experimental results and model predictions on MH at 383K and 10 bars.

**Titre : Stabilité à l'oxydation des carburants en phase liquide**

**Mots clés : Autoxydation, phase liquide, carburant modèle, n-paraffines, iso-paraffines, mécanismes cinétiques détaillés**

**Résumé : La stabilité des carburants en phase liquide est de premier ordre dans le domaine du transport. Par exemple, les carburants, les lubrifiants ou les additifs doivent être stables de leur production jusqu'à leur utilisation. Cette thèse a pour but de développer et de valider une méthodologie alliant l'acquisition de données expérimentales et le développement de modèles cinétiques pour l'autoxydation en phase liquide. Expérimentalement, une approche complémentaire a été mise en place pour obtenir à la fois des données de réactivité globales via un appareil PetroOxy et des profils d'espèces via un autoclave instrumenté.**

**Numériquement, une méthodologie basée sur un générateur de mécanismes est proposée pour obtenir une chimie détaillée en phase liquide. Les paraffines linéaires et branchées sont étudiées comme des carburants modèles représentatifs de l'autoxydation de carburants réels afin de valider l'approche proposée. Ces familles chimiques sont représentatives de la composition des carburants réels et alternatifs.**

**La réactivité des n-paraffines de C<sub>8</sub> à C<sub>16</sub> ainsi que d'isomères de l'octane a été étudiée en PetroOxy sur la gamme de température 373-433 K. Puis, des profils d'espèces détaillés de la phase gaz et de la phase liquide ont été obtenus durant l'étude de l'oxydation du n-C<sub>8</sub> et du 2-methylheptane dans un autoclave à 383 K et 10 bars. Des mécanismes cinétiques détaillés ont été développés pour toutes les molécules jusqu'à C<sub>14</sub>. Les mécanismes reproduisent qualitativement la formation des espèces majoritaires lors de l'autoxydation des alcanes ainsi que les tendances observées liées à la longueur de chaîne et la ramification. L'analyse des mécanismes cinétiques a mis en avant le rôle prédominant des radicaux peroxy (ROO) et peroxy-hydroperoxyde (HOOQOO) dans la consommation de carburants modèles.**

**Cette étude a permis d'améliorer la compréhension des processus d'autoxydation des alcanes linéaires et branchés. L'étude de nouveaux systèmes permettra d'améliorer la compréhension globale des processus d'autoxydation et, de réduire l'écart de compréhension existant entre l'autoxydation des carburants réels et des carburants modèles.**

**Title : Oxidation stability of fuel in liquid phase**

**Keywords : Autoxydation, liquid phase, fuel, surrogates, n-paraffins, iso-paraffins, detailed chemical kinetic model**

**Abstract : Liquid phase stability is a major concern in the transportation and the energy fields. Relevant examples are fuels, lubricants and additives which have to be stable from their production to their application (engine, combustors). This thesis aims to develop and validate a complete methodology combining both experimental data acquisition and the development of kinetic models for liquid phase autoxydation.**

**The experimental methodology is based on a complementary approach to obtain (i) a global reactivity descriptor (Induction Periods) and (ii) detailed species profiles respectively using a PetroOxy device and an instrumented autoclave. Numerically, the presented methodology includes detailed liquid phase mechanisms generation with an automatic mechanism generator (RMG). Normal and iso-paraffins were selected as fuel surrogates for autoxydation to validate the developed methodology. They were selected regarding their large contribution in fuel composition and their growing interest as drop-in fuels.**

**The reactivity of both n-paraffins from C<sub>8</sub> to C<sub>16</sub> and several C<sub>8</sub> iso-paraffins was investigated over a wide temperature range (373-433 K) in the PetroOxy with liquid phase analyses. Then, detailed species profiles from the autoxydation of both n-octane and 2-methylheptane in autoclave were obtained at 383 K and 10 bars. Detailed liquid phase mechanisms were developed for all molecules tested up to C<sub>14</sub>. Mechanisms qualitatively reproduce the overall phenomenology of the chain length, the branching and the major species profiles observed experimentally. Mechanisms analysis allow to identify the main consumption pathways of alkanes through peroxy (ROO) and peroxy-hydroperoxide radicals (HOOQOO) over the temperature range investigated (373-473 K).**

**This study permitted to increase the comprehension of autoxydation processes involved in normal and branched alkanes. The study of new chemical systems will increase the global comprehension of autoxydation processes and *in fine* it will reduce the gap between the current autoxydation knowledge and the real fuel autoxydation.**

